Transactions of the ASME, Journal of Heat Transfer (ISSN 0022-1481) is published monthly by The American Society of Mechanical Engineers, Three Park Avenue, New York, NY 10016. Periodicals postage paid at New York, NY and additional mailing offices. POSTMASTER: Send address changes to Transactions of the ASME, Journal of Heat Transfer, c/o THE AMERICAN SOCIETY OF MECHANICAL ENGINEERS, 22 Law Drive, Box 2300, Fairfield, NJ 07007-2300. **CHANGES OF ADDRESS** must be received at Society headquarters seven weeks before they are to be effective. Please send old label and new address. **STATEMENT from By-Laws.** The Society shall not be responsible for statements or opinions advanced in papers or ... printed in its publications (B7.1, Para. 3).

Journal of Heat Transfer

Published Monthly by ASME

VOLUME 133 • NUMBER 3 • MARCH 2011

Special Issue on Advanced Thermal Processing

GUEST EDITORIAL

RESEARCH PAPERS

TECHNOLOGY REVIEWS

(**Contents continued on inside back cover**)

This journal is printed on acid-free paper, which exceeds the ANSI Z39.48-1992 specification for permanence of paper and library materials. ♾™
♻ 85% recycled content, including 10% post-consumer fibers.

Journal of Heat Transfer **Volume 133, Number 3** **MARCH 2011**

The ASME Journal of Heat Transfer is abstracted and indexed in the following:

Applied Science and Technology Index, Chemical Abstracts, Chemical Engineering and Biotechnology Abstracts (Electronic equivalent of Process and Chemical Engineering), Civil Engineering Abstracts, Compendex (The electronic equivalent of Engineering Index), Corrosion Abstracts, Current Contents, E & P Health, Safety, and Environment, Ei EncompassLit, Engineered Materials Abstracts, Engineering Index, Enviroline (The electronic equivalent of Environment Abstracts), Environment Abstracts, Environmental Engineering Abstracts, Environmental Science and Pollution Management, Fluidex, Fuel and Energy Abstracts, Index to Scientific Reviews, INSPEC, International Building Services Abstracts, Mechanical & Transportation Engineering Abstracts, Mechanical Engineering Abstracts, METADEX (The electronic equivalent of Metals Abstracts and Alloys Index), Petroleum Abstracts, Process and Chemical Engineering, Referativnyi Zhurnal, Science Citation Index, SciSearch (The electronic equivalent of Science Citation Index), Theoretical Chemical Engineering

Journal of Heat Transfer

Guest Editorial

Special Issue on Advanced Thermal Processing

Significant advances have been made over the last decade on the study of thermal transport phenomena in manufacturing and material processing, where thermal science has been applied to drive innovations. Powerful experimental tools, as well as multiscale computational modeling, have been utilized to unravel the associated material transformation and structural modification processes down to a nanoscale, with great detail and unprecedented spatial and temporal resolutions. Such breakthroughs are appearing across a number of disciplines, but a common thread arises within thermal processing. The focus of this special issue is to bring together scientists and engineers across various disciplines to address the thermal aspects of materials processing issues with high societal impact applications.

This special issue was initiated through the organization of a U.S. National Science Foundation-sponsored Symposium on Advanced Thermal Processing, held during the 2008 ASME International Mechanical Engineering Congress & Exposition on November 5, 2008 in Boston, MA.[1] The ASME Heat Transfer Division's K-15 Technical Committee on Transport Phenomena in Manufacturing and Materials Processing organized a multisession symposium during which experts were invited from industry, research laboratories, and academia to present the latest thermal processing challenges in their field. Topics discussed included nuclear energy, nanomanufacturing, photovoltaics, fuel cells, tissue engineering, and photonics. Both speakers and attendees were invited to contribute to this special issue.

On behalf of the ASME Heat Transfer Division's K-15 Technical Committee on Transport Phenomena in Manufacturing and Materials Processing, we are honored to present this special issue consisting of 12 technical and review articles. Contributions cover various aspects of advanced thermal processing, including the synthesis of novel nanomaterials, multiphase flow with applications to welding, machining, thermal management, fuel cells, food processing, thermal barrier coatings, and materials processing challenges in novel scaffold materials for tissue engineering. We hope that these papers inspire further research and innovation in thermal science application in manufacturing and materials processing.

Organizing this special edition on advanced thermal processing has endured a long process and would have been impossible without the committed support of various sources. We are especially indebted to Professor Y. Jaluria, the editor of the ASME Journal of Heat Transfer, for his unwavering support of this edition from the conception of the idea until its fruition. Our thanks go to the authors and reviewers for their relentless effort to ensure that their work meets the uncompromised quality standards of the journal.

We acknowledge the financial support provided by the National Science Foundation under Grant No. CBET-0820605 and additional support from the American Society of Mechanical Engineers. May readers enjoy and discoveries continue.

Wilson K. S. Chiu
Guest Editor
Department of Mechanical Engineering,
University of Connecticut,
191 Auditorium Road,
Storrs, CT 06269-3139
e-mail: wchiu@engr.uconn.edu

Costas P. Grigoropoulos
Guest Editor
Department of Mechanical Engineering,
University of California,
6177 Etcheverry Hall,
Berkeley, CA 94720-2525
e-mail: cgrigoro@me.berkeley.edu

Ben Q. Li
Guest Editor
Department of Mechanical Engineering,
University of Michigan,
Dearborn, MI 48128
e-mail: benqli@umich.edu

[1] http://www.engr.uconn.edu/nsfworkshop.

Myung Gwan Hahm
Department of Mechanical and Industrial Engineering,
NSF Nanoscale Science and Engineering Center for High-Rate Nanomanufacturing,
Northeastern University,
Boston, MA 02115
e-mail: mghahm@coe.neu.edu

Young-Kyun Kwon
e-mail: ykkwon@khu.ac.kr
Department of Physics and Research Institute for Basic Sciences,
Kyung Hee University,
Seoul 130-701, Korea

Ahmed Busnaina

Yung Joon Jung[1]
e-mail: jungy@coe.neu.edu

Department of Mechanical and Industrial Engineering,
NSF Nanoscale Science and Engineering Center for High-Rate Nanomanufacturing,
Northeastern University,
Boston, MA 02115

Structure Controlled Synthesis of Vertically Aligned Carbon Nanotubes Using Thermal Chemical Vapor Deposition Process

Due to their unique one-dimensional nanostructure along with excellent mechanical, electrical, and optical properties, carbon nanotubes (CNTs) become a promising material for diverse nanotechnology applications. However, large-scale and structure controlled synthesis of CNTs still have many difficulties due to the lack of understanding of the fundamental growth mechanism of CNTs, as well as the difficulty of controlling atomic-scale physical and chemical reactions during the nanotube growth process. Especially, controlling the number of graphene wall, diameter, and chirality of CNTs are the most important issues that need to be solved to harness the full potential of CNTs. Here we report the large-scale selective synthesis of vertically aligned single walled carbon nanotubes (SWNTs) and double walled carbon nanotubes (DWNTs) by controlling the size of catalyst nanoparticles in the highly effective oxygen assisted thermal chemical vapor deposition (CVD) process. We also demonstrate a simple but powerful strategy for synthesizing ultrahigh density and diameter selected vertically aligned SWNTs through the precise control of carbon flow during a thermal CVD process. [DOI: 10.1115/1.4002443]

1 Introduction

Nanotechnologies based on carbon nanotubes (CNTs) are developed very rapidly from the discovery in 1993 [1] because of their exceptional mechanical, electrical, and optical properties [2]. The applications of CNTs are their use in nanoscale electronics such as nanosensors, interconnects, and field effect transistors by their specific electronic structures, superior transport properties, and unique one-dimensional nanostructures [3–5]. In the synthesis of CNTs, the catalytic chemical vapor deposition (CVD) method has been developed actively for the large-scale synthesis of CNTs [6–12]. However, still challenging difficulties are the control of morphology and structure of CNTs with the ability of synthesizing them in a large quantity. The key parameters in CNT growth using thermal CVD processes are chemical and physical characteristics of catalyst nanoparticles, hydrocarbons, and reaction environment during growth of CNTs. In the CVD process, the dissociation of hydrocarbon molecules catalyzed by the transition metal and the precipitation of sp^2 carbon bonds from supersaturated metal catalyst nanoparticles lead to the formation of CNTs. Therefore, the diameter of CNTs is closely related to the size of metal catalyst nanoparticles. However, it is very difficult to control the size of catalyst nanoparticles precisely with the uniform distribution. In this paper, we report the large-scale selective growth of vertically aligned (VA) SWNTs and DWNTs using an ethanol based thermal CVD process. We also demonstrate the large-scale synthesis of diameter controlled vertically aligned SWNTs by controlling the flow rate of ethanol vapor. To understand the diameter selected growth of SWNTs, we also carried out a computational investigation of the fundamental SWNT growth mechanism and kinetics under different ethanol flow rates in the CVD process using various computational techniques, including the first-principles formalism.

2 Experimental Method

Vertically aligned CNTs were synthesized by employing a thermal ethanol CVD technique [13]. Figure 1 is a schematic showing our ethanol CVD system and experimental procedure for the growth of high density and vertically aligned CNTs. First, a 20 nm thick Al film was deposited onto a SiO_2 layer using a sputter coater and exposed to the air for the formation of aluminum-oxide buffer layer to grow highly dense and vertically aligned CNTs (Fig. 1(*b*)). Then, an ultrathin Co catalyst film with 0.5–1 nm thickness was deposited on an Al_2O_x/SiO_2 multilayer using an e-beam evaporator (Fig. 1(*c*)). The prepared substrate ($Co/Al_2O_x/SiO_2$) was placed inside of a quartz tube and the CVD chamber was evacuated to 15 mTorr. Then the temperature was increased to 850°C while being exposed to an argon-hydrogen mixture gas (5% hydrogen balanced Ar) with 100 SCCM (SCCM denotes cubic centimeter per minute at STP) flow rate. In a desired reaction temperature (850°C), controlled high purity anhydrous ethanol (99.95%) was supplied as a carbon source for the high density nucleation and growth of CNTs resulting in vertically aligned CNT arrays (Fig. 1(*d*)). For the characterization of the CNT structure and morphology, transmission electron microscope (TEM), Raman spectroscopy, and scanning electron microscopy (SEM) were used. Especially, to investigate the large-scale diameter distribution of synthesized vertically aligned SWNTs, a Raman radial breathing mode (RBM) mapping process was employed with an excitation wavelength at 785 nm. Raman RBM maps were recorded using a Raman microscope (LabRAM HR 800, HORIBA Jobin Yvon) and a mechanical-optical mapping stage.

3 Results and Discussion

Figure 2(*a*) shows a cross-sectional optical image of CNT film grown using an ethanol CVD process. During the CVD reaction, controlled amounts of oxygen in ethanol molecules (C_2H_5OH) work as a weak oxidizer that would selectively remove amor-

[1]Corresponding author.
Manuscript received June 15, 2009; final manuscript received January 13, 2010; published online November 15, 2010. Assoc. Editor Wilson K. S. Chiu.

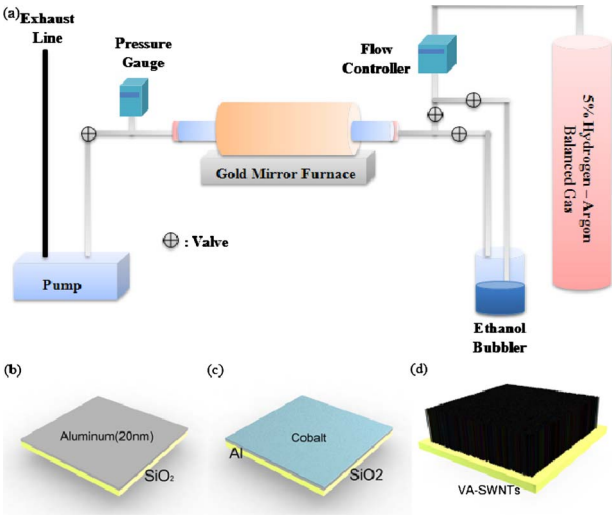

Fig. 1 Schematics of ethanol CVD systems and experimental procedures for the growth of vertically aligned SWNT

phous carbon around catalyst nanoparticles but would not damage CNTs, thereby enhancing the activity and lifetime of catalyst nanoparticles [14,15]. In our result, it is clearly seen that CNTs are vertically aligned due to the high density nucleation and growth in a highly effective ethanol CVD process. The height of vertically aligned CNT film is about 2.3 mm with the 90 min growth time. Under the same CVD parameters such as catalyst system, growth temperature, pressure, and the amount of carbon source, the height of aligned CNTs could be tailored in the range 20–2500 μm by controlling the growth time. Figures 2(*b*) and 2(*c*) show the representative SEM images of highly dense and vertically aligned SWNTs and microsized line blocks of them. Assembling CNTs into macro-/microscale architectures having vertical orientation

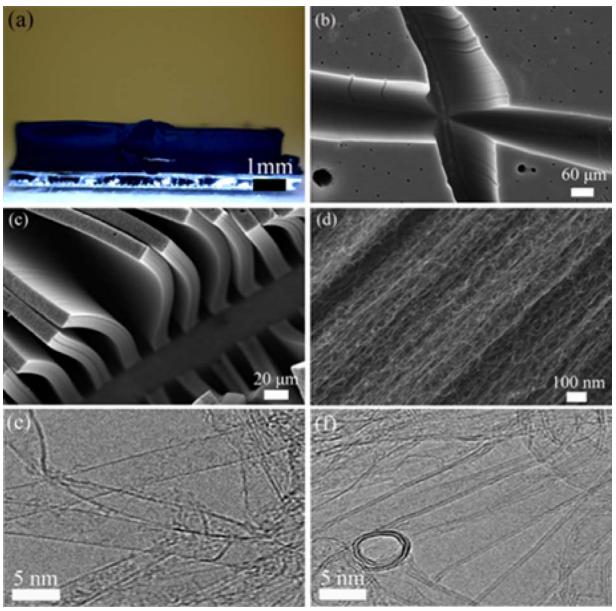

Fig. 2 (*a*) A cross-sectional optical image of highly dense and vertically aligned SWNTs grown with ethanol vapor as a carbon source, (*b*) low magnification SEM image of vertically aligned SWNTs, (*c*) low magnification SEM image of vertically aligned SWNT microblocks, (*d*) high magnification SEM image showing aligned nature of SWNTs grown in a thermal ethanol CVD process, high-resolution TEM images showing selectively synthesized (*e*) SWNTs and(*f*) DWNTs

and diverse configurations can be performed by combining conventional microfabrication techniques and the CVD process described above. For this, first, the photoresist film was spin coated and patterned on the silicon substrate using an optical lithography process. After that, the Co catalyst film (5–10 Å) was deposited and followed by photoresist lift-off process resulting in patterned catalyst film on the substrate. Then, an ethanol CVD process was conducted to create a vertically aligned and highly organized CNT architecture. Figure 2(*d*) is a high magnification SEM image indicating the aligned nature of SWNT film.

For the selective synthesis of vertically aligned SWNTs and DWNTs, different thicknesses and deposition rates of a Co catalyst film were used. For example, in order to grow SWNTs, the deposition rate of a Co catalyst film was 1 Å/s for 3 s. For the growth of DWNTs, the Co catalyst film was deposited with 3 Å/s deposition rate for 3 s. When a thicker Co catalyst film (1 nm) was deposited and used, relatively larger Co catalyst nanoparticles (4–7 nm) were formed during CVD reaction resulting in the growth of DWNTs. However, thinner Co catalyst films (0.3–0.5 nm) are directly formed into smaller catalyst nanoparticles (1–4 nm) during high temperature CVD process that can effectively prompt the growth of SWNTs on the substrate [13]. HRTEM images (Figs. 2(*e*) and 2(*f*)) show selective growth of SWNTs and DWNTs, respectively, using our controlled catalyst nanoparticle systems. From the HRTEM characterization, we also confirmed that multiwalled carbon nanotubes (MWNTs) were rarely formed in our CNT growth process.

To control the diameter of vertically aligned SWNTs, we have controlled the flow rate of ethanol (carbon source for the growth of SWNTs) while maintaining all other CVD parameters such as the size distribution of catalyst nanoparticles, temperature, pressure, and CVD process time and constant. Figure 3(*a*) shows the typical G and D band Raman spectra from SWNTs grown with 50 SCCM and 200 SCCM ethanol flow rate, respectively. G band is in a spectral range of 1550–1600 cm^{-1} identified with the tangential stretch of graphene structure. The disorder induced D band mode is at 1300 cm^{-1}. Using the peak intensity of D (I_D) and G (I_G) bands, we can determine the degree of disorder in CNT. The I_D/I_G ratio of vertically aligned SWNTs synthesized with 50 SCCM and 200 SCCM flow rates are 0.14 and 0.15, respectively. It shows that our synthesized SWNTs have very small amounts of defects, indicating that our ethanol CVD process is very effective in growing high quality SWNTs. In order to investigate the large area diameter distribution of vertically aligned SWNTs, we have used the Raman mapping process and imaging of the RBM region (the spectral range of 100–450 cm^{-1}) with its high spatial resolution. Raman maps were recorded with a mapping stage and a 785 nm excitation laser. The Raman mapping area was 10×10 μm^2 with 0.4 μm laser steps. The beam exposure time was 4 s/spectrum, and the number of accumulation is 12 for one Raman spectrum. The diameter of the confocal hole was set to 200 μm, a 600 grooves/mm grating was used, and the objective lens is 100×. The maps were recorded in standard point mapping mode with a 0.4 μm step, resulting in 625 spectra ($=25 \times 25$ spectra) and the data normalized to unit area. Figure 3(*b*) shows a representative RBM spectrum of high density and vertically aligned SWNTs after the mapping process on 10×10 μm^2. The RBM modes correspond to the atomic vibration of carbon atoms in the radial direction that allows us to calculate the diameter of SWNTs using the following equation: $\omega_{RBM}=A/d_t+B$ [16], where A and B are the proportional constants determined experimentally. For the typical SWNT bundles, A is 234 cm^{-1} nm and B is 10 cm^{-1}, where B is a blue-shift coming from a nanotube-nanotube interaction [16]. Three major RBM peak positions (three highest intensities in RBM) of Raman RBM map recorded from SWNTs grown with 50 SCCM flow rate of ethanol are 211 cm^{-1}, 230 cm^{-1}, and 303 cm^{-1} (Fig. 3(*b*)). A multivariate analysis algorithm was applied in an unsupervised mode to extract significant different spectra and to calculate cores of individual spectra.

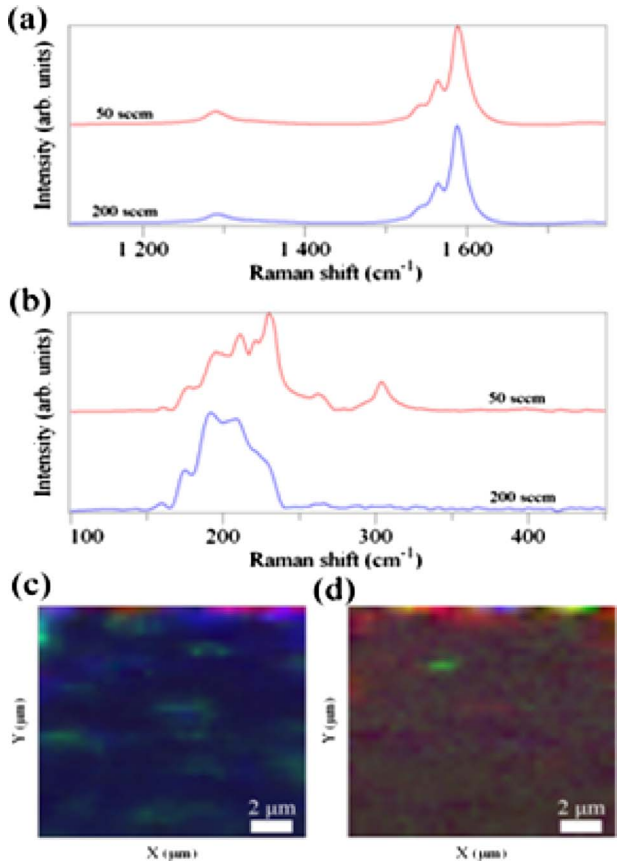

Fig. 3 (*a*) **D, G band spectra of vertically aligned SWNTs grown with 50 SCCM (red) and 200 SCCM (blue) flow rates of ethanol;** (*b*) **representative RBM spectra of vertically aligned SWNTs synthesized with 50 SCCM and 200 SCCM ethanol flow rates extracted from RBM mapping process, Raman RBM hyperspectral images from SWNTs grown with** (*c*) **50 SCCM and** (*d*) **200 SCCM;** (*c*) **the spatial diameter distribution of VA-SWNTs grown with 50 SCCM flow rate of ethanol is very uniform (blue color occupied 93% of the entire SWNT film);** (*d*) **the RBM image showing wide diameter distribution of vertically aligned SWNTs grown with 200 SCCM**

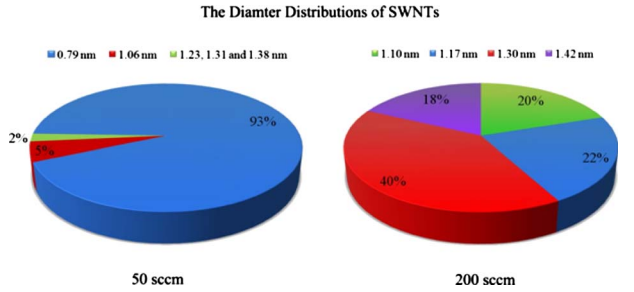

Fig. 4 The charts of the major diameter distribution of VA-SWNTs grown with two different flow rates of ethanol (50 SCCM and 200 SCCM). The major SWNTs diameters grown with 50 SCCM ethanol flow rate are 0.79 nm (93%) and 1.06 nm (5%). In the case of 200 SCCM flow rate of ethanol, the four major SWNTs diameters (1.10 nm, 1.17 nm, 1.30 nm, and 1.42 nm) are distributed in similar ratio on the surface.

These three RBM frequencies correspond to the diameters of SWNTs in 1.16 nm, 1.06 nm, and 0.79 nm, respectively. The corresponding hyperspectral RBM image (Fig. 3(*c*)) gives a spatial distribution of vertically aligned SWNTs with three different colors (red, green, and blue). The statistical treatment of RBM images can quantify the diameter of SWNTs. In the Raman hyperspectral image, the brightness of each color represents the intensity of the RBM spectrum and the intensity of the RBM peak is closely correlated with the density of SWNTs. Each color represents a group of vertically aligned SWNTs of the same diameter distribution. The blue area in the hyperspectral RBM image (Fig. 3(*c*)) represents a 303 cm^{-1} peak in RBM and the green area corresponds to a 230 cm^{-1} peak. Therefore, all of the SWNTs in the blue and green areas have 0.79 nm and 1.06 nm in a diameter, respectively. Figure 3(*c*) also clearly shows that the diameter distribution of SWNTs is very uniform with blue color. The blue (0.79 nm) and green (1.06 nm) areas occupy over 98% on the surface. In the case of SWNTs grown with 200 SCCM ethanol flow rate, however, the hyperspectral RBM image shows many components of color (Fig. 3(*d*)). They have four major RBM peaks and the peak positions are 174.3 cm^{-1}, 191.1 cm^{-1}, 208.7 cm^{-1}, and 224.7 cm^{-1}. The corresponding diameters of SWNTs are 1.42 nm (174.3 cm^{-1}), 1.30 nm (191.1 cm^{-1}), 1.17 nm (208.7 cm^{-1}), and 1.10 nm (224.7 cm^{-1}). In Fig. 3(*d*), the blue, green, red, and yellow colored regions represent 1.10 nm, 1.17 nm, 1.30 nm, and 1.42 nm diameters of SWNTs, respectively. Also, all these four major SWNT diameters are distributed in a similar portion in the substrate, as shown Fig. 3(*d*). This means that SWNTs grown with 200 SCCM ethanol flow rate have a larger SWNT diameter distribution on the surface than SWNTs synthesized with the 50 SCCM flow rate of ethanol. We have also determined major diameter distributions of vertically aligned SWNTs grown with two different flow rates of ethanol (50 SCCM and 200 SCCM) using peak fitting and integrated band width from each representative RBM spectrum extracted from the RBM mapping process. As shown in Fig. 4, 98% of vertically aligned SWNTs synthesized with a 50 SCCM flow rate of ethanol have diameters in the range 0.79–1.06 nm. However, for SWNTs grown with a 200 SCCM ethanol flow rate, all four different diameters are distributed in similar ratio on the surface.

To scrutinize our experimental observation of the correlation between the SWNT diameter and flow rate of carbon source, we have performed the first-principles density functional theory [17–19] to calculate the diffusion barrier of carbon atoms on the surface of Co catalyst nanoparticles and Al surface, and kinetic Monte Carlo simulations to study the kinetics of carbon nanotube formation on Co catalyst nanoparticles. From our previous work [13], the calculated diffusion barrier of a carbon atom on the Co (001) surface is ~0.15 eV along the minimum barrier path, which connects the face center of a Co triangle, which is the equilibrium position, and the middle of a Co–Co bonding, whereas it is ~1.5 eV through the top of a Co atom [13]. Most carbon atoms will diffuse along the minimum barrier directions. In the case of an Al surface, the diffusion barrier is around 0.1–0.4 eV, but near the boundary of the Co catalyst nanoparticle, the bonding energy of a carbon atom is much higher than those on the Al surface and Co surface. Both the binding energy and the repelling barrier become trap energy of carbon atom to overcome in order to diffuse onto Co catalyst nanoparticles [13].

The differences of carbon source flow rates provide different carbon fluxes on the substrate. Carbon source molecules are dissociated into atoms and smaller molecules at around 850°C (optimum SWNT growth temperature). We assumed only carbon atoms that diffuse on the Al surface to study SWNT nucleation on Co catalyst nanoparticles. While diffusing the carbon source at 850°C, they encounter each other to form carbon aggregations, which also diffuse, but more slowly than a single carbon atom or smaller carbon aggregations. Carbon atoms or carbon aggregations diffuse further until they meet Co catalyst nanoparticles. Since their diffusion on the Al surface is faster than their escaping ratio on the Co perimeter, they are accumulated at the perimeter of Co catalyst nanoparticles. The density of the accumulated carbon at the boundary of Co catalyst nanoparticles is determined by the

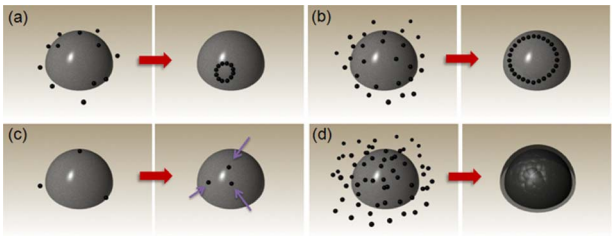

Fig. 5 Schematics of our simple model for SWNT growth with different flow rates: (*a*) and (*b*) shows different flow rates of carbon sources at the Co nanoparticle perimeters, which will make nucleation of carbon nanotubes with different sizes; (*a*) corresponds to the flow rate of 50 SCCM, which makes smaller diameter nanotubes, while (*b*) corresponds to 200 SCCM making larger diameter nanotubes. (*c*) If the flow rate is too low, then collected carbon source at the perimeter of the Co particle is not enough to form a nucleation, so no carbon nanotube would grow. (*d*) In the case of overflow rate, the collected carbon source at the perimeter of the Co nanoparticles covers the surface of Co nanoparticles and the catalyst nanoparticles are deactivated for the growth of SWNTs [13].

carbon flux or the flow rate. Then, aggregations of some carbon atoms at the perimeter enter onto the surface of Co catalyst nanoparticles, while some stay at the perimeter or diffuse out to the Al surface [13]. Figures 5(*a*) and 5(*b*) shows schematics of the different densities of carbon sources at the Co catalyst nanoparticle boundaries, which will make single walled carbon nanotube nucleation with different sizes (different diameters). A different density at the perimeter corresponds to different flow rates of carbon source. As shown Fig. 5(*a*), an ethanol flow rate of 50 SCCM makes smaller diameter single walled carbon nanotubes, while 200 SCCM makes larger nanotubes, as shown in Fig. 5(*b*). Figure 5(*c*) shows that when flow rate is too low, collected carbon source at the perimeter of the Co catalyst nanoparticle is not sufficient to form a nucleation site for a carbon nanotube to grow [13]. On the other hand, if the carbon source flow rate is overflowed, the surface of catalyst nanoparticles is covered with amorphous carbon and they are deactivated (Fig. 5(*d*)).

This paper shows an approach to diameter-selective growth of carbon nanotubes. However, to harness the full potential of CNTs, we also need to control chirality. This remains as a major challenge in facing carbon nanotube synthesis. There is a need for full understanding that will have to include multiscale modeling coupled with experiments to develop a better understanding of the atomic-scale physical and chemical reactions during the nanotube growth process and how to control it. This will only happen if the growth process is completely under control including the thermal and concentration gradients locally at the nanotube scale and globally within the CVD chamber.

4 Conclusion

In conclusion, we have demonstrated the selective growth of vertically aligned SWNTs and DWNTs by controlling the size of catalyst nanoparticles in a highly effective ethanol thermal CVD process. We have also investigated the effect of ethanol flow rate during CVD for the diameter controlled growth of vertically aligned SWNTs by using the Raman RBM mapping process, providing a large-scale spatial diameter distribution of SWNTs. SWNTs synthesized with a lower ethanol flow have a uniform diameter distribution and a smaller diameter compared with that used higher ethanol flow rate. We have also presented a theoretical SWNT growth model under different flow rates of carbon source. From our experimental and theoretical results, it is assumed that a lower flow rate of carbon source makes a smaller nucleation site for a SWNT resulting in a smaller diameter formation. On the other hand, a higher flow rate of carbon source forms a larger nucleation site forming a SWNT with the larger diameter.

Acknowledgment

This work was supported by the Fundamental R&D Program for Core Technology of Materials funded by the Ministry of Knowledge Economy, Republic of Korea and the National Science Foundation (NSF)-Nanoscale Science and Engineering Center (NSF-NSEC) for High-Rate Nanomanufacturing. Y.J.J. also acknowledges Dr. Lijie Ci at Rice University for the TEM characterization.

References

[1] Iijima, S., and Ichihashi, T., 1993, "Single-Shell Carbon Nanotubes of 1-nm Diameter," Nature (London), **363**(6430), pp. 603–605.
[2] Ajayan, P., 1999, "Nanotubes From Carbon," Chem. Rev., **99**(7), pp. 1787–1800.
[3] Graham, A. P., Duesberg, G. S., Seidel, R. V., Liebau, M., Unger, E., Pamler, W., Kreupl, F., and Hoenlein, W., 2005, "Carbon Nanotubes for Microelectronics?," Small, **1**(4), pp. 382–390.
[4] Küttel, O. M., Groening, O., Emmenegger, C., and Schlapbach, L., 1998, "Electron Field Emission From Phase Pure Nanotube Films Grown in a Methane/Hydrogen Plasma," Appl. Phys. Lett., **73**(15), pp. 2113–2115.
[5] Ngo, Q., Cruden, B. A., Cassell, A. M., Sims, G., Meyyappan, M., Li, J., and Yang, C. Y., 2004, "Thermal Interface Properties of Cu-Filled Vertically Aligned Carbon Nanofiber Arrays," Nano Lett., **4**(12), pp. 2403–2407.
[6] Cheng, H., Li, F., Sun, X., Brown, S., Pimenta, M., Marucci, A., Dresselhaus, G., and Dresselhaus, M., 1998, "Bulk Morphology and Diameter Distribution of Single-Walled Carbon Nanotubes Synthesized by Catalytic Decomposition of Hydrocarbons," Chem. Phys. Lett., **289**(5–6), pp. 602–610.
[7] Ci, L., Xie, S., Tang, D., Yan, X., Li, Y., Liu, Z., Zou, X., Zhou, W., and Wang, G., 2001, "Controllable Growth of Single Wall Carbon Nanotubes by Pyrolizing Acetylene on the Floating Iron Catalysts," Chem. Phys. Lett., **349**(3–4), pp. 191–195.
[8] Colomer, J., Benoit, J., Stephan, C., Lefrant, S., Van Tendeloo, G., and Nagy, J. B., 2001, "Characterization of Single-Wall Carbon Nanotubes Produced by CCVD Method," Chem. Phys. Lett., **345**(1–2), pp. 11–17.
[9] Colomer, J., Stephan, C., Lefrant, S., Van Tendeloo, G., Willems, I., Kónya, Z., Fonseca, A., Laurent, C., and Nagy, J., 2000, "Large-Scale Synthesis of Single-Wall Carbon Nanotubes by Catalytic Chemical Vapor Deposition (CCVD) Method," Chem. Phys. Lett., **317**(1–2), pp. 83–89.
[10] Nikolaev, P., Bronikowski, M., Bradley, R., Rohmund, F., Colbert, D., Smith, K., and Smalley, R., 1999, "Gas-Phase Catalytic Growth of Single-Walled Carbon Nanotubes From Carbon Monoxide," Chem. Phys. Lett., **313**(1–2), pp. 91–97.
[11] Satishkumar, B., Govindaraj, A., Sen, R., and Rao, C., 1998, "Single-Walled Nanotubes by the Pyrolysis of Acetylene-Organometallic Mixtures," Chem. Phys. Lett., **293**(1–2), pp. 47–52.
[12] Zhou, W., Ooi, Y., Russo, R., Papanek, P., Luzzi, D., Fischer, J., Bronikowski, M., Willis, P., and Smalley, R., 2001, "Structural Characterization and Diameter-Dependent Oxidative Stability of Single Wall Carbon Nanotubes Synthesized by the Catalytic Decomposition of Co," Chem. Phys. Lett., **350**(1–2), pp. 6–14.
[13] Hahm, M. G., Kwon, Y.-K., Lee, E., Ahn, C. W., and Jung, Y. J., 2008, "Diameter Selective Growth of Vertically Aligned Single Walled Carbon Nanotubes and Study on Their Growth Mechanism," J. Phys. Chem. C, **112**(44), pp. 17143–17147.
[14] Murakami, Y., Chiashi, S., Miyauchi, Y., Hum, M., Ogura, M., Okubo, T., and Maruyama, S., 2004, "Growth of Vertically Aligned Single-Walled Carbon Nanotube Films on Quartz Substrates and Their Optical Anisotropy," Chem. Phys. Lett., **385**, pp. 298–303.
[15] Hata, K., Futaba, D. N., Mizuno, K., Namai, T., Yumura, M., and Iijima, S., 2004, "Water-Assisted Highly Efficient Synthesis of Impurity-Free Single-Walled Carbon Nanotubes," Science, **306**, pp. 1362–1364.
[16] Jorio, A., Pimenta, M. A., Souza Filho, A. G., Saito, R., Dresselhaus, G., and Dresselhaus, M. S., 2003, "Characterizing Carbon Nanotube Samples With Resonance Raman Scattering," New J. Phys., **5**, pp. 139.1–139.17.
[17] Ihm, J., Zunger, A., and Cohen, M. L., 1980, "Momentum-Space Formalism for the Total Energy of Solids," J. Phys. C, **13**, pp. 3095.
[18] Kohn, W. and Sham, L., 1965, "Self-Consistent Equations Including Exchange and Correlation Effects," Phys. Rev., **140**, pp. A1133–A1138.
[19] Payne, M. C., Teter, M. P., Allan, D. C., Arias, T. A., and Joannopoulos, J. D., 1992, "Iterative Minimization Techniques for Ab Initio Total-Energy Calculations: Molecular Dynamics and Conjugate Gradients," Rev. Mod. Phys., **64**, pp. 1045–1097.

Modeling of Ceramic Particle Heating and Melting in a Microwave Plasma

Kaushik Saha

Swetaprovo Chaudhuri

Baki M. Cetegen[1]
Fellow ASME
e-mail: cetegen@engr.uconn.edu

Department of Mechanical Engineering,
University of Connecticut,
Storrs, CT 06269-3139

A comprehensive model based on finite volume method was developed to analyze the heat-up and the melting of ceramic particles injected into a microwave excited laminar air plasma flow field. Plasma flow field was simulated as a hot gas flow generated by volumetric heat addition in the microwave coupling region, resulting in a temperature of 6000 K. Alumina and zirconia particles of different diameters were injected into the axisymmetric laminar plasma flow at different injection velocities and locations. Additionally, noncontinuum effects, variation of transport properties of plasma surrounding the spherical particles and absorption of microwave radiation in the ceramic particles were considered in the model. Model predictions suggest that zirconia and alumina particles with diameters less than 50 μm can be effectively melted in a microwave plasma and can produce more uniform melt states. Microwave plasma environment with the ability to inject particles into the plasma core provide the opportunity to create more uniform melt states as compared with dc arc plasmas that are influenced by characteristic arc root fluctuations and turbulent dispersions. [DOI: 10.1115/1.4002448]

Keywords: microwave plasma, ceramic particles, heat-up, melting

1 Introduction

Thermal spray is a well-known process in industry for its utility in the application of functional coatings on hardware components. For example, thermal barrier coatings are applied on gas turbine blades for thermal protection from hot combustion gases. Anticorrosive, thermal shock, and wear resistant coatings are employed for protection of many components. The utility of thermal spray can also be found in electronics industry and biomedical applications, as well as in providing electrode materials for solid oxide fuel cells. In a typical thermal spray process, powder material is injected externally into a dc arc plasma jet. Depending on the momentum ratio of the plasma and the particle stream, the particles are either partially or fully entrained into the plasma jet. Entrained particles are heated and melted before they impact on a substrate [1]. In the plasma, injected particles undergo intense heating, some melting, and, possibly, surface vaporization. Depending on the heating conditions, they may or may not have a solid core by the time they reach the deposition location. Also, if the particle moves to lower temperature regions of the plasma, it may start losing heat and the particle surface may resolidify.

Turbulent dispersions in a plasma jet lead to considerable amounts of variations of the particle states (velocity, temperature, and melt state), resulting in an inhomogeneous coating microstructure. Furthermore, factors, such as electrode erosion and arc root fluctuations, in a dc arc plasma result in enhancement of particle dispersion. Experimental observations have revealed that the periodic variations of mean particle temperature and velocity can be up to 800 K and 200 m/s during one voltage cycle in a dc arc plasma jet [2,3].

A possible alternative to dc arc plasmas for material processing is the use of microwave plasmas. Microwave plasmas have been used for a wide variety of applications such as welding, cutting, waste incineration, processing of ceramic fibers, incineration of biological agents, and production of carbon nanotubes [4–6]. However, the potential of microwave plasmas for making thick coatings has not been fully explored as of yet. In order to facilitate the determination of thermophysical processes of particulates injected into microwave plasma, a modeling study was undertaken. The modeling effort, as described in this article, utilizes a computational approach to predict trajectories and thermal histories of ceramic particles of various sizes when injected at different locations with different initial velocities into microwave plasma.

Microwave plasmas have been successfully generated at atmospheric pressure as described in literature [5,7,8]. Green et al. [7] conducted electronic excitation temperature measurements in such microwave plasmas by emission spectroscopy. They determined that the peak temperature in these plasmas is around 6000 K without much variation with respect to the type of gas used for the plasma medium. Microwave plasma processing of ceramic oxides has already been investigated in literature. Wylie et al. [5] generated the atmospheric microwave plasma and made alumina particles of various sizes from an alumina rod. Vollath and Sickafus [9] studied the processing of $ZrO_2-Y_2O_3-Al_2O_3$ composites in a nonequilibrium microwave plasma, where the plasma was used as a source of pyrolysis heat for synthesis of nanosized particles with crystallite sizes less than 10 nm.

Modeling of particle heat-up and particle thermal histories requires that plasma temperature and velocity fields are known. For this purpose, plasma is simulated utilizing computational fluid dynamics (CFD), assuming that plasma is formed by volumetric absorption of microwave power. Similar types of volumetric heating approaches have been adopted in some modeling studies of dc arc plasmas [10] in order to avoid the complications of magnetohydrodynamic approach. Clearly, the most comprehensive approach is to solve plasma flow field and particle variables in a fully coupled manner. However, this is difficult at best, and typically plasma flow field is solved or determined separately from computations and/or experimental measurements. Particles or droplets are then injected into the a priori determined plasma flow field. The basic underlying assumption in this approximation is that the plasma flow field remains relatively unperturbed by the injected particles, provided that the number density of particles or droplets is not large.

Modeling of particulates embedded in thermal plasmas or combustion flames have been carried out extensively for the last sev-

[1]Corresponding author.

Manuscript received June 17, 2009; final manuscript received November 5, 2009; published online November 15, 2010. Assoc. Editor: Wilson K. S. Chiu.

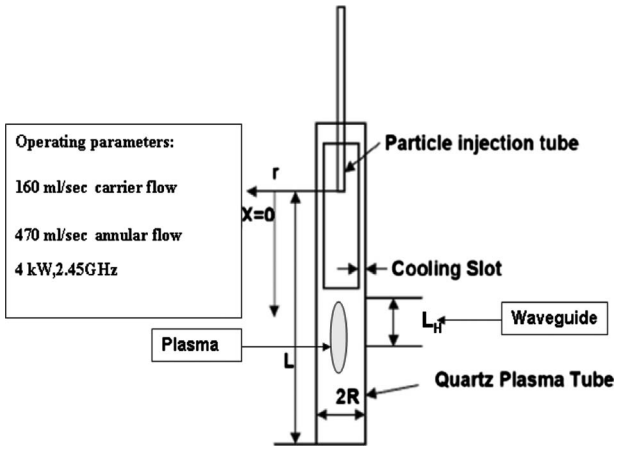

Fig. 1 Schematic of the experimental setup of the microwave plasma torch

eral decades, owing to the importance of the thermal and kinetic states of the particles at the moment of impact for generating a coating. A recent review of modeling efforts for both plasma and high velocity oxy fuel (HVOF) thermal spray processes were reported by Cetegen and Basu [11]. Majority of the work has been done for the case of conventional dc arc plasmas. But to our knowledge, no comprehensive analysis of particle behavior in microwave plasmas exists in literature. Modeling of plasma-particle interactions including mass, momentum, and energy transfer have been studied since the 1980s [12–25]. Injection of micron size particles into a high temperature plasma jet requires assessment of continuum hypothesis for the spherical particles moving through spatially and temporally varying velocity and temperature fields. In cases where the problem no longer remains within the continuum regime, appropriate slip velocity and temperature jump boundary conditions can be applied. In such cases where the length scales correspond to the near-continuum or slip flow regime [15,17], transport variables need to be modified by proper correction factors. Additionally, there are appreciable variations of transport properties across the boundary layer around spherical particles that require a specific method of calculating the average transport properties, such as plasma thermal conductivity and specific heat, and of including further correction factors for the momentum and energy transport. Extensive research has already been done to address these issues [12,14,15,17]. In the following sections, the geometrical configuration and the modeling approach used in this study are first described. This is followed by the presentation and the discussion of the results from the modeling effort.

2 Geometry and Operating Conditions

A schematic of the quartz tube assembly used in the experiment is shown in Fig. 1. The plasma operates at a maximum power of 4 kW and uses a 2.45 GHz magnetron source. The flow carrying the particles was 160 ml/s and the annular flow rate was varied from 350 ml/s to 470 ml/s. The length from the tip of the particle injection tube to the end of the quartz tube was 0.24 m. The inner radius R of the quartz tube containing the plasma was 0.0045 m. The gap through which the annular flow emerges to mix with the carrier gas flow for protecting the quartz tube from melting was varied between 0.4 mm and 0.5 mm. Typically, in this type of experimental setup, the plasma can be started by using a tungsten hertz spark loop and once the plasma is formed, it is sustained by electromagnetic (EM) waves from the 2.45 GHz magnetron source. There is a provision of triple stub tuner, which ensures almost complete absorption (>95%) of the microwave power by the plasma by tuning the impedance of the microwave source with that of the plasma. This setup is designed such that once a standing wave is built up, the peak electric field is located at the center of the quartz tube [5,8]. Detailed operational procedures can be obtained from literature [7,8]. In the experimental setup described in literature, swirl flow was used for cooling the quartz wall. However, this cooling scheme was not found to be suitable for injecting particles as they are centrifuged outward to the walls and deposited there. Thus, an annular cooling scheme was devised to protect the quartz wall from melting and at the same time to prevent the impact of the particles on the quartz wall.

3 Modeling Approach

3.1 Plasma Modeling. An axisymmetric model of the microwave plasma region was implemented in FLUENT 6.3.26 software by volumetric heat addition in the region of the waveguide, where the microwave radiation is incident onto the incoming air stream. The microwave radiation generated by a magnetron couples with the air stream in a quartz tube, resulting in a plasma with a peak temperature of around 6000 K. The formed plasma is surrounded by a shield gas stream to protect the quartz wall from melting. The annular gas flow for the shield stream between the central plasma and the quartz wall was optimized in a series of CFD simulations to mitigate the quartz wall melting. High temperature transport properties of air plasma were incorporated into the CFD simulations by using piecewise polynomial correlations developed from the data available in the literature [26].

The underlying assumption in the modeling of the microwave plasma is that local thermodynamic equilibrium (LTE) is valid for the plasma generated in the experimental setup described in the preceding section. Ensuring the validity of LTE in a plasma is always difficult. For arc plasmas, the validation of LTE is generally assumed to be valid for those generated at a pressure above 10 kPa [26]. However, even the microwave plasmas generated at atmospheric pressure do not ensure the validity of LTE assumption [5]. A threshold value of electron density of the plasma needs to be estimated for determining the proximity of the plasma to LTE. In the microwave plasma used here, the electron density of the plasma was estimated to be above the threshold value, suggesting that the LTE assumption is valid [7].

3.2 Particle Modeling. The particle heat-up and melting are modeled by a one-dimensional (radial) finite volume model within each particle. Once the melting starts, the tracking of the solid-liquid interface is performed to determine the instantaneous location of the melt front. The internal convection within the melt region is neglected in this model. The plasma flow field solution is used to provide the local plasma variables as boundary conditions for computing the particle heat-up.

3.2.1 Particle Motion and Trajectories. Generally, for analyzing particle motion in a plasma, only the effect of drag force is considered [13,15,20–22,24] since drag force is usually an order of magnitude higher than thermophoretic or body forces [14]. Additionally, Basset history term is also added in the momentum equations if the pseudosteady or quasi-steady-state assumption is not valid [14]. However, since the relaxation time of the hydrodynamic and thermal boundary layers surrounding the particle is of the order of microseconds compared with the residence time of the particles in the plasma being few milliseconds, pseudo steady-state assumption is considered to be valid [12,16].

The equations of motion of the particle then take the following form:

$$\frac{dU}{dt} = \frac{3}{4D} C_{\mathrm{D,eff}} \left(\frac{\rho_g}{\rho_p} \right) |U_\infty - U| (U_\infty - U) \tag{1a}$$

$$\frac{dV}{dt} = \frac{3}{4D} C_{\mathrm{D,eff}} \left(\frac{\rho_g}{\rho_p} \right) |V_\infty - V| (V_\infty - V) \tag{1b}$$

where U and V are the particle velocities and U_∞ and V_∞ are the plasma velocities in the axial (x) and radial (r) directions, D is the

particle diameter, and ρ_g and ρ_p are the plasma and particle densities. Several semi-empirical relations exist for the drag coefficient C_D of a spherical particle moving through a steady, constant property gas environment. In thermal plasmas, the effect of viscous drag force is dominant and, in most cases, the flow around the particle can be considered to be a low Reynolds number flow $\mathrm{Re}=(\rho_g D\Delta U/\mu_g)<100$. The well-accepted correlation for drag coefficient is used as suggested in literature [14,27].

$$C_D = \frac{24}{\mathrm{Re}} + \frac{6}{1+\sqrt{\mathrm{Re}}} + 0.4 \tag{2}$$

This expression is not valid for particles moving through rarefield medium of plasma as particles move through an environment of rapidly varying transport properties. This requires consideration of correction factors for the noncontinuum and variable property effects. For noncontinuum and variable properties, the employed correction factors are given by [15,16]

$$f_{\mathrm{Kn}} = \left[1 + \left(\frac{2-a}{a}\right)\left(\frac{\gamma}{\gamma+1}\right)\frac{4}{\mathrm{Pr}_w}\,\mathrm{Kn}^*\right]^{-1} \tag{3}$$

Here, a stands for the thermal accommodation coefficient, which is taken to be equal to 0.8 as recommended by Chen and Pfender [17]. γ stands for the specific heat ratio of the plasma at the film temperature surrounding the particle. Pr_w is the Prandtl number of the plasma corresponding to the surface temperature of the particle. Kn^* is the Knudsen number evaluated for the plasma at particle surface temperature.

For the rarefied gas effect, Kn^* is calculated from Refs. [17,20] as

$$\mathrm{Kn}^* = \frac{2\mathrm{Pr}_w}{\rho_w v_w D}\frac{\overline{k_f}}{\overline{C_{p,f}}} \tag{4a}$$

$$\lambda^* = \frac{2\mathrm{Pr}_w}{\rho_w v_w D}\frac{\overline{k_f}}{\overline{C_{p,f}}} \tag{4b}$$

where ρ_w and ν_w are the density and the mean molecular speed in the plasma at the surface temperature, respectively. $\overline{k_f}$ and $\overline{C_{p,f}}$ are the average thermal conductivity and the specific heat of plasma.

The effective drag coefficient can then be written as

$$C_{\mathrm{D,eff}} = C_D f_{\mathrm{Kn}}^{0.45} f_{\mathrm{prop}}^{-0.45} \tag{5}$$

where

$$f_{\mathrm{prop}} = \frac{\rho_g \mu_g}{\rho_w \mu_w}$$

ρ_g and ρ_w are the densities of plasma at free stream and particle surface temperature, respectively. μ_g and μ_w are the viscosity of plasma at free stream and particle surface temperatures.

When particles start melting, then surface vaporization can occur and drag coefficient needs to be modified due to the surface blowing effect. In this case, the drag coefficient is modified as [14]

$$C_{\mathrm{D,evap}} = C_{\mathrm{D,eff}}/(1+B) \tag{6}$$

where B stands for the mass transfer number.

3.2.2 Energy and Mass Transport Around the Particle. The governing equation for energy transport for radial conduction in a spherical particle is given by

$$\rho_p C_p \frac{\partial T}{\partial t} = \frac{1}{r^2}\frac{\partial}{\partial r}\left(r^2 k_p \frac{\partial T}{\partial r}\right) + q''' \tag{7}$$

where C_p and k_p are the particle specific heat and the thermal conductivity, respectively. The particle specific heat and the thermal conductivity are assumed to be constant for the materials studied in this article as their variation with temperature is small. For example, alumina specific heat value is around 1300 J/(kg K) for a temperature range of 600–2000 K and alumina thermal conductivity is around 6 W/m K for a temperature range of 1000–2000 K [28]. For zirconia, the specific heat can typically vary from 450 J/(kg K) to 600 J/(kg K) from 300 K to 2000 K [29] and the thermal conductivity can vary from 2 W/(m K) to 4 W/(m K) for a temperature range of 400–2400 K [28].

The boundary conditions and the initial condition for the particle energy equation are

$$\left.\frac{\partial T}{\partial r}\right|_{r=0} = 0 \tag{8a}$$

$$\pi D^2 \left.\left(k_p \frac{\partial T}{\partial r}\right)\right|_{r=D/2} = \dot{Q}_{\mathrm{conv}} - \dot{Q}_{\mathrm{rad}} - \dot{Q}_{\mathrm{vap}} \tag{8b}$$

$$T(r,0) = T_{\mathrm{carrier\ gas}} = 300\ \mathrm{K} \tag{8c}$$

The convective heat transfer coefficient is computed using the modified Ranz and Marshall correlation as

$$\mathrm{Nu} = (2 + 0.6\mathrm{Re}^{1/2}\mathrm{Pr}^{1/3}) f_{\mathrm{Kn}} f_{\mathrm{prop}}^{0.6} f_v \left(\frac{C_{p\infty}}{C_{pw}}\right)^{0.38} \tag{9}$$

where C_{pw} and $C_{p\infty}$ are the specific heats of plasma at the surface and ambient temperatures.

Here f_v stands for the correction factor, taking into account the surface evaporation effect [20]

$$f_v = \frac{\dot{m}_v \overline{C_{p,f}}/\pi D \overline{k_f}}{\exp(\dot{m}_v \overline{C_{p,f}}/\pi D \overline{k_f}) - 1} \tag{10}$$

At the particle surface, the total heat flux penetrating the particle surface is the resultant effect of the convective flux from the plasma and the radiation loss from the particle surface. Once the particle starts melting, there can be vaporization from the particle surface and it has been unraveled in literature that even though the mass rate of vaporization can be very small when multiplied with latent heat of vaporization, the effect of surface evaporation in the heat transfer from the plasma to the particle can be important [20]. Convective, radiative, and evaporative energy fluxes are obtained from the following relations:

$$\dot{Q}_{\mathrm{conv}} = \pi D^2 h (T_\infty - T_w) \tag{11a}$$

$$\dot{Q}_{\mathrm{rad}} = \pi D^2 \varepsilon \sigma T_w^4 \tag{11b}$$

$$\dot{Q}_{\mathrm{vap}} = \dot{m}_v L_v \tag{11c}$$

Finally, when the surface temperature of the molten droplet reaches the boiling point, then the entire convective heat flux is expended in vaporization.

$$\dot{m}_v = \text{mass vaporization rate} = (\overline{\rho D}_v)_f \pi D \ln(1+B)\mathrm{Sh} \tag{12}$$

where Sh is the Sherwood number and D_v is the mass diffusivity of ceramic oxide vapor. B is the mass transfer number

$$B = \frac{Y_{vw} - Y_{v\infty}}{1 - Y_{vw}} \tag{13}$$

where Y_{vw} is the mass fraction of ceramic oxide vapor at the particle surface and $Y_{v\infty}$ is the mass fraction of ceramic oxide vapor at infinity with respect to the particle surface with

$$Y_{vw} = \frac{M_p}{M_p + M(p/p_v - 1)} \tag{14}$$

where M_p is the molecular weight of the ceramic oxide vapor and M is the molecular weight of the mixture excluding the vapor. p is the total pressure surrounding the particle and p_v is the vapor

pressure, which is a function of the surface temperature.

Usually, the effects of noncontinuum have been ignored for mass transfer. However, a recently published study has taken this effect into account [21]. For mass transfer expressions at steady state being analogous to heat transfer at steady state, we can consider [20,21]

$$\mathrm{Sh} = (2 + 0.6\mathrm{Re}^{0.5}\mathrm{Sc}^{0.33}) f_{\mathrm{Kn}} \tag{15}$$

where the Schmidt number is defined as

$$\mathrm{Sc} = \frac{\mu_f}{(\bar{\rho} D_v)_f} \tag{16}$$

In calculating the average plasma thermal conductivity and specific heat, variation of these properties with temperature are considered and they are integrated across the thermal boundary layer thickness and the average properties are determined across the temperature difference between the surface and the surrounding plasma [12,25] as

$$\overline{k_f} = \frac{1}{T_\infty - T_w} \int_{T_w}^{T_\infty} k(T) dT \tag{17}$$

$$\overline{C_{p,f}} = \frac{1}{T_\infty - T_w} \int_{T_w}^{T_\infty} C_p(T) dT \tag{18}$$

When melting occurs, the interface tracking is based on the interface energy balance to calculate the surface regression rate from

$$k_{p,s}\left(\frac{\partial T}{\partial r}\right)_{r_m^-} - k_{p,l}\left(\frac{\partial T}{\partial r}\right)_{r_m^+} = \rho_p L_m \frac{\partial r_m}{\partial t} \tag{19}$$

Similarly, the solid-liquid interface can be tracked when surface resolidification occurs.

For modeling the melting front within a particle, two approaches have been usually adopted in literature: (i) use of adaptive grid to track the melting front, i.e., solving three equations; one each for the solid, the interface, and the molten part or (ii) use of a fixed grid approach and casting all the three equations into one combined form. For the fixed grid approach, the enthalpy method is quite common but here in our modeling study, we have adopted a temperature transformation model, where all the three equations are expressed in terms of temperature in one single equation. The advantage of this approach is that it can be used for convection, as well as conduction controlled melting and the numerical oscillations that can occur in the enthalpy method can be avoided [30]. The final form of the energy equation is given as

$$\rho_p \frac{\partial (C_p T)}{\partial t} = \frac{1}{r^2}\frac{\partial}{\partial r}\left(r^2 k_p \frac{\partial T}{\partial r}\right) + q''' - \rho_p \frac{\partial b}{\partial t} \tag{20a}$$

$$b = \begin{cases} C_{p,s}\Delta T & T < T_m - \Delta T \\ \left(\dfrac{C_{p,s} + C_{p,l}}{2}\right)\Delta T + \dfrac{L_m}{2} & T_m - \Delta T < T < T_m + \Delta T \\ C_{p,s}\Delta T + L_m & T > T_m + \Delta T \end{cases} \tag{20b}$$

$$C_p(T) = \begin{cases} C_{p,s} & T < T_m - \Delta T \\ \left(\dfrac{C_{p,s} + C_{p,l}}{2}\right) + \dfrac{L_m}{2\Delta T} & T_m - \Delta T < T < T_m + \Delta T \\ C_{p,l} & T > T_m + \Delta T \end{cases} \tag{20c}$$

In microwave plasmas, there is a possibility of the direct coupling of microwave radiation with particles in addition to the surface heating experienced by the particles in the hot plasma environment. Comprehensive work has been conducted to describe the heating of ceramics by microwave radiation [31–38]. Absorption of microwave radiation has been studied extensively in biomedical applications and for food and materials processing. Sintering of ceramics doped with high dielectric loss materials in a microwave cavity has also been studied in literature [31–34]. A generalized expression for the power absorbed by a material per unit volume has been derived in literature [35] and is well accepted for analyzing the heat dissipated in the material for various applications [34,36–41]

$$q''' = \sigma |E_i|^2 = 2\pi f \varepsilon_o \varepsilon_r \tan\delta |E_i|^2 = 2\pi f \varepsilon_o \varepsilon'' |E_i|^2 \tag{21}$$

where σ stands for the electrical conductivity of the material, ε_o is the permittivity in free space (=8.86 pF/m), f is the frequency of the EM wave, ε_r is the relative dielectric constant, ε'' is the dielectric loss factor, and $\tan\delta$ is the loss tangent defined as the ratio $\varepsilon''/\varepsilon_r$. E_i is the rms internal electric field developed within the material in response to the external electric field.

At room temperature, the electrical conductivity of ceramic materials is extremely low but after a critical temperature, the electrical conductivity increases abruptly and a characteristic phenomenon known as "thermal runaway" occurs. Ceramic material suddenly starts coupling with the microwave radiation after surpassing the critical temperature. Thermal runaway has been studied in literature [38] and the abrupt rise in coupling of ceramic materials with microwave radiation has been investigated. The highly convective heating in a plasma environment is sufficient to raise the temperature of the particle to values near the critical temperature within milliseconds. Thus, there is a possibility that these particles will couple with microwave radiation within the microwave active zone. If the particle's electrical conductivity surpasses the threshold value, then strong microwave coupling can occur. Variations of electrical conductivity of zirconia and alumina with temperature were obtained from different sources [28,42]. The most challenging part is, however, the estimation of internal electric field. For given frequency and power of microwave, i.e., for a given external electric field, the magnitude of the internal electric field is not only a function of material property but it also depends on the size, geometry, and orientation of the object with respect to the external electric field [35,40]. For a very small sphere, the orientation with respect to the external electric field does not matter, as the spherical particle being small with respect to the wavelength of microwave radiation, the particle will experience uniform electric field. For a spherical particle, the external electric field is attenuated in its interior by a factor of $3/(\varepsilon_r + 2)$ [40]. The value of the relative material dielectric constant not only depends on temperature but also on frequency. The values of the real part of the dielectric constants at 2.45 GHz were obtained from literature [36]. The external electric field for this application was evaluated using the expression proposed by Pozar [43] for microwave radiation through a rectangular waveguide as

$$P_{\max} = 2.6 \times 10^{13}\left(\frac{E_o}{f}\right)^2 \tag{22}$$

where $P_{\max}$ denotes the maximum power of the microwave source, f is the microwave frequency, and E_o is the external electric field. Equations (21) and (22) were used to compute the particle internal heat addition during microwave coupling.

4 Results and Discussion

4.1 Plasma Flow Field. Plasma velocity and temperature distributions were obtained from computational fluid dynamics simulations using the software package FLUENT 6.3.26. Volumetric heat source was incorporated in the microwave coupling region such that the peak temperature in the plasma reaches 6000 K and the wall temperature does not exceed the melting point of quartz. The plasma temperature in the coupling region is maximum at the center at 6000 K and decays in the radial direction to temperatures below the melting point of quartz. It was found that for an oper-

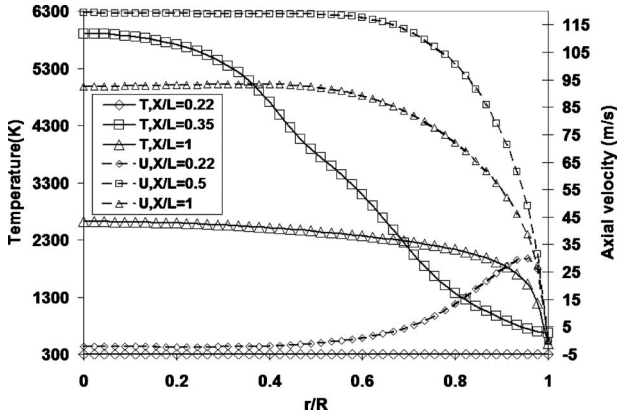

Fig. 2 Evolution of temperature and axial velocity distributions at three axial locations

ating condition of 4 kW power of the microwave source, 470 ml/s of annular cooling flow rate was required for the main operating flow rate of the plasma of 160 ml/s. These flow rates were also employed in the experiments without an incidence of quartz plasma chamber wall melting, thus giving some confidence to the modeling results. In these simulations, a recirculation zone was found to exist just above the waveguide zone, where the particle carrier gas flow in the center and the cooling wall jet flow emerging through the annular slot interacted. The evolution of downstream axial temperatures and velocities are displayed in Fig. 2. The velocity peak at $x/L=0.22$ is due to the injected cooling air along the quartz tube wall. With increasing distance, the velocity in the tube increases due to the dilatation caused by the heat release from the formation of microwave plasma at around $x/L=0.50$. Beyond the microwave coupling region at the exit of the tube, centerline velocity is around 90 m/s. The evolution of centerline temperature and wall temperature of the quartz tube is shown in Fig. 3. The plasma gas temperature reaches 6000 K in the coupling zone to match the peak temperature in the plasma [7] and then decreases with increasing axial distance downstream. The quartz wall temperature also increases to a very high value near 1900 K in the hot zone but gradually cools down as the hot plasma is shielded by the cooling jet along the inner walls.

4.2 Particle Heating. The model described earlier was used to determine the thermal history of zirconia and alumina particles of different sizes injected into microwave plasma. The physical properties of the injected particles are tabulated in Table 1.

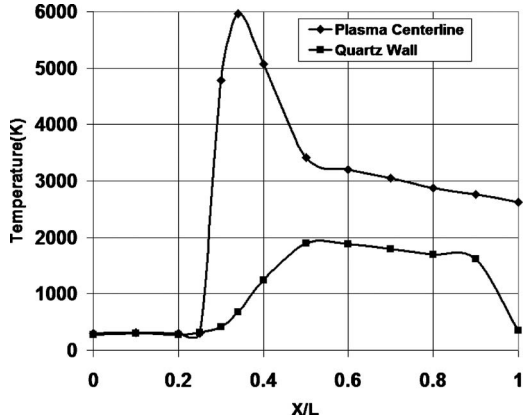

Fig. 3 Variations of plasma temperature along the centerline and the temperature of the outer surface of the quartz wall along the axial direction

Table 1 Physical properties of injected materials

Physical properties	ZrO_2	Al_2O_3
Density (kg/m^3)	5780	4000
Solid phase specific heat (J/kg K)	604	1383
Liquid phase specific heat (J/kg K)	714	1200
Solid phase thermal conductivity (W/m K)	2	6.3
Liquid phase thermal conductivity (W/m K)	3	6.3
Melting point (K)	2983	2323
Boiling point (K)	4600	4000
Latent heat of fusion (kJ/kg K)	812.4	1089.5
Latent heat of evaporation (kJ/kg)	6000	24,670

4.2.1 Model Validation and Grid Independence. The time implicit finite volume model was first validated with the results of Bourdin et al. [12]. Bourdin et al. [12] analyzed the temperature rise of a stationary 100 μm alumina particle in a nitrogen plasma environment at 10,000 K. The model predictions from this study were compared with those results and it was found that the predicted time for the surface temperature of the 100 μm alumina particle to reach the melting point was similar to that predicted by Bourdin et al. [12]. The time evolution of the surface and center temperatures of the particle are shown in Fig. 4 and it was observed that there was around 10% difference for the surface temperature with the data of Bourdin et al. [12] in the initial stage but better agreement was obtained at later times. The center temperature prediction was also in good agreement with the published result [12].

Grid independence study was carried out for a 30 μm zirconia particle for three different radial computational grids of 50, 100, and 150 shells. It was found that at the instant when the surface temperature reaches melting point, the temperature profiles for 100 and 150 shells overlapped and the predictions for 50 shells exhibited a slight discrepancy in the inner part of the particle. Based on these results, 100 computational shells were used with 1 μs time step interval in the subsequent simulations.

4.2.2 Effect of Knudsen Number and Variable Property Correction Factors. The general notion about noncontinuum effects in a plasma environment is that for particle sizes smaller than 10 μm, noncontinuum effects are important. Noncontinuum effect has been investigated for 10 μm and 30 μm zirconia particles injected along the centerline from the particle injection tube with an initial velocity of 45 m/s. Figure 5 shows the particle internal temperature distributions when the surface temperature reaches the melting point. Without considering the noncontinuum effect, the particles reach the melting point at about 0.04 ms sooner compared with the case where the noncontinuum effects

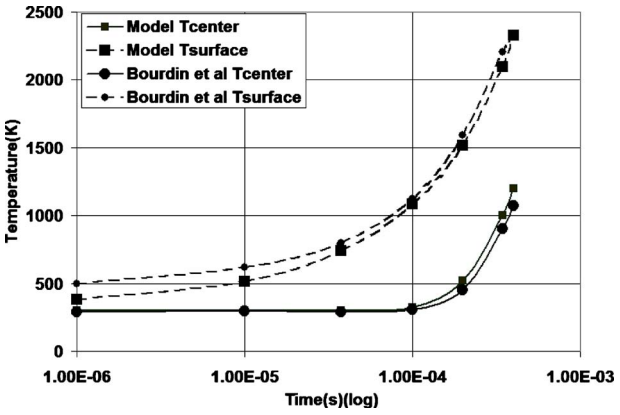

Fig. 4 Model validation with Bourdin et al. [12] for a stationary 100 μm alumina particle in a nitrogen plasma bath at 10,000 K

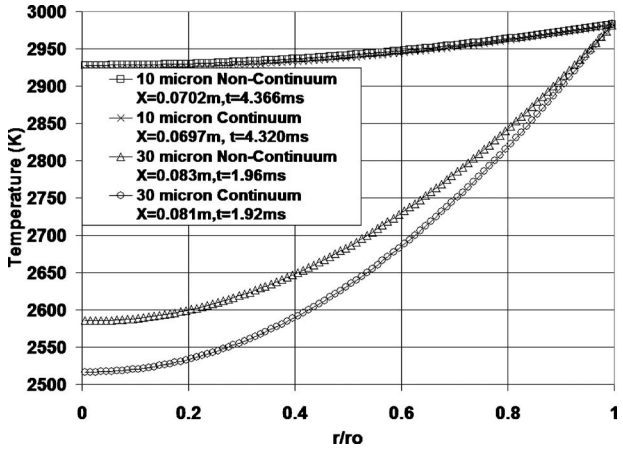

Fig. 5 Effect of noncontinuum on heat-up of 10 μm and 30 μm zirconia particles up to melting point injected with a velocity of 45 m/s along the centerline

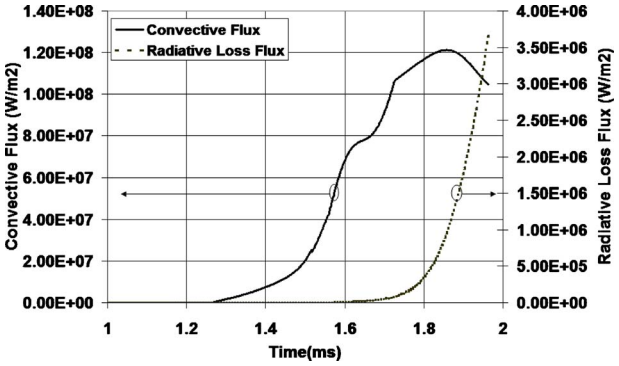

Fig. 6 Comparison of convective and radiative fluxes experienced by a 30 μm zirconia particle up to melting point injected along the centerline with an initial velocity of 45 m/s

have been taken into account. This is due to the slip boundary conditions as the momentum and the heat transfer are slower in the slip regime. For the 10 μm particle diameter case, a maximum difference of around 5 K was found at the center of the particle while a difference of around 100 K was observed at the center of the 30 μm particle. Although noncontinuum effect should have been more dominant for the 10 μm particle, this effect was masked by the fact that the plasma temperature was 3520 K when the 10 μm particle surface reaches the melting point, whereas the corresponding temperature is 5760 K for the 30 μm diameter particle due to the different transit times of different size particles.

The effect of variable property correction factors was also investigated for a 30 μm zirconia particle injected along the centerline and it was observed that there was not much difference in the temperature profiles, as well as the final axial locations and time instants. Thus, variable property correction factors are not as important as the Knudsen number correction factors as far as the heat-up of particles are concerned.

4.2.3 Effect of Thermal Radiation. Thermal radiation loss from the particle surface to its surroundings was also evaluated. Thermal radiation from the plasma to the particle has not been considered since the plasma is optically thin due to the Stark effect, provided that the particle loading rate is not large. It has been found in literature that the flux due to the radiative losses can be as small as 1% of the convective heat flux [20]. Comparison of convective and radiative heat fluxes have been made for 30 μm and 50 μm particles injected along the centerline with an initial velocity of 45 m/s from the particle injection tube. The results are shown in Fig. 6 for the 30 μm zirconia particle. It was observed in all the cases that convective flux was an order of magnitude higher than the radiative heat loss. It has been pointed out in literature that radiation loss becomes important for large particles and for the cases where the surface temperature exceeds 2000 K and plasma temperature falls below 4000 K [16,19]. The melting point of zirconia being higher than that of alumina ($T_{\mathrm{melt,ZrO_2}}$ = 2983 K and $T_{\mathrm{melt,Al_2O_3}}$ = 2323 K) radiation loss can be more important for zirconia particles before reaching the melting point. On the other hand, the radiation loss for 50 μm particles is somewhat higher than in the case of 30 μm particles.

4.2.4 Effect of Initial Particle Injection Velocity. The initial velocity with which the particles are injected into the plasma determines the residence time and, consequently, the extent of particle heat-up in the plasma zone. To evaluate the effect of initial velocity in the heating of particles, 30 μm zirconia and alumina particles were injected along the centerline with initial velocities of 30 m/s, 40 m/s, and 45 m/s from the particle injection tube. The results showing the outcome of different initial velocities in particle heat-up are shown in Fig. 7 for zirconia and alumina particles. For both zirconia and alumina particles, lower initial velocity resulted in longer times to reach the melting point and more internal heat-up of the particles because longer residence time allows deeper penetration of heat into the particle. Higher initial velocities resulted in shorter times to reach the high temperature region. Although the heat transfer coefficient is not altered much due to the particles heating in the conduction regime, the particle surface temperature reaches the melting point faster with increasing velocity. Internal particle temperature gradient is also higher for the shorter particle residence time as expected.

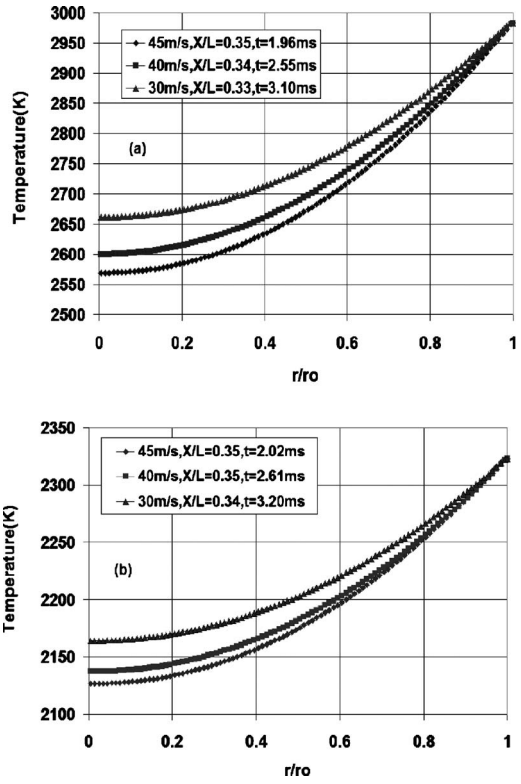

Fig. 7 Temperature profiles of 30 μm (*a*) zirconia and (*b*) alumina particles injected along the centerline with different initial velocities from the particle injection tube at the instant when surface temperature reaches melting point

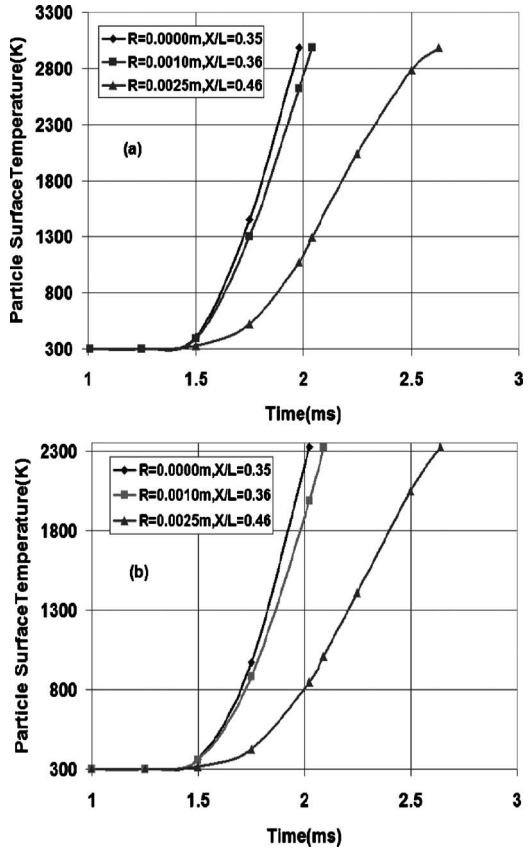

Fig. 8 Effect of injection locations in heat-up of 30 μm (*a*) zirconia and (*b*) alumina particles with an initial velocity of 45 m/s from the particle injection tube

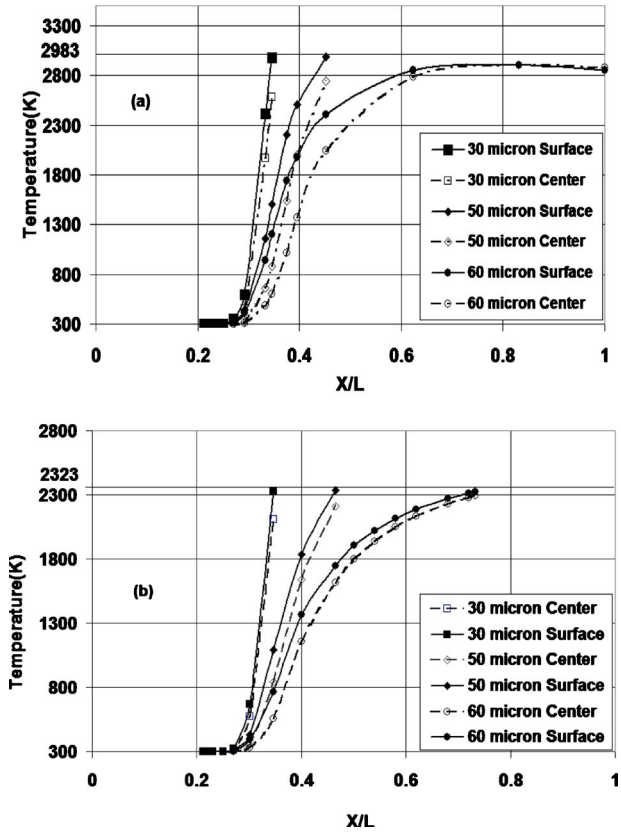

Fig. 9 Surface and center temperatures of the particles injected along the centerline with an initial velocity of 45 m/s. Time: (*a*) zirconia: 30 μm–1.96 ms, 50 μm–2.55 ms, and 60 μm–5 ms and (*b*) alumina: 30 μm–2.02 ms, 50 μm–2.7 ms, and 60 μm–3.7 ms.

4.2.5 Effect of Particle Injection Locations. Since most of the analysis done so far was for the particles injected along the centerline, the heat-up of particles injected at locations away from the centerline of the plasma is worth examining. On emergence from the particle injection tube, the particles traverse through the inner quartz tube before getting entrained into the plasma formed at the microwave coupling region. For 30 μm particles of zirconia and alumina injected with an initial velocity of 45 m/s from the particle injection tube, the particles emerge from the inner quartz tube with an axial velocity of around 35 m/s. Thus, alumina and zirconia particles of diameter 30 μm were injected along the centerline 1 mm and 2.5 mm away from the centerline with an axial velocity of 35 m/s while emerging from the inner quartz tube. The time evolution of surface temperature of 30 μm particles for different injection locations at the instant when the surface temperature reaches melting point are shown in Fig. 8. It was observed that for zirconia and alumina particles, the surface temperature of the particle injected away from the centerline reached the melting point ($T_{\mathrm{melt,ZrO_2}}=2983$ K and $T_{\mathrm{melt,Al_2O_3}}=2323$ K) at later time instants and, consequently, farther axial downstream locations compared with the case when the particle was emerging from the inner quartz tube along the centerline. This is due to the nature of the radial temperature profile of the plasma as the particles that are injected off-centerline experience lower local plasma temperatures as compared with the particles injected along the centerline. It was observed in the results that the particle injected along the centerline and the particle injected 1 mm away from the centerline reach the melting point almost at the same axial location at slightly different time instants. But the particle injected 2.5 mm away from the centerline reaches the melting point at a farther downstream location after traversing about 45% of the total length of the quartz tube.

4.2.6 Effect of Microwave Radiation. The particles, after emerging from inner quartz and travel a certain distance downstream, pass through the microwave coupling zone and interact with the EM field until they cross the coupling zone. It was observed that microwave radiation did not have any effect in particle heating. The reason for the weak coupling can be attributed to the small size and spherical shape of the particles. The external electric field can be assumed to be uniform in magnitude with respect to the particle, owing to the formation of the standing wave. Since the external electric field is greatly reduced in the interior of the particle, even though the electrical conductivity of the particle can be very high near its melting point, for example, 1500 S/m for zirconia and ~400 S/m for alumina [44], the magnitude of the heat source, say for a 10 μm particle, is only of the order of 10^{-7} W or 10^{-6} W. In comparison, for the same 10 μm particle, the convective heat flux is of the order of 10^{-3} W or 10^{-2} W.

4.2.7 Effect of Particle Size. To explore the particle size effects, 30 μm, 50 μm, and 60 μm zirconia and alumina particles were injected along the centerline with same initial velocity of 45 m/s from the particle injection tube. The variations of particle surface and center temperatures with the normalized axial distance are shown in Fig. 9 for zirconia and alumina particles. It was found that the 60 μm zirconia particle emerges from the quartz tube without reaching the melting point while the 60 μm alumina particle reaches the melting point after traversing almost 80% of the total length. For both alumina and zirconia particles, 30 μm and 50 μm diameter particles reached the melting point after traversing 35% and 50% of the total length, respectively, and these particles exhibited considerable degree of melting.

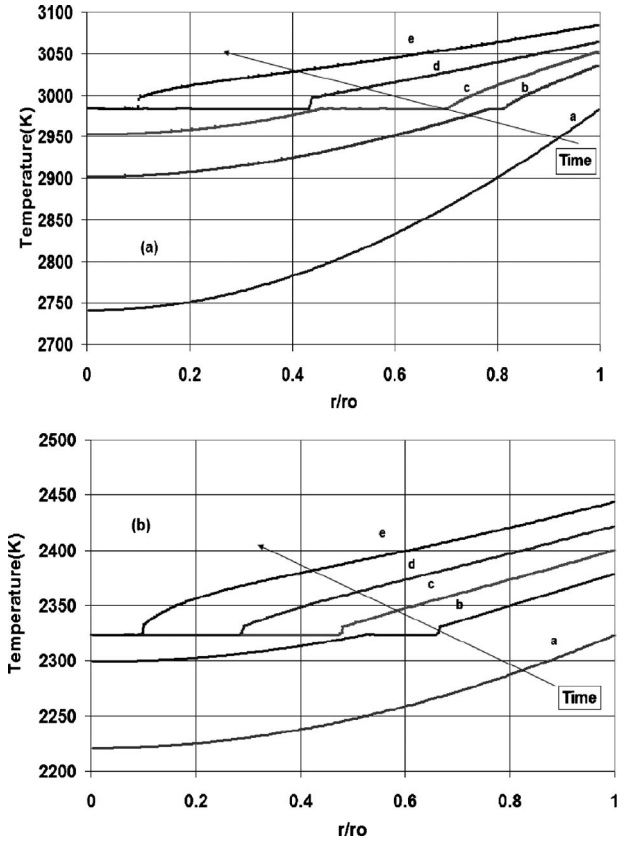

Fig. 10 Melt front movement of a 50 μm alumina injected along the centerline with an initial velocity of 45 m/s: (*a*) zirconia: a−*t*=2.55 ms, *X*=0.112 m, b−*t*=2.70 ms, *X*=0.119 m, c −*t*=2.77 ms, *X*=0.123 m, d−*t*=2.85 ms, *X*=0.126 m, and e−*t* =2.92 ms, *X*=0.130 m and (*b*) alumina: a−*t*=2.7 ms, *X* =0.119 m, b−*t*=2.77 ms, *X*=0.124 m, c−*t*=2.81 ms, *X* =0.125 m, d−*t*=2.84 ms, *X*=0.127 m, and e−*t*=2.88 ms, *X* =0.129 m

4.2.8 Melt Front Propagation. Zirconia and alumina particles smaller than 50 μm diameters exhibited good possibility of melting since they reached melting point after covering about 50% of the total length of the quartz tube. The melt front propagation of 50 μm particles injected along the centerline of the plasma is shown in Fig. 10 at different time instants and corresponding axial locations. It was found that the surface vaporization during the melting of a 50 μm particle was small due to the very low vapor pressure of ceramic oxides even at these high temperatures. Thus, the results presented did not account for the surface vaporization effect. For both zirconia and alumina particles, it was observed that a 50 μm particle experiences significant amount of melting in the plasma region and these results are in qualitative agreement with some preliminary observations from experiments currently underway.

5 Concluding Remarks

A comprehensive particle heating and melting model capable of predicting the internal temperature profiles of the particles, as well as the tracking of melt front was developed for microwave plasma processing. The modeling of a single particle of zirconia and alumina of different diameters was carried out for predicting the final thermal and kinetic states considering the convective heat addition from the plasma, the radiation loss from the particle surface, and the coupling of ceramic materials with microwave radiation in the microwave coupling region. A shield gas stream was utilized to prevent the plasma chamber quartz wall from melting, as well as to prevent the impact of molten particles on the quartz walls. Based on the conversion efficiency of microwave energy to thermal energy in the plasma, a volumetric heat source was incorporated in the computational fluid dynamics model using FLUENT 6.3.26 software and variations of the transport properties of the plasma with temperature were considered to simulate the microwave excited plasma environment. The observations and conclusions that can be drawn from the work presented in this article are as follows.

- The microwave excited plasma flow field was laminar and steady in nature. The maximum temperature of the microwave excited plasma flow field was around 6000 K while that of a dc arc plasma is typically around 10,000 K. However, the arc root fluctuations and the turbulent dispersions can cause large particle temperature differences in dc arc plasmas. This translates to inhomogeneity in the final microstructure due to the accumulation of fully or partially molten and unmelted or unpyrolized materials even for the properly optimized operating conditions.
- In conventional dc arc plasmas, the powder feedstock is typically fed transversely into the plasma jet emerging from the gun nozzle and hence the entrainment of the particles into the plasma is greatly dependent on the momentum ratio while in the case of microwave plasma, the powder feedstock can be axially fed into the plasma core and the uncertainty of proper entrainment can be diminished to a large extent.
- The results presented in this article suggest that well-controlled injection of particles into a microwave plasma can achieve full melting of small particles ($\leq$50 μm).
- The particles being spherical in shape and small in size, the internal electric field developed within the particle is not large enough to generate a considerable volumetric heat source within the particle and as such, the microwave radiation does not directly participate in particle heating and melting in the presence of the high temperature plasma.

However, further modeling and extensive experimental work still need to be performed to evaluate the prospect of microwave plasmas for the purpose of depositing coatings.

Acknowledgment

The research reported in this article was conducted in conjunction with a DARPA program for synthesis of optical ceramic materials. The authors would like to acknowledge discussions of this work with Prof. Eric Jordan (Mechanical Engineering Department, University of Connecticut) and Dr. Makhlouf Redjdal (Amastan LLC).

Nomenclature

a = thermal accommodation coefficient
B = mass transfer number
$C_D, C_{D,\text{eff}}, C_{D,\text{evap}}$ = drag coefficient of particle
$C_{p,f}$ = average specific heat of plasma, J/(kg K)
C_p = particle specific heat, J/(kg K)
$C_{p,w}$ = specific heat of plasma at surface temperature, J/(kg K)
$C_{p,\infty}$ = specific heat of plasma at freestream temperature, J/(kg K)
D = diameter of the particle, m
D_v = mass diffusivity of ceramic vapor, m^2/s
E_i = rms internal electric field, V/m
E_o = external electric field, V/m
f_{Kn} = Knudsen number correction factor
f_{prop} = variable property correction factor
f_v = correction factor due to evaporation
f = frequency of microwave radiation, Hz

h = heat transfer coefficient, $W/m^2\,K$
Kn^* = Knudsen number
$\overline{k_f}$ = average plasma thermal conductivity, $W/(m\,K)$
k_p = particle thermal conductivity, $W/(m\,K)$
L_v = latent heat of vaporization, J/kg
L_m = latent heat of melting, J/kg
M_p = molecular weight of ceramic oxide vapor, g/mol
M = molecular weight of mixture except ceramic oxide vapor, g/mol
$\dot{m}_v$ = mass rate of evaporation, kg/s
Nu = Nusselt number
Pr = Prandtl number of plasma
Pr_w = Prandtl number of plasma at surface temperature of the particle
P_{max} = maximum power of microwave source, kW
p = total pressure surrounding the particle, atm
p_v = partial pressure of ceramic oxide vapor
$\dot{Q}_{conv}$ = convective heat transfer rate, J/s
$\dot{Q}_{rad}$ = radiative heat transfer rate, J/s
$\dot{Q}_{vap}$ = heat transfer rate due to surface evaporation, J/s
q''' = volumetric heat source, W/m^3
Re = particle Reynolds number
r_m = position of solid-liquid interface, m
r_m^-, r_m^+ = vicinity of melt interface, m
r = local radial coordinate in particle, m
Sc = Schmidt number
Sh = Sherwood number
T = particle temperature, K
T_∞ = freestream plasma temperature, K
T_w = particle surface temperature, K
T_m = melting point, K
t = time, s
U, V = particle axial and radial velocities, m/s
U_∞, V_∞ = plasma axial and radial velocities, m/s
v_w = mean molecular speed of plasma at particle surface temperature
Y_{vw} = mass fraction of ceramic vapor at particle surface
$Y_{v\infty}$ = mass fraction of ceramic vapor at infinity with respect to particle surface

Greek Symbols

γ = specific heat ratio of plasma, $J/(kg\,K)$
ε = surface emissivity
ε_o = permittivity of free space, F/m
ε_r = relative dielectric constant
ε'' = relative dielectric loss factor
λ^* = mean free path, m
μ = average plasma viscosity, Pa s
μ_g = viscosity of plasma at freestream temperature, Pa s
μ_w = viscosity of plasma at particle surface temperature, Pa s
ρ_g = average plasma density, kg/m^3
ρ_p = particle density, kg/m^3
ρ_w = density of plasma at particle surface temperature, kg/m^3
$\overline{\rho_f}$ = mean density of vapor-gas mixture around the vaporizing particle, kg/m^3
σ = Stefan–Boltzmann constant, $W/(m^2\,K^4)$; electrical conductivity, S/m

Subscripts

f = film around the particle
g = plasma
i = internal
l = liquid
m = melting
o = external
p = particle
s = solid phase
v = vapor phase

References

[1] Pawlowski, L., 1995, *The Science and Engineering of Thermal Spray Coatings*, Wiley, New York.
[2] Bisson, J. F., Gauthier, B., and Moreau, C., 2003, "Effect of Plasma Fluctuations on In-Flight Particle Parameters," J. Therm. Spray Technol., **12**(1), pp. 38–43.
[3] Bisson, J. F., and Moreau, C., 2003, "Effect of Direct-Current Plasma Fluctuations on In-Flight Particle Parameters: Part II," J. Therm. Spray Technol., **12**(2), pp. 258–264
[4] Al-Shamma'a, A. I., Wylie, S. R., Lucas, J., and Stuart, R. A., 2002, "Microwave Plasma Jet for Material Processing at 2.45 GHz," J. Mater. Process. Technol., **121**, pp. 143–147.
[5] Wylie, S. R., Al-Shamma'a, A. I., Lucas, J., and Stuart, R. A., 2004, "An Atmospheric Microwave Plasma Jet for Ceramic Material Processing," J. Mater. Process. Technol., **153–154**, pp. 288–293.
[6] Hong, Y. C., Uhm, H. S., and Cho, S. C., 2009, "Microwave Plasma Torch Operating at a Low Pressure for Material Processing," Thin Solid Films, **517**, pp. 4226–4228.
[7] Green, K. M., Borras, M. C., Woskov, P. P., Flores, G. J., III, Hadidi, K., and Thomas, P., 2001, "Electronic Excitation Temperature Profiles in an Air Microwave Torch," IEEE Trans. Plasma Sci., **29**(2), pp. 399–406.
[8] Hadidi, K., and Woskov, P., 1999, "Efficient, Modular Microwave Plasma Torch for Thermal Treatment," PSFC MIT.
[9] Vollath, D., and Sickafus, K. E., 1993, "Synthesis of Ceramic Oxide Powders in a Microwave Plasma Device," J. Mater. Res., **8**(11), pp. 2978–2984.
[10] Meillot, E., Guenadou, D., and Bourgeois, C., 2008, "Three-Dimension and Transient D.C. Plasma Flow Modeling," Plasma Chem. Plasma Process., **28**(1), pp. 69–84.
[11] Cetegen, B. M., and Basu, S., 2009, "Review of Modeling of Liquid Precursor Droplets and Particles Injected Into Plasmas and High Velocity Oxy-Fuel (HVOF) Flame Jets for Thermal Spray Applications," J. Therm. Spray Technol., **18**(5), pp. 769–793.
[12] Bourdin, E., Fauchais, P., and Boulos, M., 1983, "Transient Heat Conduction Under Plasma Conditions," Int. J. Heat Mass Transfer, **26**(4), pp. 567–582.
[13] Vardelle, M., Vardelle, A., and Boulos, M. I., 1983, "Plasma-Particle Momentum and Heat Transfer: Modelling and Measurements," AIChE J., **29**(2), pp. 236–243.
[14] Pfender, E., and Lee, Y. C., 1985, "Particle Dynamics and Particle Heat and Mass Transfer in Thermal Plasmas. Part I. The Motion of a Single Particle Without Thermal Effects," Plasma Chem. Plasma Process., **5**(3), pp. 211–237.
[15] Chyou, Y. P., and Pfender, E., 1989, "Behavior of Particulates in Thermal Plasma Flows," Plasma Chem. Plasma Process., **9**(1), pp. 45–71.
[16] Lee, Y. C., Chyou, Y. P., and Pfender, E., 1985, "Particle Dynamics and Particle Heat and Mass Transfer in Thermal Plasmas. Part II. Particle Heat and Mass Transfer in Thermal Plasmas," Plasma Chem. Plasma Process., **5**(4), pp. 391–414.
[17] Chen, X., and Pfender, E., 1983, "Effect of Knudsen Number on Heat Transfer to a Particle Immersed Into a Thermal Plasma," Plasma Chem. Plasma Process., **3**(1), pp. 97–113.
[18] Lee, Y. C., and Pfender, E., 1987, "Particle Dynamics and Particle Heat and Mass Transfer in Thermal Plasmas. Part III. Thermal Plasma Jet Reactors and Multiparticle Injection," Plasma Chem. Plasma Process., **7**(1), pp. 1–27.
[19] Chen, X., and Pfender, E., 1982, "Unsteady Heating and Radiation Effects of Small Particles in a Thermal Plasma," Plasma Chem. Plasma Process., **2**(3), pp. 293–316.
[20] Wan, Y. P., Prasad, V., Wang, G.-X., Sampath, S., and Fincke, J. R., 1999, "Model and Powder Particle Heating, Melting, Resolidification, and Evaporation in Plasma Spraying Processes," ASME J. Heat Transfer, **121**, pp. 691–699.
[21] Wan, Y. P., Fincke, J. R., Sampath, S., Prasad, V., and Herman, H., 2002, "Modeling and Experimental Observation of Evaporation From Oxidizing Molybdenum Particles Entrained in a Thermal Plasma Jet," Int. J. Heat Mass Transfer, **45**, pp. 1007–1015.
[22] Xiong, H.-B., Zheng, L.-L., Sampath, S., Williamson, R. L., and Fincke, J. R., 2004, "Three-Dimensional Simulations of Plasma Spray: Effects of Carrier Gas Flow and Particle Injection on Plasma Jet and Entrained Particle Behavior," Int. J. Heat Mass Transfer, **47**, pp. 5189–5200.
[23] Ettouil, F. B., Patreyon, B., Ageorges, H., Ganaoui, M. E., Fauchais, P., and Mazhorova, O., 2007, "Fast Modeling of Phase Changes in a Particle Injected Within a D.C. Plasma Jet," J. Therm. Spray Technol., **16**, pp. 744–750.
[24] Ahmed, I., and Bergman, T., 2000, "Three-Dimensional Simulation of Thermal Plasma Spraying of Partially Molten Ceramic Agglomerates," J. Therm. Spray Technol., **9**(2), pp. 215–224.
[25] Li, H.-P., and Xi, C., 2002, "Three-Dimensional Modeling of the Turbulent

Plasma Jet Impinging Upon a Flat Plate and With Transverse Particle and Carrier-Gas Injection," Plasma Chem. Plasma Process., **22**(1), pp. 27–58.
[26] Boulos, M. I., Fauchais, P., and Pfender, E., 1994, *Thermal Plasmas Fundamentals and Applications*, Vol. 1, Plenum, New York.
[27] White, F. M., 1974, *Viscous Fluid Flow*, McGraw-Hill, New York.
[28] Touloukian, Y. S., 1967, *Thermophysical Properties of High Temperature Solid Materials, Vol. 4: Oxides and Their Solutions and Mixtures*, Macmillan, New York.
[29] NIST Structural Ceramics Database (SCD), SCD Citation No. Z00181.
[30] Cao, Y., and Faghri, A., 1990, "A Numerical Analysis of Phase-Change Problems Including Natural Convection," ASME J. Heat Transfer, **112**, pp. 812–816.
[31] Zhao, C., Vleugels, J., Groffils, C., Luypaert, P. J., and Van Der Biest, O., 2000, "Hybrid Sintering With a Tubular Susceptor in a Cylindrical Single-Mode Microwave Furnace," Acta Mater., **48**, pp. 3795–3801.
[32] Mizuno, M., Obata, S., Takayama, S., Ito, S., Kato, N., Hirai, T., and Sato, M., 2004, "Sintering of Alumina by 2.45 GHz Microwave Heating," J. Eur. Ceram. Soc., **24**, pp. 387–391.
[33] Wang, J., Binner, J., Vaidyanathan, B., Joonum, N., Kilner, J., Dimitras, G., and Cross, T. E., 2006, "Evidence for the Microwave Effect During Hybrid Sintering," J. Am. Ceram. Soc., **89**(6), pp. 1977–1984.
[34] Zhang, C., Zhang, G., Leparoux, S., Liao, H., Li, C., Li, C.-J., and Coddet, C., 2008, "Microwave Sintering of Plasma-Sprayed Yttria Stabilized Zirconia Electrolyte Coating," J. Eur. Ceram. Soc., **28**, pp. 2529–2538.
[35] Osepchuk, J. M., 1981, "Microwave Technology," *Kirk–Othmer, Encyclopedia of Chemical Technology*, R. E. Kirk and D. F. Othmer, eds., Wiley, New York, pp. 492–522.
[36] Darby, G. J., Di Fiore, R. R., Schulz, R. L., and Clark, D. E., 1996, "Microwave Processing of Al_2O_3–ZrO_2 Composites," Ceram. Eng. Sci. Proc., **17**(3), pp. 147–154.
[37] Clark, D. E., and Sutton, W. H., 1996, "Microwave Processing of Materials," Annu. Rev. Mater. Sci., **26**(1), pp. 299–331.
[38] Sutton, W. H., 1989, "Microwave Processing of Ceramic Materials," Ceram. Bull., **68**(2), pp. 376–386.
[39] Datta, A. K., 1990, "Heat and Mass Transfer in the Microwave Processing of Food," Chem. Eng. Prog., **86**, pp. 47–53.
[40] Christiansen, D. E., and Unruh, W. P., 1991, "Use of a TM_{010} Microwave Cavity at 2.45 GHz for Aerosol and Filament Drying," Ceram. Trans., **21**, pp. 597–604.
[41] Roddy, D., 1986, *Microwave Technology*, Prentice-Hall, Englewood Cliffs, NJ.
[42] Van Arkel, A. E., Flood, E. A., and Bright, N. F. H., 1953, "The Electrical Conductivity of Molten Oxides," Can. J. Chem., **31**, pp. 1009–1019.
[43] Pozar, D. M., 1998, *Microwave Engineering*, 2nd ed., Wiley, New York.
[44] Homer, F., 1966, "The Electrical Conductivity of Liquid Al_2O_3 (Molten Corundum and Ruby)," J. Phys. Chem., **70**(3), pp. 890–893.

Modeling of Ultrafast Phase Change Processes in a Thin Metal Film Irradiated by Femtosecond Laser Pulse Trains

Jing Huang

Yuwen Zhang[1]
Fellow ASME
e-mail: zhangyu@missouri.edu

J. K. Chen
Fellow ASME

Department of Mechanical and Aerospace Engineering,
University of Missouri,
Columbia, MO 65211

Mo Yang
College of Energy and Power Engineering,
University of Shanghai for Science and Technology,
Shanghai 200093, China

Ultrashort laser pulses can be generated in the form of a pulse train. In this paper, the ultrafast phase change processes of a 1 μm free-standing gold film irradiated by femtosecond laser pulse trains are simulated numerically. A two-temperature model coupled with interface tracking method is developed to describe the ultrafast melting, vaporization, and resolidification processes. To deal with the large span in time scale, variable time steps are adopted. A laser pulse train consists of several pulse bursts with a repetition rate of 0.5–1 MHz. Each pulse burst contains 3–10 pulses with an interval of 50 ps–10 ns. The simulation results show that with such configuration, to achieve the same melting depth, the maximum temperature in the film decreases significantly in comparison to that of a single pulse. Although the total energy depositing on the film will be lifted, more energy will be transferred into the deeper part, instead of accumulating in the subsurface layer. This leads to lower temperature and temperature gradient, which is favorable in laser sintering and laser machining. [DOI: 10.1115/1.4002444]

1 Introduction

Because of its unique characteristics in material processing, fast fabrication, and diagnostic, the interaction between ultrashort pulse lasers, especially femtosecond lasers, with metals has received a lot of research attentions in the past 2 decades. Various computational models were put forward and developed to describe the nonequilibrium energy transport phenomena during the process. One of the classical methods is the two-temperature model, which was originally proposed by Anisimov et al. [1] and then rigorously derived by Qiu and Tien [2] based on the Boltzmann equation. The nonequilibrium energy transport between electron and lattice can also be described by the dual-phase-lag model [3,4]. Jiang and Tsai extended the existing two-temperature model to high electron temperatures by using full-run quantum treatments [5]. Chen et al. [6] proposed a semiclassical two-step heating model to investigate thermal transport in metals caused by ultrashort laser irradiation.

Ultrashort laser pulses can be generated by a mode-locked laser in the form of pulse train. With the rapid development of modern laser technology, currently, the laser pulses are highly controllable with a wide range of parameters. A pulse train consists of a certain number of laser bursts launched at a fixed repetition rate f_{rep}, usually at the order of 10^3–10^6 Hz. Each burst can be composed of several consecutive femto- to picosecond laser pulses with a separation time (t_{sep}) of 100 fs to thousands of picoseconds. However, in most existing theoretical works, only the heating of thin films by a single femtosecond pulse was studied [7–11]. While these works provided basic understanding on the mechanism of interaction between ultrashort pulses and metals, there is still some distance between the physical models and real applications. Jiang and Tsai [12] studied the laser heating of gold thin films by femtosecond pulse trains and the effects of repetition rate and pulse separation were studied. Phase change was not considered in their model since the lattice temperature was well below melting point of gold. The same group also carried out research on the interaction of laser pulse trains with dielectrics [5,13].

Most existing two-temperature model dealt with the case that lattice temperature is well below the melting point and only pure conduction is considered. Under higher laser fluence and/or short pulse, the lattice temperature can exceed the melting point and melting takes place [14]. At even higher laser fluence, the liquid surface temperature may exceed the saturation temperature and evaporation may occur. Both melting and evaporation processes were considered and integrated into the simulation in Refs. [10,15]. Chen and Beraun [16] proposed a computational model, which considered the superheating and material ablation and studied the ablation depth caused by two consecutive pulses split from a laser beam. Huang et al. [15] studied the phase change of gold thin film during the irradiation of multiple femtosecond laser pulses. To understand the relationship between the maximum vaporization temperature and melting depth, ablation depth were analyzed and compared with those of the sing pulse irradiation.

In this paper, based on the two-temperature model, the interface tracking methods is coupled to delineate the phase change processes during the interaction of femtosecond laser pulse trains and thin gold film. To conquer the large time scale involved in the problem, variable time steps are used to control the computation time. The effects of repetition frequency, separation time between pulses, and pulses number per train on the phase change processes are investigated.

2 Physical Model

Figure 1 shows the physical model of the problem under consideration. A laser pulse train impinges on the right side of a free-standing gold film, which has a thickness of L. The thickness is very small in comparison to the radius of the laser beam; therefore, this problem can be approximated to be one-dimensional. Figure 2 shows the structure of a laser pulse train. As stated above, f_{rep} and t_{sep} are the repetition rate and separation time, respectively. Each single pulse is assumed to be temporally Gaussian. The pulse duration (t_p), defined as the full width at half maximum (FWHM), is fixed to be 100 fs in the current work.

The two-step heating model for free electrons and the lattice are given by [10]

[1]Corresponding author.

Manuscript received April 13, 2009; Final manuscript received November 25, 2009; published online November 15, 2010. Assoc. Editor: Wilson K. S. Chiu.

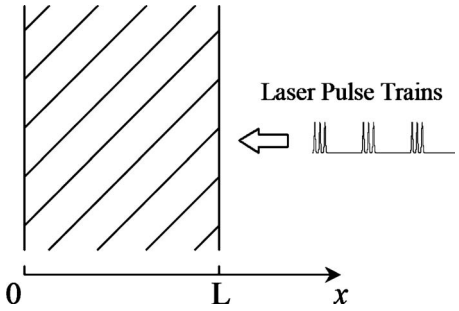

Fig. 1 Laser irradiation on thin film

$$C_e\frac{\partial T_e}{\partial t}=\frac{\partial}{\partial x}\left(k_e\frac{\partial T_e}{dx}\right)-G(T_e-T_l)+S \tag{1}$$

$$C_l\frac{\partial T_l}{\partial t}=\frac{\partial}{\partial x}\left(k_l\frac{\partial T_l}{dx}\right)+G(T_e-T_l) \tag{2}$$

The heat capacity of electron C_e, as suggested by Chen et al. [6], is approximated by

$$C_e=\begin{cases}B_eT_e, & T_e<T_F/\pi^2\\ 2B_eT_e/3+C_e'/3, & T_F/\pi^2\le T_e<3T_F/\pi^2\\ Nk_B+C_e'/3, & 3T_F/\pi^2\le T_e<T_F\\ 3Nk_B/2, & T_e\ge T_F\end{cases} \tag{3}$$

where

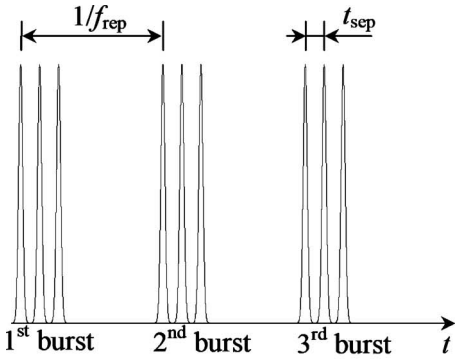

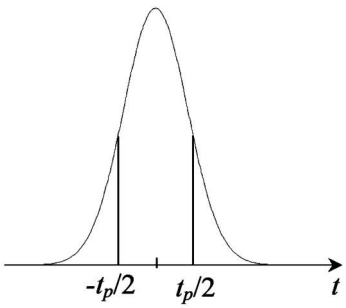

Fig. 2 Laser pulse train

$$C_e'=B_eT_F/\pi^2+\frac{3Nk_B/2-B_eT_F/\pi^2}{T_F-T_F/\pi^2}(T_e-T_F/\pi^2) \tag{4}$$

The thermal conductivity of electron k_e can be obtained by [17]

$$k_e=\chi\frac{(\vartheta_e^2+0.16)^{5/4}(\vartheta_e^2+0.44)\vartheta_e}{(\vartheta_e^2+0.092)^{1/2}(\vartheta_e^2+\eta\vartheta_l)} \tag{5}$$

where $\vartheta_e=T_e/T_F$ and $\vartheta_l=T_l/T_F$.

In Eqs. (1) and (2), G is the electron-lattice coupling factor. A phenomenological temperature-dependent G suggested by Chen et al. [18] is adopted:

$$G=G_{RT}\left[\frac{A_e}{B_1}(T_e+T_l)+1\right] \tag{6}$$

Since the electrons are more likely to collide with liquid atoms than the atoms in solid crystals, in the liquid phase, G is taken to be 20% higher than that of the solid [19].

The laser irradiation is considered as a source term S in Eq. (1):

$$S=\sum_{i=1}^{K}\sum_{j=1}^{N}\frac{0.94J_i(1-R)}{t_P(\delta+\delta_b)[1-e^{-L/(\delta+\delta_b)}]}\exp\left[-\frac{x}{(\delta+\delta_b)}-2.77\left(\frac{t-\frac{i-1}{f_{\text{rep}}}-(j-1)t_{\text{sep}}}{t_p}\right)^2\right] \tag{7}$$

where K is the number of trains, N is the number of pulses in each train, t_{sep} is separation time between each single pulse, f_{rep} is the repetition rate, R is the reflectivity of the thin film, δ is the optical penetration depth, J is the laser pulse fluence, δ_b is the for the ballistic depth, and $[1-e^{-L/(\delta+\delta_b)}]$ is to correct the finite film thickness effect.

For a metal at its thermal equilibrium state, the thermal conductivity k_{eq} is the sum of the electron thermal conductivity k_e and the lattice thermal conductivity k_l. In most cases, k_e dominates k_{eq} because free electrons contribute to the majority part of heat conduction. For gold, k_l is usually taken to be 1% of k_{eq} [20], i.e.,

$$k_l=0.01k_{\text{eq}} \tag{8}$$

A uniform temperature distribution is set to be the initial condition:

$$T_e(x,-2t_p)=T_l(x,-2t_p)=T_0 \tag{9}$$

Selecting $-2t_p$ as the initial time implies that the first laser pulse reaches its peak when $t=0$.

On the right side of the film, which receives laser irradiation, the heat loss caused by radiation will be considered while on the other side adiabatic boundary condition is applied:

$$\left.\frac{\partial T_e}{\partial x}\right|_{x=0}=\left.\frac{\partial T_e}{\partial x}\right|_{x=L}=\left.\frac{\partial T_l}{\partial x}\right|_{x=0}=0 \tag{10}$$

$$q_R''|_{x=L}=\sigma\varepsilon(T_{\text{sur}}^4-T_\infty^4) \tag{11}$$

Before evaporation takes place, T_{sur} is the surface lattice temperature at $x=L$. After evaporation begins, T_{sur} is the liquid-vapor interface temperature, which varies with the heating condition and needs to be determined.

The energy balance at the solid-liquid interface is described by [21]

$$k_{l,s}\frac{\partial T_{l,s}}{\partial x}-k_{l,\ell}\frac{\partial T_{l,\ell}}{\partial x}=\rho_\ell h_m u_{s\ell}\quad x=s(t) \tag{12}$$

where $T_{l,s}$ and $T_{l,\ell}$ are the solid and liquid lattice temperatures, respectively, ρ is the mass density, h_m is the latent heat of fusion, and u_s is the solid-liquid interfacial velocity. The additional interfacial velocity due to the density change during melting and resolidification has been considered.

Table 1 Thermophysical and optical properties of gold

Coefficient for electronic heat capacity, B_e		70 [2]
Material constant, A_e		1.2×10^{7} [18]
Material constant, B_1		1.23×10^{11} [18]
Electron-lattice coupling factor at room temperature, G_{RT}	Solid	2.2×10^{16} [18]
(W/m^3 K)	Liquid	2.6×10^{16} [18]
Specific heat, C_p (J/kg K)		$105.1+0.2941T_1-8.731\times10^{-4}T_1^2+1.787\times10^{-6}T_1^3-7.051$
	Solid	$\times10^{-10}T_1^4+1.538\times10^{-13}T_1^5$ [15]
	Liquid	163.205 [19]
Latent heat of evaporation at T_b, h_{l_v} (J/kg)		1.698×10^{6} [24]
Latent heat of fusion, h_m (J/kg)		6.373×10^{4} [24]
Molar weight, M (kg/kmol)		196.967 [24]
Reflection coefficient, R		0.6
Universal gas constant, R_u (J/kmol K)		8314.0
Boiling temperature, T_b (K)		3127
Critical temperature, T_c (K)		5590
Melting temperature, T_m (K)		1336
Fermi temperature, T_F (K)		6.42×10^{4}
Limit velocity, V_0 (m/s)		1300 [19]
Coefficient for electronic conductivity, χ (W/m K)		353 [17]
Optical penetration depth, δ (nm)		20.6
Ballistic range, δ_b (nm)		105 [19]
Thermal conductivity at equilibrium, k_{eq} (W/m K)	Solid	$320.973-0.0111T_1-2.747\times10^{-5}T_1^2-4.048\times10^{-9}T_1^3$
	Liquid	$37.72+0.0711T_1-1.721\times10^{-5}T_1^2+1.064\times10^{-9}T_1^3$
Density, ρ (kg/m^3)	Solid	19.3×10^{3}
	Liquid	17.28×10^{3}

For rapid melting and solidification processes, the velocity of the interface is dominated by nucleation dynamics, instead by the energy balance, Eq. (12). For ultrashort-pulsed laser melting of gold, the velocity of the solid-liquid interface is described by [19]

$$u_{s\ell} = V_0\left[1-\exp\left(-\frac{h_m}{R_g T_m}\frac{T_{l,I}-T_m}{T_{l,I}}\right)\right] \tag{13}$$

where V_0 is the maximum interface velocity, R_g is the gas constant for the metal, and $T_{l,I}$ is the interfacial temperature. The interfacial temperature $T_{l,I}$ is higher than the normal melting point T_m during melting and lower than T_m during solidification.

Although the evaporation process is included in the current model, the simulation results show that within a wide range of parameters, the temperature will not exceed the boiling point. Therefore, the introduction to the vaporization model is omitted here.

3 Numerical Model

The governing equations (1) and (2) are discretized by the standard finite volume method [22]. A fixed uniform grid with 2050 control volumes is adopted. The time step is variable in the numerical solution. The smallest time step is $10^{-2}t_p$, which is implemented during $(-2t_p, 2t_p)$ of each single pulse. The largest time step is $10^{4}t_p$, which is implemented when the difference between electronic and lattice temperature is less than 1 K.

In each time step, an iterative procedure will be employed to deal with the nonlinear relationship between electron energy equation, lattice energy equation, and solid-liquid and liquid-vapor interfaces. Electron energy equation (1) will be solved first using tridiagonal matrix method (TDMA), then the lattice energy equation (2) will be solved. After obtaining an estimated electron and lattice temperature field, the velocity and temperature of solid-liquid interface will be obtained by using the method provided in Ref. [23] and is briefly described as follows:

(1) The solid-liquid interfacial temperature T_{sl} is assumed and the solid-liquid phase interfacial velocity is determined according to the interfacial energy balance.
(2) The interfacial velocity from the nucleation dynamics is obtained from Eq. (13).
(3) The interfacial velocities got from steps (1) and (2) are compared. If the interfacial velocity obtained from the energy balance is higher than that from the nucleation dynamics, the interfacial temperature will be increased; otherwise, the interfacial temperature is decreased.

Steps 1–3 are repeated until the difference between the interfacial velocities obtained from the two methods is less than 10^{-5} m/s.

4 Results and Discussion

4.1 Melting and Resolidification of Gold Film With Pulse Train Irradiation. First of all, the development of lattice temperature and solid-liquid interface during a typical irradiation process of a pulse train will be shown. The duration of each single pulse will remain constant as 100 fs and the thicknesses of the gold film for all cases are fixed at 1 μm. The initial temperature T_0 is set to be 300 K. The thermophysical and optical properties are given in Table 1.

At the repetition frequency of 1000 Hz, ten pulse burst irradiation with three single pulses in each burst separated by 100 ps will cause the evolution of surface lattice temperature as shown in Fig. 3. As can be seen in Fig. 3(*a*), with each pulse burst depositing energy on the metal film, the temperature rises abruptly and drops rapidly. Figure 3(*b*) is the detailed temperature history for the eighth burst. In every burst, each single pulse will cause a peak in lattice temperature. After each peak, the temperature will fall with the conduction of heat into deeper part of the film. At the fifth burst, the lattice temperature exceeds the melting temperature (Fig. 3(*a*)), and the melting process will begin.

Figure 4 shows the evolution of the melting depth under the same condition as Fig. 3. It can be seen from Fig. 4(*a*) that after the fifth and sixth burst, resolidification will start and all the melted gold becomes solid state soon. This is because for pulse train irradiation, there is enough time for the heat to be transferred into the deeper part of the film. After the seventh burst, the melted gold solidifies very slowly. At this stage, the entire film is heated to be close to the melting point. All the incoming laser energy is used to provide the latent heat of melting.

4.2 Comparison With Single Pulse Irradiation. To compare the result of pulse train with single pulse, five different single

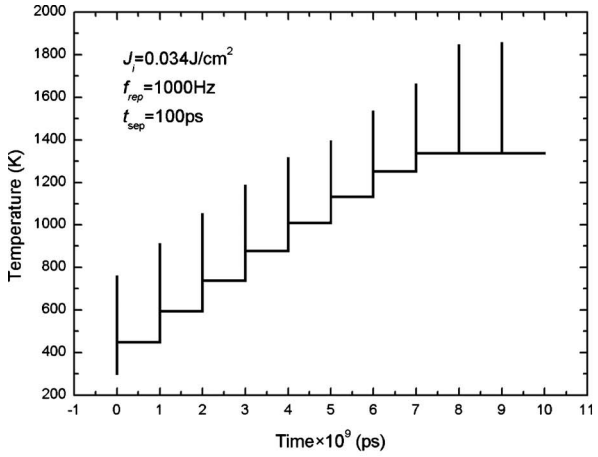

(a) Whole process

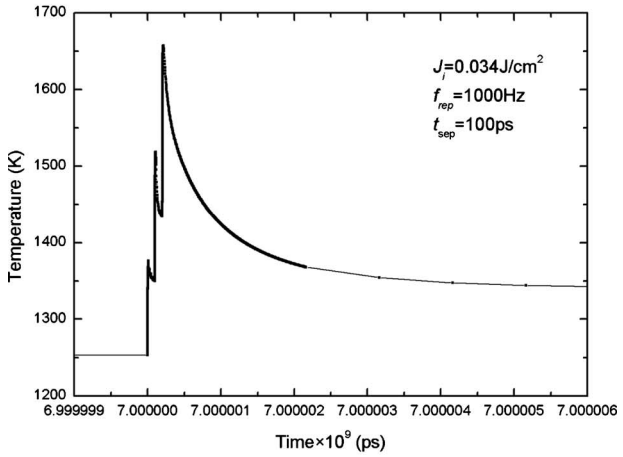

(b) During the 8th burst

Fig. 3 The surface lattice temperature caused by a typical laser pulse train

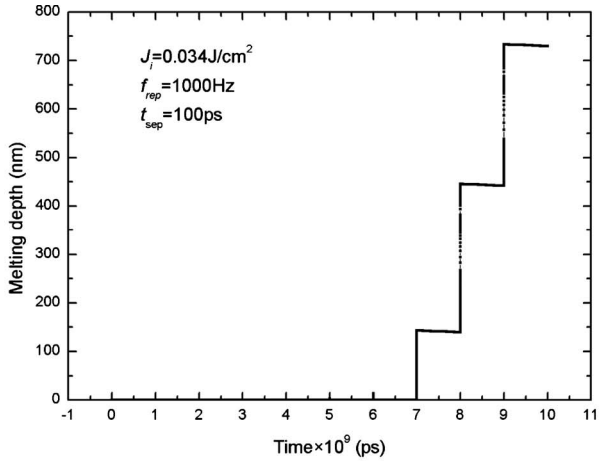

(a) Whole process

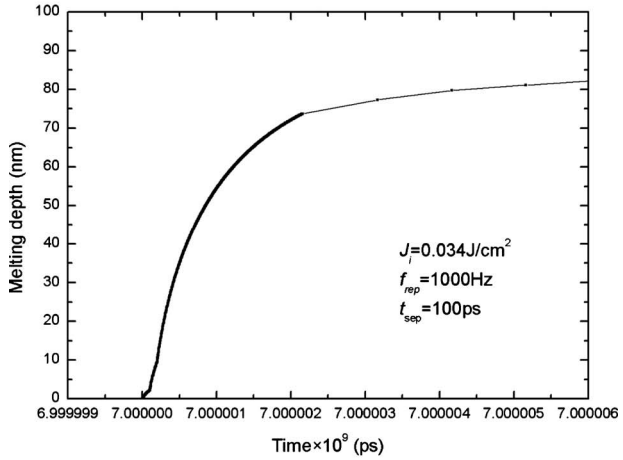

(b) During the 8th burst

Fig. 4 The evolution of melting caused by a typical laser pulse train

pulse fluences are used: 0.022 J/cm^2, 0.026 J/cm^2, 0.030 J/cm^2, 0.034 J/cm^2, and 0.036 J/cm^2. The other parameters are kept the same: repetition frequency of 1000 Hz, separation time of 100 ps, and ten pulse bursts. The dependence of maximum lattice temperature and melting depth on the fluence is shown in Fig. 5. It is obvious that with higher laser fluence, deeper melting will be achieved and higher temperature will be caused. In the ultrafast laser-materials processing, it is desirable that the melting depth can be accurately controlled and the temperature rise should be as low as possible to reduce the thermal stress.

To compare the results of pulse train and single pulse irradiation, the relationship between the maximum lattice temperature and melting depth is shown in Fig. 6. The lower line is for single pulse while the upper one is for pulse train. With the increase of pulse train power, the melting depth increases rapidly while the maximum lattice temperature increased relatively slowly. It is clear that with the same lattice temperature, the melting depth caused by pulse trains is much deeper than that caused by the single pulse. For example, the highest lattice temperature caused by a single 0.3 J/cm^2 pulse irradiation is almost the same as pulse trains, which consists of ten trains with three single 0.036 J/cm^2 pulses in a train, but its melting depth is only 50 nm, much less than the melting caused by the pulse train, which is almost 900 nm. On the other hand, to achieve the same melting depth, a pulse train will cause much lower lattice temperature, which is an advantage for laser-materials processing. However, it should also be noted that the energy needed for a pulse train is much higher that of a single pulse. According to Fig. 6, the melting depth caused by a single 0.3 J/cm^2 pulse is almost the same as the pulse train, which consists of ten bursts with three single 0.026 J/cm^2 pulses in a burst. But the total energy for the pulse train is 0.78 J/cm^2. This is because more energy is used to heat up the deeper part of the film for the case of pulse train.

It should be noted that in Fig. 6, the lattice temperatures never reach 2000 K, far below the normal boiling point of gold, 3127 K. This is true for all the calculations in this paper. Before the lattice temperature reaches 3127 K, the whole film will be melted, at which point the calculation will stop.

From the above discussion, the merits of pulse train can be seen clearly. But to utilize laser pulse trains, there are much more parameters to be controlled than a single pulse irradiation did. The effects of parameters, including repetition rate, pulse numbers per train, and separation time between single pulses will be studied below.

4.3 Repetition Rate. Typical repetition rate for femtosecond lasers ranges from 100 Hz to tens of MHz. Numerical simulations are carried out for eight frequencies between 500 Hz and 1 MHz

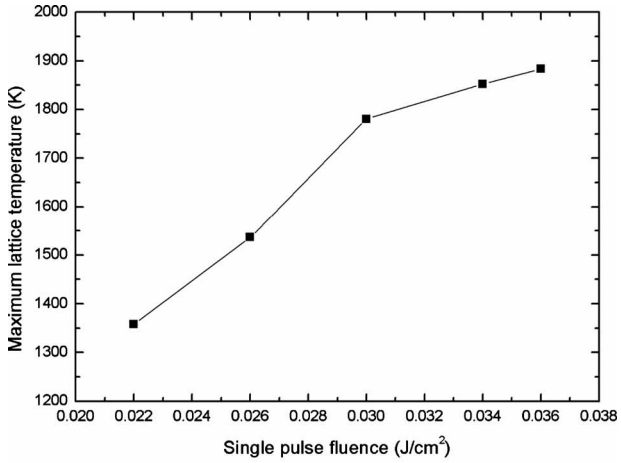

(a) Lattice temperature

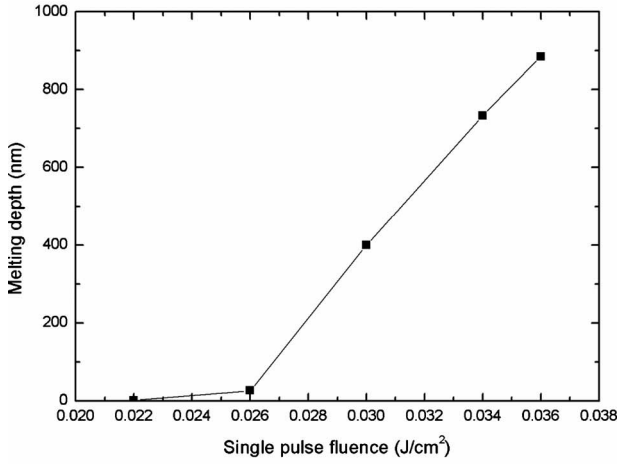

(b) Melting depth

Fig. 5 The effects of single pulse fluence on the irradiation process

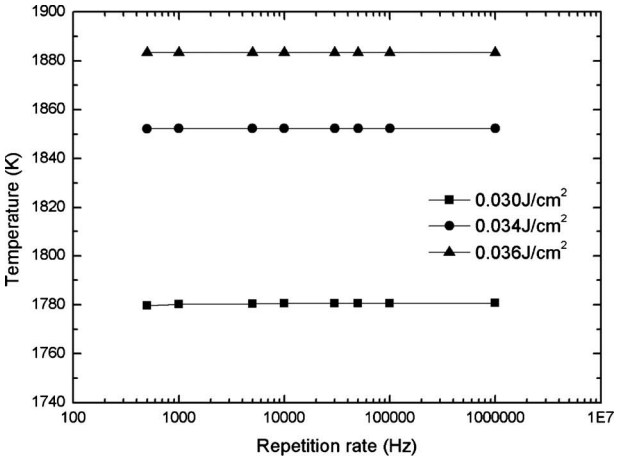

(a) Lattice temperature

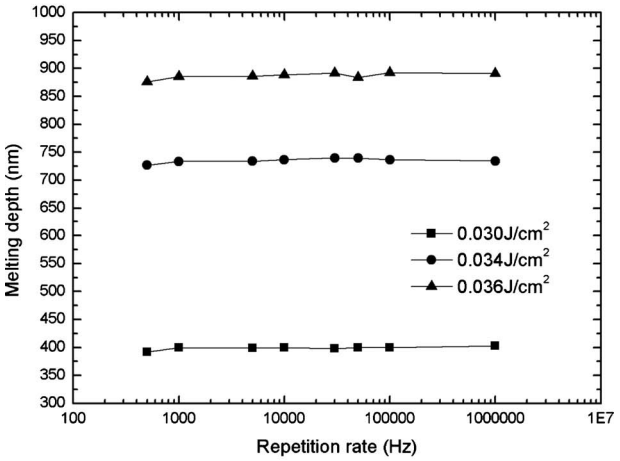

(b) Melting depth

Fig. 7 The effects of repetition rate

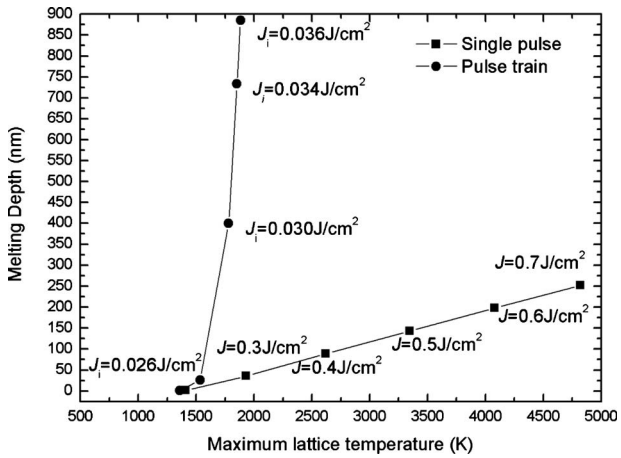

Fig. 6 The relationship between melting depth and maximum temperature; comparison between single pulse and pulse train

and different pulse fluences, and the results are shown in Fig. 7. Figure 7(*a*) shows the influence of repetition rate on the peak lattice temperature, while Fig. 7(*b*) shows the effects on the melting depth. It is clear that repetition rate has little effects on the maximum temperature and the melting depth. This is because even for a high repetition rate as 1 MHz, there is still enough time between each train for the heat to transfer in the thin film and the melting depth will mainly be decided by the amount of energy deposited on the film.

4.4 Pulse Number Per Burst. Figure 8 shows the effect of pulse number in each burst while the total energy are kept at 0.09 J/cm^2, 0.102 J/cm^2, and 0.108 J/cm^2. The repetition rate, separation time between single pulses, and total burst number are kept at 10000 Hz, 100 ps, and 10, respectively. Figure 8(*a*) indicates that splitting laser pulse into more small pulses lowers the maximum temperature, but this effect weakens with the increase of pulse number per burst. Meanwhile, according to Fig. 8(*b*), the melting depth slightly increases with increasing number of pulse per burst.

4.5 Separation Time. The separation time between two pulses in a burst is another important parameter. As stated in our earlier work [15], an appropriate separation time in multiple pulses irradiation will cause deeper melting and lower temperature.

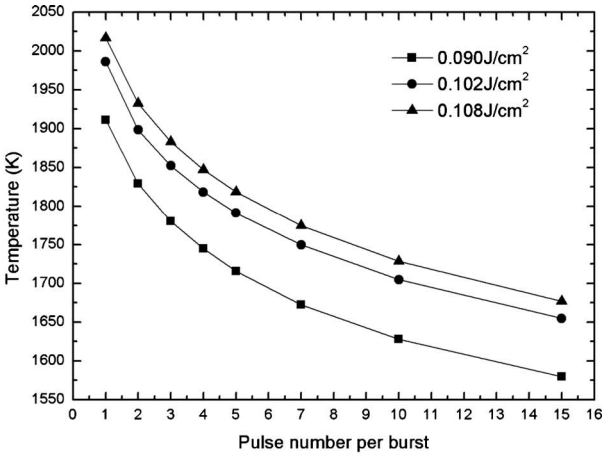

(a) Lattice temperature

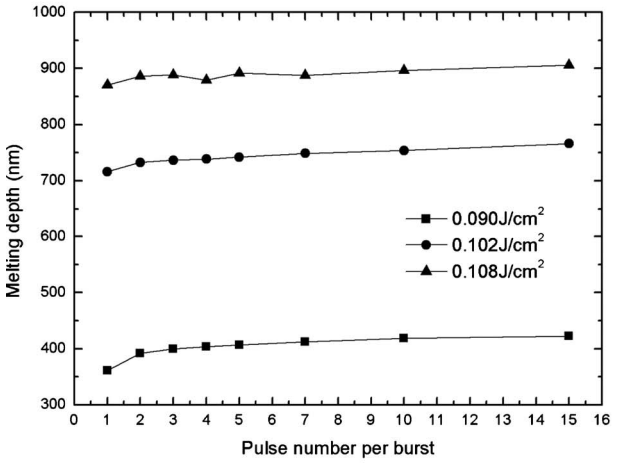

(b) Melting depth

Fig. 8 The effects of pulse number per train

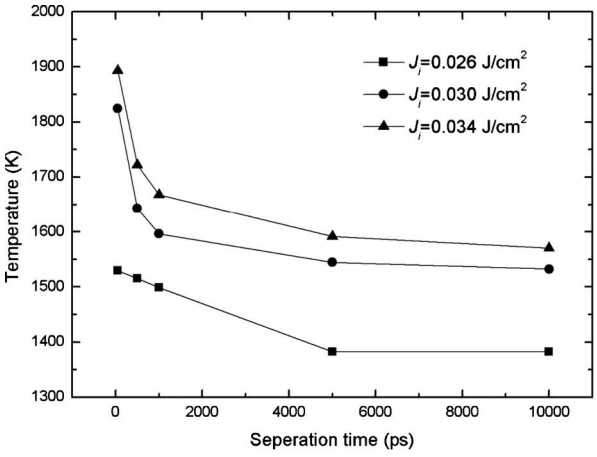

(a) Lattice temperature

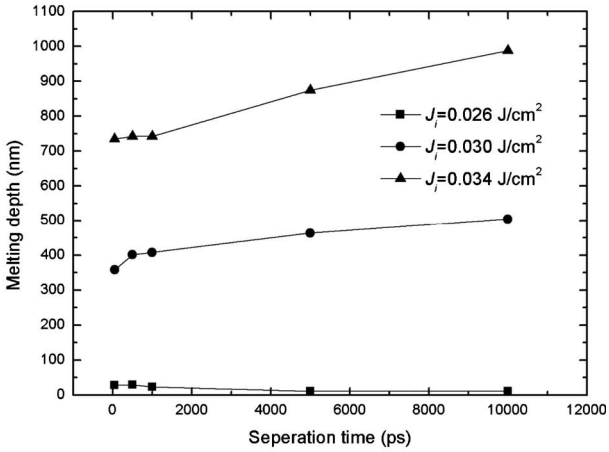

(b) Melting depth

Fig. 9 The effects of separation time between single pulses

Figure 9 shows the effects of separation time on pulse train irradiation. The separation time ranges from 50 ps to 10,000 ps. In Fig. 9(*a*), it shows that with the increase of separation time, the maximum temperature is lowered. But when the separation time is larger than 5000 ps, the difference becomes very small. Figure 9(*b*) shows that in most cases longer separation time increases the melting depth but with small pulse fluence, it decreases the melting depth instead.

4.6 Effects of Boundary Heat Loss. In most computational study on laser metal interaction, the heat loss at the heating surface was neglected, which is proved to be reasonable in our earlier work [10]. But for pulse train irradiation, the time scale is much larger in orders. The pulse train with a repetition rate of 1000 Hz means the interval between two laser bursts is 10^{10} times of the duration of a typical 100 fs laser pulse. Under this condition, the radiation caused heat loss may play a more important role in the process. Two computations were carried out. The first assumed adiabatic boundary condition on the surface that received laser irradiation. The other one took the radiation heat loss into account.

$$q''_R|_{x=L} = \sigma\varepsilon(T_{\text{sur}}^4 - T_\infty^4) \tag{14}$$

where ε is the total emissivity, which is set to be 0.03 in the calculation. Before evaporation takes place, T_{sur} is the surface lattice temperature at $x=L$. After evaporation begins, T_{sur} is the liquid-vapor interface temperature. In both cases, the other side of the film remained as adiabatic boundary condition.

The results are shown in Fig. 10. The comparison between maximum lattice temperatures shows no obvious difference. But because the radiation at the surface will cause the laser energy to escape from the film, the melting depth will be smaller than the results estimated by models ignoring this factor, as shown in Fig. 10(*b*). This means neglecting heat loss at surface will lead to an overestimation on melting depth when the repetition rate is low enough.

5 Conclusion

The interaction femtosecond laser pulse trains and a 1 μm free-standing gold film are simulated numerically. A two-temperature model coupled with interface tracking is employed to describe melting and resolidification processes during the irradiation. To deal with the large span in time scale, variable time steps are adopted. The laser beam consists of ten pulse bursts with a repetition rate of 200–1000 Hz. Each pulse burst contains 3–10 single 100 fs laser pulses with an interval of 20–200 ps. The simulation results showed the following:

(1) Compared with single pulse irradiation, laser pulse train showed better performance in achieving deeper melting depth with the same temperature rise, although more total

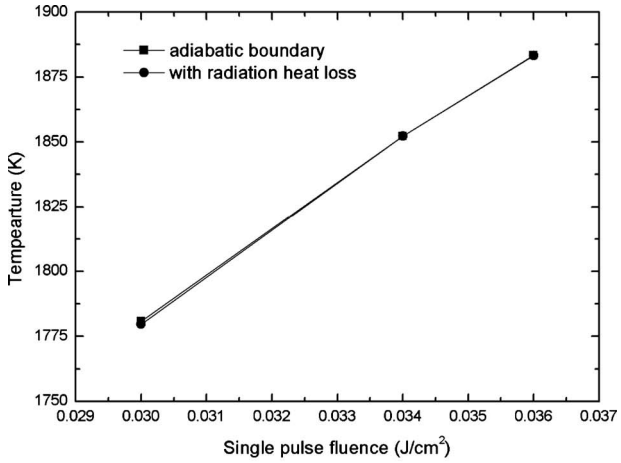

(a) Lattice temperature

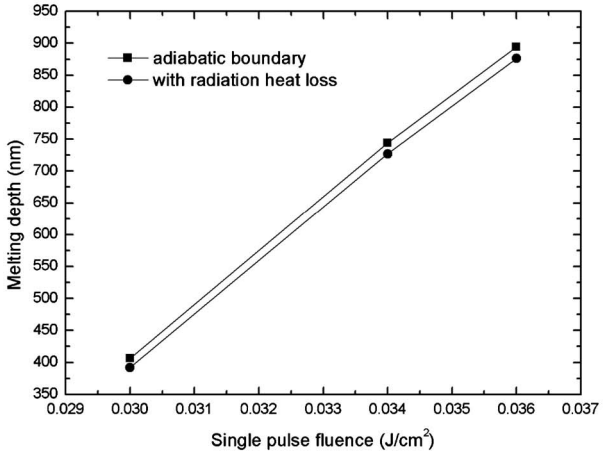

(b) Melting depth

Fig. 10 The effects of heat loss at surface

laser energy was needed. The melting depth increases rapidly with the increase of total laser energy deposited on the film.

(2) Repetition rate has little influence on the process. With the repetition rate ranges of 500 Hz to 1 MHz, the maximum lattice temperature and melting depth showed little change with all other parameters kept unchanged.

(3) By splitting a laser beam into many small single pulses, deeper melting depth and lower temperature will be achieved. Higher number of pulse per burst is preferable.

(4) With high laser power, the increase of separation time between single pulses will lead to lower temperature and deeper melting.

(5) With the repetition rate of 500 Hz, neglecting the heat loss caused by radiation on the surface may lead to an overestimation of melting depth.

Acknowledgment

Support for this work by the U.S. National Science Foundation (NSF) under Grant No. CBET-0730143 and Chinese National Natural Science Foundation under Grant No. 50828601 are gratefully acknowledged.

Nomenclature

B_e = coefficient for electron heat capacity ($J/m^3\,K^2$)
C = heat capacity ($J/m^3\,K$)
c_p = specific heat ($J/kg\,K$)
f_{rep} = repetition rate (Hz)
G = electron-lattice coupling coefficient ($W/m^3\,K$)
h = latent heat of phase change (J/kg)
J_i = single pulse fluence (J/cm^2)
J_t = total energy of a pulse train (J/cm^2)
k = thermal conductivity ($W/m\,K$)
L = thickness of the metal film (m)
M = molar mass (kg/kmol)
q'' = heat flux (W/m^2)
R = reflectivity
R_g = specific gas constant ($J/kg\,K$)
R_u = universal gas constant ($J/kmol\,K$)
s = interfacial location (m)
S = intensity of the internal heat source (W/m^3)
t = time (s)
t_p = pulse width (s)
t_{sep} = separation time (s)
T = temperature (K)
T_F = Fermi temperature (K)
T_m = melting point (K)
u = interfacial velocity (m/s)
V_0 = interfacial velocity factor (m/s)
x = coordinate (m)

Greek Symbols

δ = optical penetration depth (m)
δ_b = ballistic range (m)
ε = total emissivity
ρ = density (kg/m^3)
σ = Stefan–Boltzmann constant ($W/m^2\,K^4$)

Superscripts

0 = last time step

Subscripts

0 = initial condition
e = electron
eq = thermal equilibrium state
i = pulse sequence
l = lattice
ℓ = liquid
R = thermal radiation
s = solid
$s\ell$ = solid-liquid interface
sur = surface
∞ = ambient environment

References

[1] Anisimov, S. I., Kapeliovich, B. L., and Perel'man, T. L., 1974, "Electron Emission From Metal Surfaces Exposed to Ultra-Short Laser Pulses," Sov. Phys. JETP, **39**(2), pp. 375–377.
[2] Qiu, T. Q., and Tien, C. L., 1993, "Heat Transfer Mechanisms During Short-Pulse Laser Heating of Metals," ASME J. Heat Transfer, **115**(4), pp. 835–841.
[3] Tzou, D. Y., 1997, *Macro- to Microscale Heat Transfer*, Taylor & Francis, Washington, DC.
[4] Tzou, D. Y., 2006, "Computational Techniques for Microscale Heat Transfer," *Handbook of Numerical Heat Transfer*, 2nd ed., W. J. Minkowycz, E. M. Sparrow, and J. Y. Murthy, eds., Wiley, Hoboken, NJ.
[5] Jiang, L., and Tsai, H. L., 2005, "Improved Two-Temperature Model and Its Application in Ultrashort Laser Heating of Metal Films," ASME J. Heat Transfer, **127**(10), pp. 1167–1173.
[6] Chen, J. K., Tzou, D. Y., and Beraun, J. E., 2006, "A Semiclassical Two-Temperature Model for Ultrafast Laser Heating," Int. J. Heat Mass Transfer, **49**(1–2), pp. 307–316.
[7] Chowdhury, I. H., and Xu, X., 2003, "Heat Transfer in Femtosecond Laser Processing of Metal," Numer. Heat Transfer, Part A, **44**(3), pp. 219–232.
[8] Fang, R. R., Zhang, D. M., Wei, H., Hu, D. Z., Li, Z. H., Tan, X. Y., Sun, M., and Yang, F. X., 2008, "A Unified Thermal Model of Thermophysical Effects With Pulse Width From Nanosecond to Femtosecond," Eur. Phys. J.: Appl. Phys., **42**(3), pp. 229–234.

[9] Chen, J. K., and Beraun, J. E., 2001, "Numerical Study of Ultrashort Laser Pulse Interactions With Metal Films," Numer. Heat Transfer, Part A, **40**(1), pp. 1–20.
[10] Huang, J., Zhang, Y. W., and Chen, J. K., 2009, "Ultrafast Solid-Liquid-Vapor Phase Change of a Gold Film Induced by Pico- to Femtosecond Lasers," Appl. Phys. A: Mater. Sci. Process., **95**(3), pp. 643–653.
[11] Sim, H. S., and Lee, S. H., 2007, "Numerical Investigation on Nonequilibrium Energy Transfer in Thin Metal Film Structures During the Irradiation of Femtosecond Pulse Laser," Transactions of the Korean Institute of Electrical Engineers, **56**(2), pp. 367–373.
[12] Jiang, L., and Tsai, H.-L., 2007, "Modeling of Ultrashort Laser Pulse-Train Processing of Metal Thin Films," Int. J. Heat Mass Transfer, **50**(17–18), pp. 3461–3470.
[13] Jiang, L., and Tsai, H. L., 2006, "Energy Transport and Nanostructuring of Dielectrics by Femtosecond Laser Pulse Trains," ASME J. Heat Transfer, **128**(9), pp. 926–933.
[14] Zhang, Y., and Chen, J. K., 2007, "Melting and Resolidification of Gold Film Irradiated by Nano- to Femtosecond Lasers," Appl. Phys. A: Mater. Sci. Process., **88**(2), pp. 289–297.
[15] Huang, J., Zhang, Y. W., and Chen, J. K., 2009, "Ultrafast Solid-Liquid-Vapor Phase Change in a Thin Gold Film Irradiated by Multiple Femtosecond Laser Pulses," Int. J. Heat Mass Transfer, **52**(13–14), pp. 3091–3100.
[16] Chen, J. K., and Beraun, J. E., 2004, "Superheating and Material Ablation of Metals by Multiple Ultrashort Laser Pulses," Journal of Directed Energy, **1**, pp. 93–109.
[17] Anisimov, S. I., and Rethfeld, B., 1997, "Theory of Ultrashort Laser Pulse Interaction With a Metal," Proc. SPIE, **3093**, pp. 192–202.
[18] Chen, J. K., Latham, W. P., and Beraun, J. E., 2005, "The Role of Electron-Phonon Coupling in Ultrafast Laser Heating," J. Laser Appl., **17**(1), pp. 63–68.
[19] Kuo, L. S., and Qiu, T. Q., 1996, "Microscale Energy Transfer During Picosecond Laser Melting of Metal Films," ASME National Heat Transfer Conference, Vol. 1, pp. 149–157.
[20] Klemens, P. G., and Williams, R. K., 1986, "Thermal Conductivity of Metals and Alloys," International Metals Reviews, **31**(5), pp. 197–215.
[21] Faghri, A., and Zhang, Y., 2006, *Transport Phenomena in Multiphase Systems*, Elsevier Academic, Burlington, MA.
[22] Patankar, S., 1980, *Numerical Heat Transfer and Fluid Flow*, McGraw-Hill, New York.
[23] Zhang, Y., and Chen, J. K., 2008, "An Interfacial Tracking Method for Ultrashort Pulse Laser Melting and Resolidification of a Thin Metal Film," ASME J. Heat Transfer, **130**(6), pp. 062401.
[24] Barin, I., 1993, *Thermochemical Data of Pure Substance*, Pt.1, VCH, New York.

Characteristics of Pool Boiling Bubble Dynamics in Bead Packed Porous Structures

Calvin H. Li

Ting Li

Paul Hodgins

Department of Mechanical, Industrial, and Manufacturing Engineering,
University of Toledo,
Toledo, OH 43606

G. P. Peterson

G. W. Woodruff School of Mechanical Engineering,
Georgia Institute of Technology,
Atlanta, GA 30332

Spherical glass and copper beads have been used to create bead packed porous structures for an investigation of two-phase heat transfer bubble dynamics under geometric constraints. The results demonstrated a variety of bubble dynamics characteristics under a range of heating conditions. The bubble generation, growth, and detachment during the nucleate pool boiling heat transfer have been filmed, the heating surface temperatures and heat flux were recorded, and theoretical models have been employed to study bubble dynamic characteristics. Computer simulation results were combined with experimental observations to clarify the details of the vapor bubble growth process and the liquid water replenishing the inside of the porous structures. This investigation has clearly shown, with both experimental and computer simulation evidence, that the millimeter scale bead packed porous structures could greatly influence pool boiling heat transfer by forcing a single bubble to depart at a smaller size, as compared with that in a plain surface situation at low heat flux situations, and could trigger the earlier occurrence of critical heat flux by trapping the vapor into interstitial space and forming a vapor column net at high heat flux situations. The results also proved data for further development of theoretical models of pool boiling heat transfer in bead packed porous structures.
[DOI: 10.1115/1.4000952]

Keywords: two-phase heat transfer, porous structure, bubble dynamics, critical heat flux

1 Introduction

Phase change heat and mass transport are critically important in many industrial applications and scientific frontiers, such as the capillary pumped loop systems (CPLs), in which the evaporation capacity was demonstrated to limit the overall performance of CPLs [1–4], as well as liquid-feed direct methanol fuel cells (DMFCs), in which the effect of nonequilibrium evaporation and condensation of methanol and water played a key role in efficiency [5–7].

In CPLs, phase change heat transfer has been effectively enhanced by modifying the evaporating surface with fin and porous structures. Liter and Kaviany [8] experimentally tested the pool boiling critical heat flux (CHF) of a periodically nonuniform, thickness porous layered, capillary artery-evaporating surface and found that the CHF (762 kW/m^2) was three times greater than that of a plain surface. This study demonstrated that a nonuniform thickness porous layered surface had a better ability of increasing the CHF while reducing the superheat than did a uniform thickness porous layered surface. It was also proposed that the hydrodynamic limit and the viscous-drag limit would be plausible liquid choking mechanisms of those kinds of systems. The hydrodynamic limit would determine the liquid and vapor counter flow behavior, which was suggested to be controlled to optimize the vapor escape paths and to increase the hydrodynamic limit by reducing the wavelength of the nonuniform thickness and reducing the particle size of the porous layer. This effort was continued by experimentally measuring the CHF of the uniform thickness porous layered surfaces of different copper particle diameters (between 40μ and 80μ) in loosely packed, shaken, and pressed forms [9], in which the porous layer thickness varied between three and five particle diameters, and a 1.8 times CHF was achieved, compared with that of a plain surface in the study. Li and Peterson [10,11] experimentally tested the boiling heat transfer coefficient and CHF of sintered mesh porous layered surfaces. The thickness of 56 μm diameter copper wire mesh layers ranged from 0.21 mm, 0.37 mm, 0.57 mm, 0.74 mm, to 0.82 mm, and the results gave a maximum value of 245.5 kW/m^2 K for the heat transfer coefficient, and 367.9 W/cm^2 for the critical heat flux,. It is concluded that the critical heat flux was strongly dependent on the wire porous layer thickness, wire mesh size, and volumetric porosity.

Considering the importance of the bubble dynamics to the two-phase heat transfer under the restraint of structures, many researchers have tried to experimentally visualize the bubble behavior and phase change heat transfer during the pool boiling on layered surfaces. Liao and Zhao [12] employed a high speed video imaging system to capture the bubble growth behavior and the two-phase zone in a two-dimensional staggered miniature silver-copper circular cylinder (20 mm in diameter) porous structure. This visual study compared the bubble formation, growth, and collapse in a porous structure against various applied heat fluxes ranging from 16 kW/m^2 to 322 kW/m^2, with an inlet temperature ranging from 50°C to 80°C. Wang et al. [13] used an analogy charge coupled device (CCD) camera to observe the bubble growth and departure in a three-dimensional glass bead staggered porous structure (7 mm diameter beads) with applied heat fluxes of both 36.8 kW/m^2 and 121.3 kW/m^2. The study illustrated the replenished liquid and associated transport effect through a force balance on the bubble. And those visualized images of bubble dynamics combined with experimental data of surface superheat and critical heat flux have greatly improved people's understanding of how the hydrodynamics mechanisms influence the two-phase heat transfer in porous structures and under restraint.

Two-phase mass and heat transfer is equally important in fuel cell devices as it is in the capillary pumped loop systems, especially on the design of flow channels of polar plates. In a direct methanol fuel cell, CO_2 bubbles produced in the anode flow field will block the gas diffusion layer and form a counter liquid-gas

Contributed by the Heat Transfer Division of ASME for publication in the JOURNAL OF HEAT TRANSFER. Manuscript received February 8, 2009; final manuscript received December 12, 2009; published online November 15, 2010. Assoc. Editor: Wilson K. S. Chu.

two-phase flow situation. In order to control CO_2 gas removal and maintain good performance of the fuel cell, it is important to understand bubble generation and growth behavior in the catalyst site of the DMFC. Hence, the design of the channel has particular important geometric influences on two-phase heat and mass transfer of the DMFC. Many simulations and modeling were studied in the past to target this task, such as the one-dimensional model of Murgia et al. [14], the two-dimensional model of Wang and Wang [15], the numerical study of the two-dimensional model of Birgersson et al. [16], the two-dimensional two-phase model of Divisek et al. [17], the two-dimensional transient model of Rice and Faghri [18], and the three-dimensional two-phase model of Yang et al. [19]. All these models have grasped the physics of the two-phase flow/bubble-liquid interaction in fuel cell devices. However, more experimental results are critically needed to verify and modify current models.

Experimental visualization of the two-phase mass transfer has also been conducted in all types of fuel cell devices to assistant researchers in the understanding of the complicated two-phase heat and mass transfer involved. In the 1990s, researchers started to experimentally visualize the two-phase flow pattern in anode and cathode channels under different working conditions. Tüber et al. [20] discovered that CO_2 bubbles, as a result of methanol electrochemical oxidation, would block the flow channel and substantially reduce the fuel cell performance if they could not be removed promptly. Yang et al. [21] revealed bubbles nucleated at certain locations and from large and discrete gas slugs in the channel. Bubble detachment from the backing layer is significantly retarded by strong surface tension. As in a regular rectangular channel, the bubble diameter must reach 0.5 mm to be detached by the buoyancy force. Yang et al. [22] videotaped CO_2 bubble generation, bubble growth, and two-phase flow in a serpentine channel with a high speed camera. It was shown that the two-phase flow of CO_2 gas slugs would not block the channel at all operating temperatures studied. It was further shown that the orientation of the channel played an important role in determining the fuel cell performance.

Moreover, bubble-driven micropumps have been studied to utilize bubble dynamics to move deoxyribonucleic acid (DNS) and proteins through microfluidic systems. Thermal generation of vapor and/or gas bubbles by boiling is the most common approach for bubble actuation in this field of lab-on-chip systems [23,24]. But due to the fact that two-phase heat and mass transfer are a complex physical phenomenon, and that bubble dynamics is significantly affected by liquid/vapor properties and by surrounding conditions, it is critically important to understand the many factors, which influence bubble dynamics to precisely predict and control bubble growth and actuation.

As a result, in order to further assist in the understanding of the bubble dynamic process and the influence of the geometric constraints, an experimental and computer simulation integrated investigation was conducted to study the phase change and bubble dynamics in a three-dimensional staggered glass bead porous structure. Additionally, an effort was made to obtain an insight of two-phase heat transfer behavior in bead packed porous structures.

2 Experiments

2.1 Experimental Setups. The experimental apparatus consisted of a $200 \times 62.7 \times 67.7$ mm^3 rectangular glass vessel with a copper plate heating surface at the bottom, as shown in Fig. 1. Nine T-type thermocouples were inserted into the underside of the copper plate to monitor the temperature of the heating surface and to obtain the heat flux using Fourier's law (five thermocouples were placed 0.5 mm beneath the heating surface, and the other four thermocouples were 4.5 mm beneath the heating surface). The uncertainty of the temperature measurement was less than 1°C, and the uncertainty of the heat flux was less than 5%. A bottom view distribution of the thermocouples and the geometrical dimensions are shown in Fig. 2. All experiments were conducted at 1 atm. The nucleate pool boiling of saturated water was investigated, first on a plain surface, then on staggered glass bead porous structures, and finally on staggered copper bead porous structures.

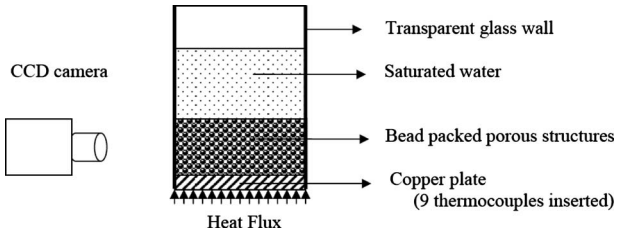

Fig. 1 Sketch of experimental setup

The spherical glass beads used in the experiments had uniform diameters of 1 mm and 3 mm, and the spherical copper beads had a uniform diameter of 3 mm. Heat flux was supplied by a heating assembly consisting of a 41.5 Ω ceramic band resistance heater, mounted at the bottom of the copper plate. Heat flux was conducted through this copper plate to the heating surface of the glass vessel. Power was supplied to the heater by an Agilent 6031A DC power supply. Applied heat flux ranged from 18.9 kW/m^2 to 76.3 kW/m^2 during the tests. Superheat, $T_{surface} - T_{sat}$, varied from 4.31°C to 14.20°C for the staggered copper bead porous structures, 6.64°C to 15.41°C for the staggered glass bead porous structures, and 8.22°C to 22.25°C for the plain surface.

A Redlake MotionScope M3 (CCD camera) imaging system having a 520 fps rating of full resolution at 1280×1024 and a maximum of 33,000 fps at a partial resolution of 1280×16 was employed in the experiment. A 28 mm Micro Nikkor lens was used with the CCD camera to take a detailed video of the nucleate pool boiling bubble dynamics processes at the view shown in Fig. 1. Although the video images were taken through a flat glass-wall of the vessel and the phenomena observed occurred in the region adjacent to the glass-wall, they closely represent the bubble dynamics in the inner regions of the bead packed porous structures in the experiment, due to the similar geometric structure of the perimeter region and the inner region inside the porous structures. This was confirmed by visual observation of the nucleate pool boiling bubble dynamics experiment. The heating surface superheat was measured using nine thermocouples connected to an Agilent 34970A data logger. The data of heat flux against the superheat on the heating surface were calculated simultaneously.

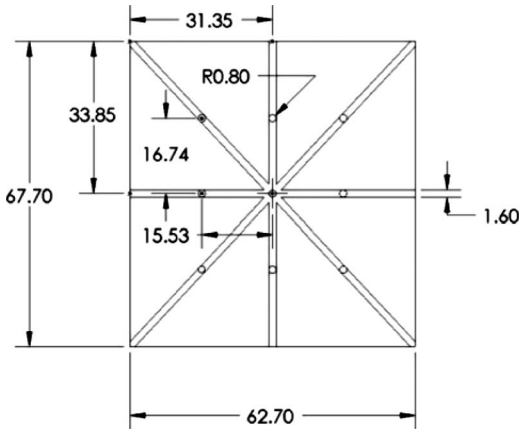

Fig. 2 Bottom view of the thermocouple distribution and geometrical dimensions (in millimeters) of the copper plate

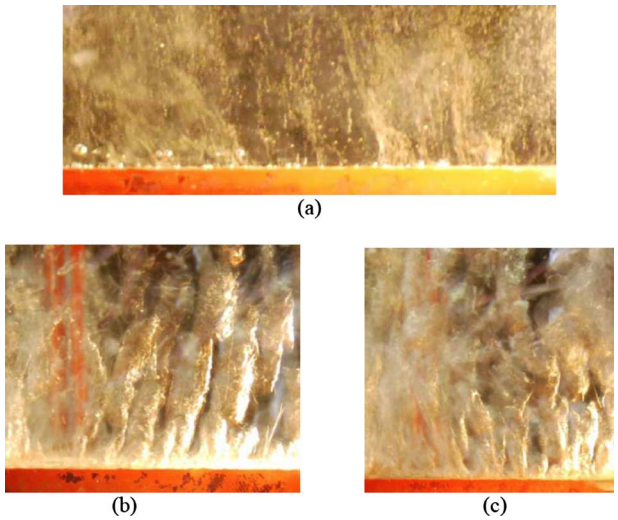

Fig. 3 Bubble dynamics and phase change nucleate pool boiling on a plain surface

2.2 Nucleate Pool Boiling Bubble Dynamics Visualization

2.2.1 Bubble Dynamics on Plain Surface. Nucleate pool boiling on a plain surface is presently well understood. In this work, the nucleate pool boiling test on a plain surface served as a reference for the staggered bead porous structure tests. When a small heat flux (18.9 kW/m^2) was applied to the heating surface, it was clear that small vapor bubbles were generated on the plain surface. And with the increase in heat flux, the bubble generation frequency rapidly increased, as shown in Fig. 3(*a*). This bubble dynamic process is unlike the previous report on the subcooled water jet and bubble dynamic process [25], in which a high temperature water jet existed on the top of large bubbles. When heat flux was increased to 47 kW/m^2 in this experiment, the vapor generated on the plain surface formed several major vapor slugs and columns, shown in Fig. 3(*b*). At this stage, single bubbles were still detectable by the naked eye. These vapor columns and slugs fit well into the description of the Rayleigh–Taylor hydrodynamic stability theory [26]. There was no obvious collapse between vapor columns due to the fact that the characteristic size of the columns was still less than the critical hydrodynamic wavelength. When heat flux was increased to 76.3 kW/m^2, the entire image of the vapor columns could only be recorded with the high speed camera. A picture of this staged phase change process is shown in Fig. 3(*c*). The superheat of the nucleate pool boiling on a plain surface changed from 8.22°C at 18.9 kW/m^2 to 22.25°C at 76.3 kW/m^2, as shown in Fig. 4.

The collected experimental data closely matched the theoretical prediction of pool boiling using the Rohsenow correlation, Eq. (1), for saturated water at 1 atm [27]. The prediction of Eq. (1) is presented as the dashed line in Fig. 4 as well

$$\Delta T = \frac{h_{f,g}}{c_{p,l}} \mathrm{Pr}_l^s \; C_{sf} \left[\frac{q''_w}{\mu_l h_{f,g}} \left(\frac{\sigma}{g(\rho_l - \rho_v)} \right)^{1/2} \right]^r \tag{1}$$

In this equation, ΔT is the heating surface superheat, $h_{f,g}$ is the latent heat of water, $c_{p,l}$ is the specific heat of liquid water, Pr is the Prantl number of liquid water, q''_w is the heat flux on the heating surface, μ_l is the viscosity of liquid water, σ is the surface tension of liquid water, g is the gravitational acceleration, ρ_l is the density of liquid water, ρ_v is the density of water vapor, C_{sf}, r, and s are constants with values of 0.053, 1, and 0.66, respectively.

2.2.2 Bubble Dynamics in Staggered Glass Bead Porous Structure. A range of heat flux was also applied in the nucleate pool boiling tests on the staggered glass bead porous structures to study the nucleate pool boiling bubble dynamics. At low heat flux (18.9 kW/m^2), it was observed that a single small bubble generated in the pore region on the heating surface. This bubble grew to fill the available space between glass beads and truncated at the neck when the bubble elongated itself vertically. The top section of the bubble broke away and rose through the porous structure toward the water surface. The bubble growth, elongation, truncation, and departure cycle is shown in Fig. 5, where (a), (b), and (c) are the periods of bubble growth. The images show that the shape of the bubble's bottom section did not obviously change, but the top section grew. Figures 5(*d*), 5(*e*), and 5 are of bubble elongation and necking. They again show the static size of the bottom section and the rapid growth of the top section. Figure 5(*f*) is of the bubble top section, breaking away from the bottom section and departing. This bubble growth process was also previously reported in Ref. [13].

Bubble necking occurred at a distance of 1.5 mm above the heating surface. This is explained in Ref. [13], which stated that a force balance between the forces retaining and detaching the bubble was reached immediately before the top section detaches from the bottom section of the bubble, i.e., when the interfacial

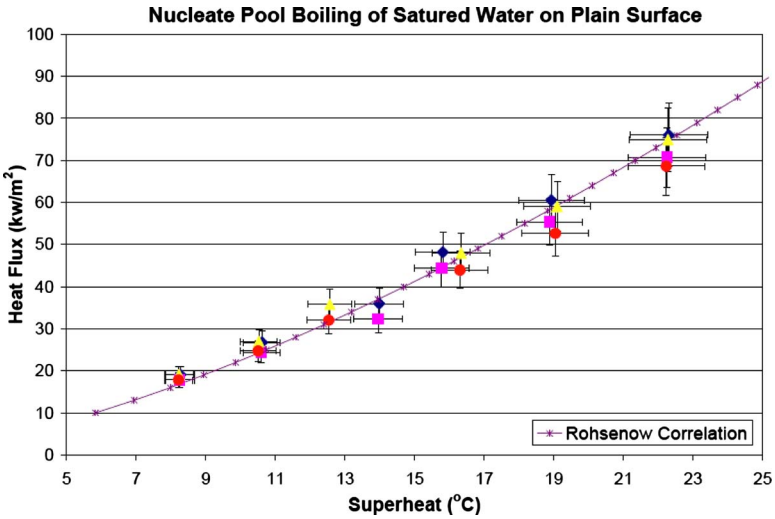

Fig. 4 Heat flux versus superheat on the heating surface of saturated water nucleate pool boiling on a plain surface

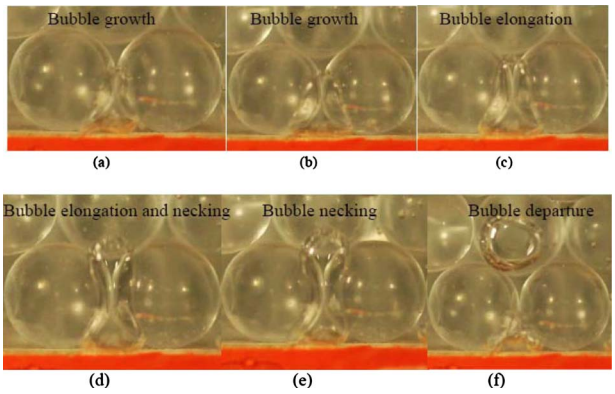

Fig. 5 Single bubble growth, elongation, truncation, and departure cycle in 3 mm diameter glass bead staggered porous structures

tension at the neck and the buoyant force of the top section of the bubble equal each other. In the work [13], the force balance was analyzed in the vertical direction, but the inertial force was neglected.

In this experiment, it was found that the drag force should be taken into account in the force balance analysis as well, particularly when the same site bubble generation frequency is high and when a new bubble grew quickly in the departure wake of the previous bubble. This drag effect will be explained in Sec. 3.3.1.

When heat flux was increased to 47 kW/m^2, bubbles grew on several pore regions and there was no truncation after elongation. Rather, a vapor column net was formed by neighboring vapor columns in the first two bead layers, as shown in Fig. 6. It is clearly shown that bubbles did not experience a truncation or a departure, and that new vapor columns dominated the space between glass beads in the first two layers above the heating surface. At this relatively high temperature stage, glass beads in those two layers served as an extended heating surface. Hence, the superheat of the copper plate surface was reduced, compared with that in the plain plate heating surface situation with the same heat flux value.

The bubble dynamics at this relatively high heat flux demonstrated a very different mechanic, compared with that of bubble dynamics at a lower heat flux, in which the bubble dynamics of

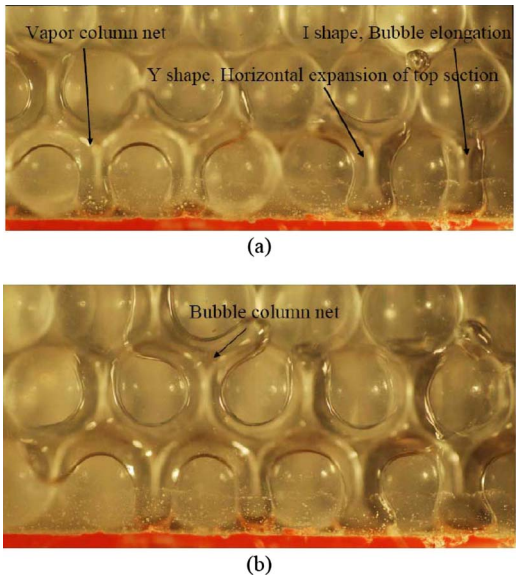

Fig. 6 Vapor columns net formation in 3 mm diameter glass bead packed porous structure

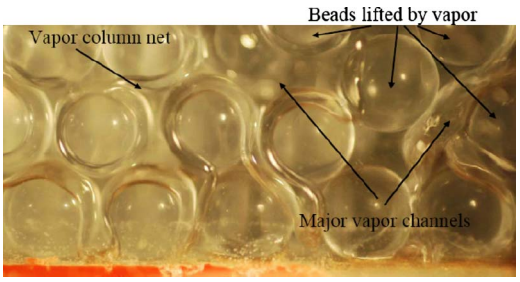

Fig. 7 Strong vapor columns forming across several 3 mm diameter glass bead layers above the heating surface

each relatively independent single bubble is largely decided by the force balance between buoyancy, interfacial tension, and drag force in the wake of the previous bubble departure. At a higher heat flux, liquid water rapidly changed into vapor at nucleation sites on the heating surface to form elongated bubbles. The top section of a single bubble quickly reached into the interstitial space between the first and second bead layers, and expanded horizontally due to the geometric constraints and limited space (Fig. 6(*a*)). When vapor bubbles generated at adjacent sites on the heating surface, the top sections joined each other horizontally before they reached the next layer, hence, a vapor column net existed, as shown in Figs. 6(*a*) and 6(*b*).

Obviously, the growth process of bubbles did not have necking at the narrowest space, one bead radius above the heating surface. Rather, the bubbles expanded both vertically and horizontally into the available space between solid beads due to a strong inertial force involved when a large amount of liquid water instantaneously changes into vapor.

When the heat flux reached its highest value of 76.3 kW/m^2 in this experiment, it was observed that the vapor columns occupied the space between the glass beads in the first two layers next to the heating surface, and the momentum of vapor columns was so strong that the glass beads inside the main vapor channels of the staggered structure were pushed upward by the vapor. The phase change process at this stage is shown in Fig. 7. Bubble dynamics at a heat flux of 76.3 kW/m^2 did not show a stronger tendency to expand horizontally, as compared with the bubble dynamics at a heat flux of 47 kW/m^2, but rather, the vertical expansion of the bubble columns took a more dominating role in bubble dynamics. Additionally, the vertical expansion was so forceful that the glass beads were lifted (Fig. 7) when the vapor rushed out of the porous structure through the main vapor channels. Inertial force exclusively took control of the bubble dynamics at this stage.

2.2.3 Bubble Dynamics in Staggered Copper Bead Porous Structures. A staggered porous structure was constructed of 3 mm diameter copper beads and the same range of heat flux as the glass bead tests was applied to study the bubble dynamics of nucleate pool boiling. Even with a low heat flux of 18.9 kW/m^2, very few single bubble growth processes were observed. Bubbles appeared not only at nucleation sites on the heating surface, but also at many nucleation sites on the copper bead surfaces, even several layers above the heating surface. The increased number of nucleation sites and greater thermal conductivity of copper brought the heating surface superheat to 6.64°C, compared with 8.22°C of glass bead packed porous structures at the same heat flux. Before a single bubble grew large enough to allow its buoyant force to remove the bubble from the nucleation site, most bubbles touched one or more adjacent bubbles to generate a vapor column net in the space between the copper beads. The greater the heat flux, the greater the number of vapor column nets formed among the copper beads. It was concluded that copper beads served as an extended heating surface for more nucleation sites, even at low heat flux. At the highest heat flux of 76.3 kW/m^2, the interstitial space inside the porous structure was mostly taken over by vapor col-

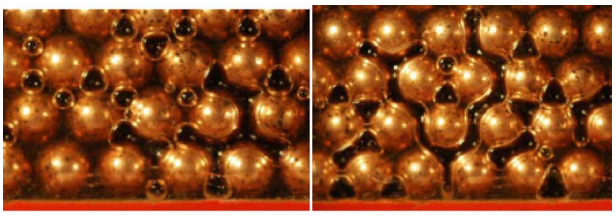

(a) Bubble dynamics process at heat flux of 18.9 kW/m^2

(b) Phase change process at heat flux of 37 kW/m^2

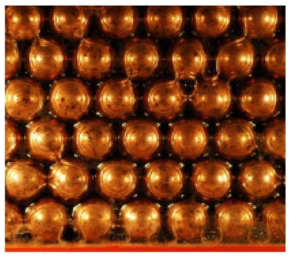

(c) Phase change process at heat flux of 76.3 kW/m^2

Fig. 8 Phase change images in 3 mm diameter copper bead packed porous structures

umn nets, and then was constantly occupied by the vapor in all copper bead layers. The difference between glass and copper bead packed porous structures was that copper beads were much heavier than glass beads. Consequently, the vapor momentum was able to lift glass beads, but not strong enough to lift copper beads. Instead, the vapor momentum had to use more interstitial space within the copper bead packed porous structure to accommodate the high vapor phase flow rate. Interestingly, the highest heating surface superheat for copper bead packed porous structures was 14.20°C, very close to the 15.41°C of glass bead packed porous structures. This meant that the increased thermal conductivity of copper beads played a minor role in the two-phase heat transfer at high heat flux. The bubble dynamics pictures in a copper bead packed porous structure are shown in Fig. 8.

2.3 Heat Flux Versus Superheat in Bead Packed Porous Structures. The heating surface superheats of the 1 mm and 3 mm diameter glass bead packed structures were recorded and plotted in Fig. 9. It illustrated that, at a low heat flux of 18.9 kW/m^2, superheat of 1 mm glass bead packed porous structures was close to the superheat of a plain surface, while 3 mm glass bead packed porous structures had a much smaller superheat. When heat flux increased to 47 kW/m^2—and even 76.3 kW/m^2—the superheat of 1 mm glass bead packed porous structures deviated from the superheat of the plain surface, but became close to the superheat of 3 mm glass bead packed structures. Based on experimental observations, this was caused by the following two reasons. First reason of the superheat's change is that, when heat flux was low, single bubble dynamics dominated the two-phase heat transfer, i.e., the number of nucleation sites on the heating surface was the major factor of the two-phase heat transfer. The glass beads applied a geometric constraint to the bubble growth process in that the absolute space between each pair of glass beads was limited, meaning, a single bubble growing in the interstitial space would depart at a smaller size in 3 mm glass bead packed porous structures, compared with the bubble departure size on a plain surface. While for the 1 mm glass bead packed porous structures, the single bubble growing process did not exist as in the 3 mm glass bead packed porous structures or in the plain surface case because the vapor would be trapped in the tiny interstitial spaces due to the far smaller growing space available. Therefore, the superheat of 3 mm glass bead packed porous structures was lower than that of 1 mm glass bead packed porous structures. The other reason of the superheat's change is that, when heat flux increased, column bubble dynamics dominated the two-phase heat transfer. At this stage, the major factor of the two-phase heat transfer was the liquid-vapor counter flow in porous structures. 1 mm glass bead packed porous structures experienced more difficulty in water replenishment to the heating surface than the 3 mm glass bead packed porous structures. However, with further increase in heat flux, vapor column nets appeared at the bottom of both porous structures, and the superheats of both sizes of glass bead packed porous structures became very close.

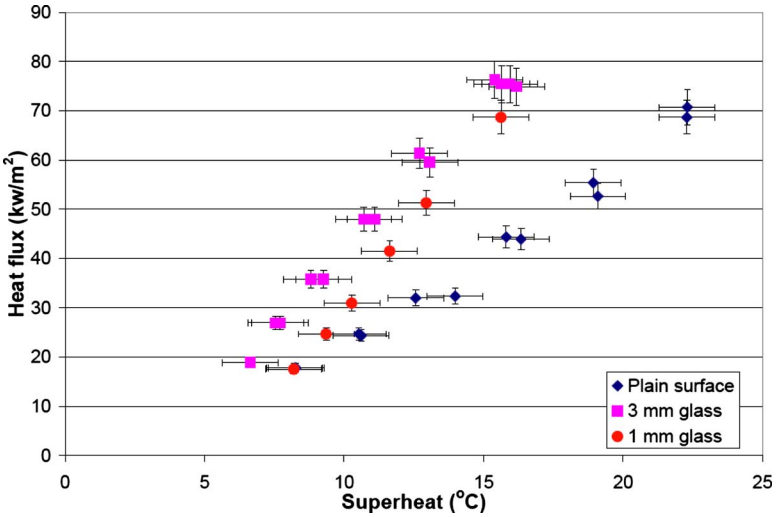

Fig. 9 Heat flux versus superheat for 1 mm and 3 mm diameter glass bead packed structure tests with reference to a plain surface test

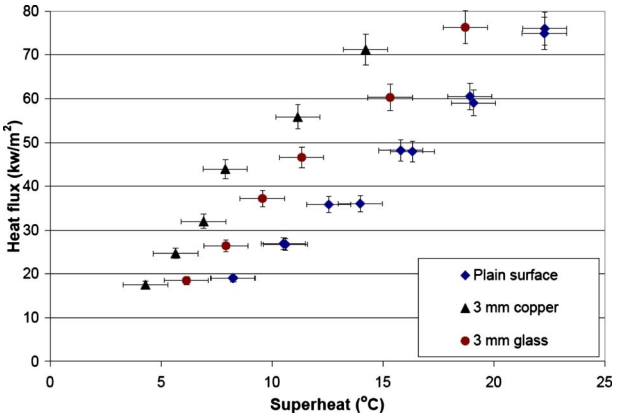

Fig. 10 Heat flux versus superheat of the heating surface of three nucleate pool boiling structures

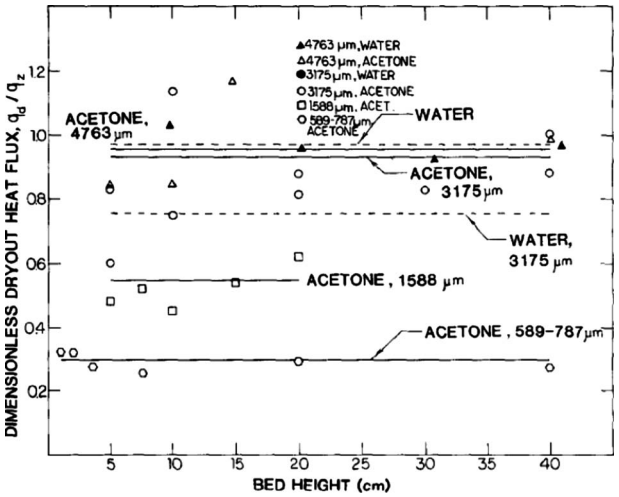

Fig. 11 Experimental results for large spheres [28]

The superheat and heat flux of a 3 mm copper bead packed porous structure were also recorded to compare with the results of the 3 mm glass bead test, as presented in Fig. 10. It is clear that copper bead tests showed smaller superheat values at all heat fluxes than that in 3 mm glass bead tests. This is explained by the greater thermal conductivity of copper, as compared with glass. It is further explained by the number of bubbles growing directly on the surface of copper beads. The number of nucleation sites on the heating surface was critically important when the heat flux was low and the single bubble dynamics dominated the two-phase heat transfer. As heat flux increased, vapor columns appeared sooner in copper bead tests than in glass bead tests at the same heat flux. This also meant that more vapor was generated in copper bead tests than in glass bead tests. The superheat difference between the two material porous structures would become smaller when the heat flux further increased. Eventually, the constrained geometry of the bead packed porous structures would induce the earlier occurrence of dryout, i.e., a vapor blanket totally covering the heating surfaces in both copper and glass bead packed porous structures.

The induced early occurrence of dryout in a porous structure was also studied by Dhir and Catton [28], both experimentally and theoretically. Based on the assumptions of no liquid inertia, inviscid vapor, small cross-sectional area occupied by vapor, and spherical particles of near uniform size, a correlation of normalized dryout heat flux was developed as Eq. (2). The prediction of the dimensionless dryout heat flux in 3 mm bead packed porous structures would be 0.75 for this study on 3 mm bead tests. This is consistent with the experimental results of Ref. [28], which are shown in Fig. 11. The correlation of normalized dryout heat flux is

$$\frac{q_{vd}}{q_z} = \frac{QL(1-\varepsilon)}{q_z} = C_1 K d^{*2} \Gamma^{1/2} M \tag{2}$$

where Q is the heat generation rate, L is the bed height, ε is the bed void fraction, and q_z is the critical heat flux from Zuber's equation [29] as

$$q_z = 0.131^* \rho_v h_{fg} \left[\frac{\sigma(\rho_l - \rho_v)g}{\rho_v^2} \right]^{1/4} \tag{3}$$

with the parameters in the last term of Eq. (2) defined as

$$K = \frac{\varepsilon^3}{(1-\varepsilon)^2} \tag{4}$$

$$\Gamma = \rho_l / \rho_v \tag{5}$$

$$M = \left[\frac{\rho_l^4 \sigma^3}{\mu_l^4 g(\rho_l - \rho_v)^3} \right]^{1/4} \tag{6}$$

$$d^* = \frac{d}{[\sigma/g(\rho_l - \rho_v)]^{1/2}} \tag{7}$$

where C_1 is a constant, ρ_l is the water density, ρ_v is the vapor density, σ is the water surface tension, μ_l is the water viscosity, g is the gravitational acceleration, and d is the sphere diameter.

3 Numerical Simulation

A numerical simulation was conducted to observe bubble dynamic behavior of nucleate pool boiling inside bead packed porous structures. The purpose of this effort was to understand the bubble dynamics characteristics when a bubble grows, expands, departs and/or coalesces with other bubbles under the influence of a range of heat fluxes. The simulation presented details about necking under geometric constraints and the drag force applied to a new bubble in the departure wake flow field of the previous bubble. Simulation results supplemented phase contour details to the experimental observation. Experimental and simulation efforts were combined in an effort to better explain the geometric effect on bubble dynamics of nucleate pool boiling in bead packed porous structures.

3.1 Computational Domains and Boundary Conditions. As shown in Fig. 12, the bubble dynamics systems of single and six layer bead packed porous structures consisted of 3 mm uniform diameter beads and rectangular domains. The heating surfaces were on the bottom of each domain, and different superheats were assigned to the heating surfaces according to experimental data at

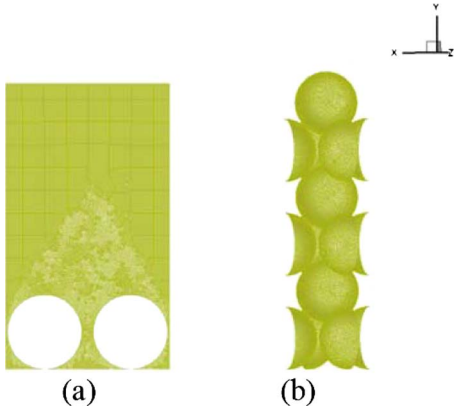

Fig. 12 Meshes of 2D and 3D simulation domains

different heat fluxes. The single layer domain was for the low superheat investigation, and the six layer bead packed porous structure was created for medium and high superheat studies. For the single bubble dynamic simulation, the two-dimensional (2D) domain mesh is shown in Fig. 12(*a*), and for the medium and high heat flux bubble dynamic study, the three-dimensional (3D) domain mesh is shown in Fig. 12(*b*).

For the sake of conciseness, the 3D domain of the one layer bead packed structure is not shown here, but the work will be discussed in Sec. 3.3. The surface of the spheres was set to be isothermal, and side walls of the domain were symmetric. The top sides of the domains were set to be the pressure outlet at 1 atm and 373 K. The bottom heating surfaces of both domains were set to a fixed temperature. Overall dimension of the 3D domain was $3.2\times3.2\times18$ mm^3, and the overall dimension of the 2D domain was 5.7×10 mm^2. Initially, the domains were filled with saturated water at 373 K, and a small vapor parcel was set on the center of the heating surface of each domain. The initial vapor parcel had a character radius of 0.5 mm.

3.2 Computational Methodology. Numerical simulations of 2D and 3D, unsteady, two-phase flow in the computational domains were performed using FLUENT [30]. For the mass and momentum conservation governing equations, a volume-of-fluid (VOF) method was employed. The energy conservation equation was also applied, along with the mass and momentum equations. The VOF model dealt with the interaction between two immiscible phases of liquid water and vapor, with a focus on phase interface, which was a good fit for the emphasis of the current study on bubble dynamics. The user defined function (UDF) file for this nucleate pool boiling simulation effort included a mass exchange source term in the mass equations for both liquid and vapor phases, and a source term of latent heat transfer in the energy equation.

The mass, momentum, and energy conservation equations of each phase used are

$$\frac{\partial\rho}{\partial t}+\nabla\cdot(\rho\boldsymbol{V})=S_{\alpha s} \tag{8}$$

$$\frac{\partial(\rho\boldsymbol{V})}{\partial t}+\nabla\cdot(\rho\boldsymbol{V}\boldsymbol{V})=-\nabla p+\nabla\cdot[\mu(\nabla\boldsymbol{V}+\nabla\boldsymbol{V}^T)]+\rho g+\boldsymbol{F} \tag{9}$$

$$\frac{\partial(\rho E)}{\partial t}+\nabla\cdot[\boldsymbol{V}(\rho E+p)]=\nabla\cdot(k_{\text{eff}}\nabla T)+S_h \tag{10}$$

where ρ is the fluid density, t is the time, $\boldsymbol{V}$ is the velocity vector, p is the static pressure, μ is the fluid viscosity, g is the gravitational acceleration, E is the internal energy, k_{eff} is the effective thermal conductivity, and ∇T is the temperature gradient. The force due to surface tension on the liquid/vapor interface is defined based on the continuum surface force (CSF) model proposed by Brackbill et al. [30] as

$$\boldsymbol{F}=\sigma\frac{\overline{\rho}\kappa\nabla\alpha}{1/2(\rho_l+\rho_v)} \tag{11}$$

where $\overline{\rho}$ is the average density, κ is the interface curvature, σ is the surface tension coefficient, and α is the phase volume fraction.

The source term is defined as

$$S_{\alpha s}=-\frac{(q_v''-q_l'')\cdot\nabla\alpha}{L} \tag{12}$$

where $S_h=-S_{\alpha s}\cdot L$ is the energy source term of q_l'' and q_v'', which are the heat flux across the interface per unit area on both phases, and L is the latent heat [31].

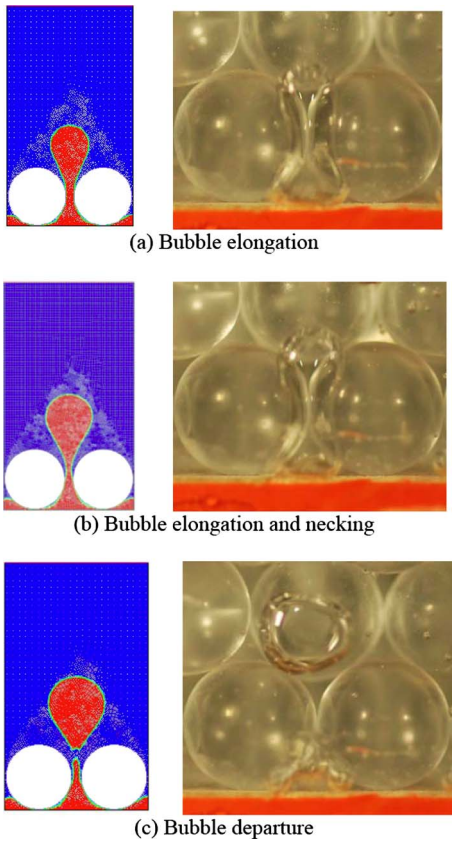

Fig. 13 Phase contour comparison—single bubble growth process under geometric constraint of solid beads (in the simulation, red is the vapor phase, blue is the liquid phase, and white is the solid bead)

3.3 Simulation Results

3.3.1 Single Bubble Dynamics Due to Geometric Constraints of Beads. In the simulation, the initial bulk temperature was set at 372 K for liquid water, matching the water temperature in the experiments. First, a 2D case was developed to study the bubble dynamics of a single bubble under the geometric constraint of solid beads, Fig. 13. Results were compared with experimental images. The photo in Fig. 13(*a*) shows the bubble elongation in the interstitial spaces between solid beads. Because there were two dimensions in the 2D simulation, the top section of the bubble expanded while the bubble elongated vertically. Figure 13(*b*) shows a typical necking effect at one bead radius above the heating surface. And the simulation image in Fig. 13(*c*) shows the top section of the bubble breaking away from the bottom section.

The connecting part of the top section retracted upward to make the top section a spherical shape, and the connecting part of the bottom section retracted downward to make the bottom section a semispherical cap shape. This retracting movement was caused by the surface tension and is captured in the left image of Fig. 14, in which the highest velocity occurred at the connecting parts of the two sections (red and yellow). The single bubble dynamic has been observed in 3D numerical simulation results of multilayer bead packed porous structures as well, and will be discussed in Fig. 17.

The 2D simulation of single bubble dynamics was extended to a 3D simulation. As shown in Fig. 15(*a*), the streamlines show that a vortex sheet accompanied bubble departure, and liquid water replenished the nucleation sites through the interstitial spaces between beads. The wake of the departing bubble would significantly influence new bubble growth by applying a drag force on the new bubble. In turn, there was a different bubble dynamics in

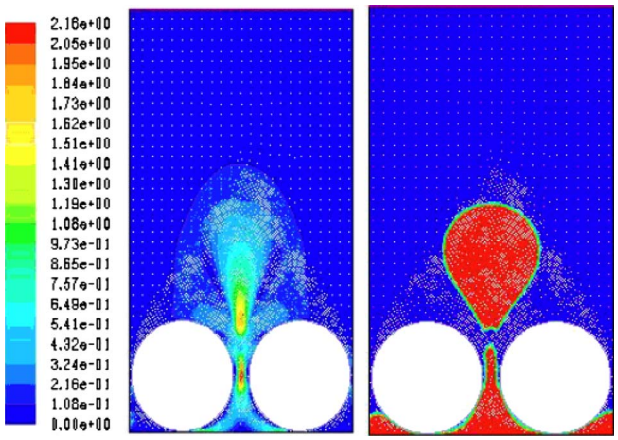

Fig. 14 Retracting movement of connecting parts of two sections after breaking. Left image is velocity contour and right image is phase contour (scale bar is velocity index).

that the new bubble would elongate more before necking, as compared with the previous bubble. This effect can be more clearly seen in Figs. 15(*b*) and 15(*c*), where the vortex and velocity vectors appear in 2D. A departing bubble induced a pair of vortices on both sides of the bubble, and the flow of liquid water in its wake added a drag force on the new bubble, in addition to a buoyant force and a surface tension force.

Compared with the dynamics of the previous bubble, the new bubble elongated more due to the drag force on its surface, caused by the wake flow field of the previous bubble, and the new bubble would separate before the top section gained the same buoyant force as the previous bubble. At the separating stage of the previous bubble, the buoyant force exclusively balanced the vertical surface tension force at the connecting point. Similar vortex and wake flow patterns after a single bubble departure were also reported by other researchers [32]. The experimental evidence was presented in Ref. [33], in which the bubble growth rate, bubbling frequency, and bubble site density of dielectric coolant (FC-72) boiling were imaged. It was shown that "*The wake from a departing bubble did exert a pulling force on its successor*" at low wall superheats of 4°C to 7°C.

3.3.2 Bubble Dynamics of Medium Heat Flux in Bead Packed Porous Structures. At medium heat flux, bubble growth process did not have a necking stage, and hence, the top section of the bubble did not separate from the bottom section. Instead, the top section expanded horizontally due to the geometric constraint imposed by the next bead layer. Neighboring bubbles coalesced and then extended to the next layer. The simulation results in Figs. 16(*a*) and 16(*b*) are reproductions of the experimental observation of the medium heat flux in Fig. 6(*a*). The bubble broke after it penetrated into the upper layers (Fig. 16(*c*)), but this breakage was

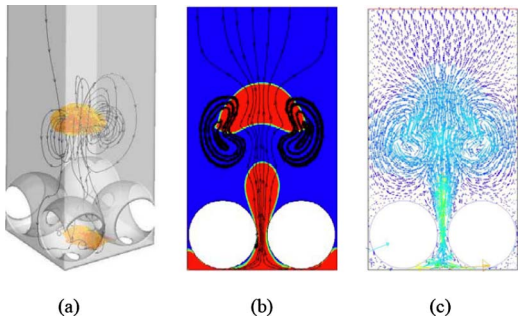

Fig. 15 Vector contour comparison with simulation results

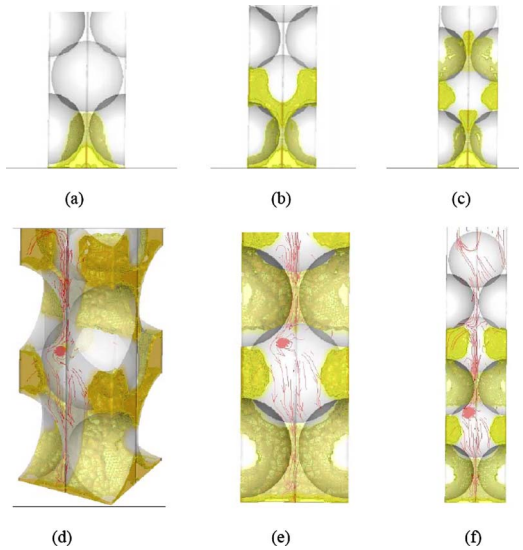

Fig. 16 Phase contour of vapor behavior at medium heat flux and liquid water replenishing streaklines (red arrows)

not caused by the necking effect under geometric constraints as it was in single bubble dynamics. Rather, the breakage was caused by the hydrodynamic instability due to the counter flow of vapor and liquid. Liquid water replenishment is illustrated with red arrow streaklines in Figs. 16(*d*)–16(*f*).

3.3.3 Bubble Dynamics of High Heat Flux in Bead Packed Porous Structures. A series of simulation images of bubble dynamics at high heat flux is presented in Fig. 17. Each image represents the instantaneous behavior when a vapor column filled the interstitial space of a porous structure. The simulation results showed that, at high heat flux, the interstitial spaces between solid

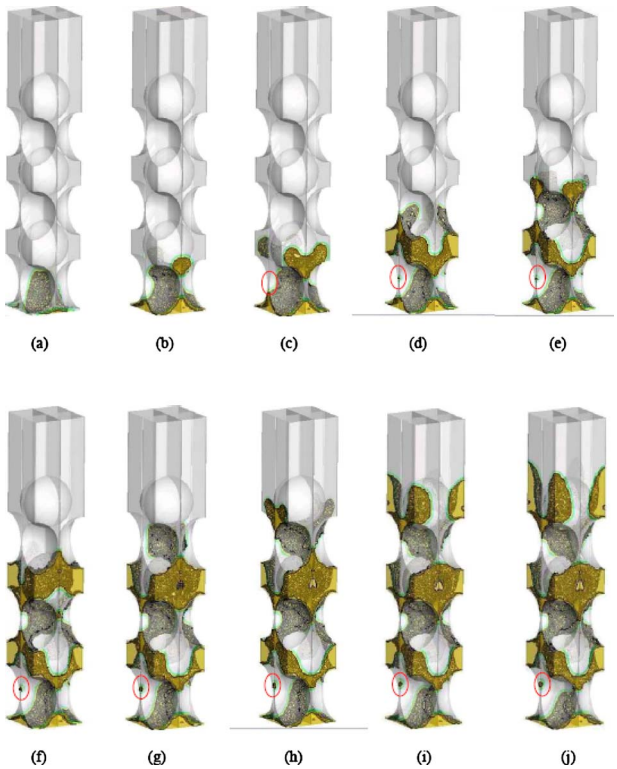

Fig. 17 Vapor column behavior at high heat flux

beads were quickly occupied by vapor, and only a small fraction was filled with liquid water. This vapor domination inside the porous structure could cause a lack of liquid replenishment on the heating surface, and the lack of liquid water to replenish the heating surface could cause a shortage of new vapor mass flux to support the growth of vapor columns. Finally, in Figs. 17(*i*) and 17(*j*), the vapor column broke at the bottom, partially due to the lack of constant new vapor mass flux, and partially due to the hydrodynamic instability of the two-phase counter flow. It is interesting to note that even though vapor column was the major phenomenon occurring in high heat flux situations, single bubble dynamics was still occurring beside the vapor column, as shown in the red circles of Fig. 17. Computer simulation indicates that the single bubble dynamics observed at high heat flux was exactly the same as at the low heat flux. However, single bubble dynamics is only a minor player of two-phase heat transfer at high heat flux situations.

4 Conclusions

Bubble dynamic behaviors in bead packed porous structures were studied both with experiments and computer simulations. Visualization efforts were conducted to investigate the mechanisms of nucleate pool boiling in bead packed structures. The following observations were identified in the study.

1. At a fixed heat flux, the superheat of a plain surface is always the highest, followed by the superheat of 1 mm glass bead packed porous structures, then by the 3 mm glass beads, and finally by the 3 mm copper beads. With increasing heat flux, the differences of superheat will decrease between the two sizes of glass beads, while the superheat differences between the 3 mm copper beads and glass beads will increase. Heat transfer difference between the 1 mm and 3 mm glass beads are caused by the different size of the pores between the beads. The 1 mm glass bead porous structures had a small pore size, which trapped vapor bubbles and formed bubble columns at relatively low heat flux, compared with that of 3 mm glass beads. The heat transfer difference between 3 mm glass and copper beads is due to, first, the fin effect. As the thermal conductivity of copper is much higher than that of glass, there is better nonphase change heat transfer in 3 mm copper beads. Second, and more importantly, copper bead surfaces offer many bubble nucleation sites, while glass bead surfaces have virtually no nucleation sites. And the number of bubble nucleation sites on copper bead surfaces will increase even more when the superheat of copper bead surfaces increase with heat flux. This increased number of bubbles enhances two-phase heat transfer and greatly reduces superheat on heating surfaces. Another interesting fact is that, at the highest heat flux, 3 mm glass bead packed porous structures have several major vertical vapor escape paths, while 3 mm copper bead packed porous structures have a totally different scenario—vapor column nets are developed uniformly in both the vertical and horizontal directions.
2. Both experimental observations and computer simulation results show that single bubble dynamics is the main mechanics for the two-phase heat transfer at low heat flux. The forces involved are buoyancy, interfacial tension, and drag in the departure wake of the preceding bubble. The addition of the drag force greatly aids in earlier single bubble departure from the heating surface at a smaller size.
3. At medium heat flux, vapor columns appear in porous structures. Top sections of the vapor columns break from the bottom sections in the interstitial space due to the hydrodynamic instability, which gives a sufficiently large space for the downflow of liquid water to replenish the heating surface. With increasing heat flux, the momentum of vapor columns is strong enough that a vertical vapor escape path is generated from the heating surface up through the top of the porous structures. The vapor path column will not break until the replenishing liquid water is insufficient to maintain new vapor mass flux to support the vapor path columns.

Acknowledgment

The authors would like to acknowledge financial support of this work through the University of Toledo startup funding, deArce Memorial Endorsement Award, and Strategic Enhancement Award.

References

[1] Peterson, G. P., 1994, *An Introduction to Heat Pipe: Modeling, Testing and Applications*, Wiley, New York.
[2] Faghri, A., 1995, *Heat Pipe Science and Technology*, Taylor & Francis, Washington, DC.
[3] Wang, Y., and Cheng, P., 1997, "Multiphase Flow and Heat Transfer in Porous Media," *Advances in Heat Transfer*, J. P. Hartnet, T. F. Irvine, Y. I. Cho, and G. A. Greene, eds., Academic, New York, Vol. 30, pp. 93–196.
[4] Zhao, T. S., and Cheng, P., 1998, "Heat Transfer in Oscillatory Flows," *Annual Review of Heat Transfer*, C.-L. Tien, ed., Begell House Publishers, New York, Vol. 9, Chap. 7.
[5] Zhao, T. S., Kreuer, K.-D., and Van Nguyen, T., 2007, *Advances in Fuel Cell*, Elsevier, New York, Vol. 1.
[6] Zawodzinski, T. A., Derouin, C., Radzinski, S., Sherman, R. J., Smith, V. T., Springer, T. E., and Gottesfeld, S., 1993, "Water Uptake by and Transport Through Nafion® 117 Membranes," J. Electrochem. Soc., **140**, pp. 1041–1047.
[7] Geiger, A. B., Tsukada, A., Lehmann, E., Vontobel, P., Wokaun, A., and Scherer, G. G., 2002, "In Situ Investigation of the Two-Phase Flow Patterns in Flow Fields of Polymer Electrolyte Fuel Cells by Neutron Radiography and Locally Resolved Current Measurements," *Proceedings of the 2002 Fuel Cell Seminar*, Palm Springs, CA, Nov. 18–21, pp. 125–161.
[8] Liter, S. G., and Kaviany, M., 2001, "Pool-Boiling CHF Enhancement by Modulated Porous-Layer Coating: Theory and Experiment," Int. J. Heat Mass Transfer, **44**, pp. 4287–4311.
[9] Hwang, G. S., and Kaviany, M., 2006, "Critical Heat Flux in Thin, Uniform Particle Coatings," Int. J. Heat Mass Transfer, **49**, pp. 844–849.
[10] Li, C., Peterson, G. P., and Wang, Y. X., 2006, "Evaporation/Boiling in Thin Capillary Wicks (I)—Wick Thickness Effects," ASME J. Heat Transfer, **128**, pp. 1312–1319.
[11] Li, C., and Peterson, G. P., 2006, "Evaporation/Boiling in Thin Capillary Wicks (II)—Effects of Volumetric Porosity and Mesh Size," ASME J. Heat Transfer, **128**, pp. 1320–1328.
[12] Liao, Q., and Zhao, T. S., 2000, "A Visual Study of Phase-Change Heat Transfer in a Two-Dimensional Porous Structure With a Partial Heating Boundary," Int. J. Heat Mass Transfer, **43**(7), pp. 1089–1102.
[13] Wang, Z., Peng, X. F., and Ochterbeck, J. M., 2004, "Dynamic Bubble Behavior During Boiling in Bead-Packed Structures," Int. J. Heat Mass Transfer, **47**, pp. 4771–4783.
[14] Murgia, G., Pisani, L., Shula, A. K., and Scott, K., 2003, "A Numerical Model of a Liquid-Feed Solid Polymer Electrolyte DMFC and Its Experimental Validation," J. Electrochem. Soc., **150**, pp. A1231–A1245.
[15] Wang, Z. H., and Wang, C. Y., 2003, "Mathematical Modeling of Liquid-Feed Direct Methanol Fuel Cells," J. Electrochem. Soc., **150**, pp. A508–A519.
[16] Birgersson, E., Nordlund, J., Vynnycky, M., Picard, C., and Lindbergh, G., 2002, "Reduced Two-Phase Model for Analysis of the Anode of a DMFC," J. Electrochem. Soc., **151**, p. A21574.
[17] Divisek, J., Fuhrmann, J., Gartner, K., and Jung, R., 2003, "Performance Modeling of a Direct Methanol Fuel Cell," J. Electrochem. Soc., **150**, pp. A811–A825.
[18] Rice, J., and Faghri, A., 2006, "A Transient, Multi-Phase and Multi-Component Model of a New Passive DMFC," Int. J. Heat Mass Transfer, **49**, pp. 4804–4820.
[19] Yang, W. W., Zhao, T. S., and Xua, C., 2007, "Three-Dimensional Two-Phase Mass Transport Model for Direct Methanol Fuel Cells," Electrochim. Acta, **53**, pp. 853–862.
[20] Tüber, K., Pócza, D., and Hebling, C., 2003, "Visualization of Water Buildup in the Cathode of a Transparent PEM Fuel Cell," J. Power Sources, **124**, pp. 403–414.
[21] Yang, X. G., Zhang, F. Y., Lubawy, A. L., and Wang, C. Y., 2004, "Visualization of Liquid Water Transport in a PEFC," Electrochem. Solid-State Lett., **7**, pp. A408–A411.
[22] Yang, H., Zhao, T. S., and Ye, Q., 2005, "In Situ Visualization Study of CO2 Gas Bubble Behavior in DMFC Anode Flow Fields," J. Power Sources, **139**, pp. 79–90.
[23] Ozaki, K., 1995, "Pumping Mechanism Using Periodic Phase Changes of a Fluid," *Proceedings of the IEEE Micro Electro Mechanical Systems*, Amsterdam, Netherlands, pp. 31–36.
[24] Jun, T. K., and Kim, C. J., 1998, "Valveless Pumping Using Traversing Vapor Bubbles in Microchannels," J. Appl. Phys., **83**, pp. 5658–5664.
[25] Wang, H., Peng, X. F., Christopher, D. M., Lin, W. K., and Pan, C., 2005, "Investigation of Bubble-Top Jet Flow During Subcooled Boiling on Wires,"

Int. J. Heat Fluid Flow, **26**, pp. 485–494.
[26] Drazin, P. G., 2002, *Introduction to Hydrodynamic Stability*, Cambridge University Press, Cambridge, England.
[27] Rohsenow, W. M., 1962, "A Method of Correlating Heat Transfer Data for Surface Boiling of Liquids," Trans. ASME, Ser. B, **84**, pp. 969–976.
[28] Dhir, V. K., and Catton, I., 1982, "Boiling in a Porous Bed," Appl. Sci. Res., **38**, pp. 69–76.
[29] Zuber, N., 1959, "Hydrodynamic Aspects of Boiling Heat Transfer," AEC Report No. AECU-4439.
[30] Brackbill, J. U., Kothe, D. B., and Zemach, C., 1992, "Continuum Method for Modeling Surface Tension," J. Comput. Phys., **100**, pp. 335–354.
[31] Fluent, Inc., 2006, *Fluent 6.3. User's Guide*, Fluent Inc., Ann Arbor, MI.
[32] Pillapakkam, S. B., Singh, P., Blackmore, D., and Aubry, N., 2007, "Transient and Steady State of a Rising Bubble in a Viscoelastic Fluid," J. Fluid Mech., **589**, pp. 215–252.
[33] Ramaswamy, C., Joshi, Y., Nakayama, W., and Johnson, W. B., 2002, "High-Speed Visualization of Boiling From an Enhanced Structure," Int. J. Heat Mass Transfer, **45**, pp. 4761–4771.

Thermal Science of Weld Bead Defects: A Review

P. S. Wei
Xi-Wan Chair Professor
Fellow ASME
Department of Mechanical and Electro-Mechanical Engineering,
National Sun Yat-Sen University,
Kaohsiung 80424, Taiwan, China

Mechanisms for the formation of bead defects, such as humping, gouging, rippling, and other unexpected surface patterns, encountered in welding or drilling are interpreted and reviewed from thermal-fluid science viewpoint. These defects usually accompanying with porosity, undercut, segregation, stress concentration, etc., seriously reduce the properties and strength of the joint or solidification. Even though different mechanisms for formation of the defects have been extensively proposed in the past, more systematical understanding of pattern formations from thermal, fluid, physics, electromagnetic, pattern selections, and metallurgy sciences is still limited. The effects of working parameters and properties on humping and rippling, for example, can be systematically and quantitatively interpreted from scale analysis presented in this work. Good comparison with experimental results reveals mechanisms of different surface patterns. The mechanistic findings for bead defects are also useful for other manufacturing and materials processing. [DOI: 10.1115/1.4002445]

Keywords: weld defects, bead defects, surface patterns, pattern selection, humping, rippling

1 Introduction

Productivity in different arc, laser, and electron beam welding technologies can be improved by increasing welding speed and current. This strategy, however, is limited by the appearance of weld defects such as rippling, humping, and undercutting [1–3]. Weld ripples exhibit rather regular, arc-shaped topographic features on a solidified surface, for example, as shown in Figs. 1(*a*) and 1(*b*) in EBW of Al 6061 for different welding speeds [4]. The ripples slightly elevate above the surface. On the other hand, more complicated humping shows an irregular and unpredictable surface contour consisting of a series of swelled protuberance, as can be seen later. Humping also often accompanies with serious defect of undercut, which is the depression at the edge of the fusion boundary. Microstructure features, such as solute segregation, porosity, fracture, crack, and deformation, are closely related to formation of rippling, humping and undercutting [1,5,6], and strongly deteriorate the properties and strength of the joint.

The often-used welding technique [2] includes gas metal arc welding (GMAW or MIGW), which is accomplished by heating from a generated arc and droplet deposition from a consumable wire electrode continuously fed from a spool. Gas is fed through the torch to shield the electrode and molten weld pool from the surroundings. Others are gas tungsten arc welding (GTAW or TIGW), accomplished from heating by an arc generated between a nonconsumable tungsten electrode and the metal being welded. Electron beam welding (EBW) is formed by impinging a beam of high energy electrons to heat the weld joint. Welding by a pulse or continuous wave laser beam (LBW) is also achieved by high power density, determined by the spot size and focal location of the polarized, electromagnetic laser beam.

Good or poor welding usually depends on rippling and humping on a solidified surface. Bennett and Mills [7] observed that surface ripples can be reduced by reducing nitrogen content of high manganese stainless steels in GTAW. Matsuda et al. [8] found that more serious ripples or complicated surface patterns appeared when magnetic field was greater than 100 G and its frequency greater than 10 Hz in GTAW of aluminum alloys. Okada et al. [9] noted that the ripples on the surface of welds were fine for steels exhibiting poor penetration and coarse for those with good penetration. Ripples are commonly mixed with coarse and fine ripples (see Figs. 1(*a*) and 1(*b*)). Sundell et al. [10] noted that the weld made by GTAW at low current exhibited regular, closely spaced weld surface ripples. The high S steels, however, showed periodic ripples of longer wavelength, which were superimposed on the fine ripple background. The ripples of low frequency appeared to be related to the lower surface tension and inward surface flow induced by the surfactant of sulfur. Mills and Keene [11] further mentioned that a quiescent fluid surface coupled with fine ripples was characterized by high surface tension and its negative temperature gradient.

The measured rippling spacing for different currents and frequencies of ac with superimposed current ripples in GTAW of aluminum alloy and mild steel was presented by Garland and Davies [12]. The frequency of ripples was found to be the same as that of the power source. Provided that welding speed was changed, rippling spacing can be found around 0.084 mm corresponding to 50 Hz in welding speeds between 4.9 mm/s and 3.1 mm/s. Changing arc frequency to 100 Hz also showed the similar change of rippling spacing. Arata and Miyamoto [1,13] measured average pitches of ripples in ac excited LBW of SUS27 stainless steel. Regardless of different surface conditions, the average pitch exhibited a unique linear increase from 0.0025 cm to 0.01 cm as welding speed increased from 0.3 cm/s to 1.2 cm/s. Ishida [14] measured ripples in pulsed current GTAW of mild steel and found that number of ripples increased with decreasing welding speed and increasing pulse frequency. The best bead formation occurred at pulse frequencies of 2.5 Hz and 5 Hz and travel speed of 0.47 cm/s. Clear ripples, however, were found for low pulse frequency rather than high travel speed. In contrast, Wei et al. [15] measured and scaled average pitches between fine and coarse ripples, which were around 10^{-6} m and 10^{-4} m, respectively, whereas average amplitude was 10^{-6} m in EBW of Al 1100 and type 304 stainless steel. Roughness is reduced by decreasing beam power and increasing welding speed. It is worthy of mentioning that the measured roughness was also found to increase with increasing incident flux, reducing travel speed of a pulsed laser beam micromilling of Si wafers [16]. The contradicted results may be due to unclear definitions between fine and coarse ripples, and humps (see Fig. 1) and uncertain measurements involving many

Manuscript received June 15, 2009; final manuscript received: March 15, 2010; published online November 15, 2010. Assoc. Editor: Wilson K. S. Chiu.

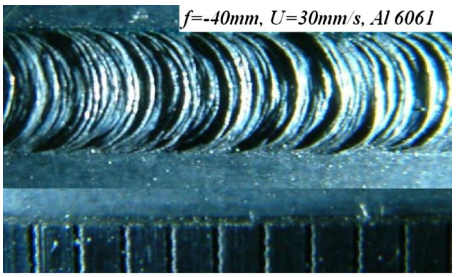

(a)

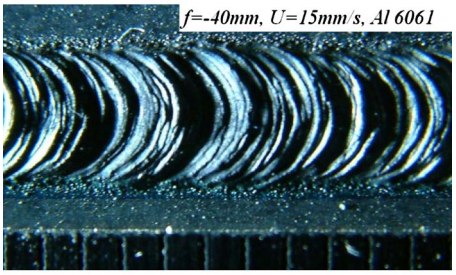

(b)

Fig. 1 Photographs of rippling in welding Al 6061 for welding speeds of (*a*) 30 mm/s and (*b*) 15 mm/s [4]

working parameters. Rippling spaces affected by surface active solutes of sulfur and oxygen in EBW of steels were also measured and scaled by Wei et al. [17].

Humping, which can be around several millimeters, has been found in GMAW [18–21], submerged arc welding (SAW) [22–24], GTAW [25–27], LBW [28,29], and EBW [30–32], and in other fields such as laser texturing [33], digital microfabrication [34], MEMS [35], and packaging [36]. In view of the added filler metal, humping is more serious in GMAW than other welding and manufacturing processes. Morphologies of humped welds are quite complicated, which were roughly categorized into the gouging region and beaded cylinder morphologies [37]. Typical gouging region morphology defects in GTAW at high currents and high travel speeds are shown in Fig. 2(*a*) [38]. The front of the weld pool exhibits a large depression known as the gouging region. Open, unfilled dry spots in between the humped beads can also be seen. In some cases, two small channels appear at the walls of the gouging region. The weld bead having parallel grooves at the side is the undercutting defect. The cross sections A-A and B-B in the original photos in the literature is interchanged in this work by a close examination of their sizes and shadow. Figure 2(*b*) shows a parallel humping or a split bead, separated by an empty channel. Figure 2(*c*) shows beaded cylinder morphology defects, which are quite different from the gouging region morphology [19]. The beaded cylinder morphology includes beadlike protuberances that sit above the workpiece surface and are connected by a narrow central channel. In some cases of disconnected protuberances, traces of a central channel can still be seen. It is interesting to find that the gouged region and bead cylinder morphology are inverse phenomenon. Different morphologies therefore can be revealed by simply interchanging the liquid and gas phases. Figures 2(*d*) and 2(*e*) show humping in EBW of Al 5083 for different welding speeds [4]. Strong evaporation from volatile element Mg results in serious humping.

Surface morphology as a function of beam power, welding current, and travel speed in low pressure GTAW was presented by Shimada and Hoshinouchi [39] and redrawn by Mendz et al. [40] and shown in Fig. 3(*A*). Based on observations, it showed that each region contains a particular type of weld bead. Type A in low

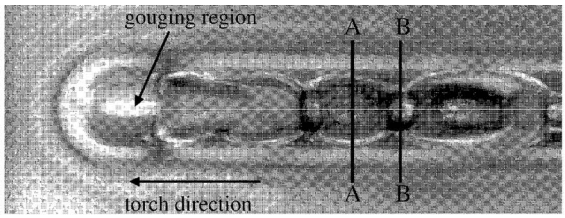

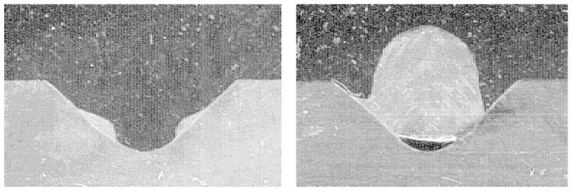

A-A B-B

(a)

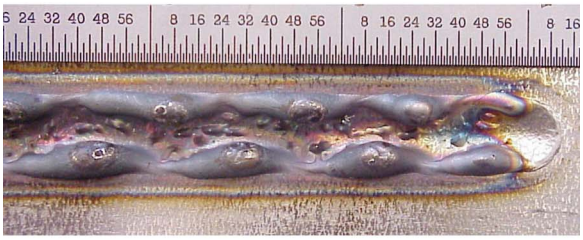

(b)

(c)

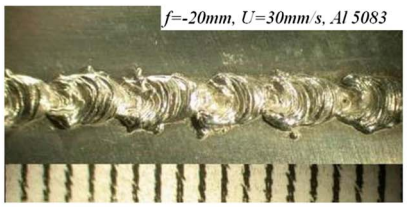

(d)

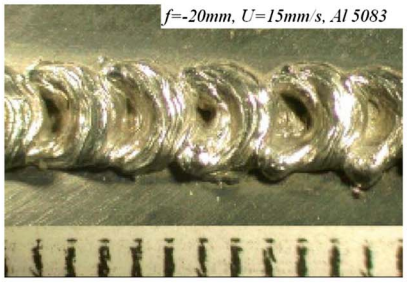

(e)

Fig. 2 Photographs of (*a*) humps with gouged region and (*b*) parallel hump in GTAW [38], (*c*) cylinder beads in GMAW [19], and ((*d*) and (*e*)) humps in EBW for different welding speeds [4]

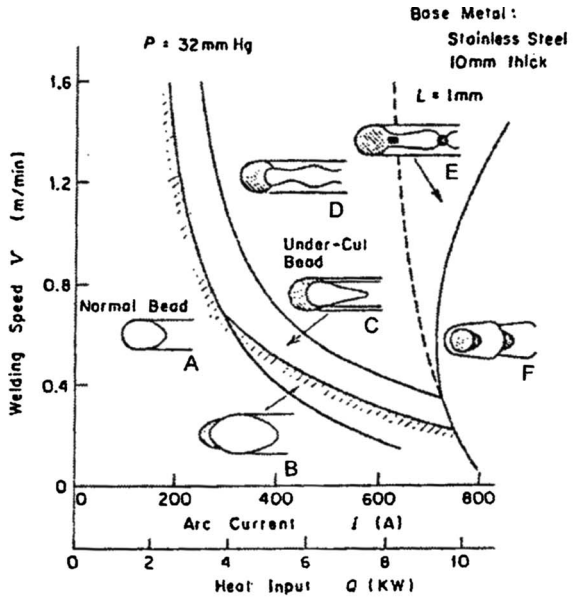

(A)

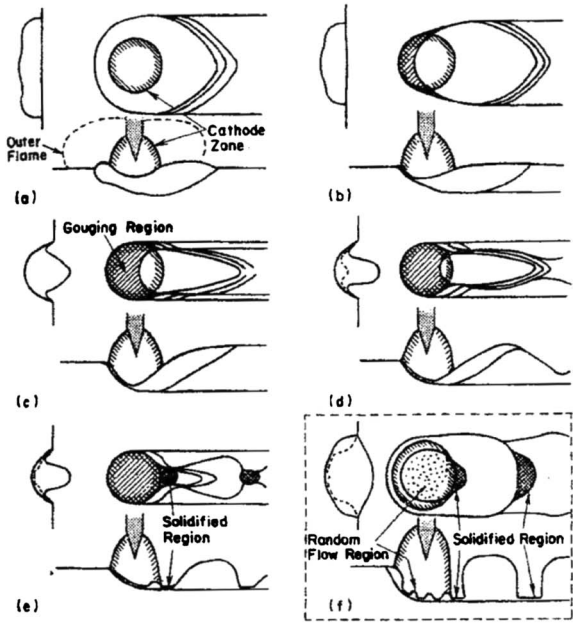

(B)

Fig. 3 (*A*) Morphologies affected by beam power and welding speed [39,40], and (*B*) molten pool changes with increasing welding speed in low pressure GTAW [39]

power or current is a normal weld pool, with little surface depression. Type B obtained by slightly increasing power is a sound weld, but the front of the weld pool is being "gouged." A further increase in power results in type C, which has more severe gouging together with an undercut. Type D presents two parallel humped beads at the side of the welds, and a "dry" path in between them. Type E is similar to type D, but the parallel beads collapse into each other, sometimes producing dry spots. Type F presents dry spots in between humps. They also sketched changes in the molten pool shape by increasing welding speed, as shown in Fig. 3(*B*). It shows the trailing edge of the molten pool increases its depth and volume significantly and becomes waves and gouged shape as welding speed increases.

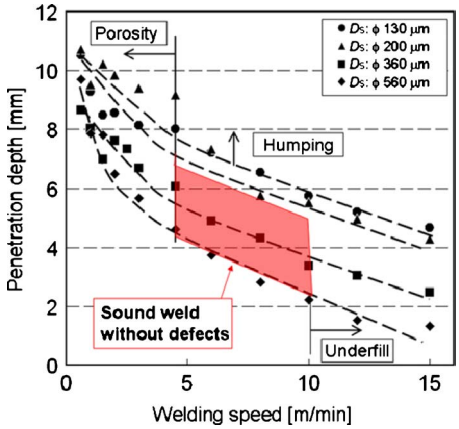

Fig. 4 Effects of fiber laser beam diameter and welding speed on weld penetration and welding defect formation [44]

The pitch of humping was measured by Tsukamoto et al. [41] and found to be reduced by decreasing surface bead width, and increasing welding speed, focal current or the object-to-focal spot distance ratio of EBW. They also observed from a high speed cine-camera that humping was apt to be formed when the focal spot was just on or slightly below the workpiece surface and the bead width was reduced. Marya and Edwards [42] found that in CO_2 LBW of AM50 amplitude of humps increased with decreasing beam power and increasing welding speed (whereas rippling was reduced by increasing welding speed). These measurements were roughly interpreted from Rayleigh's capillary instability. Unlike the linear relationship between amplitude and pitch of ripples [15], it is necessary to find the relationship between the amplitude and pitch of humping to interpret the above paradoxical or contradictory results.

Operation or parametric maps of arc voltage versus welding speed can be effectively used to understand and avoid humping. As for GMAW of mild steel, Nishiguchi et al. [43] found that humping occurred as the welding speed increased above a certain critical welding speed and that there existed an inverse relationship between this critical welding speed and welding voltage or power used. Yamamoto and Shimada [26] also provided parametric maps for GTAW further showing occurrence of gouged type undercut bead under high current and high speed conditions. Savage et al. [27] extensively provided different parametric maps together with measured arc forces for interpretation, indicating that humping readily took place by increasing welding speed, current, pulse frequency, and electrode-to-work distance ratio, decreasing tip angle and radius of the electrode in GTAW. In view of reducing arc pressure and depression of the pool, welding speeds could be more than doubled when He was used instead of Ar as shielding gas. Albright and Chiang [29] provided similar parametric maps characterized by different surface patterns as functions of welding currents and speeds and thicknesses of AISI 1015 carbon steel and type 304 stainless steel in LBW. For a fixed power, ropy bead, undercut, and humping were obtained with increasing welding speed. Humping was enhanced with increasing thickness of the workpiece. The observed surface patterns were similar to those found by Shimada and Hoshinouchi [39] in GTAW. The onset of hole formation could be predicted by using Rayleigh's capillary instability.

In high power LBW with a 6 kW and 130 μm, 200 μm, 360 μm, and 560 μm spot diameters, the weld penetrations and defects as functions of welding speed in bead-on-plate welding of type 304 steel plates are shown in Fig. 4 [44]. The depth-to-surface width ratios ware around 10 or greater, as a consequence

of the existence of a deep and narrow keyhole (or cavity) [45]. When the energy beam impinges on the workpieces to be joined, a thin layer of material is melted. With continued heating, the reactive force of evaporating material and the force induced by surface tension and surface tension gradient caused the liquid layer to flow upward and outward continuously [46–48]. A vapor-filled deep and narrow keyhole thus is produced. The energy beam therefore can readily pass through the keyhole core to the liquid layer surrounding the keyhole to make a deep weld joint. This figure shows that the maximum penetration can be produced for small welding speed and spot diameter. However, porosity, underfilling, and humping were also quantitatively found at welding speed less than 0.075 m/s (4.5 m/min) and greater than 0.17 m/s (10 m/min) and with the tightly focused LB of 130 μm and 200 μm spot diameter, respectively. Sound partially penetrated welds without welding defects could be produced under the wide conditions of the welding speeds between 4.5 m/min and 10 m/min with laser beams of 360 μm and 560 μm spot diameters. On each of the process maps, welding process parameters such as the shielding gas composition, the ambient pressure, torch angle, or electrode geometry are normally kept constant. Any minor change to these constant process parameters will alter the results, and more experimental work is thus needed to produce new process maps. A systematic understanding of the penetrative mechanisms therefore becomes important.

Adjusting other process parameters may also reduce tendencies of humping and undercutting [37,49]. For example, uses of large electrode tip angle [27,50] and hollow electrode [51] in GTAW, and large electrode wire diameter in GMAW [43] can decrease humping as a result of reduction of arc forces and depression of the pool. In the absence of strong swelling induced by magnetic force, EBW and LBW facilitate production of defect-free welds. Focusing the electron beam away from the workpiece surface reduced humping [30,31]. The effects of pulsed wave shapes also affected humping formation in GTAW [52] and LBW [53], respectively. Decrease in sulfur and bismuth contents reduced humping tendency and variation of the bead width as measured by Ishizaki et al. [54] and Hirata et al. [55], and Takeuchi et al. [56], respectively. Owing to impinging on the unmelted base metal and less able to depress near the trailing edge of the free surface, use of a forward inclined heat source reduced humping [39,57]. The welding in the downhill direction reduced humping and undercutting because the backward flow was reduced from gravitational force [58]. Tsukamoto et al. [31] argued that a deep and narrow square groove prevented the flow of the molten metal to the trailing edge and reduced humping. Fluid flow controlled by polarity of applied magnetic field and thermoelectric field due to temperature gradient between solidified seam material and melt, as well as between the base material and melt can reduce humping in laser beam welding [59]. Pulsed GTAW enhanced humping tendency in the middle frequencies of 50 Hz and 200 Hz [14,60]. Reduction of volatile element such as Mg reduced humping [4]. Humping and undercutting can also be reduced in tandem electrode GTAW [50,51], tandem wire GMAW [61,62], and dual beam LBW [63,64] and EBW [1,65], and hybrid welding processes [66–68]. This is because the total energy was split into two beams and the trailing electrode beam reduced cooling rates to prolong solidification time. The humping phenomenon in these welding processes has been found to be influenced by many welding parameters.

The present work reviews and interprets rippling, humping, and gouging patterns on weldment surfaces from systematical viewpoint of thermal-fluid science. Morphology will be analyzed by their appearance as seen through experimental observations and theories that have been developed to describe them. After physical mechanisms of the defects are disclosed, controlling and avoiding surface defects become achievable [69–71].

2 Factors Affecting Surface Defects

Proposed mechanisms of rippling and humping on a surface are presented as follows.

Rippling. Rippling induced by different working parameters is briefly described as follows:

1. *Solidification rate fluctuations*. Cheever and Howden [72] observed ripples in arc and laser spot welds and proposed that ripples were the result of incremental solidification. This was because solidification proceeded in discrete increments due to instability in heat transfer or solidification halt caused by release of latent heat of fusion. Rippling appeared to be inherent to rapid solidification. D'annessa [73] proposed that the rippling resulted from complicated interactions between solidification growth rate fluctuations and surface tension effects on the weld pool surface and fluid flow in GTAW. The peaks and valleys of ripples corresponded with increasing and decreasing growth rate intervals, respectively, affected by a proposed and cyclic two-stage growth processes, namely, the primary projected dendrite stalks and secondary dendrite side branching in a diffuse interface region. Solidification rate fluctuations, however, should account for more reliable studies involving interactions between incident flux and heat conduction in liquid and solid and latent heat evolution, affected by convection and interfacial phenomena near the triple phase line.
2. *Power source effects.* Garland and Davies [12] measured rippling spacing for different currents and frequencies of ac and dc with superimposed current ripples in GTAW of aluminum alloy and mild steel, respectively. It showed that the ripples were related to the cyclic current supply. However, surface rippling did not correspond to that in 3% amplitude variation of beam current in EBW. An interpretation for rippling in ac was that the maximum and minimum electric current coincided with maximum and minimum heat inputs, and oscillations of surface temperature and solidification rate, and rippled surface. The proposed rippling formation for dc welding of copper and electron beam welding stainless steels, involving the so-called solidification halt, time of diffusion, interface and meniscus interactions at rapid solidification, and changes of surface tension, however, was unclear. Kotecki et al. [74] observed from high speed motion pictures and found shutting off an arc suddenly released the plasma pressure, setting the pool into oscillation like a stroked drumskin and giving rise to rippling in GTA spot welding. The number of ripples counted agreed well with the number of pool oscillations. Using a pulsed arc source, Ecer et al. [75] observed up and down oscillations of GTAW pool, which exhibited a constant period, leading to liquid metal above the weld surface into which solid can grow and ripples were formed. Altshulin et al. [76] measured the effects of intensity and pulses of laser beam on concentric ripples of carbon steel and their displacement.
3. *Thermocapillary or Marangoni instability.* Thermocapillary instability is induced by thermocapillary force, namely, a temperature-dependent surface tension gradient along the liquid-vapor interface, given by [77–80]

$$\mu \frac{\partial u_t}{\partial n} = \frac{d\gamma}{dT}\frac{\partial T}{\partial s} \tag{1}$$

where u_t is tangential velocity, coordinates n and s are, respectively, directed in the upward and outward directions. In the case of negative surface tension coefficients $d\gamma/dT$ for all pure liquid metals, the surface flow directs from the hot central region to the cold edge of a molten pool. Unlike thermocapillary instability and convective cell induced by heating from below (negative temperature gradient) [81], thermocapillary instability in welding and manufacturing processing can also occur from heating from above, as will

be discussed later. Fujimura et al. [82] found that thermocapillary was one of the possible mechanisms to create the roughness of a resolidified surface of stainless steels and several pure metals irradiated by a hydrogen ion beam. Applying linear stability analysis of a horizontal thin melt layer on metals, they found that the critical wave number for Marangoni number ranged from 0.1 to 1 for stainless steel can be comparable with the measured roughness on the resolidified surface of the molten layer [83].

4. *Kelvin–Helmholtz instability.* The Kelvin–Helmholtz instability occurs at the interface of stratified fluids in relative parallel motion. Ang et al. [84] observed large scale ripples around 30 μm, which was much longer than the laser wavelength. They found regular wavelike patterns looked much like the wind-driven surface wave in a pond. This recognition directed their attention to the Kelvin–Helmholtz instability at the interface between the molten aluminum and plasma plume, whereas, Rayleigh–Taylor and thermocapillary instabilities can be ignored. Introducing molten layer thickness, the spatial extent and kinetic energy density in the laser-produced plasma plume, Kelvin–Helmholtz instability was found to be a viable mechanism for the rippling formation.
5. *Rayleigh–Taylor instability.* The Rayleigh–Taylor instability occurs if the density of the overlying fluid is greater than the underlying fluid subject to gravitational force in the downward direction [85]. The instability also occurs in a reference frame of the melt experiencing acceleration because of its indistinguishableness from a gravitational body force. Bennett et al. [86] observed surface topography of gold experiencing sputtering subject to 248 nm laser pulses at near-threshold fluence. The development of surface topography was identified with a hydrodynamic response to phase change occurring at the surface of the target, as a consequence of Rayleigh–Taylor instability. The melt acceleration can be estimated from phase change across the liquid-solid interface, which was an order of magnitude greater than acceleration due to thermal expansion of solid. The acceleration and its direction toward the solid depended on the change in densities between liquid and solid. With the melt acceleration of around 10^8 m/s^2 for gold, the most dangerous wavelength agreed with the period of around 5 μm of topography formation. Seifert et al. [87] applied finite difference method together with MAC (Marker-and-Cell) scheme to solve linearized Navier–Stokes equation and heat conduction with phase changes. The estimations and concepts from Bennett et al. [86] were confirmed. In pulsed laser-material interactions with target surface, Lugomer [88] proposed that different surface structures can be generated from a shock-accelerated fluid. That is, the Richtmyer–Meshkov instability develops when a plane shock wave interacts with a corrugated contact interface between two different fluids. It can also be arisen from fast mixing of gases at the contact front between the plasma plume and ambient medium. Surface structures thus depended on the target material and laser parameters, such as power density, wavelength, pulse duration, and polarizations via Richtmyer-Meshkov instability. Figure 5(*a*) shows that a generation of Richtmyer–Meskhow environment in the laser spot on an indium target surface. The surface is vaporized and the melted layer has a slightly concave shape. Incident flux causes that the melted surface layer comprises a high-temperature, high-velocity, low-density (ρ_1) top layer, and a lower temperature, slow, high-density (ρ_2) bottom layer. The layers are separated by the density interface, delineated by a black curve. Figure 5(*b*) shows the density perturbed by the blow-off during pulsed vaporization. The perturbation amplitude is larger in the central zone and gradually decreases toward the peripheral zone. The shock wave generated in the center moves toward the periphery of the spot and strikes tilted and periodically perturbed interface, causing the vorticity deposition, as shown in Fig. 5(*c*). Vorticity evolution and roll-up in the near field zone behind the shock which travels toward the periphery are shown in Fig. 5(*d*). By the end of pulse, the ultrafast cooling wave, which is generated at the periphery and moves in opposite direction (toward the center), causes surface structures to stay frozen permanently. The surface structures frozen in the far field zone are the wavy structures, which belong to the vorticity deposition. The structures near the central, or the near field zone belong

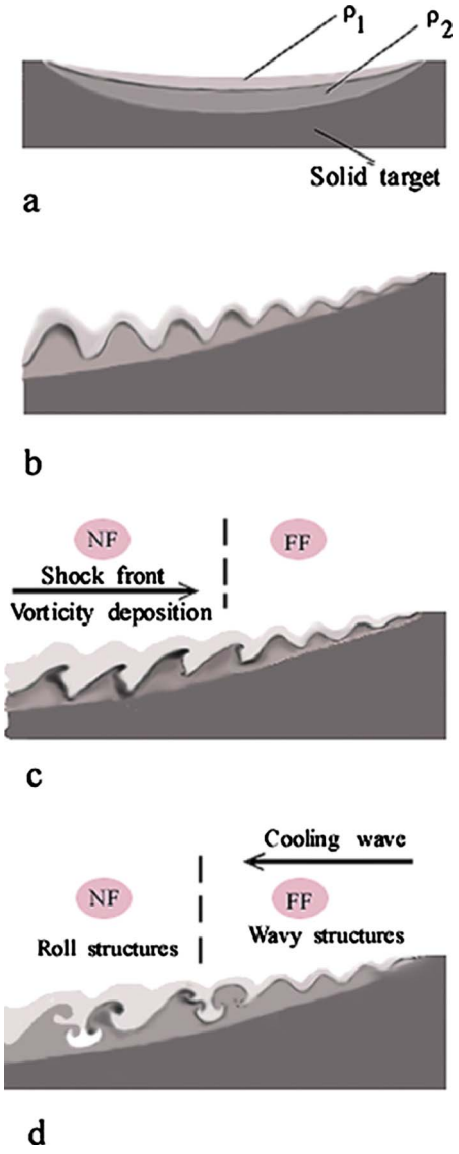

Fig. 5 Scenario of Richtmyer–Meskhow environment in the laser spot on an indium target surface: (*a*) melted surface with slightly concave shape. The melted surface layer comprises high-temperature and velocity, low-density top layer, and a lower temperature, slow, high-density bottom layer, separated by the density interface (black curve); (*b*) the density perturbed by the blow-off during pulsed vaporization; (*c*) the shock wave generated in the center moves toward the periphery and strikes tilted and periodically perturbed interface, causing the vorticity deposition; (*d*) vorticity evolution and roll-up in the near field zone behind the shock. By the end of pulse, the ultrafast cooling wave generated at the periphery moves toward the center, causing that surface structures to stay frozen permanently in the wavy structures [88].

to the late, and the very late phase of the vorticity evolution. Their evolution started first and stopped last.

6. *Instability due to evaporation.* Surface rippling induced by instability from recoil pressure due to evaporation may cause rippling [89–91]. For example, Emel'yanov et al. [90] studied the formation of periodic surface ripples on fused silica under normal incidence of a pulsed linearly polarized wavelength-tunable CO_2 laser. It showed that the formation of periodic surface ripples was the generation of capillary wave in the liquid owing to vapor recoil pressure and nonuniform removal of the substance by evaporation. They also concluded that good agreement between experimental and theoretical results can be achieved, if electrodynamic and thermal processes, and calculation of growth rates of capillary waves were accounted.
7. *Solidification morphological instability.* Surface roughness may be induced by the morphological instability, which was originated from constitutional supercooling and mathematically extended by Mullins and Sekerka [92] by including surface tension and deformation of the solidification front. Constitutional supercooling as first found by Rutter and Chalmers [93] takes place for the interfacial temperature below the melting temperature due to solute accumulation ahead of the solidification front. Bösch and Lemons [94] reported that on heating of silicon with a laser, the heated area were melted and broken up into small regions of solid and liquid, leading to undesirable surface roughness on the surface. The inhomogeneous melt gave rise to melting instabilities from constitutional supercooling. Weizman et al. [95] observed a periodic structure on the surface of a silicon-germanium thin film irradiated by a pulsed laser beam. The planar shape of the moving solid-liquid interface was broken down into a periodically modulated interface and caused a cellular structure with a high dopant concentration on the cell wall. Based on the Mullins–Sekerka theory to elucidate the critical Ge content, the periodic length of the self-organized structure was found to be a function of solidification velocity. At the final stage, the SiGe liquid piled up in the last area to solidify due to the trapping of capillary waves between the coalescing solid boundaries. However, constitutional supercooling was not an adequate mechanism to explain weld ripples, since ripples were formed on welds in 99.9999+% purity aluminum [72]. Surface roughness of an order of a microscale may be also affected by evaporatively driven supersaturation that allows fluctuations of the solid-liquid interface to grow in a manner qualitatively similar to the growth of the solid-liquid interface induced by above-mentioned constitutional supercooling [96].
8. *Laser interactions.* The effects of laser characteristics such as ultrafast pulse (for example, a duration of 10 fs), wavelength, and polarizations and their interactions on rippling spacing (less than 1 μm) on workpiece surfaces should be accounted in welding or microwelding [97,98]. The rippling spacing induced by hydrodynamics instabilities, as discussed previously, is much greater than the laser wavelength. Furthermore, a purely hydrodynamic or thermal analysis is unable to explain the preferential orientation of laser-induced periodic structures in a direction perpendicular to the incident laser polarization, and having pattern spacing in scale with the laser wavelength [99,100]. Rather than previous discussion for high energy melting the surface widely, the laser fluence in this case is only sufficient to melt the surface locally. Preferential orientation of laser-induced periodic structures was first observed in semiconductor materials irradiated with a Q-switched ruby laser by Birnbaum [100] and, since then, ripples have been observed in homogeneous dielectrics [101] and semiconductors and metals [102]. The constructive and destructive from interference of the incident laser beam with surface scattered laser beam creates high- and low-density energy fields and a periodic modulation of the temperature near the surface, giving rise to lateral liquid flow or differential ablation and inducing ripples about laser wavelength on the molten surface. The rippling can also be initiated by the scattering of a small amount of light out of the primary laser beam by random variations in surface height, defect density, or any other optically significant physical properties, and circularly and linearly polarized light [103]. For metals or molten semiconductors surfaces, which may support plasma waves, or thin film surfaces, which may support guided surface waves, their ripple period strongly depends on the electromagnetic or waveguiding properties of the surface. Provided that the primary laser beam is away from normal incidence, the spontaneous surface structures split up into complex ripple patterns showing multiple periodicities in either overlapping or separated regions of the surface. In the laser beam polarized with electric field in the plane of incidence, the ripples break up into two distinct spacing with periods in different directions given by

$$\lambda_{\mathrm{rip}} = \frac{\lambda_{\mathrm{L}}}{\mathrm{n}(1 \pm \sin \phi_{\mathrm{i}})} \tag{2}$$

which can be simply derived from the grating theory. An atomic force microscopy image of rippling structure on silicon surface irradiated by a p-polarized laser beam, provided by Pedraza et al. [104], is shown in Fig. 6(*a*). It shows a very regular grating produced by 400 pulses at a laser fluence of 0.8 $\mathrm{J/cm^2}$ with irradiation just off normal incidence. This ripple structure has a wave vector parallel to the projection of the electric field, and its wavelength equals the laser wavelength, viz., 248 nm. This result is consistent with the value that is calculated assuming a scattered wave in reflection from Eq. (2). In the case of nonzero incident angle, the averaged rippling spacing is of the right order of magnitude as two distinct spacing based on two incident angles within an allowable range owing to optical spread through its focus. Atomic force microscopy image of surface structure irradiated by a laser fluence of 0.7 $\mathrm{J/cm^2}$ at 50 pulses using a p-polarized single beam at an incident angle of 38.5 deg with a rippling spacing 673 nm is shown in Fig. 6(*b*). Notice tiny little "fingers" in lower rim of fringes and asymmetry in fringe profile taken in downward direction [104].
9. *Fluid flow related phenomena.* Instability analysis is a valuable and efficient tool to predict tendency for rippling formation. However, quantitative prediction of surface roughness needs to solve the evolution equation or original fluid flow and heat transfer equations. Anthony and Cline [105] were the first to propose a simplified integral model or evolution equation to study rippling resulted from thermocapillary force in the laser melting of stainless steel 304. In the case of a negative surface tension coefficient, the surface flow is outward, resulting in the liquid at the back of the pool to climb and produce a raised section upon solidification. By assuming liquid pressure to be hydrostatic and ignoring capillary pressure, the elevation of the edge of the molten pool was found to be proportional to temperature difference across the free surface and surface tension coefficient, and inversely proportional to hydrostatic pressure or the depth of the liquid layer at the edge. The liquid pressure, however, can be significantly deviated hydrostatic pressure by strong thermocapillary flow with velocity of around 1 m/s in a millimeter width of the pool. If the scanning speed exceeded a critical velocity, the liquid does not have sufficient time to form ripples, and rippling from thermocapillary force can be avoided. This agreed with observation from Glicksman and Schaefer [106], Ryzhkov et al. [107], and scale analysis from Wei et al. [15]. Thermocapillary force plays an important role in welding as can be seen from a

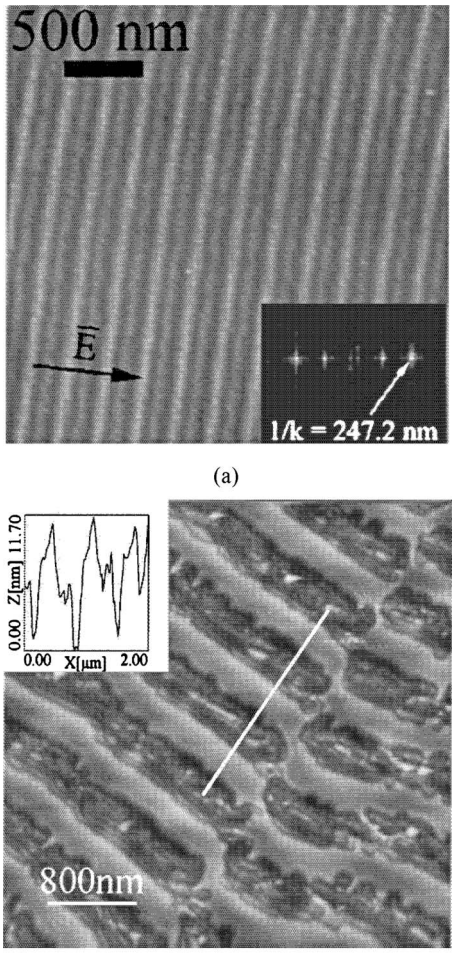

Fig. 6 Atomic force microscopy images of rippled structure (*a*) generated at near normal incidence with 400 pulses of a single beam of p-polarized light at a fluence of 0.8 J/cm^2. The direction of the projected electric field of the electromagnetic wave is also indicated and (*b*) irradiated by 50 pulses at a laser fluence of 0.7 J/cm^2, using a p-polarized single beam and incident angle of 38.5 deg. Notice tiny little "fingers" in lower rim of fringes and asymmetry in fringe profile taken in downward direction [104].

scaling of Eq. (1). The scaled velocity due to thermocapillary force was

$$u_c = \left[\left(\frac{d\gamma}{dT} \frac{\Delta T}{\mu} \right)^2 \frac{\mu}{\rho w} \right]^{1/3} \quad (3)$$

which was originally and successfully derived by Ostrach [108] and used by Chen [109] for dealing with manufacturing processes. Equation (3) was derived by considering inertia and viscous forces, and thermocapillary force and viscous stress in the surface shear layer to be of the same order of magnitude. Substituting typical values $d\gamma/dT = -10^{-4}$ N/m K, temperature difference $\Delta T = 10^3$ K, and width $w = 10^{-3}$ m of liquid metal pool gives the maximum surface velocity around 1 m/s, which is about the measured velocities in EBW [1,110], LBW [111,112], GTAW [75,113], and predicted values in GMAW [19,114], GTAW [115–117], EBW [47], and LBW or laser beam heating [118–122]. Thermocapillary force thus cannot be ignored. Wei et al. [15] recognized that deformation of the free surface near the solidification front is responsible for the formation of rippling. Wei et al. [15,17] therefore accounted for the shear layer driven by thermocapillary convection from the center to edge of the pool to predict spacing and amplitude of ripples on pure metals and alloys having negative surface tension coefficients, and alloys containing surface active solute having positive surface tension coefficient, respectively. The algebraic expressions provided for the rippling space and amplitude were for the first time found to be functions of incident flux, surface tension and its coefficient, thermal and fluid transport properties, free surface deformation, and solidification rate near the edge of the pool. The predicted roughness agreed well with experimental data. Schwarz-Selinger et al. [123] observed and measured morphologies of Si surfaces irradiated by single, tightly focused nanosecond laser pulses. They also proposed a simplified liquid layer flow model driven by thermocapillary force and neglecting the variations of liquid and capillary pressures and inertia force and end effects of the pool. It was found that time-averaged morphology agreed quite well with the prediction. The scaled peak-to-peak roughness of dimples can be of the fourth power of incident flux, after replacing the film thickness by a linear relationship with incident flux. Balandin et al. [124] measured and computed solute segregation, and attributed rippling formation as a result of impurity- and temperature-dependent thermocapillary forces. Röntzsch et al. [125] also numerically confirmed that long-range-ordered regular surface patterns on thin polymethyl methacrylate films above a metallic substrate were dominated by thermocapillary force induced by standing surface-plasmon-polariton waves.

Humping and undercutting. Bradstreet [18] used a high speed camera to observe humping and undercutting phenomena, associated with the formation of a cavity at the front of the weld and flow from the front to the rear of the pool in GMAW. The flow of the pool was composed of three streams, which were one from the filler metal and two from the base metal flowing around the sides of the pool. A more clear video observation of humping in GMAW from Nguyen et al. [58] is shown in Fig. 7(*A*). Since humping phenomenon is periodic in nature, Fig. 7(*A-a*) a began at the completion of a previous hump. A portion of the weld, connecting the previous swelling and the new tail of the weld pool, had completely solidified, although the upper region of the previous swelling was still molten. Prior to solidification, this portion of the weld was part of the wall jet that supplied the swelling with molten weld metal. In Fig. 7(*A-b*), at the tail of the weld pool, the molten weld metal accumulated to form a new swelling. The wall jet became elongated over an ever increasing distance between the forward moving welding arc and the stationary swelling. Rapid solidification of the wall jet would choke off the flow of molten metal to the swelling. As indicated in Fig. 7(*A-b*) and Fig. 7(*A-c*), the bright region of solidified metal increased in height as the solidification of the molten weld metal proceeded upwards. The wall jet solidified completely, as shown in Fig. 7(*A-d*). Solidification of the wall jet formed the valley typically observed between swellings in a humped GMA weld bead. This was soon followed by the initiation and growth of a new swelling closer to the arc and further along the weld bead (Fig. 7(*A-a*)).

Fluid flow and heat transfer for humping during a pulsed GMAW at a high travel speed were numerically and quantitatively simulated by Cho and Farson [19]. The humps resulted from backward fluid flow induced by the arc pressure and the drop momentum redirected by the sloping edge of the gouged region at the front of the weld pool. Two mechanisms responsible to the hump formation were identified. The first requirement was for a thin liquid channel generated by elongation of the molten metal deposit. The high transverse curvature associated with a narrow, thin channel caused a strong surface tension normal force that prevented backfilling of metal from any accumulation at the back of the pool. The other requirement for hump formation was pinching

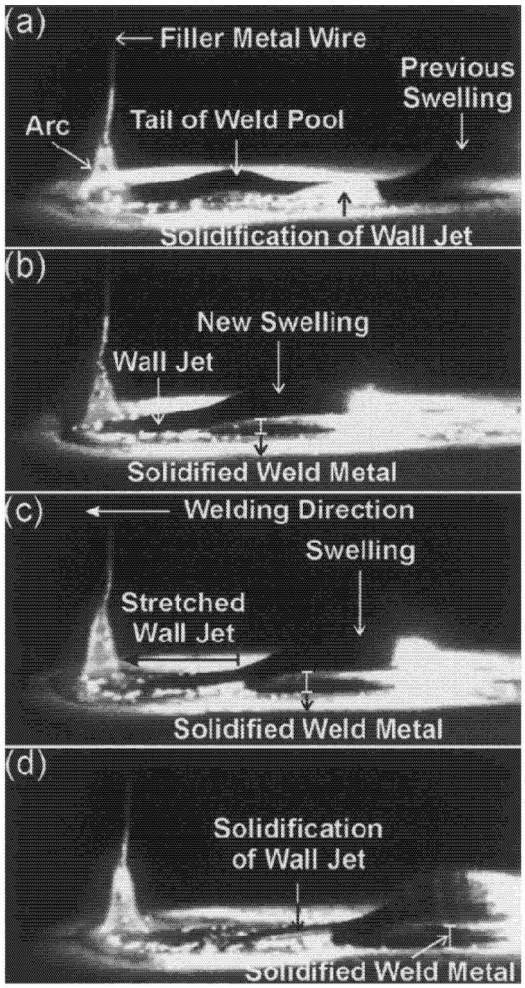

(A)

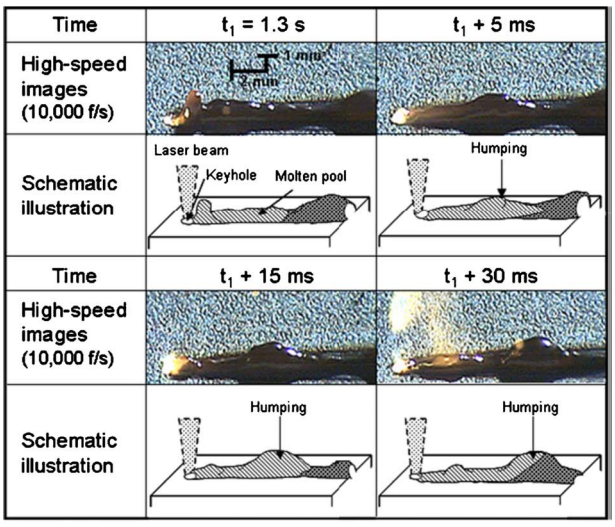

(B)

Fig. 7 Video observation of humping: (*A*) GMAW [58] and (*B*) LBW [44]

and rapid solidification of the thin channel, dividing the molten pool into front and rear sections. Usually the first hump that occurred was a bulged hump. Subsequent humps were either bulged or elongated. If the backward flow rate was not as high, elongated humps were usually formed after the first hump. The slope of the leading edge of a gouging region efficiently redirects the downward momentum of incoming droplets toward the back of weld pool, increasing the velocity of the backward fluid flow. A gouged region also helps to constrain the melt deposit laterally, which promotes hump formation. Hu et al. [114] provided an elaborate three-dimensional computation to simulate interactions between droplet impingement, electromagnetic force, plasma arc force, and Marangoni effects on transient pool shape, temperature, velocity, and species distributions in GMAW. It showed that the pool was opened as a result of droplet impingement, and its close-up was caused by liquid pressure. Rippling or humping was affected by complicated periodic impingement of droplets, weld pool dynamics, and solidification.

High-speed video observation images of the humping in molten pool in LBW are shown in Fig. 7(*B*) [44]. The molten pool had a narrow width of about 2 mm. A humping was gradually formed at the rear end of the molten pool rather than at the laser-irradiated position. The humping appeared to be caused by superimposed production of melt back flow accompanied by laser-induced plume and higher surface tension induced by the narrow molten pool width. Detailed descriptions of swelling of the pool were also extensively provided by Arata et al. [126] and Irie et al. [127] in electron beam keyhole welding.

Humping mechanisms summarized by Soderstrom and Mendez [37] include the Marangoni, compound vertex, hydraulic jump, capillary instability, and arc induced humping models. They were, respectively, referred to convection induced by Marangoni force, vortex flow induced by surface tension and electromagnetic forces, flow beyond a critical velocity due to hydraulic jump phenomenon, instability induced by surface tension, and flow induced by arc pressure balanced by capillary and hydrostatic pressures. Nguyen et al. [49] also proposed humping resulted from Rayleigh jet instability, arc pressure, supercritical flow, and curved wall jet models. In fact, capillary instability model is Rayleigh jet instability, hydraulic jump is related to supercritical flow, and arc induced humping is arc pressure models. The enhanced backward flow caused by the curved wall jet is solely a consequence of the impact of the filler droplets in GMAW. Mechanisms of humping and undercutting are described as follows:

1. *Rayleigh's capillary instability.* The Rayleigh's instability theory is referred to instability of a thin free liquid cylinder. As time proceeds, such a column develops corrugations in its shape and ultimately breaks into discrete drops. In view of apparent similarities between capillary jet instability and humping phenomenon, Bradstreet [18] proposed for the first time that humping could be explained by Rayleigh's capillary instability during GMAW. He considered internal pressure being inversely proportional to radius of a cylinder to balance surface tension in the Young–Laplace equation. Since the onset of Rayleigh's instability was when the wavelength of a disturbance imposed upon the cylinder exceeded its circumference, he therefore suggested that humping occurred due to breakage of the cylindrical liquid metal and its premature solidification when the length of the weld pool exceeded this critical length. This relation, however, is purely geometrical and independent of surface tension of the liquid. Gratzke et al. [128] extended the Rayleigh's instability analysis to find the conditions at the contact line along the edge of a liquid deposit and determine whether humps form. If a molten bead on a surface satisfies the wetted condition, meaning that the internally measured contact angle is less than $\pi/2$, it is not susceptible to hump formation by capillary instability with the critical length

$$L_R = 2\pi\bar{R}/\sqrt{1-\left(\frac{\pi}{2(\pi-\phi_0)}\right)^2} \quad (4)$$

However, in the welding application, the wetting and spreading of molten metal is controlled not only by surface energies at the interface of liquid, solid, and gas phases but also by heat transfer and phase transformation [129]. That is, the spreading of molten metal is arrested when the metal freezes. Therefore, the humping phenomenon during the high speed welding process is not fully explained by capillary instability. Albright and Chiang [29] used Rayleigh's capillary instability to successfully predict the onset of periodic hole formation in LBW, even though liquid velocity was the welding speed, cylinder area was the cross-sectional area of the weld, temperature was uniform and no solidification took place. It is interesting to find that the parallel humping and bead cylinder morphologies are inverse phenomenon (see Figs. 2(*b*) and 2(*c*)).

2. *Kelvin–Helmholtz instability.* Tytkin et al. [130] theoretically studied the mechanism of a coarse flaky surface of weld pool under high power conditions. The pressure component that coincided in phase with the profile of the surface became so high that the free surface changed from the static to wavy states. This is Kelvin–Helmholtz instability. The instability of the front wall on the side of the tail part of the pool induced waves on the surface, which reached the solidification front and formed a coarse flaky structure of the weld structure. By ignoring shear stresses and pressure component in phase with the slope of the wave and assuming aerodynamic pressure being proportional to displacement of the free surface, periodic solutions of Young–Laplace equation was found. Kumar and DebRoy [131] proposed a more appropriate and general model to predict the onset of humping based on Kelvin–Helmholtz instabilityin GTAW. Gas and liquid pressures required in Young–Laplace equation were determined by solving complete fluid equations, by accounting for different densities of the shielding gas and molten metal, weld pool size, shear stresses, surface tension, and thermocapillary force of the molten metal. The shielding gas velocity was calculated from an analytical relation. The predicted critical welding speed for humping versus arc current for different shielding gases, electrode tip angles, and low ambient pressures agreed quite well with experimental results available in the literature.
3. *Hydraulic jump.* Shimada and Hoshinouchi [39] proposed that the theory of hydraulic jump was responsible for formation of humping (see Fig. 3(*B*)). It can be seen that humping is a consequence of a jump of a weld pool at the rear. The hydraulic jump is similar to the pipe expansion, kitchen sink, or a vertical liquid jet impinging on a horizontal surface and spreads out radially on the surface. Hydraulic jump has two types of states depending on the depth of liquid in the downstream region, as illustrated in Figs. 8(*a*)–8(*c*) [132]. Type I jump is the standard circular hydraulic jump in which the flow near the free surface is radially outward, whereas the interior flow exhibits a recirculating region just downstream of the jump. Type IIa jump is similarly marked by a subsurface "separation bubble," but also by a region of reversed surface flow adjoining the jump. As the outer depth increases further, the jump transforms into Type IIb jump marked by a tiered or "double-jump" structure. If flow rate is high, the jumps become irregular in time and space. In view of a thick molten layer and strong back flow, humping takes place in the rear of weld pool [39]. Figure 9 shows the etching of regular holes in Mo films with an Ar^+ laser beam immersed in Cl_2 atmosphere [133,134]. It can be seen that a "starlike" or finger structure develops as well as the number of rays increases with increasing laser power. Due to the strong eject of liquid flow, hydraulic jump seems to play an important role in humping formation. Mathur et al. [135] experimentally found that in the absence of gravity a hydraulic jump can be created by surface tension in spreading submicron molten metal droplets created by pulsed laser ablation. A careful control of initial conditions leads to solid femtoliter cups of gold, silver, copper, niobium, and tin.

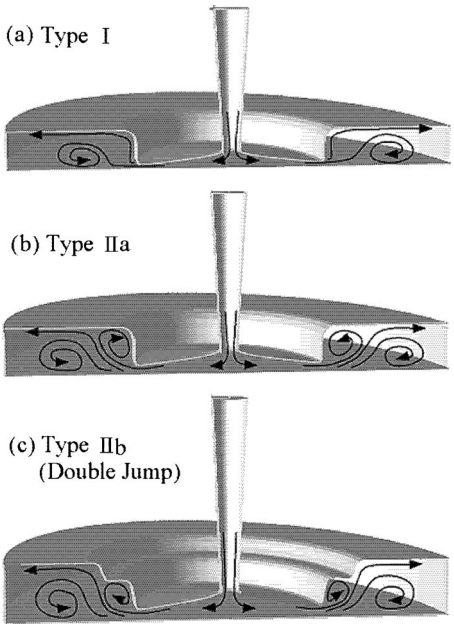

Fig. 8 Schematic sketch for two states in hydraulic jump [132]

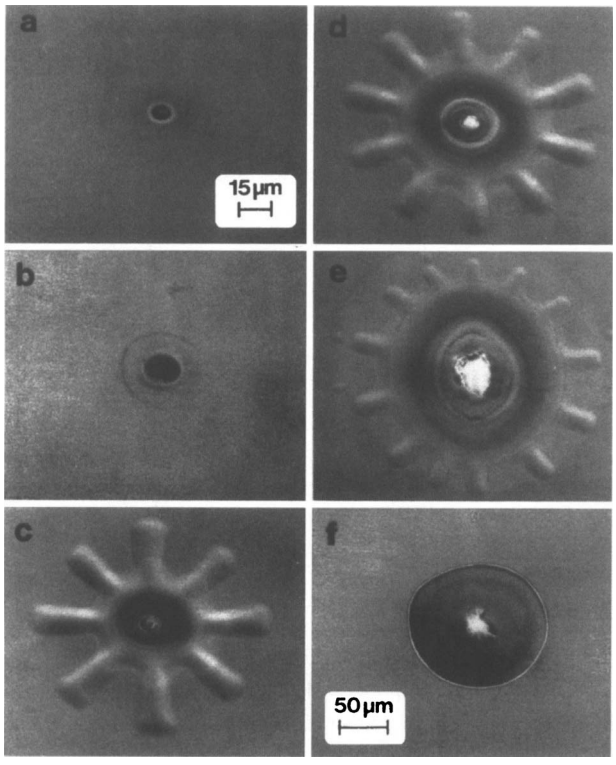

Fig. 9 Photographs of a "starlike hole" in etching Mo films with an Ar^+-laser in Cl_2 atmosphere with powers (*a*) 10 mW, (*b*) 20 mW, (*c*) 50 mW, (*d*) 100 mW, (*e*) 500 mW, and (*f*) 150 mW [133,134]

4. *Fluid flows.* Many theories have been proposed to interpret humping formation strongly affected by convection. Paton et al. [25] and Mendez and Eagar [38] proposed a theory of arc induced humping based on the pressure under heating ranges of the arc. Nguyen et al. [58] proposed a curved wall jet model to describe humping. Humping resulted from strong back flow of the liquid layer enhanced by the redirected filler droplets after hitting the sloping leading edge of the weld pool. Lin and Eagar [136] explained humping by a compound vortex theory based on electrically driven rotational flow. Mills and Keene [11] proposed that humping resulted from Marangoni force. High sulfur steel has a positive surface tension gradient that induces inward fluid flow on the weld pool surface. This flow elevates the pool surface at the center and depresses it near the edge, being susceptible to hump formation. Undercutting, however, would not occur in the case of negative surface tension coefficient, which induces an outward surface flow. Apparently, a positive surface tension coefficient is not the only criterion for onset of humping. Finding the unified theory to interpret humping encountered in different welding and manufacturing processes is challenging.

3 Thermal Science Analysis of Surface Patterns

Rippling or humping is determined by the formation of capillary wave on the free surface, as mentioned previously. Under surface tension, the pressure differences created at a curve interface support deformation of the interface known as capillary wave. Mathematically speaking, it is governed by Young–Laplace equation

$$p_\ell - p_g = \gamma\left(\frac{1}{R_1} + \frac{1}{R_2}\right) \tag{5}$$

Any physical or chemical variables affecting pressures at the interface are responsible for capillary wave and rippling or humping formation. Hydrodynamic instabilities [80], such as thermocapillary instability, Kelvin–Helmholtz instability, Rayleigh–Taylor instability, and instability due to recoil pressure from evaporation, are, respectively, resulted from a change of dynamic pressures induced by surface tension difference along the free surface, velocities and densities across the free surface, and evaporation on the free surface. Therefore, the onset and mechanisms of instability are determined from perturbed Eq. (5) by substituting perturbed liquid and gas pressures, obtained by solving perturbed fluid flow equations in the liquid and gas. However, if unsteady deformation of the free surface is of interest, an evolution equation derived from the kinematic condition of the free surface can be effectively used for prediction. The factors affecting surface patterns are briefly described as follows:

Kelvin–Helmholtz instability. Kelvin–Helmholtz instability is the simplest and widely encountered instability, derived from Young–Laplace equation, where liquid and gas pressures are determined from Bernoulli's equation with specified constant liquid and gas velocities, $U_{\ell 0}$ and U_{g0}, far away the location considered. Since the dominant forces are inertial and capillary forces, small deformation of the free surface can be effectively determined by scaling equation (A4),

$$p_\ell - p_g \approx \rho_\ell (U_{\ell 0} - c)^2 \frac{\eta_c}{h_{\ell 0}} + \rho_g (U_{g0} - c)^2 \frac{\eta_c}{h_{g0}} \sim \gamma \frac{\eta_c}{\lambda_{KH}^2} \tag{6}$$

Scale analysis is conducted by considering two dominant terms in an equation as the same order of magnitude. These terms are then evaluated or scaled by linear approximations [137]. Equation (6) shows that perturbed liquid and gas pressures are antiphase with small deformation ($\eta > 0$ for upward deflection in this work) of the free surface. Provided that deformation is toward the gas, the perturbed pressures are increased and decreased in the liquid and gas, respectively. This results in a further increase in deformation. In fact, perturbed pressure can also be in phase of the slope of deformation, giving instability, namely, Miles mechanism, from normal stress induced by viscous stress and sheltering effect on the lee side of a wave, respectively [138–141]. Instability induced by Miles mechanism therefore gives rise to short wave from weak wind, whereas Kelvin–Helmholtz instability raises longer waves from strong wind [142]. In the case of $h_{g0} \to \infty$, wave speed $c = U_{g0}$ to satisfy conservation of mass, as can be found from Eq. (A5). Provided that wave numbers in depth and horizontal directions $1/h_{\ell 0} \sim 1/\lambda_{KH}$, as proposed by Yih [143], the rippling spacing estimated from Eq. (6) is found to be

$$\lambda_{KH} \sim \frac{\gamma}{\rho_\ell (U_{\ell 0} - U_{g0})^2} \tag{7}$$

which is identical to the result from Hogan and Ayyaswamy [141]. Equation (7) indicates that wavelength of ripples due to Kelvin–Helmholtz instability reduces if the difference in velocities between gas and liquid increases. Provided that gas velocity is 10 m/s, the length for roughness in ordinary liquid metals is around 10 μm. It is within a relevant range of rippling spacing, as mentioned previously. Since velocity difference is of the second power, roughness induced by Kelvin–Helmholtz instability decreases rapidly. Kelvin–Helmholtz instability can be modified by heat and mass transfer, compressibility, and viscosity ratio between two layers [144–147].

Rayleigh–Taylor instability. The pressure involved in Rayleigh–Taylor instability is hydrostatic pressure, which is a function of gravitational acceleration and the depth location considered. The pressure difference induced by a surface deformation thus is given by

$$p_\ell - p_g = -(\rho_\ell - \rho_g) g \eta \tag{8}$$

Scaling $\gamma \partial^2 \eta / \partial x^2 \sim \gamma \eta_c / \lambda_{RT}^2$, Eq. (5) by substituting Eq. (8) or Eq. (A4) by ignoring inertial force, gives the surface roughness induced by Rayleigh–Taylor instability

$$\lambda_{RT} = \sqrt{\frac{\gamma}{g(\rho_\ell - \rho_g)}} \tag{9}$$

which is also the critical wavelength for onset of Rayleigh–Taylor instability [85,143]. Rayleigh–Taylor instability occurs when a heavier liquid overlies a lighter liquid subject to gravitational force in the downward direction. Provided that deformation is toward the lighter fluid, a positive perturbed pressure deviated from the base state results. A negative perturbed pressure simultaneously results from deformation toward the heavier liquid. Hence, deformation further increases. At later times, initial perturbations grow into spikes of heavier fluid "falling" into lighter fluid and bubble of the lighter fluid "rising" into the heavier fluid. Rayleigh–Taylor instability in the literature therefore has also been stated to occur when the pressure and density gradients are in opposite directions, or a lighter fluid pushes or accelerates a heavier fluid [148]. It can be seen from Eq. (9) that Rayleigh–Taylor instability depends on the direction of gravitational acceleration or relative positions between liquid and gas. Acceleration may be different from earth's gravity. In this case, gravitational acceleration in Eq. (9) is replaced by dv_i/dt. Rayleigh–Taylor instability can also occur at a material interface or an interface separating fluid of different densities through which a blast wave has been transmitted from a heavier to a lighter fluid. In this case, the instability induced by an impulsive interface is Richtmyer–Meshkov instability, as mentioned previously [149,150]. Hence, Richtmyer–Meshkov instability is often referred to as impulsive or shock-induced Rayleigh–Taylor instability. The interface deformation containing spikes and bubbles can be predicted from the kinematic condition and Bernoulli's equation subject to an impulsive force [151]. In high intensity welding or other manufacturing processes, high energy produces shock waves propagating with discontinuities of densities, pressures, and velocities in different

magnitudes and directions. Provided that an interface between two fluids subject to an oblique shock, it will give rise to complicated evolution of perturbations at the interface. The normal component of the shock generates Richtmyer–Meshkov instability, and the parallel component generates Kelvin–Helmholtz instability. If a constant normal acceleration is also present, it induces Rayleigh–Taylor instability, depending on the sign of gravitation force and difference in densities between two fluids. Accounting for interactive mechanisms affected by an oblique shock can refer to analytical description by Mikaelian [152]. Rayleigh–Taylor instability can be modified by Marangoni force, heat and mass transfer, compressibility, and phase change [145,153,154]. Piriz et al. [155] interestingly applied Newton's second law for an intuitive and physically appealing explanation of the physical mechanisms underlying Rayleigh-Taylor instability affected by surface tension and viscous stresses.

Rayleigh's capillary instability. Rayleigh's capillary instability is a crucial factor to understand a bulged region of humping or gouging. The gouged region exhibits an inverse feature of the bulged region (see Fig. 2(*a*)). Rayleigh's capillary instability can be derived from Young–Laplace equation evaluated at two locations,

$$p_A - p_\infty = \gamma\left(\left.\frac{\partial^2 \eta}{\partial x^2}\right|_A + \frac{1}{r_A}\right), \quad p_B - p_\infty = \gamma\left(\left.\frac{\partial^2 \eta}{\partial x^2}\right|_B + \frac{1}{r_B}\right) \tag{10}$$

where terms on the right-hand side of the equality sign are surface tension induced by two principal curvature. Subtracting between Eq. (10) leads to

$$p_B - p_A \approx \gamma\left(\left.\frac{\partial^2 \Delta}{\partial x^2}\right|_A - \frac{\Delta}{r_A^2}\right) \tag{11}$$

where amplitude of humps $\Delta \equiv \eta_B - \eta_A = r_B - r_A$. Radius r_B is at a location B near the minimum radius r_A. The first term on the right-hand side of Eq. (11) evaluated at location A thus is positive, whereas the last term is a fixed value. Provided that the wavelength of surface deformation is short, this leads to a higher positive curvature and higher positive value of the first term. The positive difference in pressures between p_B and p_A thus induces a flow from locations of p_B to p_A and tends to restore the cylindrical form. The system therefore is stable. On the other hand, if the wavelength of deformation is large, the positive curvature of the first term on the right-hand side becomes small. The right-hand side may become negative. The flow thus is from location r_A to r_B, leading to an unstable system and breakup of the cylinder into droplets. Since the difference in pressures at two locations affects instability, the minimum wavelength for onset of instability is the balance between two components of capillary pressure. That is, two terms on the right-hand side of Eq. (11) must be of the same order of magnitude. This leads to $\lambda_{R\,min} \sim r_c$ [85]. Rayleigh's capillary wavelength λ_R can be estimated from radial momentum equation and kinematic condition of the free surface,

$$\frac{\partial w}{\partial t} \approx \frac{1}{\rho}\frac{\partial p}{\partial r} \quad \text{and} \quad w \approx \frac{\partial r_s}{\partial t} \tag{12}$$

which are scaled to give $t_c = r_c\sqrt{\rho / p_c}$. Liquid pressure can be scaled as γ / r_c from a normal stress balance with capillary pressure. Substituting scales of liquid pressure and $t_c = \lambda_R / u_c$, the critical length for instability yields

$$\lambda_R = u_c\sqrt{\frac{\rho r_c^3}{\gamma}} \tag{13}$$

which was first derived by Rayleigh [85] for $\lambda_{R\,min} \approx \lambda_R = r_c$. A liquid cylinder therefore is unstable and breaks up into a series of distinct droplets for a disturbance having wavelength greater than λ_R. The effect of surface active solute on Rayleigh's instability was also described in detail by Miller and Neogi [80]. Stability of a bead should also depend on the boundary conditions at its contact lines on the surface. Davis [156] derived a disturbance kinetic energy equation in a form of a damped linear harmonic oscillator equation to find sufficient conditions for stability of rivulet. It was found that like Rayleigh's liquid cylinder, the beads whose contact angle remains fixed at an equilibrium value while the contact lines are free to move, and the beads whose contact angle depends on the contact line speed, but reduces to an equilibrium value at zero speed are unstable for some disturbance wavelength. On the other hand, a perturbed bead whose contact lines are arrested in a parallel state, while the contact angle is free to change will be stable if contact angle is less than 90 deg. Schiaffino and Sonin [34] experimentally studied the formation and stability of small-scale beads of wax deposited onto a cold solid surface by sweeping a droplet stream over it. It showed that a molten bead forms with parallel contact lines which have been arrested by freezing while the bead itself is still largely in a liquid state, and that the still molten material is stable when the contact angle is less than 90 deg, and unstable when it exceeds 90 deg, consistent with Davis's theory. Gau et al. [157] experimentally found that cylindrical segments for water on hydrophilic stripes with the apparent contact angle less than 90 deg did not break up into droplets, as would be expected. It displayed long-wavelength instability where all excess fluid gathered into a single bulge on a hydrophilic stripe. Based on the finding of Gau et al., Speth and Lauga [158] theoretically confirmed their results by performing a linear stability analysis together with a collocation method to predict instability of the capillary flow in the inviscid limit on a surface. It was found that the cylindrical segment is linearly unstable if and only if their apparent contact angle is larger than 90 deg. The most unstable wavenumber for the instability—the one which was observed in an experimental setting—decreases to zero when the apparent fluid contact angle reached 90 deg. The creation of bulges in the experiment corresponded with a zero-wavenumber capillary instability [157]. The gouged region determined by viscous liquid layer flow and two components of capillary pressure, for example, can refer to apply an evolution equation with a thin film approximation and small-slope approximation to study breakup of a liquid film in a cylindrical capillary, respectively [159,160].

Morphological instability due to solidification. Temperature at the solid-liquid interface is governed by Gibbs–Thomson equation [161].

$$T_s - T_m = \frac{\gamma T_m}{\rho h_{s\ell}}\frac{\partial^2 \eta}{\partial x^2} + mC \tag{14}$$

where the slope of the liquidus line (m) is negative in a dilute solution. Equation (14) shows that interfacial temperature becomes lower than the normal melting temperature by surface tension effect associated with forward deformation of the interface and solute accumulation in the course of solidification. The net deviation of temperature and concentration profiles from the base state near the solidification front can be approximated as

$$T_s - T_m - mC \sim (G_T - mG_c)\eta_c \tag{15}$$

where the base temperature and concentration gradients are, respectively, positive and negative in the course of solidification. Surface curvature on the right-hand side of Eq. (14) is scaled as $\partial^2 \eta / \partial x^2 \sim -\eta_c / \lambda_M^2$, where the negative sign is introduced due to negative curvature for a positive deflection of the interface. Substituting Eq. (15) into scaled Eq. (14) gives

$$\lambda_M \sim \sqrt{\frac{\gamma T_m}{\rho h_{s\ell}(mG_c - G_T)}} \tag{16}$$

which is identical to the perturbation result from Kurz and Fisher [161]. Morphology of the interface thus becomes unstable by decreasing surface tension [92] and increasing constitutional supercooling (namely, $mG_c - G_T > 0$) [93]. Temperature and concentration gradients in Eq. (16) are implicitly affected by many factors

involving solidification rate, thermal conductivities, and convection [92,161]. In the case of evaporative driven morphological instability [96], solute supersaturation is induced by evaporation. Equation (16) thus is modified by replacing solute gradient $G_c = jC_{s\ell,0}/\rho D$ from satisfaction of one-dimensional solute conservation, where $C_{0,s\ell}$ is the solute concentration in the liquid on the solid-liquid interface at the base state.

Instability due to evaporation. Instability due to evaporation of a semi-infinite liquid heated below is susceptible to instability, as first studied with a linear stability analysis by Prosperetti and Plesset [162]. However, the liquid layer is heated from above ($dT/dz>0$) in welding and manufacturing processes. To study instability due to evaporation, Young–Laplace equations at a given location, and a location at the base state which is far away from the location considered, respectively, give

$$p_\ell - p_g = j^2\left(\frac{1}{\rho_g} - \frac{1}{\rho_\ell}\right) - \gamma\frac{\partial^2\eta}{\partial x^2}, \quad p_{\ell 0} - p_{g0} = j_0^2\left(\frac{1}{\rho_g} - \frac{1}{\rho_\ell}\right) \tag{17}$$

where the first terms on the right-hand side of equality sign represent evaporation or condensation at the location considered and base state, respectively. Subtracting between Eq. (17) and considering uniform gas pressure leads to

$$p_\ell - p_{\ell 0} \approx \frac{2j_0}{\rho_g}(j - j_0) - \gamma\frac{\partial^2\eta}{\partial x^2} \tag{18}$$

where perturbed evaporation rate can be determined by

$$j - j_0 = \left.\frac{dj}{dT}\right|_0 T_s' = \left.\frac{dj}{dT}\right|_0 \left.\frac{dT}{dz}\right|_0 \eta \tag{19}$$

The critical wavelength then can be found by scaling Eq. (18) and substituting Eq. (19)

$$\lambda_E = \sqrt{-\frac{\rho_g\gamma}{j_0 \left.\frac{dj}{dT}\right|_0 \left.\frac{dT}{dz}\right|_0}} \tag{20}$$

differentiating Eq. (18) after substituting Eq. (19) gives

$$\frac{\partial p_\ell}{\partial x} = \frac{2j_0}{\rho_g}\left.\frac{dj}{dT}\right|_0\left(\left.\frac{dT}{dz}\right|_0\frac{\partial\eta}{\partial x} + \left.\frac{\partial^2 T}{\partial x\,\partial z}\right|_0\eta\right) - \frac{d\gamma}{dT}\frac{\partial T_s}{\partial x}\frac{\partial^2\eta}{\partial x^2} - \gamma\frac{\partial^3\eta}{\partial x^3} \tag{21}$$

where three terms on the right-hand side, respectively, represent horizontal variations of pressure due to evaporation or condensation, thermocapillary force, and capillary pressure. For a liquid irradiated by an incident flux, temperature is highest at the free surface. Its base state is referred to an equilibrium temperature at the flat interface subject to a uniform mass transfer. As the free surface is disturbed, a deformation that is closer to the bottom surface than the flat surface is at a temperature lower than the equilibrium temperature, meaning that lower evaporation will take place at a location near the bottom surface than the base state (see Eq. (19)). On the other hand, a deformation away from the bottom surface leads to greater evaporation rate than that at the base state. Liquid pressure therefore is dropped from the surface crest to trough, as can be seen from the first term in the parenthesis on the right-hand side of Eq. (21). The induced flow from the crest to trough thus reduces surface deformation, leading to stability due to evaporation. On the contrary, a liquid heated from below is susceptible to instability due to evaporation [162]. However, the second term in the parenthesis of Eq. (21) reveals evaporation may induce instability subject to base temperature variation along the free surface. For typical welding process, the vertical gradient of the base temperature along the free surface increases in the outward direction $\partial^2 T/\partial x\,\partial z>0$ near the pool edge, as can be revealed from the isothermal fields in roughly spherical shape [115]. Provided that surface deformation is toward the bottom $\eta<0$, the temperature at the crest, which is close to the pool edge, can be lower than that at the trough. This is attributed to an increase in the vertical gradient of base temperature along the free surface in the outward direction. The positive value of the first term in the parenthesis thus can be overriden by a negative value of the second term. The decrease in pressures therefore drives the liquid from the trough to the crest and leads to instability. Zhang and Chao [163] observed polygonal tessellation for a liquid layer subject to evaporation and thermocapillary force, and cooling from below. Surface flow of the liquid was radially outward in any polygon. Instability thus was interpreted as a result of high evaporation, which reduced surface temperature near the edges of the polygons and gave rise to a further increase in thermocapillary flow. Formation of ripples and corrugations near the edge further increased evaporation, reduced surface temperature, enhanced thermocapillary flow, and gave rise to instability. In fact, an increase in surface temperature enhances evaporation rate (see Eq. (19)). As mentioned previously, instability due to evaporation and outward surface flow should be a an increase in positive vertical temperature gradient along the outward horizontal direction.

Thermocapillary instability. All pure liquid metals and alloys in the absence of surface active solutes, such as O, S, Se, and Te, have negative surface tension coefficient, $d\gamma/dT<0$. A negative surface tension coefficient induces an outward surface flow and shallow pool. Aperiodic instability resulted from thermocapillary force of a thin liquid layer heated from below was first found by Pearson [81]. In this instability vertical gradient of temperature ($dT/dz<0$) does not produce any macro flows. However, it can lead to thermocapillary instability [80]. Thermocapillary instability can be induced by either surface deformation [78] or thermocapillary flow beyond a critical Marangoni number [77]. Thermocapillary instability in the absence of the base flow can be revealed from an evolution equation of a liquid layer derived from Eq. (B5),

$$\frac{\partial\eta}{\partial t} = -\frac{1}{\mu}\frac{d\gamma}{dT}\left(\left.\frac{\partial^2 T'}{\partial x^2}\right|_{z=h_0} + \left.\frac{dT}{dz}\right|_{z=h_0}\frac{\partial^2\eta}{\partial x^2}\right)\frac{h_0^2}{2} \tag{22}$$

The terms on the right-hand side indicates that the horizontal variation of perturbed thermocapillary force is comprised of the horizontal variation of perturbed temperature gradient and curvature of surface deformation. The former can be related to the distribution of incident flux and deformation of the liquid layer. That is, its scaling gives $\partial^2 T'/\partial x^2 \sim (\eta/t\alpha)dT/dz$, as can be obtained from energy balance between horizontal conduction and vertical convection. The horizontal variation of perturbed temperature gradient for the first term on the right-hand side of Eq. (22) therefore cannot be neglected if surface deformation is large. Provided that surface deformation is slight, a liquid layer heated from below with a negative surface tension coefficient in most cases is unstable [80,81]. This is attributed to a more negative deformation rate $\partial\eta/\partial t$ for $\eta<0$, $\partial^2\eta/\partial x^2>0$ and $dT/dz<0$, as can be seen from the last term on the right-hand side of Eq. (22). Physically speaking, it is usually considered that an interface is displaced toward a hot surface [80]. Local temperature at the trough thus is hotter than other point on the deformed surface. This results in an outward lateral flow from the trough to crest along the interface. To conserve mass, liquid with high temperature flows upward from the interior to the surface of trough. Surface temperature at the trough thus further increases and enhances lateral surface flow from the trough toward crest. The system thus is unstable and aperiodic instability and cells occur. This well-accepted interpretation is incorrect. The perturbed vertical liquid velocity should be downward due to an increase in thermocapillary force and satisfaction of mass conservation, as can be seen from Eqs. (B2) and (B3). This leads to a further downward deformation of the surface, giving rise to instability, as indicated from Eq. (22) or (B5). On the other hand, the free surface heated from above subject to a negative surface tension coefficient may still

cause instability [164,165]. This is a consequence of strong surface deformation. Provided that the surface is strongly deformed toward the bottom ($\eta<0$), the first term on the right-hand side of Eq. (22) becomes more negative $\partial^2 T'/\partial x^2<0$, which can override the second term for positive curvature of surface deformation ($(dT/dz)\partial^2\eta/\partial x^2>0$). Referring to the last term on the right-hand side of Eq. (22) or the case similar to the mechanism provided by Pearson [81], thermocapillary instability also takes place near the edge of the molten pool, where $d\gamma/dT>0$ in the presence of surface active solutes subject to positive vertical temperature gradient. This is another reason responsible for serious roughness encountered in alloys having surface active solutes, as mentioned previously. The effects of pulsation of incident flux on thermocapillary instability were analytically studied by Smorodin et al. [166]. It has been known that the hydrodynamic disturbances are supported by the thermal waves on the free surface, which also affect the development of temperature disturbances. The disturbances of temperature during their growth uphold the disturbances of vertical velocity component on the upper boundary and maintain the surface deformation. Thermocapillary instability subject to a pulsed incident flux thus can be explained by the length ratio between the penetration depth of the hydrodynamic disturbances and depth of the molten pool. This length ratio can be estimated by $\delta/h\sim\sqrt{\mathrm{Pr}}\,\alpha/\omega h^2$, where the penetration depth of the hydrodynamic disturbances is scaled as the length for momentum diffusion ($\delta\sim\sqrt{\nu t}$) in a time scale ($1/\omega$) for the modulation of the incident flux. As $\mathrm{Pr}\to 0$, hydrodynamic disturbances supplied by incident energy exist in a very thin shear layer near the free surface in comparison with the molten pool depth. Hence, thermocapillary instability readily occurred by decreasing Prandtl number. A decrease in shear layer thickness and increase in molten pool depth are, respectively, responsible for thermocapillary instability induced by high and low frequencies of laser beam.

Thermocapillary edge flow. Deformation of the free surface near the solidification front is responsible for rippling formation. Deformation of a free surface near a wall can be predicted by Young–Laplace equation at two locations, which are away and near the edge of the pool surface,

$$p_0 - p_\infty = -\gamma\frac{\partial^2\eta_0}{\partial x^2}, \quad p_e - p_\infty = -\gamma\frac{\partial^2\eta_e}{\partial x^2} \tag{23}$$

Subtracting between these equations and scaling give

$$p_e - p_0 \sim \gamma_m\frac{a}{w^2} \tag{24}$$

where surface deformation ($\eta_e-\eta_0$) is scaled as the average amplitude of ripples (a) within a spatial extent scaled by the pool width. The pressure difference between two locations can be determined from Bernoulli's equation,

$$p_e - p_0 = (1 - K_{loss})\rho u_c^2 \tag{25}$$

where the loss coefficient is introduced to account for energy losses encountered near the pool edge or solidification front. Since the surface layer is expanded with velocities decreasing from 1 m/s to nearly zero in a short distance of 1 mm, and its direction is turned downward as the pool edge is approached, the loss coefficient is selected to be near unity. In the absence of wall, the loss coefficient is roughly zero. Substituting Eq. (25) into Eq. (24), the average amplitude of ripples is found to be

$$\frac{a\gamma_m}{\rho\alpha^2} = (1 - K_{loss})\left(\frac{u_c w}{\alpha}\right)^2 \tag{26}$$

Equation (26) together with Eq. (3) was first provided by Wei et al. [15] to successfully predict the average amplitude of coarse ripples as a function of working parameters. Equation (3) is the general expression for predicting the maximum surface speed induced by thermocapillary force [167,168]. Based on the maximum surface velocity of 1 m/s, pool width of 1 mm, and loss coefficient of 0.99, rippling amplitude predicted from Eq. (26) is around a reasonable value of 10 μm. The coarse rippling spacing thus is 10^{-4} m due to a relatively constant rippling spacing-to-amplitude ratio around 40 [15]. Rippling therefore takes place from a rapid decrease in thermocapillary surface flow and increases in liquid pressure and deformation of the free surface from the central to rear regions of the pool. The temperature difference in Eq. (26) can be replaced by incident flux from its balance with conduction at the free surface. In alloys containing a surface active solute, the surface tension is found to be [169]

$$\gamma = \gamma_m + c_\gamma(T - T_m) - R_g T\Gamma^{sat}\ln(1 + KC) \tag{27}$$

The predicted surface tension as a function of temperature for iron containing different surface active solute contents of sulfur and oxygen from Eq. (27) is shown in Fig. 10(*a*) [169,17]. It can be seen that surface tension decreases with increasing sulfur content. On the other hand, the surface tension coefficient is positive for low temperatures and high active solute content, whereas it becomes negative for high temperature. The importance of surface active solutes on the flow pattern and weld pool shape was first observed and proposed by Heiple and Roper [170]. The flow pattern in the presence of surface active solutes at high temperatures thus gives rise to an outward surface flow in the central region, and an inward surface flow near the solidification front, as sketched in Fig. 10(*b*) [17]. The flow pattern agreed with numerical predictions [171,172]. Inward surface velocity near the rear

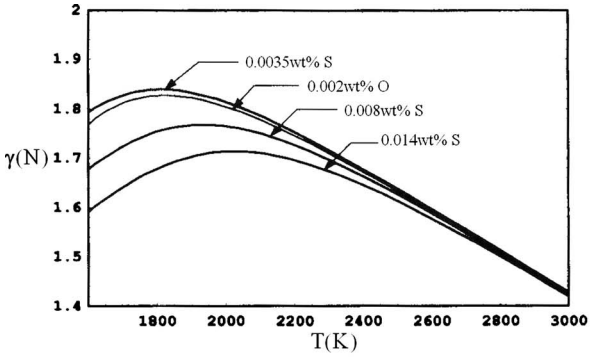

(a)

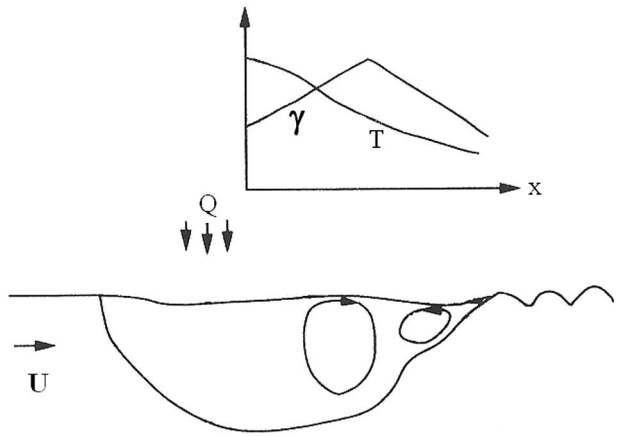

(b)

Fig. 10 (*a*) Surface tension as a function of temperature for different surface active solute contents of sulfur and oxygen in iron [169,17] and (*b*) schematic sketch of Marangoni convection in the presence of a surface active solute [17]

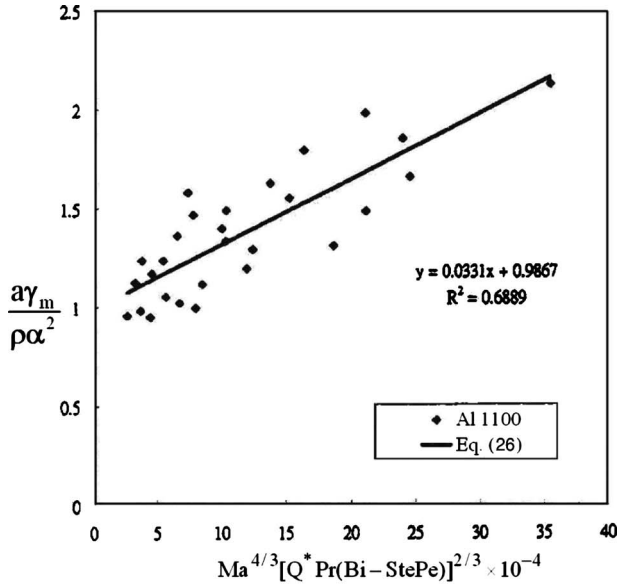

(a)

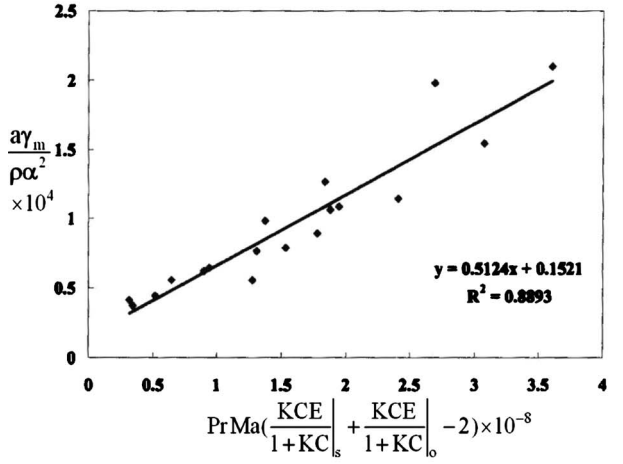

(b)

Fig. 11 Comparison between measured and predicted amplitude of ripples in EBW of (*a*) Al 1100 [15] and (*b*) alloys containing a surface active solute [17]

edge of a pool containing a surface active solute can be scaled and found to be [17]

$$u_c \sim \sqrt{\frac{d\gamma}{dT}\frac{\Delta T}{\rho w}} \tag{28}$$

Substituting Eqs. (27) and (28) into Eq. (26), rippling on alloys containing a surface active solute is found to be

$$\frac{a\gamma_m}{\rho\alpha^2} \sim Pr\,Ma\left(\frac{KCE}{1+KC}-1\right) \tag{29}$$

The scaled results from Eq. (26) together with Eq. (3), or Eq. (28) were found to agree with experimental data in welding Al 1100 or steels containing oxygen and sulfur, as shown in Figs. 11(*a*) and 11(*b*), respectively. As for humping in GMAW, GTAW, or keyhole welding, the liquid metal velocity at the surface is enhanced by liquid and gas pressures from the center or keyhole. Scaling surface speed therefore is complicated. A simple and practical way to simulate enhanced fluid flow and pressure is to introduce the

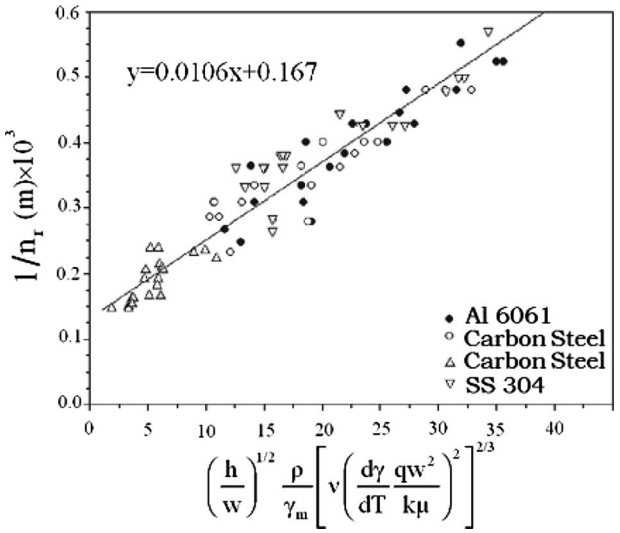

Fig. 12 Comparison between scaled and measured average pitches of humps or coarse ripples versus dimensionless parameter governing incident flux and surface tension coefficient of alloys in the absence of volatile elements [4]

depth-to-width ratio with a correlated power index [4]. They are, respectively,

$$u_c = \left(\frac{h}{w}\right)^n\left[\left(\frac{d\gamma}{dT}\frac{q}{\mu k_\ell}\right)^2\frac{\mu}{\rho}w\right]^{1/3} \tag{30}$$

$$p_e - p_0 \sim \gamma_m\frac{a}{w^2}\left(\frac{h}{w}\right)^m \tag{31}$$

In low-power-density beam welding where the fusion zone depth and width are roughly of the same magnitude, Eqs. (30) and (31) reduce to Eqs. (3) and (24), respectively. Introduction of the depth-to-width ratio with positive indices n and m implies that an increase in the fusion zone depth increases surface speed near the pool edge, and enhances humping. The effects of beam focusing characteristics and volatile elements on humping can also be accounted by choosing appropriate values of index n and m [4]. This is because an increase in the beam focusing characteristics and existence of volatile element increase gas and liquid pressures near the keyhole base [173] and increase liquid speed near the pool edge. The scale analysis is found to agree quite well with experimental data in welding stainless steel, carbon steels, and aluminum alloy, as shown in Fig. 12.

Laser interactions. This ripple structure strongly depends on incident angle, wavelength, and polarizations of a laser beam and optical properties of workpiece, as shown in Table 1 [99]. It shows that electromagnetic and thermal processes should be accounted for studying fine ripples in microscale. To determine heat transfer to rippled surface from a laser beam, Guosheng et al. [174] and Sipe et al. [175] assumed small and more or less random initial transverse variations in physical and electromagnetic properties of the illuminated surface. These transverse variations were then separated analytically into individual spatial frequency components or sinusoidal space gratings along the material surface. From grating diffraction theory, one can compute the diffraction of the primary laser by any spatial frequency components. The resulting total light intensity impinging on the surface can then be evaluated from superposition of the primary wave plus these scattered light waves. Brueck and Ehrlich [176] also analyzed the light intensity of a laser beam coupled with surfaces, which can propagate plasmon, polariton, or other guided surface wave caused by the same random initial disturbances in the surface properties. The interactions between polarized laser beams and

Table 1 Orientation and period of ripples. The mechanism considered is based on laser-induced evaporation [99,177].

Permittivity $\varepsilon=\varepsilon'+i\varepsilon''$	$\varepsilon'<-1$	$-1<\varepsilon'<0$	$0<\varepsilon'<1$	$\varepsilon'>1$
Type of grating	Normal	Anomalous	Anomalous	Normal
Orientation and period (s polarization)	$\mathbf{q}\parallel E_{ix}$, $\dfrac{\lambda_L}{\sqrt{n^{*2}-\sin^2\phi_i}}$	$\mathbf{q}\perp E_{ix}$, $0<q<k_i$	$\mathbf{q}\perp E_{ix}$, $\dfrac{\lambda_L}{\lvert\sqrt{\varepsilon'}\pm\sin\phi_i\rvert}$	$\mathbf{q}\parallel E_{ix}$, $\dfrac{\lambda_L}{\sqrt{n^{*2}-\sin^2\phi_i}}$
Orientation and period (p polarization)	$\mathbf{q}\parallel E_{iy}$, $\dfrac{\lambda_L}{n^*\pm\sin\phi_i}$	$\mathbf{q}\perp E_{iy}$, $0<q<k_i$	$\mathbf{q}\perp E_{iy}$, $\dfrac{\lambda_L}{\sqrt{\varepsilon'-\sin^2\phi_i}}$	$\mathbf{q}\parallel E_{iy}$, $\dfrac{\lambda_L}{n^*\pm\sin\phi_i}$

Note: $n^{*2}=1+(n+\kappa)^2/(n^2+\kappa^2)^2$ for $|\varepsilon|\gg 1$ with $\sqrt{\varepsilon}=n+i\kappa$, $n^{*2}=|\varepsilon'|/(|\varepsilon'|-1)\approx 1$ for $\varepsilon'<-1$ (surface electromagnetic wave).

rippled solid or liquid surfaces of metals and semiconductors, and dielectrics were extensively reviewed by Akhmanov et al. [177]. Following their coordinate systems, the z and y are, respectively, pointed into the workpiece and along the direction of wave vector or grating vector **q** of the rippled surface. If the first-order diffraction from a rough surface is taken into account, the electrical field outside the workpiece ($z<\eta(\mathbf{r},t)$, $\mathbf{r}=x\mathbf{i}+y\mathbf{j}$) is a superposition of the incident and reflected waves $\mathbf{E_i}$ and $\mathbf{E_r}$ with frequency ω, and two diffracted waves $\mathbf{E}'_\mathbf{s}$ and $\mathbf{E}'_\mathbf{as}$ with frequencies ω_s and ω_{as} and wave vectors $\mathbf{k_s}$ and $\mathbf{k_{as}}$, respectively,

$$\mathbf{E}=(\mathbf{E_i}e^{ik_zz}+\mathbf{E_r}e^{-ik_zz})\exp(ik_ty-i\omega t)+\sum_{\beta=s,as}\mathbf{E}'_\beta\exp(i\mathbf{k}_\beta\cdot\mathbf{r}+\Gamma_\beta z-i\omega_\beta t)+\ldots \tag{32}$$

where wave numbers k_z and k_t are the projections of the wave vector $\mathbf{k_i}$ ($k_i=\omega/c$) of the incident laser on the z axis and flat plane $z=0$, respectively, whereas index $\beta=s$, as stands for Stokes and anti-Stokes waves, respectively. On the other hand, the electrical field inside the workpiece ($z\geq\eta(\mathbf{r},t)$) is the sum of the transmitted wave and two diffracted waves,

$$\mathbf{E}=\mathbf{E_t}\exp(ik_ty-\gamma z-i\omega t)+\sum_{\beta=s,as}\mathbf{E}_\beta\exp(i\mathbf{k}_\beta\cdot\mathbf{r}-\gamma_\beta z-i\omega_\beta t)+\ldots \tag{33}$$

Frequencies, wave vectors, and wave numbers of electrical fields in Eqs. (32) and (33) are

$$\omega_s=\omega-\Omega_q,\quad \omega_{as}=\omega+\Omega_q,\quad \mathbf{k_s}=\mathbf{k_t}-\mathbf{q},\quad \mathbf{k_{as}}=\mathbf{k_t}+\mathbf{q}$$
$$\gamma^2=k_t^2-k_i^2\varepsilon,\quad \gamma_\beta^2=k_\beta^2-k_i^2\varepsilon,\quad \Gamma_\beta^2=k_\beta^2-k_i^2 \tag{34}$$

Equations (32)–(34) are automatically satisfied by Maxwell's equations. Amplitudes of electrical fields in Eqs. (32) and (33) are determined from continuities of tangential components of electric and magnetic field intensities at the rippled surface. After some mathematical manipulation, they are found to be

$$E_{tx}=\frac{2k_z}{k_z+i\gamma}E_{ix},\quad E_{ty}=\frac{-2i\gamma k_z}{k_t(k_z\varepsilon+i\gamma)}E_{iz},\quad E_{tz}=\frac{2k_z}{k_z\varepsilon+i\gamma}E_{iz} \tag{35}$$

$$\mathbf{E}_\beta=-\frac{2k_z(\varepsilon-1)}{\varepsilon\Gamma_\beta+\gamma_\beta}\eta_\beta\Xi(\mathbf{E_i}) \tag{36}$$

where $\Xi(\mathbf{E_i})$ is a function of the incident electric field and electrical properties. Rippling amplitudes $\eta_s=\eta_c$, $\eta_{as}=\eta_c^*$ where superscript "*" stands for complex conjugate. It is noted that a resonance can take place if the denominator of Eq. (36) is small. That is, for metals or semiconductors with permittivities $\varepsilon'<0$, $|\varepsilon'|\gg\varepsilon''$, and $|\varepsilon'|\gg 1$ the part in front of function $\Xi(\mathbf{E_i})$ in Eq. (36) can be approximated by

$$\frac{k_i(\varepsilon-1)}{\varepsilon\Gamma_\beta+\gamma_\beta}\approx\frac{k_i}{\sqrt{|\varepsilon'|}(\Delta k_\beta-i\Gamma_p)} \tag{37}$$

where

$$\Delta k_\beta\equiv k_\beta-\sqrt{\frac{|\varepsilon'|}{|\varepsilon'|-1}}k_i\approx k_\beta-k_i,\quad \Gamma_p\equiv\frac{k_i\varepsilon''}{2|\varepsilon'|^2}\ll k_i \tag{38}$$

Provided that the difference in wave numbers between Stokes or anti-Stokes waves and incident electric field $\Delta k_\beta\to 0$, Eq. (37) by substituting the second relation from Eq. (38) leads to

$$\left|-\frac{k_i(\varepsilon-1)}{\varepsilon\Gamma_\beta+\gamma_\beta}\right|\approx\frac{k_i}{\sqrt{|\varepsilon'|}\Gamma_p}\gg 1 \tag{39}$$

The resonance for high electric field is a phenomenon important for interpretation of the generation of surface structures. The interference of diffracted waves and the wave that traveled into the workpiece results in a spatially nonuniform distribution of temperature. The induced forces after melting enhance the initial modulations of the surface ripples, giving rise to capillary waves and surface roughness. The solution procedure, for example, can be described as follows. The evolution equation of a liquid layer is given by Eq. (D1),

$$\frac{\partial h}{\partial t}+\frac{d}{dx}\int_0^h u\,dz=-\frac{j(T)}{\rho_\ell} \tag{40}$$

where temperature for evaporation is determined by energy equations including interactions among laser beam, rippled surface, and thermal convection

$$\frac{\partial T}{\partial t}+\mathbf{u}\cdot\nabla T=\alpha\nabla^2T+f_0e^{-(\gamma+\gamma^*)z}+[f_se^{i\mathbf{q}\cdot\mathbf{r}-(\gamma_s+\gamma^*)z}+f_{as}e^{i\mathbf{q}\cdot\mathbf{r}-(\gamma_{as}^*+\gamma)z}]\eta \tag{41}$$

The last terms of Eq. (41) are obtained from energy absorption due to electrical field $\mathbf{E}\cdot\partial\mathbf{D}/\partial t$, where the displacement vector $\mathbf{D}=\varepsilon\mathbf{E}$. Energy absorbed due to magnetic field $\mathbf{H}\cdot\partial\mathbf{B}/\partial t$, where magnetic field intensity $\mathbf{H}=\mathbf{B}/\mu$ can also be included if needed. Therefore, functions f_0, f_s and f_{as} characterizing intensities and interactions of laser energy with surface roughness in Eq. (41) are given by

$$f_0=\frac{\omega\varepsilon''}{2\pi c_p}\|\mathbf{E_t}\|^2,\quad f_\beta=\frac{\omega\varepsilon''}{2\pi c_p}\mathbf{E_t}\cdot\mathbf{E}_\beta \tag{42}$$

In an s-polarized laser beam, these functions found from Eq. (41) are, respectively

$$f_0=\frac{2\omega\varepsilon''k_z^2}{\pi c_p|k_z+i\gamma|^2}\|\mathbf{E_i}\|^2 \tag{43}$$

$$f_s = f_0(\varepsilon - 1)\left(\frac{\gamma_s\Gamma_s \sin^2\varphi_s}{\varepsilon\Gamma_s + \gamma_s} - \frac{k_i^2 \cos^2\varphi_s}{\Gamma_s + \gamma_s}\right) \tag{44}$$

$$f_0 = \frac{2\omega\varepsilon'' k_z^2}{\pi c_p |\varepsilon k_z + i\gamma|^2}\frac{|\gamma|^2 + k_t^2}{k_i^2}\|\mathbf{E_i}\|^2 \tag{45}$$

In the case of a p-polarized laser, they are, respectively,

$$f_s = \frac{2\omega\varepsilon'' k_z^2(1-\varepsilon)\,|\gamma|^2(k_s^2 \sin^2\varphi_s - \gamma_s\Gamma_s) + k_s k_t[k_t k_s + (\gamma_s\gamma^* - \gamma\Gamma_s)\cos\varphi_s]}{\pi c_p |\varepsilon k_z + i\gamma|^2 \quad k_i^2(\varepsilon\Gamma_s + \gamma_s)}\|\mathbf{E_i}\|^2 \tag{46}$$

where $\cos\varphi_\beta = (\mathbf{k_t}\cdot\mathbf{k_\beta})/k_t k_\beta$. Functions f_{as} for s- and p-polarized waves are obtained from Eqs. (44) and (46) by substituting ε, k_s, φ_s, γ_s, Γ_s, γ by ε^*, k_{as}, φ_{as}, γ'_{as}, Γ^*_{as}, and γ^*, respectively.

Hydraulic jump. Studying hydraulic jump has conventionally assumed liquid pressure to be hydrostatic pressure. However, hydraulic jumps can also be induced by surface tension if scales are less than micrometer. The hydraulic jump occurs if the pressure gradient becomes increasingly adverse as the flow proceeds downstream and attains a magnitude large enough to counter the relevant effects. As derived in Eq. (C4) together with Eq. (C5), the equation governing hydraulic jump is

$$-\frac{1}{2}\rho g(h^2 - h_0^2) + \gamma\int_0^x h\frac{\partial^3 h}{\partial\xi^3}d\xi = \frac{Q^2}{\rho}\left(\frac{1}{h} - \frac{1}{h_0}\right) \tag{47}$$

Finding the roots of Eq. (47) gives the relation between the two depths of the jump. At the hydraulic jump, the height of the liquid suddenly varies and the flow also changes from a rapid supercritical flow to a slow subcritical flow [178]. Aside from the existence of two kinds of steady state in a circular hydraulic jump, as mentioned previously, the axial symmetry-breaking instability was observed by Ellegaard et al. [179]. They provided the first observation for the occurrence of polygonal patterns from breaking axial symmetry of a circular hydraulic jump. Experimental results of the width of the sides of the jump structure were found to agree with scaled results provided by Bush et al. [132] by introducing Rayleigh's capillary instability from a balance between inertial force and capillary pressure induced by the radius of curvature of the jump in a vertical plane aligned with the mean flow. It is, however, questionable about the horizontal wavelength of polygonal patterns of polygons being linearly proportional to the radius of curvature of the jump in vertical planes. With this assumption, the wavelength of polygonal patterns $\lambda_{HJ} \equiv 2\pi\overline{R}/n = C_1\gamma/\rho u_c^2$, where n is the number of the sides of the jump structure. The wavelengths of polygonal patterns predicted from the scaling and experimental measurements exhibited scattering by choosing correlation constant $C_1 = 74 \pm 7$.

Fingers. Fingers usually accompany with hydraulic jump (see Fig. 9). This is because pressure increases in the direction of the moving interface, leading to Rayleigh–Taylor instability. The phenomena are similar to a droplet impact on a solid surface [180]. Allen [181] was the first to propose that the splashing of a droplet impact on a surface is an example of Rayleigh–Taylor instability, caused by a rapidly decelerating interface. Mundo et al. [182] observed and found that splashing occurred when a dimensionless splash parameter $K \equiv \sqrt{We}\,Re^{1/4}$ exceeded a critical limit. Bhola and Chandra [183] interpreted the splash parameter determining the number of fingers from Rayleigh–Taylor instability governed by Eq. (9) by introducing the ratio between the maximum radius of the splat and droplet radius as a linear function of 0.25 power of Reynolds number [184]. Bejan and Gobin [185] proposed a scale analysis to scale the ring-shaped, splashing and needle-shaped flows after a droplet impact on a solid surface. They scaled the growth of the ring-shaped spread by

$$r_c \sim u_c t_c \tag{48}$$

Splashing with n fingers occurs when Rayleigh–Taylor instability is met. Replacing gravitational acceleration by u_c/t_c in Eq. (9) and substituting $r_c = n\lambda_{HJ}$ from geometrical consideration lead to

$$r_c \sim n\sqrt{\frac{\gamma t_c}{u_c\rho_\ell}} \tag{49}$$

Provided that time is short, Eqs. (48) and (49) indicate that radius of the ring-shaped spread is less than wavelength of fingers. The ring-shaped spread thus is free from fingers. On the other hand, larger time results in the ring-shaped spread covered with n fingers. Another relationship is required to determine the number of fingers. They further proposed that fingers or splashing take place at the moment viscous diffusion sweeps the entire cross section of the ring or thickness. That is,

$$\delta \sim \sqrt{\nu t_c} \sim \sqrt{A_{ring}} \tag{50}$$

where the cross section of the ring is determined from mass conservation between the droplet and ring-shaped spread

$$D^3 \sim A_{ring} r_c \sim A_{ring} u_c t_c \tag{51}$$

Combining Eqs. (48)–(51) gives the number of fingers, as derived by Bhola and Chandra [183]

$$n \sim \sqrt{We}\,Re^{1/4} \equiv K \tag{52}$$

Bejan and Gobin [185] also scaled the length of a finger from conservation of momentum and mass. They are, respectively,

$$\rho_\ell u_c^2 A \sim \tau L\sqrt{A} \qquad nAL \sim D^3 \tag{53}$$

where shear stress $\tau \sim \mu u_c/\sqrt{A}$. Regardless of a typing error for the cross-sectional area, Eq. (53) leads to

$$\frac{L}{D} \sim \sqrt{\frac{Re}{n}} \tag{54}$$

They also applied a constructal theory to find the optimal number of fingers. Minimizing the sum of the length of a finger and radius of the ring-shaped spread with respect to the number of fingers leads to a more accurate optimal number of fingers, being proportional to $K^{2/5}$. The final diameter of splats that come to rest as a disk was much greater than available experimental data as kinematic viscosity decreased. Except for needing a clarification of the proposition from Eq. (50), they contributed the deviation to be the assumption for a laminar flow during spread of the droplet. In welding or manufacturing determination of liquid velocity in Eq. (49) is difficult because it depends on inertial and thermocapillary forces, gravity, shear stress, solidification, and contact line effects. Equations (48)–(54), however, provide a systematical understanding of a mechanism of bead formation. Morphology of fingers have been extensively reviewed by Oron et al. [186] and Craster and Matar [187], and, for example, predicted by Thoroddsen and Sakakibara [180], Bussmann et al. [188], Eres et al. [189], and Dunn et al. [190], respectively.

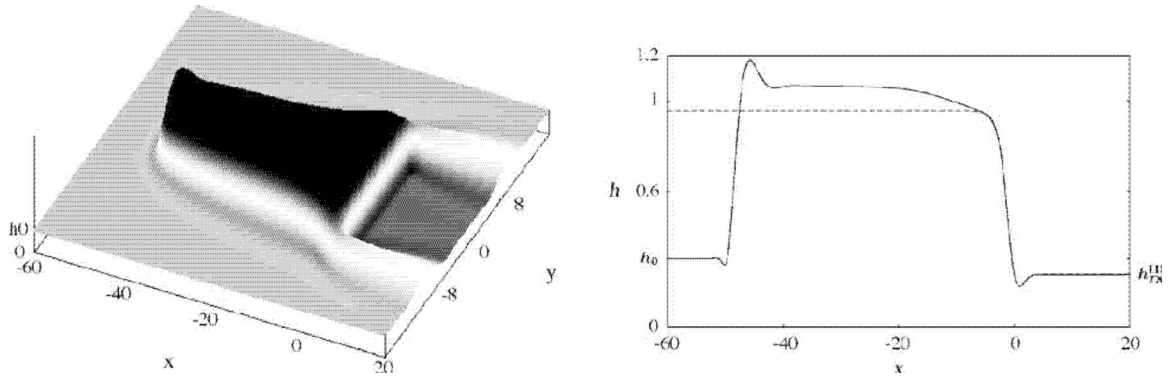

Fig. 13 (left) A two-dimensional steady state solution and (right) comparison of the centerline profile (solid curve), with the corresponding one-dimensional solution (dashed curve) [191]

Evolution equation of film thickness. Surface patterns can be effectively predicted by solving the different types of evolution equations of liquid films, as thoroughly reviewed by Oron et al. [186], and Craster and Matar [187]. A rather general equation governing thickness of a liquid film, for example, can be obtained from Eq. (D6). Accounting for an inclined surface subject to a local heating, thermocapillary and capillary forces and neglecting evaporation, Haskett et al. [191] presented a dimensionless form of an evolution equation of film thickness

$$\frac{\partial h}{\partial t} + \frac{\partial}{\partial x}(h^2 - h^3) = M\nabla_1 \cdot (h^2\nabla_1\theta) + D\nabla_1 \cdot (h^3\nabla_1 h) - \nabla_1 \cdot (h^3\nabla_1\nabla_1^2 h) \tag{55}$$

where temperature gradient along the free surface was specified by $(\partial T/\partial z)_{z=h_0}\nabla h \cong I\nabla\theta$, and

$$\theta = \frac{1}{\sqrt{2\pi\sigma_x^2}}\exp\left(-\frac{x^2}{2\sigma_x^2}\right)\left(\frac{1}{2}[1+\tanh(\sigma_y - |y|)]\right) \tag{56}$$

Numerical results are shown in the left-part of Fig. 13. It is interesting to find that the predicted fusion zone shape is quite similar to the observed humping shape (see Fig. 2(*a*)). The deviation of the liquid layer shapes along the centerline predicted by three- and one-dimensional models indicated the importance of three-dimensional analysis, as shown in the right-part of Fig. 13. In order to predict more realistic surface patterns, it is feasible and necessary to solve a relevant three-dimensional evolution equation of the liquid film. They also applied Eq. (55) to study hydraulic jump. However, the results for a horizontal liquid film met trouble owing to the normalizing length involving sine of inclination angle. An unsteady, two-dimensional study to solve evolution, rupture and instability of a liquid layer on its crystal subject to freezing and melting has been provided by Beerman and Brush [192]. The governing equations were a coupled pair of strongly nonlinear partial different equations governing the evolution of interfaces separating the thin film of a pure melt from its crystalline phase and from gas. Accounting for capillary force, thermocapillary force, latent heat for melting, van der Waals attraction, and solidification volume change effects, it was found that an increase in gas temperature stabilized the liquid film. Strong oscillations resulted in rupture by the growth of standing or traveling waves. Rupture times and the number of oscillations to rupture increased as gas temperature increased. Large amplitude disturbances increased the maximum allowable temperature for instability and decreased the time to rupture. It is interesting to develop a three-dimensional model further including gas flow and contact angle effects to simulate realistic surface patterns.

4 Conclusions

The conclusions drawn are the following:

1. Studying pattern formation of weld beads on surfaces is challenging with practical and academic importance. Understanding of the mechanisms is valuable for improving and controlling properties of workpieces in welding and various materials and manufacturing processing, such as droplet impingement, spray, deposition, and heat treatment. Realistic predictions of the weld bead defects involve not only thermal, aerodynamics, physics, electromagnetics, optics, and metallurgy, but also sciences of morphology, pattern selection, instabilities, and contact line dynamics. Phase transitions between liquid and gas, and solid and liquid are also included.
2. Inherent characteristics of rippling and humping on the surface of weldment are different. For example, rippling and humping roughness increase with decreasing and increasing welding speeds, respectively. In contrast to rippling having slight elevation in regular, arc-shaped topographic features above the surface, humping is associated with periodic swelling of molten pool on the surface. More clear definitions and understanding of fine and coarse ripples and humping are needed.
3. Instability theories reveal tendencies of humping, gouging, and rippling. Surface morphologies can be realistically predicted from three-dimensional evolution equations of the liquid layer together with energy equation experiencing solidification.
4. Spaces and amplitudes of ripping and humping can be effectively scaled by introducing liquid and gas pressures into Young–Laplace equation at two locations. If pressures are in phase or antiphase of deformation, space of roughness can be simply predicted. Otherwise, multiple or interrelated amplitude and space of roughness can be found.
5. Any factor, which can induce pressure difference in Young-Laplace equation, is responsible for specific surface patterns. Aside from the above-mentioned factors, other factors such as electromagnetic Lorentz force ($p_c \sim Lj_c^2/\sigma u_c$), viscous stresses ($p_c \sim \mu u_c L/\delta^2$), etc. are determinant to other types of surface patterns.
6. Scale analysis can be effectively used to predict different kinds of hydrodynamic instabilities and surface patterns. Equation (26) is a general equation to scale different surface patterns.
7. A more systematic category of different surface patterns is needed.

8. The effects of working parameters on secondary surface patterns such as polygons, clovers, and fingering and rupturing shapes after solidification are of interest.
9. The relationships between surface patterns and the associated undercutting, segregation, and porosity are of interest.

Nomenclature

a = roughness amplitude
A, A_{ring} = cross sections of a finger and ring
$\mathbf{B}$ = magnetic flux density
c = wave speed
C = concentration
c_γ = surface tension coefficient of pure liquid metal
D = parameter governing gravitational force [191], droplet diameter or solute diffusivity
E = elasticity number $\equiv \Gamma^{sat}\Delta H^0/(|c_\gamma|T_m)$
$\mathbf{E}$ = electric field intensity
f_0, f_s, f_{as} = function characterizing incident energy
g = gravitational acceleration
G_c, G_T = concentration and temperature gradient
h = fusion zone or liquid layer thickness
$\mathbf{H}$ = magnetic field intensity
$h_{s\ell}$ = latent heat for solidification
I = specified constant correcting temperature gradient
j = evaporation flux or electric current density
k = wave number or thermal conductivity
K = adsorption coefficient or splash parameter
K_{loss} = loss coefficient
L = finger length
m = slope of liquidus line
M = dimensionless parameter governing Marangoni force [191]
Ma = Marangoni number $\equiv |c_\gamma| wqh/\mu\alpha k$
n = normal direction, number of finger, or refractive index
n_r = number of ripples per unit length
q, $\mathbf{q}$ = heat transfer, or wave or grating vector of surface ripples
Q = flow rate
r = radius
$\overline{R}$ = average radius
Re = Reynolds number $\equiv u_c D/\nu$
R_g = gas constant
R_1, R_2 = radii of principal curvature
s = tangential coordinate
t = time
u = horizontal velocity component
U = Average or base velocity
w = vertical velocity component or fusion zone width
We = Weber number $\equiv \rho_\ell D u_c^2/\gamma$
x,y = horizontal coordinates
z = vertical coordinate

Greek Letters

α = thermal diffusivity
ε = permittivity, $\varepsilon = \varepsilon' + i\varepsilon''$
μ = dynamic viscosity or magnetic permeability
σ = beam radius or electrical conductivity
γ = surface tension or wave number
Γ = wave number
$d\gamma/dT$ = surface tension coefficient
Γ_p = variable defined in Eq. (38)
Γ^{sat} = saturation surface concentration, kg-mole/m^2
Ξ = function
λ_E = critical wavelength due to evaporation instability
$\lambda_{HJ}, \lambda_{KH}$ = critical wavelength of hydraulic jump and Kelvin–Helmholtz instabilities
λ_M = wavelength for solidification morphology
λ_L, λ_{rip} = wavelengths of laser and ripples
λ_R, λ_{RT} = critical wavelength of Rayleigh's capillary and Rayleigh–Taylor instabilities
θ = temperature
ϕ = incident angle
ω = dimensional angular speed
Ω_q = surface ripple frequency
ϕ_0 = contact angle
Δ = humping amplitude
ΔH^0 = adsorption heat, J/kg mole
Δk_β = wave number difference, defined in Eq. (38)
η = deformation of free surface, $\eta > 0$ toward upward direction
δ = viscous layer thickness
τ = shear stress

Superscripts

m, n = empirical index
‘ = perturbed quantity or diffracted wave of incident electric field
$*$ = complex conjugate

Subscripts

A,B = locations
as = anti-Stokes wave
c = characteristic or scaling quantity
e = pool edge
g = gas
i = incident
ℓ = liquid
m = melting
r = reflection
s = solid, surface, or Stokes wave
t = transmitted or tangential
z = z direction
0 = base state
β = s, or as, namely, Stoke or anti-Stokes wave
∞ = ambient

Appendix A: Kelvin-Helmholtz Instability

Liquid and gas pressures in Eq. (5) along the free surface can be found from Bernoulli's equation,

$$p_\ell + \frac{1}{2}\rho_\ell\left[\frac{(U_{\ell 0}-c)h_{\ell 0}}{h_{\ell 0}+\eta}\right]^2 + \rho_\ell g(h_{\ell 0}+\eta) = p_{\ell 0} + \frac{1}{2}\rho_\ell(U_{\ell 0}-c)^2 + \rho_\ell g h_{\ell 0} \tag{A1}$$

For small deformation $\eta \ll h_{\ell 0}$, Eq. (A1) reduces to

$$p_\ell - \frac{\rho_\ell(U_{\ell 0}-c)^2}{h_{\ell 0}+\eta}\eta + \rho_\ell g\eta \approx p_{\ell 0} \tag{A2}$$

where c is wave velocity of the interface, Similarly, gas pressure is

$$p_g + \frac{\rho_g(U_{g0}-c)^2}{h_{g0}-\eta}\eta + \rho_g g\eta \approx p_{g0} \tag{A3}$$

Substituting Eqs. (A2) and (A3) into Eq. (5) gives

$$\frac{\rho_\ell(U_{\ell 0}-c)^2}{h_{\ell 0}+\eta}\eta + \frac{\rho_g(U_{g0}-c)^2}{h_{g0}-\eta}\eta - (\rho_\ell-\rho_g)g\eta = -\gamma\frac{\partial^2\eta}{\partial x^2} \tag{A4}$$

where reference pressures $p_{\ell 0} = p_{g0}$ to maintain an initial flat surface. Wave speed can be determined from conserving of mass. That is,

$$\rho_\ell(U_{\ell 0}-c)h_{\ell 0}+\rho_g(U_{g0}-c)h_{g0}=\text{const} \tag{A5}$$

which shows that the wave speed $c=U_{g0}$ for $h_{g0}\to\infty$, or $c=U_{\ell 0}$ for $h_{\ell 0}\to\infty$.

Appendix B: Thermocapillary Instability

Perturbed shear balance Eq. (1) can be expressed as

$$\mu\left.\frac{\partial u'}{\partial z}\right|_{z=h_0}+\mu\left.\frac{\partial^2 U}{\partial z^2}\right|_{z=h_0}\eta=\tau_s' \tag{B1}$$

where the perturbed shear stress is

$$\tau_s'\approx\frac{d\gamma}{dT}\left(\left.\frac{\partial T'}{\partial x}\right|_{z=h_0}+\left.\frac{\partial T}{\partial z}\right|_{z=h_0}\frac{d\eta}{dx}\right) \tag{B2}$$

Assuming $\mu\partial^2 u'/\partial z^2=0$ and satisfying the continuity equation, free surface condition Eq. (B1) and no slip condition at wall $z=0$ for the perturbed flow lead to

$$u'=\left(-\left.\frac{\partial^2 U}{\partial z^2}\right|_{z=h_0}\eta+\frac{\tau_s'}{\mu}\right)z,\quad w'=\left(\left.\frac{\partial^2 U}{\partial z^2}\right|_{z=h_0}\frac{\partial\eta}{\partial x}-\frac{1}{\mu}\frac{\partial\tau_s'}{\partial x}\right)\frac{z^2}{2} \tag{B3}$$

The kinematic condition is

$$\frac{\partial\eta}{\partial t}=-U\frac{\partial\eta}{\partial x}+w' \tag{B4}$$

Substituting Eqs. (B1)–(B3), Eq. (B4) becomes

$$\frac{\partial\eta}{\partial t}=\left(-U+\left.\frac{\partial^2 U}{\partial z^2}\right|_{z=h_0}\frac{h_0^2}{2}\right)\frac{\partial\eta}{\partial x}-\frac{1}{\mu}\frac{d\gamma}{dT}\left(\left.\frac{\partial^2 T'}{\partial x^2}\right|_{z=h_0}+\left.\frac{\partial T}{\partial z}\right|_{z=h_0}\frac{d^2\eta}{dx^2}\right)\frac{h_0^2}{2} \tag{B5}$$

Appendix C: Hydraulic Jump

Pressure governing hydraulic jump can be obtained from momentum equations

$$-\frac{\partial p}{\partial x}=\frac{\partial\rho u^2}{\partial x}+\frac{\partial\rho uw}{\partial z},\quad -\frac{\partial p}{\partial z}=\rho g \tag{C1}$$

Integrating the first equation of Eq. (C1) over $0\le z\le h$ and substituting no slip condition at $z=0$, and kinematic condition $w=u\,\partial h/\partial x$ give

$$p_s\frac{dh}{dx}-\frac{d}{dx}\int_0^h p\,dz=\frac{d}{dx}\int_0^h\rho u^2 dz \tag{C2}$$

Integrating Eq. (C2) along the x direction after substituting liquid pressure $p=\rho g(h-z)+p_s$ obtained from the second equation of Eq. (C1) gives

$$-\int_0^x h\frac{dp_s}{d\xi}d\xi-\frac{1}{2}\rho g(h^2-h_0^2)=\int_0^h\rho u^2dz-\int_0^{h_0}\rho u^2dz \tag{C3}$$

Substituting Young–Laplace equation, $p=-\gamma\partial^2 h/\partial x^2$ at $z=h$, Eq. (C3) becomes

$$-\frac{1}{2}\rho g(h^2-h_0^2)+\gamma\int_0^x h\frac{\partial^3 h}{\partial\xi^3}d\xi=\int_0^h\rho u^2dz-\int_0^{h_0}\rho u^2dz \tag{C4}$$

The terms on the right-hand side can be approximately expressed as

$$\int_0^h\rho u^2dz-\int_0^{h_0}\rho u^2dz\cong\frac{Q^2}{\rho}\left(\frac{1}{h}-\frac{1}{h_0}\right) \tag{C5}$$

where mass flow rate Q is defined from mass conservation

$$Q=\int_0^h\rho u\,dz=\int_0^{h_0}\rho u\,dz \tag{C6}$$

Appendix D: Evolution Equation of Film Thickness

The shape or growth of a liquid layer can be determined by an evolution equation

$$\frac{\partial h}{\partial t}+\frac{d}{dx}\int_0^h u\,dz=-\frac{j}{\rho_\ell} \tag{D1}$$

Consider velocity of the liquid layer is

$$u=\frac{1}{2\mu}z(z-2h)\frac{\partial p}{\partial x}+\frac{\tau z}{\mu} \tag{D2}$$

where shear stress is balanced by thermocapillary force $\tau=(d\gamma/dT)[\partial T/\partial x+(\partial T/\partial z)\partial h/\partial x]_{z=h}$. Liquid pressure is given by

$$p=p_\infty+\rho g(h-z)-\gamma\frac{\partial^2 h}{\partial x^2}+\frac{j^2}{\rho_g} \tag{D3}$$

Mass rate in Eq. (D1) by substituting Eqs. (D2) and (D3) yields

$$\int_0^h u\,dz=\frac{1}{\mu}\left[-\frac{\rho g h^3}{3}\frac{\partial h}{\partial x}+\frac{\gamma h^3}{3}\frac{\partial^3 h}{\partial x^3}-\frac{h^3}{3}\frac{\partial}{\partial x}\left(\frac{j^2}{\rho_g}\right)+\frac{\tau h^2}{2}\right] \tag{D4}$$

Substituting Eq. (D4) into Eq. (D1)

$$\frac{\partial h}{\partial t}+\frac{1}{3\mu}\frac{\partial}{\partial x}\left(\gamma h^3\frac{\partial^3 h}{\partial x^3}\right)-\frac{\rho g}{3\mu}\frac{\partial}{\partial x}\left(h^3\frac{\partial h}{\partial x}\right)-\frac{1}{3\mu}\frac{\partial}{\partial x}\left[h^3\frac{\partial}{\partial x}\left(\frac{j^2}{\rho_g}\right)\right]+\frac{1}{2\mu}\frac{d\gamma}{dT}\frac{\partial}{\partial x}\left[h^2\left(\left.\frac{\partial T}{\partial x}\right|_{z=h_0}+\left.\frac{\partial T}{\partial z}\right|_{z=h_0}\frac{\partial h}{\partial x}\right)\right]=-\frac{j}{\rho_\ell} \tag{D5}$$

Equation (D5) can be generalized to a three-dimensional form

$$\frac{\partial h}{\partial t}+\frac{1}{3\mu}\nabla_1\cdot(\gamma h^3\nabla_1\nabla_1^2 h)-\frac{\rho g}{3\mu}\nabla_1\cdot(h^3\nabla_1 h)-\frac{1}{3\mu}\nabla_1\cdot\left(h^3\nabla_1\frac{j^2}{\rho_g}\right)+\frac{1}{2\mu}\frac{d\gamma}{dT}\left[\nabla_1\cdot(h^2\nabla_1 T|_{z=h_0})+\nabla_1\cdot\left(\left.\frac{\partial T}{\partial z}\right|_{z=h_0}h^2\nabla_1 h\right)\right]=-\frac{j}{\rho_\ell} \tag{D6}$$

where $\nabla_1\equiv\mathbf{i}\,\partial/\partial x+\mathbf{j}\,\partial/\partial y$.

References

[1] Arata, Y., 1986, *Plasma, Electron and Laser Beam Technology*, American Society for Metals, Materials Park, OH.

[2] 1991, "*Welding Handbook, Welding Processes*," Vol. 2, 8th ed., R. L. O'Brien, ed., American Welding Society, Miami, FL.

[3] Campbell, H. C., 1991, "Visual Inspection of Welds," Weld. J., **70**, pp. 79–80.

[4] Wei, P. S., Chuang, K.C., Ku, J. S., DebRoy, T., and Chen, K. H., 2011, "Mechanisms of Spiking and Humping in Keyhole Welding," (to be published in IEEE Transactions on Components and Packaging Technologies).

[5] Katayama, S., Matsunawa, A., and Kojima, K., 1998, "CO_2 Laser Weldability of Aluminum Alloys (2nd Report): Defect Formation Conditions and Causes," Weld. Int., **12**, pp. 774–789.

[6] Hall, A. C., and Robino, C. V., 2004, "Association of Microstructural Features and Rippling Phenomenon in 304 Stainless Steel Gas Tungsten Arc Welds," Sci. Technol. Weld. Joining, **9**, pp. 103–108.

[7] Bennett, W. S., and Mills, G. S., 1974, "GTA Weldability Studies on High Manganese Stainless Steels," Weld. J., **53**, pp. 548-s–553-s.

[8] Matsuda, F., Ushio, M., Nakagawa, H., and Nakata, K., 1980, "Effects of Electromagnetic Stirring on the Weld Solidification Structure of Aluminum Alloys," *An International Conference on Arc Physics and Weld Pool Behaviour*, Vol. 1, London, May 8–10, The Welding Institute, Cambridge, UK, Paper 10, pp. 337–347.

[9] Okada, T., Yokoya, S., and Ishizaki, K., 1988, "Effect of Surface-Active Ele-

ments on TIG Arc Welding Phenomena," IIW Doc.212-708-88.
[10] Sundell, R. E., Solomon, H. D., Harris, L. P., and Wojcik, L. A., Savage, W. F., and Walsh, D. W., 1983, "Minor Element Effects on Gas-Tungsten-Arc Weld Penetration," General Electric Co. Corp. Report No. SRD-83-066.
[11] Mills, K. C., and Keene, B. J., 1990, "Factors Affecting Variable Weld Penetration," Int. Mater. Rev., **35**, pp. 185–216.
[12] Garland, J. G., and Davies, G. J., 1970, "Surface Rippling and Growth Perturbations During Weld Pool Solidification," Met. Constr. Br. Weld. J., **2**, pp. 171–175.
[13] Arata, Y., and Miyamoto, I., 1972, "Some Fundamental Properties of High Power Laser Beam as a Heat Source (Report 3)-Metal Heating by Laser Beam," Trans. Jpn. Weld. Soc., **3**, pp. 163–180.
[14] Ishida, T., 1988, "Surface Bead Formation of a Mild Steel by Pulsed Current TIG Arc," J. Mater. Sci., **23**, pp. 3232–3242.
[15] Wei, P. S., Chang, C. Y., and Chen, C. T., 1996, "Surface Ripple in Electron-Beam Welding Solidification," ASME J. Heat Transfer, **118**, pp. 960–969.
[16] Lee, S., Yang, D., and Nikumb, S., 2008, "Femtosecond Laser Micromilling of Si Wafers," Appl. Surf. Sci., **254**, pp. 2996–3005.
[17] Wei, P. S., Chen, Y. H., Ku, J. S., and Ho, C. Y., 2003, "Active Solute Effects on Surface Ripples in Electron-Beam Welding Solidification," Metall. Mater. Trans. B, **34**, pp. 421–432.
[18] Bradstreet, B. J., 1968, "Effect of Surface Tension and Metal Flow on Weld Bead Formation," Weld. J., **47**, pp. 314-s–322-s.
[19] Cho, M. H., and Farson, D. F., 2007, "Understanding Bead Hump Formation in Gas Metal Arc Welding Using a Numerical Simulation," Metall. Mater. Trans. B, **38**, pp. 305–319.
[20] Nguyen, T. C., Weckman, D. C., and Johnson, D. A., 2007, "The Discontinuous Weld Bead Defect in High-Speed Gas Metal Arc Welds," Weld. J., **86**, pp. 360-s–372-s.
[21] Wu, C. S., Hu, Z. K., and Zhang, Y. M., 2009, "Suppression of Weld-Bead Defects and Increase in the Critical Welding Speed During High-Speed Arc Welding," Proc. Inst. Mech. Eng., Part B, **223**, pp. 751–757.
[22] Akahide, K., Ukebe, T., and Tsuboi, J., 1982, "Correlation Between Bead Dimensions and Welding Parameters in Submerged-Arc Welding," Trans. Jpn. Weld. Soc., **13**, pp. 76.
[23] Nomura, H., Sugitani, Y., and Tsuji, M., 1982, "Behaviour of Molten Pool in Submereged Arc Welding: Observation by X-Ray Fluoroscopy," Q. J. Jpn. Weld. Soc., **51**, pp. 767–775.
[24] Kumagai, M., and Okuda, N., 1986, "Research on Bead Formation in Submerged Arc Welding. III. Effect of Flux Height on the Bead Appearance in Submerged Arc Welding," Q. J. Jpn. Weld. Soc., **4**, pp. 283–289.
[25] Paton, B. E., Mandel'berg, S. L., and Sidorenko, B. G., 1971, "Certain Special Features of the Formation of Welds Made at High Speeds," Avt. Svarka, **8**, pp. 1–6.
[26] Yamamoto, T., and Shimada, W., 1975, "A Study on Bead Formation in High Speed TIG Arc Welding at Low Gas Pressure," *Proceedings of the Advanced Welding Technology, The Second International Symposium of the Japan Welding Society on Advanced Welding Technology*, Osaka, Japan, Japan Welding Society, Paper No. 2-2-(7), pp. 321–326.
[27] Savage, W. F., Nippes, E. F., and Agusa, K., 1979,"Effect of Arc Force on Defect Formation in GTA Welding," Weld. J., **58**, pp. 212-s–224-s.
[28] Hiramoto, S., Ohmine, M., Okuda, T., and Shinmi, A., 1987, "Deep Penetration Welding With High Power CO_2 Laser," *Proceedings of the International Conference on Laser Advanced Material Processing-Science and Application*, May 21–23, Osaka, Japan, High Temperature Society of Japan and Japan Laser Processing Society, pp. 157–162.
[29] Albright, C. E., and Chiang, S., 1988, "High-Speed Laser Welding Discontinuities," J. Laser Appl., **1**, pp. 18–24.
[30] Tsukamoto, S., Irie, H., Inagaki, M., and Hashimoto, T., 1983, "Effect of Focal Position on Humping Bead Formation in Electron Beam Welding," Trans. National Research Institute for Metals, **25**, pp. 62–67.
[31] Tsukamoto, S., Irie, H., Inagaki, M., and Hashimoto, T., 1984, "Effect of Beam Current on Humping Bead Formation in Electron Beam Welding," Trans National Research Institute for Metals, **26**, pp. 133–140.
[32] Tomie, M., Abe, N., and Arata, Y., 1989, "Tandem Electron Beam Welding (Report IX)-High Speed Tandem Electron Beam Welding," Trans. JWRI, **18**, pp. 175–180.
[33] Shiu, T. R., Grigoropoulos, C. P., Cahill, D. G., and Greif, R., 1999, "Mechanism of Bump Formation on Glass Substrates During Laser Texturing," J. Appl. Phys., **86**, pp. 1311–1316.
[34] Schiaffino, S., and Sonin, A. A., 1997, "Formation and Stability of Liquid and Molten Beads on a Solid Surface," J. Fluid Mech., **343**, pp. 95–110.
[35] Ho, C. M., and Tai, Y. C., 1998, "Micro-Electro-Mechanical-Systems (MEMS) and Fluid Flows," Annu. Rev. Fluid Mech., **30**, pp. 579–612.
[36] Lau, J. H., Shangguan, D., Lau, D. C. Y., Kung, T. T. W., and Lee, S. W. R., 2004, "Thermal-Fatigue Life Prediction Equation for Wafer-Level Chip Scale Package (WLCSP) Lead-Free Solder Joints on Lead-Free Printed Circuit Board (PCB)," *Proceedings of the 54th 2004 Electronic Components and Technology Conference*, Vol. 2, pp. 1563–1569.
[37] Soderstrom, E., and Mendez, P., 2006, "Humping Mechanisms Present in High Speed Welding," Sci. Technol. Weld. Joining, **11**, pp. 572–579.
[38] Mendez, P. F., and Eagar, T. W., 2003, "Penetration and Defect Formation in High-Current Arc Welding," Weld. J., **82**, pp. 296-s–306-s.
[39] Shimada, W., and Hoshinouchi, S., 1982, "A Study on Bead Formation by Low Pressure TIG Arc and Prevention of Under-Cut Bead," Trans. Jpn. Weld. Soc., **51**, pp. 280–286.
[40] Mendez, P. F., Niece, K. L., and Eagar, T. W., 2000, "Humping Formation in High Current GTA Welding," *Proceedings of the International Conference on Joining of Advanced and Specialty Materials II*, Cincinnati, OH, ASM International, Nov., pp. 151–158.
[41] Tsukamoto, S., Irie, H., Hashimoto, T., and Inagaki, M., 1982, "Humping Bead Formation in Electron Beam Welding (Report 1)-Effect of Focal Position on Humping Bead Formation," Q. J. Jpn. Weld. Soc., **51**, pp. 286–291.
[42] Marya, M., and Edwards, G. R., 2001, "Factors Controlling the Magnesium Weld Morphology in Deep Penetration Welding by a CO_2 Laser," J. Mater. Eng. Perform., **10**, pp. 435–443.
[43] Nishiguchi, K., Matsuyama, K., Terai, K., and Ikeda, K., 1975, "Bead Formation in High Speed Gas-Shielded Metal-Arc Welding," *Proceedings of the Second International Symposium on JWS Advanced Welding Technology*, Osaka, Japan, Japan Welding Society, Paper 2-2-(10).
[44] Kawahito, Y., Mizutani, M., and Katayama, S., 2007, "Elucidation of High-Power Fibre Laser Welding Phenomena of Stainless Steel and Effect of Factors on Weld Geometry," J. Phys. D: Appl. Phys., **40**, pp. 5854–5859.
[45] Tong, H., and Giedt, W. H., 1969, "Radiographs of the Electron Beam Welding Cavity," Rev. Sci. Instrum., **40**, pp. 1283–1285.
[46] Batteh, J. J., Chen, M. M., and Mazumder, J., 2000, "A Stagnation Flow-Analysis of the Heat Transfer and Fluid-Flow Phenomena in Laser Drilling," ASME J. Heat Transfer, **122**, pp. 801–807.
[47] Wei, P. S., and Giedt, W. H., 1985, "Surface Tension Gradient-Driven Flow Around an Electron Beam Welding Cavity," Weld. J., **64**, pp. 251-s–259-s.
[48] Wei, P. S., and Chiou, L. R., 1988, "Molten Metal Flow Around the Base of a Cavity During a High-Energy Beam Penetrating Process," ASME J. Heat Transfer, **110**, pp. 918–923.
[49] Nguyen, T. C., Weckman, D. C., Johnson, D. A., and Kerr, H. W., 2006, "Review—High Speed Fusion Weld Bead Defects," Sci. Technol. Weld. Joining, **11**, pp. 618–633.
[50] Yamauchi, N., and Taka, T., 1978, "Bead Formation in TIG Welding," International Institute of Welding, Document No. 212-437-78.
[51] Yamauchi, N., and Taka, T., 1979, "TIG Arc Welding With a Hollow Tungsten Electrode," International Institute of Welding, Document No. 212-452-79.
[52] Troyer, W., Tomsic, M., and Barhorst, R., 1977, "Investigation of Pulsed Wave Shapes," Weld. J., **56**, pp. 26–32.
[53] Shimokusu, Y., Fukumoto, S., Nayama, M., Ishide, T., Tsubota, S., Matunawa, A., and Katayama, S., 2002, "Application of Pulse Modulated High Power YAG Laser to Thick Plate Welding," Q. J. Jpn. Weld. Soc., **20**, pp. 477–483.
[54] Ishizaki, K., Yokoya, S., and Okada, T., 1988, "Weldability of Stainless Steel," Report, Nippon Institute of Technology, Saitama, Japan to VAMAS Meeting on Technical Working Area, Weld Characteristics, NPL, Teddington.
[55] Hirata, H., Ogawa, K., and Taka, T., 1999, "Effect of Chemical Compositions on Bead Formation in TIG Arc Welding-Effect of Chemical Compositions on Weldability in Fabrication in High Alloyed Steel (Report II)," Q. J. Jpn. Weld. Soc., **17**, pp. 397–402.
[56] Takeuchi, Y., Takagi, R., and Shinoda, T., 1992, "Effect of Bismuth on Weld Joint Penetration in Austenitic Stainless Steel," Weld. J., **71**, pp. 283-s–289-s.
[57] Honma, S., and Yasuda, K., 2004, "Study of Semi-Automatic TIG Welding," Weld. Int., **18**, pp. 450–455.
[58] Nguyen, T. C., Weckman, D. C., Johnson, D. A., and Kerr, H. W., 2005, "The Humping Phenomenon During High Speed Gas Metal Arc Welding," Sci. Technol. Weld. Joining, **10**, pp. 447–459.
[59] Kern, M., Berger, P., and Hügel, H., 2000, "Magneto-Fluid Dynamic Control of Seam Quality in CO_2 Laser Beam Welding," Weld. J., **79**, pp. 72-s–78-s.
[60] Hirata, Y., 2003, "Pulsed Arc Welding," Weld. Int., **17**, pp. 98–115.
[61] Michie, K., Blackman, S., and Ogunbiyi, T. E. B., 1999, "Twin-Wire GMAW: Process Characteristics and Applications," Weld. J., **78**, pp. 31–34.
[62] Ueyama, T., Ohnawa, T., Tanaka, M., and Nakata, K., 2005, "Effects of Torch Configuration and Welding Current on Weld Bead Formation in High Speed Tandem Pulsed Gas Metal Arc Welding of Steel Sheets," Sci. Technol. Weld. Joining, **10**, pp. 750–759.
[63] Kannatey-Asibu, E., Jr., 1991, "Thermal Aspects of the Split-Beam Laser Welding Concept," Trans. the ASME, **113**, pp. 215–221.
[64] Xie, J., 2002, "Dual Beam Laser Welding," Weld. J., **81**, pp. 223-s–230-s.
[65] Arata, Y., and Nabegata, E., 1978, "Tandem Electron Beam Welding (Report-I)," Trans. JWRI, **7**, pp. 101–109.
[66] Dilthey, U., and Wieschemann, A., 2000, "Prospects by Combining and Coupling Laser Beam and Arc Welding Processes," Rivista Italiana della Saldatura (Italy), **52**, pp. 749–759.
[67] El Rayes, M., Walz, C., and Sepold, G., 2004, "The Influence of Various Hybrid Welding Parameters on Bead Geometry," Weld. J., **83**, pp. 147-s–153-s.
[68] Choi, H. W., Farson, D. F., and Cho, M. H., 2006, "Using a Hybrid Laser Plus GMAW Process for Controlling the Bead Humping Defect," Weld. J., **85**, pp. 174s–179s.
[69] Hartman, D. A., DeLapp, D. R., Cook, G. E., and Barnett, R. J., 1999, "Intelligent Fusion Control Throughout Varying Thermal Regions," Industry Applications Conference, 34th IAS Annual Meeting, Oct. 3–7, IEEE, Phoenix, AZ, pp. 635–644.
[70] Kovacevic, R., and Zhang, Y. M., 1996, "Sensing Free Surface of Arc Weld Pool Using Specular Reflection: Principle and Analysis," Proc. Inst. Mech. Eng., **210**, pp. 553–564.
[71] Mirapeix, J., Cobo, A., Fernandez, S., Cardoso, R., and Lopez-Higuera, J. M., 2008, "Spectroscopic Analysis of the Plasma Continuum Radiation for On-Line Arc-Welding Defect Detection," J. Phys. D: Appl. Phys., **41**, p. 135202.
[72] Cheever, D. L., and Howden, D. G., 1969, "Technical Note: Nature of Weld Surface Ripples," Weld. J., **48**, pp. 179-s–180-s.

[73] D'annessa, A. T., 1970, "Sources and Effects of Growth Rate Fluctuations During Weld Metal Solidification," Weld. J., **49**, pp. 41-s–45-s.
[74] Kotecki, D. J., Cheever, D. L., and Howden, D. G., 1972, "Mechanism of Ripple Formation During Weld Solidification," Weld. J., **51**, pp. 386-s–391-s.
[75] Ecer, G. M., Tzavaras, A., Gokhale, A., and Brody, H. D., 1982, "Weld Pool Fluid Motion and Ripple Formation in Pulsed-Current GTAW," *Trends in Welding Research in the United States*, Nov. 16–18, S. A. David, ed., Joining Division of American Society for Metals, New Orleans, LA, pp. 419–442.
[76] Altshulin, S., Zahavi, J., Rosen, A., and Nadiv, S., 1990, "The Interaction between a Pulsed Laser Beam and a Steel Surface," J. Mater. Sci., **25**, pp. 2259–2263.
[77] Xu, J.-J., and Davis, S. H., 1984,"Convective Thermocapillary Instabilities in Liquid Bridges," Phys. Fluids, **27**, pp. 1102–1107.
[78] Kamotani, Y., and Ostrach, S., 1998, "Theoretical Analysis of Thermocapillary Flow in Cylindrical Columns of High Prandtl Number Fluids," ASME J. Heat Transfer, **120**, pp. 758–764.
[79] Keller, J. R., and Bergman, T. L., 1990, "Thermosolutal Inducement of No-Slip Free Surfaces in Combined Marangoni-Buoyancy Driven Cavity Flows," ASME J. Heat Transfer, **112**, pp. 363–369.
[80] Miller, C. A., and Neogi, P., 1985, *Interfacial Phenomena, Equilibrium and Dynamic Effects*, Dekker, New York.
[81] Pearson, J. R. A., 1958, "On Convection Cells Induced by Surface Tension," J. Fluid Mech., **4**, pp. 489–500.
[82] Fujimura, K., Ogawa, M., and Seki, M., 1992, "Possible Mechanism of the Roughness Formation on a Liquid Layer Caused by a High Heat Flux," Fusion Eng. Des., **19**, pp. 183–191.
[83] Ogawa, M., Araki, M., Seki, M., Kunugi, T., Fukaya, K., and Ise, H., 1992, "Experimental Study on Melting and Evaporation of Metal Exposed to Intense Hydrogen Ion Beam," Fusion Eng. Des., **19**, pp. 193–202.
[84] Ang, L. K., Lau, Y. Y., Gilgenbach, R. M., Spindler, H. L., Lash, J. S., and Kovaleski, S. D., 1998, "Surface Instability of Multipulse Laser Ablation on a Metallic Target," J. Appl. Phys., **83**, pp. 4466–4471.
[85] Chandrasekhar, S., 1961, *Hydrodynamic and Hydromagnetic Stability*, Oxford University Press, London.
[86] Bennett, T. D., Grigoropoulos, C. P., and Krajnovich, D. J., 1995, "Near-Threshold Laser Sputtering of Gold," J. Appl. Phys., **77**, pp. 849–864.
[87] Seifert, N., Betz, G., and Husinsky, W., 1996, "Hydrodynamic Phenomena During Laser Irradiation: a Finite Difference Approach," Appl. Surf. Sci., **96–98**, pp. 33–38.
[88] Lugomer, S., 2007, "Micro-fluid Dynamics via Laser-Matter Interaction: Vortex Filament Structures, Helical Instability, Reconnection, Merging, and Undulation," Phys. Lett. A, **361**, pp. 87–97.
[89] Keilmann, F., 1983, "Laser-Driven Corrugation Instability of Liquid Metal Surfaces," Phys. Rev. Lett., **51**, pp. 2097–2100.
[90] Emel'yanov, V. I., Konov, V. I., Tokarev, V. N., and Seminogov, V. N., 1989, "Formation of Periodic Surface Ripples Under the Action of Pulsed Carbon Dioxide Laser Radiation on Fused Silica," J. Opt. Soc. Am. B, **6**, pp. 104–114.
[91] Kolasinski, K. W., 2007, "Solid Structure Formation During the Liquid/Solid Phase Transition," Curr. Opin. Solid State Mater. Sci., **11**, pp. 76–85.
[92] Mullins, W. W., and Sekerka, R. F., 1964, "Stability of a Planar Interface During Solidification of a Dilute Binary Alloy," J. Appl. Phys., **35**, pp. 444–451.
[93] Rutter, J. W., and Chalmers, B., 1953, "A Prismatic Substructure Formed During Solidification of Metals," Can. J. Phys., **31**, pp. 15–39.
[94] Bösch, M. A., and Lemons, R. A., 1981, "Laser-Induced Melt Dynamics of Si and Silica," Phys. Rev. Lett., **47**, pp. 1151–1155.
[95] Weizman, M., Nickel, N. H., Sieber, I., and Yan, B., 2008, "Laser-Induced Self-Organization in Silicon-Germanium Thin Films," J. Appl. Phys., **103**, p. 093536.
[96] Style, R. W., and Wettlaufer, J. S., 2007, "Evaporatively Driven Morphological Instability," Phys. Rev. E, **76**, p. 011602.
[97] Gräf, S., Staupendahl, G., Seiser, C., Meyer, B.–J., and Müller, F. A., 2010, "Enhanced Melt Pool Stirring in Welding With Dynamic Polarized Laser Beam," Sci. Technol. Weld. Joining, **15**, pp. 208–212.
[98] Itoh, K., Watanabe, W., and Ozeki, Y., 2009, "Nonlinear Ultrafast Focal-Point Optics for Microscopic Imaging, Manipulation, and Machining," Proc. IEEE, **97**, pp. 1011–1030.
[99] Emel'yanov, V. I., Zemskov, E. M., and Seminogov, V. N., 1984, "Theory of the Formation of "Normal" and "Anomalous" Gratings on the Surfaces of Absorbing Condensed Media Exposed to Laser Radiation," Sov. J. Quantum Electron., **14**, pp. 1515–1521.
[100] Birnbaum, M., 1965, "Semiconductor Surface Damage Produced by Ruby Lasers," J. Appl. Phys., **36**, pp. 3688–3689.
[101] Lenzner, M., 1999, "Femtosecond Laser-Induced Damage of Dielectrics," Int. J. Mod. Phys. B, **13**, pp. 1559–1578.
[102] Young, J. F., Preston, J. S., van Driel, H. M., and Sipe, J. E., 1983, "Laser-Induced Periodic Surface Structure. II. Experiments on Ge, Si, Al, and Brass," Phys. Rev. B, **27**, pp. 1155–1172.
[103] Siegman, A. E., and Fauchet, P. M., 1986, "Stimulated Wood's Anomalies on Laser-Illuminated Surfaces," IEEE J. Quantum Electron., **22**, pp. 1384–1403.
[104] Pedraza, A. J., Guan, Y. F., Fowlkes, J. D., and Smith, D. A., 2004, "Nanostructures Produced by Ultraviolet Laser Irradiation of Silicon. I. Rippled Structures," J. Vac. Sci. Technol. B, **22**, pp. 2823–2835.
[105] Anthony, T. R., and Cline, H. E., 1977, "Surface Rippling Induced by Surface-Tension Gradients During Laser Surface Melting and Alloying," J. Appl. Phys., **48**, pp. 3888–3894.
[106] Glicksman, M. E., and Schaefer, R. J., 1968, "In Situ Observations of Dendritic Growth and Remelting Processes During Metallic Solidification," *The Solidification of Metals*, Iron and Steel Institute, London, pp. 43–48 and 124–125.
[107] Ryzhkov, F. N., and Bashkatov, A. V., and Uglov, A. A., 1972, "Mechanism of Formation of Electron-Beam Welds," Svar. Proiz., **5**, pp.10–12.
[108] Ostrach, S., 1982, "Low-Gravity Fluid Flows," Annu. Rev. Fluid Mech., **14**, pp. 313–345.
[109] Chen, M. M., 1987, "Thermocapillary Convection in Materials Processing," *Interdisciplinary Issues in Materials Processing and Manufacturing*, S. K. Samanta, R. Komanduri, R. McMeeking, M. M. Chen, and A. Tseng, eds., ASME, New York, pp. 541–558.
[110] Arata, Y., Tomie, M., Abe, N., and Yao, X.-Y., 1987, "Observation of Molten Metal Flow During EB Welding," Trans. JWRI, **16**, pp. 13–16.
[111] Low, D. K. Y., and Li, L., 2000, Laser Drilling of Transparent Media for the Study of Material Removal, Taper and Spatter Formation Mechanisms, ICALEO, pp. 105–114.
[112] Fabbro, R., 2002, "Basic Processes in Deep Penetration Laser Welding," ICALEO'2002, Oct., Scottsdale, AZ.
[113] Slavin, G. A., and Trokhinskaya, N. M., 1983, "Relationship Between Thermal and Hydrodynamic Processes in the Pool in Welding Thin Sheet Materials With a Continuous Arc," Svar. Proiz. (Weld. Production), **4**, pp. 4–6.
[114] Hu, J., Guo, H., and Tsai, H. L., 2008, "Weld Pool Dynamics and the Formation of Ripples in 3D Gas Metal Arc Welding," Int. J. Heat Mass Transfer, **51**, pp. 2537–2552.
[115] Kou, S., and Wang, Y. H., 1986, "Weld Pool Convection and Its Effect," Weld. J., **65**, pp. 63-s–70-s.
[116] Zacharia, T., David, S. A., Vitek, J. M., and DebRoy, T., 1989, "Weld Pool Development During GTA and Laser Beam Welding of Type 304 Stainless Steel, Part I—Theoretical Analysis," Weld. J., **68**, pp. 499-s–509-s.
[117] Chakraborty, N., Chakraborty, S., and Dutta, P., 2004, "Three-Dimensional Modeling of Turbulent Weld Pool Convection in GTAW Processes," Numer. Heat Transf., Part A, **45**, pp. 391–413.
[118] Iwamoto, M., Ye, M., Grigoropoulos, C. P., and Greif, R., 1998, "Numerical Analysis of Pulsed Laser Heating for the Deformation of Metals," Numer. Heat Transf., Part A, **34**, pp. 791–804.
[119] Ki, H., Mohanty, P. S., and Mazumder, J., 2002, "Modeling of Laser Keyhole Welding: Part II. Simulation of Keyhole Evolution, Velocity, Temperature Profile, and Experimental Verification," Metall. Mater. Trans. A, **33**, pp. 1831–1842.
[120] Lee, J. Y., Ko, S. H., Farson, D. F., and Yoo, C. D., 2002, "Mechanism of Keyhole Formation and Stability in Stationary Laser Welding," J. Phys. D: Appl. Phys., **35**, pp. 1570–1576.
[121] He, X., Fuerschbach, P. W., and DebRoy, T., 2003, "Heat Transfer and Fluid Flow During Laser Spot Welding of 304 Stainless Steel," J. Phys. D: Appl. Phys., **36**, pp. 1388–1398.
[122] Zhou, J., Tsai, H. L., and Wang, P. C., 2006, "Transport Phenomena and Keyhole Dynamics During Pulsed Laser Welding," ASME J. Heat Transfer, **128**, pp. 680–690.
[123] Schwarz-Selinger, T., Cahill, D. G., Chen, S.-C., Moon, S.-J., and Grigoropoulos, C. P., 2001, "Micron-Scale Modifications of Si Surface Morphology by Pulsed-Laser Texturing," Phys. Rev. B, **64**, p. 155323.
[124] Balandin, V. Yu., Gernert, U., Nink, T., and Bostanjoglo, O., 1997, "Segregation and Surface Transport of Impurities: New Mechanisms Affecting the Surface Morphology of Laser Treated Metals," J. Appl. Phys., **81**, pp. 2835–2838.
[125] Röntzsch, L., Heinig, K.-H., Schuller, J. A., and Brongersma, M. L., 2007, "Thin Film Patterning by Surface-Plasmon-Induced Thermocapillarity," Appl. Phys. Lett., **90**, p. 044105.
[126] Arata, Y., Matsuda, F., and Murakami, T., 1973, "Some Dynamic Aspects of Weld Molten Metal in Electron Beam Welding," Trans. Jpn. Weld. Research Institute, **2**, pp. 23–32.
[127] Irie, H., Tsukamoto, S., and Inagaki, M., 1984, "Relation between Beam Properties and Shape of Fusion Zone in Electron Beam Welding-Abnormally Expanded Fusion Zone," Trans. National Research Institute for Metals, **26**, pp. 287–296.
[128] Gratzke, U., Kapadia, P. D., Dowden, J., Kroos, J., and Simon, G., 1992, "Theoretical Approach to the Humping Phenomenon in Welding Processes," J. Phys. D: Appl. Phys., **25**, pp. 1640–1647.
[129] Viskanta, R., 1988, "Heat Transfer During Melting and Solidification of Metals," 50th Anniversary Issue, ASME J. Heat Transfer, **110**, pp. 1205–1219.
[130] Tytkin, Yu. M., Ryazantsev, O. V., and Chuvilo, V. N., 1981, "The Mechanism of Formation of a Coarse Flaky Surface of Weld Metal in Welding Under High-Power Conditions," Svar. Proiz., **2**, pp. 4–5.
[131] Kumar, A., and DebRoy, T. 2006, "Toward a Unified Model to Prevent Humping Defects in Gas Tungsten Arc Welding," Weld. J., **85**, pp. 292-s–304-s.
[132] Bush, J. W. M., Aristoff, J. M., and Hosoi, A. E., 2006, "An Experimental Investigation of the Stability of the Circular Hydraulic Jump," J. Fluid Mech., **558**, pp. 33–52.
[133] Mogyorósi, P., Piglmayer, K., and Bäuerle, D., 1989, "Ar^+ Laser-Induced Chemical Etching of Molybdenum in Chlorine Atmosphere," Surf. Sci., **208**, pp. 232–244.
[134] Bäuerle, D., 1996, *Laser Processing and Chemistry*, Springer-Verlag, New York.
[135] Mathur, M., DasGupta, R., Selvi, N. R., John, N. S., Kulkarni, G. U., and Govindarajan, R., 2007, "Gravity-Free Hydraulic Jumps and Metal Femto-

liter Cups," Phys. Rev. Lett., **98**, p. 164502.
[136] Lin, M. L., and Eagar, T. W., 1985, "Influence of Arc Pressure on Weld Pool Geometry," Weld. J., **64**, pp.163-s–169-s.
[137] Bejan, A., 1995, *Convection Heat Transfer*, Wiley, New York.
[138] Jeffreys, H., 1925, "On the Formation of Water Waves by Wind," Proc. R. Soc. London, Ser. A, **107**, pp. 189–206.
[139] Miles, J. W., 1957, "On the Generation of Surface Waves by Shear Flows," J. Fluid Mech., **3**, pp. 185–204.
[140] Lighthill, M. J., 1962, "Physical Interpretation of the Mathematical Theory of Wave Generation by Wind," J. Fluid Mech., **14**, pp. 385–398.
[141] Hogan, J. M., and Ayyaswamy, P. S., 1985, "Linear Stability of a Viscous-Inviscid Interface," Phys. Fluids, **28**, pp. 2709–2715.
[142] Shtemler, Y. M., Mond, M., Cherniavskii, V., Golbraikh, E., and Nissim, Y., 2008, "An Asymptotic Model for the Kelvin–Helmholtz and Miles Mechanisms of Water Wave Generation by Wind," Phys. Fluids, **20**, p. 094106.
[143] Yih, C. S., 1965, *Dynamics of Nonhomogeneous Fluids*, Macmillan, New York.
[144] Hsieh, D. Y., 1978, "Interfacial Stability With Mass and Heat Transfer," Phys. Fluids, **21**, pp. 745–748.
[145] Funada, T., and Joseph, D. D., 2001, "Viscous Potential Flow Analysis of Kelvin-Helmholtz Instability in a Channel," J. Fluid Mech., **445**, pp. 263–283.
[146] Chang, I.-D., and Russell, P. E., 1965, "Stability of a Liquid Layer Adjacent to a High-Speed Gas Stream," Phys. Fluids, **8**, pp. 1018–1026.
[147] Asthana, R., and Agrawal, G. S., 2007, "Viscous Potential Flow Analysis of Kelvin-Helmholtz Instability With Mass Transfer and Vaporization," Physica A, **382**, pp. 389–404.
[148] Sharp, D. H., 1984, "An Overview of Rayleigh-Taylor Instability," Physica D, **12**, pp. 3–18.
[149] Richtmyer, R. D., 1960, "Taylor Instability in Shock Acceleration of Compressible Fluids," Commun. Pure Appl. Math., **13**, pp. 297–319.
[150] Meshkov, E. E., 1969, "Instability of the Interface of Two Gases Accelerated by a Shock Wave," Fluid Dyn., **4**, pp. 101–104.
[151] Velikovich, A. L., and Dimonte, G., 1996, "Nonlinear Perturbation Theory of the Incompressible Richtmyer-Meshkov Instability," Phys. Rev. Lett., **76**, pp. 3112–3115.
[152] Mikaelian, K. O., 1994, "Oblique Shocks and the Combined Rayleigh–Taylor, Kelvin–Helmholtz, and Richtmyer–Meshkov Instabilities," Phys. Fluids, **6**, pp. 1943–1945.
[153] Alexeev, A., and Oron, A., 2007, "Suppression of the Rayleigh-Taylor Instability of Thin Liquid Films by the Marangoni Effect," Phys. Fluids, **19**, p. 082101.
[154] Ozen, O., and Narayanan, R., 2006, "A Note on the Rayleigh-Taylor Instability With Phase Change," Phys. Fluids, **18**, p. 042110.
[155] Piriz, A. R., Corta'zar, O. D., Lo'pezCela, J. J., and Tahir, N. A., 2006, "The Rayleigh-Taylor Instability," Am. J. Phys., **74**, pp. 1095–1098.
[156] Davis, S. H., 1980, "Moving Contact Lines and Rivulet Instabilities. Part 1. The Static Rivulet," J. Fluid Mech., **98**, pp. 225–242.
[157] Gau, H., Herminghaus, S., Lenz, P., and Lipowsky, R., 1999, "Liquid Morphologies on Structured Surfaces: From Microchannels to Microchips," Science, **283**, pp. 46–49.
[158] Speth, R. L., and Lauga, E., 2009, "Capillary Instability on a Hydrophilic Stripe," New J. Phys., **11**, p. 075024.
[159] Frenkel, A. L., Babchin, A. J., Levich, B. G., Shlang, T., and Sivashinsky, G. I., 1987, "Annular Flows Can Keep Unstable Films From Breakup: Nonlinear Saturation of Capillary Instability," J. Colloid Interface Sci., **115**, pp. 225–233.
[160] Gauglitz, P. A., and Radke, C. J., 1988, "An Extended Evolution Equation for Liquid Film Breakup in Cylindrical Capillaries," Chem. Eng. Sci., **43**, pp. 1457–1465.
[161] Kurz, W., and Fisher, D. J., 1989, *Fundamentals of Solidification*, Trans. Tech., Aedermannsdorf, Switzerland.
[162] Prosperetti, A., and Plesset, M. S., 1984, "The Stability of an Evaporating Liquid Surface," Phys. Fluids, **27**, pp. 1590–1602.
[163] Zhang, N., and Chao, D. F., 1999, "Mechanisms of Convection Instability in Thin Liquid Layers Induced by Evaporation," Int. Commun. Heat Mass Transfer, **26**, pp. 1069–1080.
[164] Takashima, M., 1981, "Surface Tension Driven Instability in a Horizontal Liquid Layer With a Deformable Free Surface. II Overstability," J. Phys. Soc. Jpn., **50**, pp. 2751–2756.
[165] Nemchinsky, V. A., 1997, "The Role of Thermocapillary Instability in Heat Transfer in a Liquid Metal Pool," Int. J. Heat Mass Transfer, **40**, pp. 881–891.
[166] Smorodin, B. L., Mikishev, A. B., Nepomnyashchy, A. A., and Myznikova, B. I., 2009, "Thermocapillary Instability of a Liquid Layer Under Heat Flux Modulation," Phys. Fluids, **21**, p. 062102.
[167] Wei, P. S., Ting, C. N., Yeh, J. S., DebRoy, T., Chung, F. K., and Yan, G. H., 2009, "Origin of Wavy Weld Boundary," J. Appl. Phys., **105**, p. 053508.
[168] Wei, P. S., Yeh, J. S., Ting, C. N., DebRoy, T., Chung, F. K., and Lin, C. L., 2009, "The Effects of Prandtl Number on Wavy Weld Boundary," Int. J. Heat Mass Transfer, **52**, pp. 3790–3798.
[169] Sahoo, P., DebRoy, T., and McNallan, M. J., 1988,"Surface Tension of Binary Metal-Surface Active Solute Systems under Conditions Relevant to Welding Metallurgy," Metall. Trans. B, **19**, pp. 483–491.
[170] Heiple, C. R., and Roper, J. R., 1982,"Mechanism for Minor Element Effect on GTA Fusion Zone Geometry," Weld. J., **61**, pp. 97-s–102-s.
[171] Lei, Y., Shi, Y., Murakawa, H., and Ueda, Y., 1997, "Numerical Analysis of the Effect of Sulfur Content Upon Fluid Flow and Weld Pool Geometry for Type 304 Stainless Steel," Trans. JWRI, **26**, pp. 8–15.
[172] Wang, Y., Shi, Q., and Tsai, H. L., 2001, "Modeling of the Effects of Surface-Active Elements on Flow Patterns and Weld Penetration," Metall. Mater. Trans. B, **32**, pp. 145–161.
[173] Wei, P. S., and Chow, Y. T., 1992, "Beam Focusing Characteristics and Alloying Element Effects on High-Intensity Electron Beam Welding," Metall. Trans. B, **23**, pp. 81–90.
[174] Guosheng, Z., Fauchet, P. M., and Siegman, A. E., 1982, "Growth of Spontaneous Periodic Surface Structures on Solids During Laser Illumination," Phys. Rev. B, **26**, pp. 5366–5381.
[175] Sipe, J. E., Young, J. F., Preston, J. S., and van Driel, H. M., 1983, "Laser-Induced Periodic Surface Structure. I. Theory," Phys. Rev. B, **27**, pp. 1141–1154.
[176] Brueck, S. R. J., and Ehrlich, D. J., 1982, "Simulated Surface-Plasma-Wave Scattering and Growth of a Periodic Structure in Laser-Photodeposited Metal Films," Phys. Rev. Lett., **48**, pp. 1678–1681.
[177] Akhmanov, S. A., Emel'yanov, V. I., Koroteev, N. I., and Seminogov, V. N., 1985, "Interaction of Powerful Laser Radiation With the Surfaces of Semiconductors and Metals: Nonlinear Optical Effects and Nonlinear Optical Diagnostics," Sov. Phys. Usp., **28**, pp. 1084–1124.
[178] Turner, J. S., 1973, *Buoyancy Effects in Fluids*, Cambridge University Press, Cambridge.
[179] Ellegaard, C., Hansen, A. E., Haaning, A., Hansen, K., Marcussen, A., Bohr, T., Hansen, J. L., and Watanabe, S., 1998, "Creating Corners in Kitchen Sinks," Nature (London), **392**, pp. 767–768.
[180] Thoroddsen, S. T., and Sakakibara, J., 1998, "Evolution of the Fingering Pattern of an Impacting Drop," Phys. Fluids, **10**, pp. 1359–1374.
[181] Allen, R. F., 1975, "The Role of Surface Tension in Splashing," J. Colloid Interface Sci., **51**, pp. 350–351.
[182] Mundo, Chr., Sommerfeld, M., and Tropea, C., 1995, "Droplet-Wall Collisions: Experimental Studies of the Deformation and Breakup Process," Int. J. Multiphase Flow, **21**, pp. 151–173.
[183] Bhola, R., and Chandra, S., 1999, "Parameters Controlling Solidification of Molten Wax Droplets Falling on a Solid Surface," J. Mater. Sci., **34**, pp. 4883–4894.
[184] Pasandideh-Fard, M., Qiao, Y. M., Chandra, S., and Mostaghimi, J., 1996, "Capillary Effects During Droplet Impact on a Solid Surface," Phys. Fluids, **8**, pp. 650–659.
[185] Bejan, A., and Gobin, D., 2006, "Constructal Theory of Droplet Impact Geometry," Int. J. Heat Mass Transfer, **49**, pp. 2412–2419.
[186] Oron, A., Davis, S. H., and Bankoff, S. G., 1997, "Long-Scale Evolution of Thin Liquid Films," Rev. Mod. Phys., **69**, pp. 931–980.
[187] Craster, R. V., and Matar, O. K., 2009, "Dynamics and Stability of Thin Liquid Films," Rev. Mod. Phys., **81**, pp. 1131–1198.
[188] Bussmann, M., Chandra, S., and Mostaghimi, J., 2000, "Modeling the Splash of a Droplet Impacting a Solid Surface," Phys. Fluids, **12**, pp. 3121–3132.
[189] Eres, M. H., Schwartz, L. W., and Roy, R. V., 2000, "Fingering Phenomena for Driven Coating Films," Phys. Fluids, **12**, pp. 1278–1295.
[190] Dunn, G. J., Duffy, B. R., Wilson, S. K., and Holland, D., 2009, "Quasi-Steady Spreading of a Thin Ridge of Fluid With Temperature-Dependent Surface Tension on a Heated or Cooled Substrate," Q. J. Mech. Appl. Math., **62**, pp. 365–402.
[191] Haskett, R. P., Witelski, T. P., and Sur, J., 2005, "Localized Marangoni Forcing in Driven Thin Films," Physica D, **209**, pp. 117–134.
[192] Beerman, M., and Brush, L. N., 2007, "Oscillatory Instability and Rupture in a Thin Melt Film on its Crystal Subject to Freezing and Melting," J. Fluid Mech., **586**, pp. 423–448.

The Experimental and Theoretical Evaluation of an Indirect Cooling System for Machining

Jay C. Rozzi
Principal Engineer
e-mail: jcr@creare.com

John K. Sanders
Engineer
e-mail: jks@creare.com

Weibo Chen
Engineer
e-mail: wbc@creare.com

Creare Incorporated,
16 Great Hollow Road,
Hanover, NH 03755

Cutting fluids have been used in machining processes for many years to decrease the temperature during machining by spraying the coolant into the machining zone directly on the cutting tool and the part. This has the effect of decreasing the tool temperature, which increases tool life and improves the part quality. These benefits come with significant drawbacks. Cutting fluids are environmentally unfriendly, costly, and potentially toxic. An alternative that has been evaluated in this paper is an internal cooling system (ICS) for lathe turning, which cools the cutting tool using a very small amount of an inert, cryogenic working fluid routed through a microchannel heat exchanger (MHX) that is mounted beneath the cutting tool insert. The working fluid absorbs the heat generated during the machining process after which it is harmlessly vented to the environment. This indirect cooling technique results in an environmentally friendly machining process that uses no cutting fluids, enables increased processing speed, and reduces manufacturing costs. An approximate heat transfer model was developed and used to predict the tool life as a function of the tool cooling approach for various speeds. Machining experiments were completed to validate the heat transfer model and confirm that the ICS can significantly improve tool life relative to conventional flood cooling. The validated model was then used to evaluate alternative cooling approaches using the ICS. It was found that the use of a cryogenic working fluid can significantly improve tool life at all cutting speeds but that the latent heat capacity of the working fluid should exceed the expected maximum heat transfer rate into the tool. This work established that the ICS approach is an effective means to increase tool life without the disadvantages associated with external cryogenic cooling methods. [DOI: 10.1115/1.4002446]

Keywords: heat transfer, two-phase, cryogenic, machining, microchannel

1 Introduction

Cutting fluids have been used in machining processes for many years to increase lubricity and decrease the cutting temperature, increasing tool life and part quality. These fluids are needed because the lathe turning process is characterized by severe plastic deformation of the material in regions known as the primary and secondary shear zones. Within the primary shear zone for orthogonal machining (Fig. 1), the material strain rate reaches a range of 10^3–10^4 s^{-1}, which is several orders of magnitude higher than most metal forming and deformation processes. For orthogonal machining, about 10–15% of the mechanical energy expended during material deformation in the primary shear zone is stored as strain energy in the chip. The remaining thermal energy generated in orthogonal machining results in local sensible heating, which induces local changes in the thermophysical and mechanical properties of the material and overall process conditions such as the occurrence of BUE (built-up-edge), the degradation of the final surface quality, and the presence of significant wear on the tool [1,2]. The region along the tool-chip interface is known as the secondary shear zone. For most metals, this zone is comprised of sticking and sliding regions. Within the sticking region, the chip material velocities at the tool-chip interface are zero and the shear stress is equal to the material shear strength. At the onset of sliding, the increase of the local material shear strength by work hardening exceeds the flow induced shear stress, resulting in the largest tool-chip interface temperatures due to frictional heating. For some materials, the flank wear zone is another significant source of thermal energy due to frictional heating. The sources of heat in the primary, secondary, and flank wear zones raise the temperature of the tool and rapidly accelerate the rate of tool wear by thermal erosion at high cutting speeds [3].

The machining zone is typically flooded with cutting fluid, which removes some, but not all, of the generated thermal energy. Low speeds and feeds are typically used with conventional flood cooling, minimizing the heat buildup at the tool tip [4]. The use of these fluids is costly. Contaminated cutting fluid must be disposed of safely. These fluids must be cleaned from contaminated chips prior to disposal. Burned-on fluid residue from heat-treated parts can add another step in the production process and increase costs. In a recent study, the procurement, maintenance, and disposal of these fluids represented 16% of the total machining cost [5]. These fluids also pose significant health risks to operators. Contact with cutting fluids causes skin diseases (dermatitis) and some of the cutting fluid additives are carcinogens. Continuous exposure to the mist generated from cutting fluids also causes respiratory problems. As a result, there have been recent efforts to use alternative approaches to cool cutting tools during machining including high-pressure cooling systems, minimum quantity lubricant (MQL) systems, external cooling with cryogens, and internal cooling approaches. Each of these is discussed below.

1.1 High-Pressure Cooling. High-pressure coolants with very precise delivery systems have been used in lathe turning operations to try to force the coolant into the tool-chip interface or onto the tool surfaces and prolong tool life [6]. These systems typically require high-pressure pumping systems capable of pressurizing the coolant to 70 MPa or more. They also require small, precisely placed nozzles to direct the coolant into specific locations.

1.2 MQL. In MQL systems, a small flow rate of an oil-based

Manuscript received June 25, 2009; final manuscript received January 12, 2010; published online November 15, 2010. Assoc. Editor: Wilson K. S. Chiu.

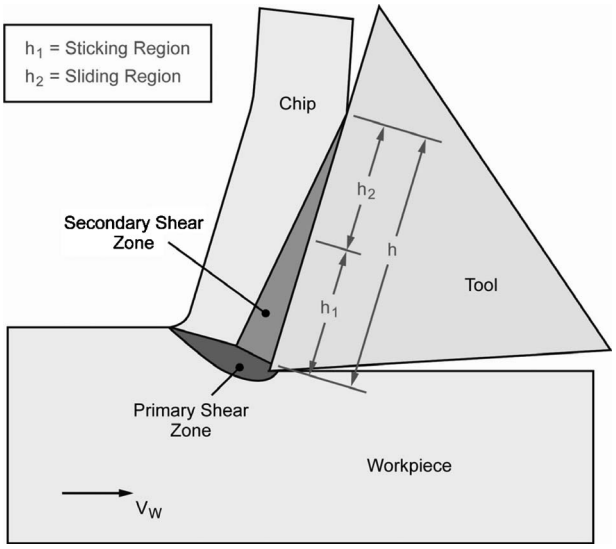

Fig. 1 Schematic illustrating heat generation during orthogonal machining

coolant pumped at high-pressure through a specialized nozzle produces a fine coolant mist. This mist contains high velocity microdroplets of coolant that are directed by a carrier gas at specific locations on the cutting tool. When combined with the high velocity of the gas, the droplets and the gas jet cool the tool more effectively than a conventional flood coolant. Because MQL is not integrated with the tool, the nozzles must be precisely located during machining operations to be effective. In some industrial machining applications, the nozzles require frequent cleaning and maintenance.

1.3 Cryogenic Machining. Cryogenic machining approaches involve directing a stream of liquid nitrogen or other cryogen into the machining zone or onto the cutting tool [7–11]. Some experiments have shown no substantial improvement in the tool life because the strength of some metals increases as the temperature decreases, limiting the benefit of cutting tool cooling. Because this is essentially the direct replacement of a flood coolant with a cryogen, the flow rates required are typically large (>5 l/min). The consequent large amount of generated vapor requires the use of handling and ventilation hardware, additional operator training, and process controls.

1.4 Indirect Approaches. Indirect cooling approaches for cooling cutting tools during machining have been attempted [12–14]. In most cases, these systems were comprised of heat pipes or liquid flows (e.g., water) used to transport heat from the tip of the cutting tool to an external heat sink. These approaches have not been able to sufficiently improve performance relative to flood cooling to offset implementation and operational costs.

The difficulty in effectively cooling the cutting edge during machining has three critical elements. First, the heat fluxes near the cutting edge are high (>500 W/cm^2) and confined to a small area corresponding the location of tool-chip contact (<1 mm^2). This fact limits the effectiveness of any external cooling approach because the achievable tool-chip interface temperature will be determined by the thermal resistances associated with the material or the tool geometry. In addition, such high heat fluxes are not easily removed using an internal cooling method with a single-phase fluid without a large flow rate and correspondingly large pumping power, cost, and infrastructural support. Second, the ability to locate the heat sink near the cutting edge is severely limited by the tooling itself, which was not designed to accommodate a cooling system of any type. Third, to achieve wide implementation, any approach to indirectly cool the cutting tool during machining must be affordable and able to be integrated with conventional machine tools.

The following sections describe the work completed to develop an ICS approach for lathe turning. First, analytical modeling was completed to design the ICS. Second, the ICS and the associated support system was designed and fabricated. Third, exhaustive testing to characterize the performance of the ICS was completed. Fourth, the analytical modeling was compared with the experimental results and other cooling options were evaluated. Each of these elements is discussed in more detail in the following sections.

2 Modeling

The objective of the numerical modeling was to enable the design of the ICS approach for nominal machining conditions. First, the interfacial heat transfer rate between the cutting tool and the chip was evaluated using established analytical models. Second, an approach was developed to relate the temperature of the cutting tool during machining to the produced tool wear. Third, a thermal resistance model was developed to quantify the tool-chip interface temperature and enable predictions of the effectiveness of various cooling approaches. Each of these is discussed in more detail below.

2.1 Estimate of Heat Transfer Rate. The volumetric heat generation, q''' associated with a machining operation is expressed as $q''' = \psi / V \int_V \dot{\varepsilon} \overline{\sigma} dV$, where $\dot{\varepsilon}$, $\overline{\sigma}$, and V are the strain rate during machining, the material flow stress, and the volume of the strained material in the primary shear zone, respectively. The constant ψ represents the fraction of the deformation energy that is dissipated as sensible heating. For metals, the value of this constant is 0.8 or higher [1,2]. The energy generated in the primary shear zone can be manifested as the heating of the eventual chip after machining or can be transferred to the tool. The fraction of heat flowing into the tool is a function of the tool geometry, the material, the machining conditions, and other variables. Established methods were used to estimate the maximum heat transfer rate into each cutting edge on the tool, q_t. For simplicity, an orthogonal (i.e., 2D planar) model was used to develop estimates of the cutting forces and the heat transfer to the tool.

Over the last several years, commercial software packages (ABAQUS®, DEFORM®, and ADVANTEDGE®) have enabled detailed calculations of machining mechanics and, to a limited extent, heat transfer. However, computational models can be complex to build and the software can be expensive to purchase. For these reasons, a simplified approach was used that was based on analytical modeling [15]. While potentially not as accurate as a full computational simulation, it was determined that this approach was suitable for engineering calculations, where the objective was to develop order-of-magnitude estimates of the total heat transfer into the tool during machining. To complete these calculations, the frictional force on the tool in orthogonal machining [16] for a zero rake angle tool is first estimated as

$$F_t = \frac{\cos \beta}{\sin(\phi + \beta)} \left(\frac{\mu \tau_s t_c w}{\sin \phi} \right) \tag{1}$$

where F_t is the frictional force on the rake face of the cutting tool, β is the friction angle, ϕ is the shear plane angle, μ is the friction coefficient between the chip and the tool, τ_s is the shear strength of the machined material, t_c is the chip thickness, and w is the width of the cut. Some of these quantities can be evaluated directly for given materials (μ and τ_s) while others are a function of the mechanics of the process. The chip thickness for a zero rake angle tool is estimated as

$$t_c = d(\tan \phi) \tag{2}$$

where d is the depth of cut. The friction angle is given by

Table 1 Machining conditions used to estimate energy generated at tool-chip interface

Variable	Value
Material	416 stainless steel
Nominal cutting speed	91.4 m/min
Feed rate	0.33 mm/rev
Depth of cut	1 mm
Tool-chip contact length	0.25 mm

$$\beta = \arctan \mu \tag{3}$$

These values were then used to calculate the total heat transfer to the cutting tool. As a part of this calculation, the strain at the shear plane is required. This was calculated using a fundamental mechanical model of orthogonal (2D) machining [17]. Using a slip-line method, the shear angle is calculated as

$$\phi = \frac{\pi}{4} - \beta \tag{4}$$

The calculation of the cutting force enabled the estimation of the heat transfer rate to the tool expressed as

$$q_t = (1 - \xi) F_t V_c \tag{5}$$

where V_c is the average chip velocity, calculated from a local mass balance of material flow. The factor, ξ describes the fraction of energy generated at the tool-chip interface that remains with the chip material and is estimated using the theory of Ref. [15] as

$$\xi = \frac{\dfrac{u_t V_w d\overline{A}}{k_t} - \dfrac{u_s}{\rho_w c_{p,s}}\left[1 + 1.328\sqrt{\dfrac{\alpha_s \overline{\gamma_s}}{V_w d}}\right]}{\dfrac{u_t V_w d\overline{A}}{k_t} + \dfrac{0.754 u_t}{\rho_w c_{p,c}}\sqrt{\dfrac{V_w d}{(\zeta/t_c)\alpha_c}}} \tag{6}$$

where the specific energy consumed by friction at the tool is given by

$$u_t = \frac{F_t V_c}{wd} \tag{7}$$

and the specific energy consumed at the shear plane is given as

$$u_s = \frac{F_s V_s \cos \phi}{wd} \tag{8}$$

and the mean shear strain for zero rake angle is expressed as

$$\overline{\gamma_s} = \frac{1}{\tan \phi} + \tan \phi \tag{9}$$

and where V_w is the mean workpiece velocity across the depth of cut, k_t is the thermal conductivity of the tool material, α_s and α_c are the thermal diffusivities of the workpiece material at the shear plane and chip temperatures, respectively, ρ_w is the density of the workpiece material, and $c_{p,s}$ and $c_{p,c}$ are the specific heats of the workpiece material at the shear plane and chip temperatures, respectively. The values of $\overline{A}$ and ζ are dependent upon the cutting tool configuration.

Using this model, the total heat transfer to the cutting tool as a function of process conditions was evaluated. For the machining conditions for 416 stainless steel [18] at the conditions given in Table 1, the total heat transfer into the tool was approximately 53 W. This fixed the nominal heat transfer rate into the tool over an area with the dimensions of the assumed tool-chip contact length (0.25 mm) and the depth of cut (1 mm). The local heat flux is, thus, 21.2 kW/cm^2 or 212 MW/m^2. During this project, only the cutting speed was changed to evaluate the changes in flank wear progression and other characteristics for otherwise fixed machining conditions. As shown in Fig. 2, the heat transfer rate into the tool is nearly a linear function of the cutting speed, as expected. At the highest cutting speed anticipated, 200 m/min, the total heat transfer rate is approximately 74 W.

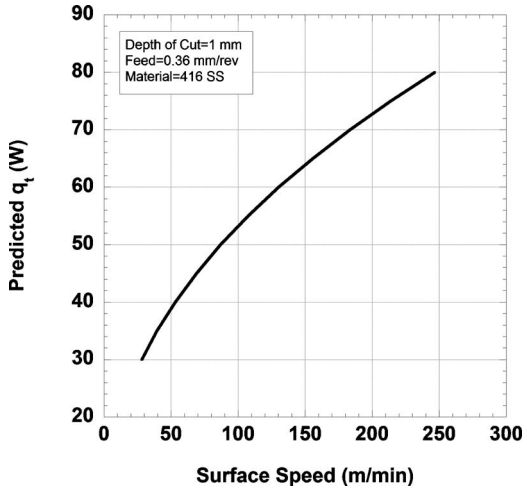

Fig. 2 Estimated heat transfer rate to the cutting tool for machining 416 stainless steel at conditions corresponding to Table 1 with varying surface (cutting) speed

As previously mentioned, the typical cutting tool is not perfectly sharp; hence, flank wear becomes the dominant wear mechanism for most hard materials. Depending upon the materials and the machining conditions, the heat input due to abrasive flank wear can be as large as that associated with sticking and sliding along the rake face. However, for the purposes of this work, this is a reasonable approach to estimate the total approximate heat transfer rate into the cutting tool.

2.2 Tool Wear Model. It has been established that for the conventional machining of metallic materials, the tool life (TL) can be expressed as

$$TL = D \cdot V_w^{-m} \tag{10}$$

where the constants D and m are unique to the material and tool combination and are typically established using experimental data. This relationship is known as Taylor's law [19]. There is a similar dependence of tool life on the tool-chip interface temperature [19], which can be expressed as

$$TL = C \cdot T_{ct}^{-n} \tag{11}$$

where the constants C and n are unique to the material and tool combination and determined using experimental data. For the purposes of this paper, the tool wear expression was nondimensionalized in the following manner:

$$\overline{TL} = C \cdot \overline{T_{ct}}^{-n} \tag{12}$$

where the nondimensional tool life and temperature are expressed as

$$\overline{TL} = \frac{TL}{TL_o} \tag{13}$$

where TL_o was chosen to be 60 min and

$$\overline{T_{ct}} = \frac{T_{ct}}{T_m} \tag{14}$$

where T_m is the material melting temperature.

Using the relationship expressed in Eq. (12), a predictive model for tool life can be developed if the tool-chip interface temperature can be predicted and if the empirical constants are known. In the next section, a simple thermal model for cutting tool cooling is described to enable the prediction of the tool-chip interface tem-

perature for various tool cooling approaches. Later in this paper, experiments will be used to establish the values of the empirical constants, enabling evaluation of the effectiveness of the ICS approach compared with flood cooling.

2.3 Tool-Chip Interface Temperature Model. A thermal model of cutting tool cooling using a thermal resistance approach was developed to enable prediction of the tool-chip interface temperature for various tool cooling approaches, flood cooling and the ICS. Each of these is discussed in more detail below.

2.4 Conventional Flood Cooling. The first model that was developed was for conventional flood cooling. Thermal energy that is input at the tip of the tool is first conducted through the insert. Next, the thermal energy is either absorbed by the heat sink associated with the shank of the tool or dissipated by convective cooling associated with the flood coolant flowing over the insert and shank. For the purposes of this calculation, it was assumed that the tool shank could absorb heat without a measurable temperature rise for the duration of machining. Given the large mass and size of the tool shank relative to the heat input, this was a reasonable assumption. Also, the transport of thermal energy through the chip to the flood coolant was neglected. To compute the values of the conduction resistances, the geometry of a commercially available lathe turning tool (Kennametal CSRPR 164D) and coated insert (Kennametal SPG 422 K720) was used. This tool and insert were also used for all of the experiments.

Because the tool-chip interface area is small compared with the tool insert, the spreading resistance through the insert was expressed as

$$R_{\mathrm{SPR}} = \frac{1}{S \cdot k_{\mathrm{INS}}}, \quad S = 2 \cdot D_{\mathrm{eff}} \tag{15}$$

where the conduction shape factor S was calculated using an effective diameter (D_{eff}) of the tool-chip interface region. The conduction resistance through the shank of the cutting tool was simply expressed as

$$R_{\mathrm{SH}} = \frac{L_{\mathrm{SH}}}{A_{\mathrm{SH}} \cdot k_{\mathrm{SH}}} \tag{16}$$

Finally, the convection resistance associated with flood cooling was expressed as

$$R_{\mathrm{CONV}} = \frac{1}{\overline{h}_{\mathrm{CONV}} A_{\mathrm{INS}}} \tag{17}$$

where $\overline{h}_{\mathrm{CONV}}$ is the average convection heat transfer coefficient and A_{INS} is the exposed surface area of the insert. Convection from the tool shank to the coolant was neglected. To compute the convection heat transfer coefficient, the Martin correlation for a single round nozzle [20] was used. Because the flood coolant used in the later experiments is 95% water by volume, water properties were used in the calculation. The 6.35 mm flood coolant nozzle was located approximately 50 mm above the cutting tool insert and issued coolant at approximately 5 l/min during the experiments and these values were also used in the calculation. The overall temperature rise at the tool-chip interface was approximated as

$$T_{ct} = q_t \left[R_{\mathrm{SPR}} + \left(\frac{1}{R_{\mathrm{SH}}} + \frac{1}{R_{\mathrm{CONV}}} \right)^{-1} \right] + T_{\mathrm{FLOOD}} = q_t R_{\mathrm{FLOOD}} + T_{\mathrm{FLOOD}} \tag{18}$$

Using the tool geometry and flood coolant conditions described above, the values of the various resistances were found to be 15.9 K/W for R_{SPR}, 18.2 K/W for R_{SH}, and 0.49 K/W for R_{CONV} for a total resistance for flood cooling R_{FLOOD} of 16.4 K/W. While this model is approximate, it does indicate that the overall thermal resistance is dominated by the spreading resistance within the insert itself; hence, any external, near-ambient temperature cooling method will not significantly reduce the overall thermal resistance or the tool-chip interface temperature.

2.5 ICS. The second model that was developed was for the ICS. In this approach, a MHX was placed directly beneath the cutting tool insert to remove the generated heat during machining. A small flow rate of two-phase, cryogenic fluid was used to provide cooling within the microchannel heat exchanger via latent heat transfer. Under certain conditions, the inlet cryogenic nitrogen flow may be completely vaporized without the heat flux exceeding the critical heat flux (CHF); thus, some portion of the generated thermal energy at the tool-chip interface would be dissipated by sensible heating of the nitrogen gas.

For the cases where the heat transfer rate from the tool exceeds the latent heat capacity of the MHX, i.e., $q_t > (1-x)\dot{m}h_{\mathrm{fg}}$, the temperature of the tool-chip interface was calculated as

$$\Delta T_{ct} = \Delta T_{\mathrm{MHX,TP}} + \Delta T_{\mathrm{MHX,SP}} \tag{19}$$

where the total temperature rise has been at the cutting edge and has been approximated as the temperature rise through the two-phase region for heat input less than or equal to $(1-x)\dot{m}h_{\mathrm{fg}}$ added to the total temperature rise through the single-phase region of the MHX for the remaining portion of the total heat input q_t that is larger than $(1-x)\dot{m}h_{\mathrm{fg}}$. Significant work in microchannel heat exchanger design and modeling has been completed by other researchers in the technical literature [21–24]. In this case, an ad hoc modeling approach was used to represent the complex interaction of the fixed heat transfer rate from the cutting tool and the potential single-phase heat transfer occurring in the MHX in a simplified manner. Using this approach, the thermal resistance of the MHX can be expressed as

$$R_{\mathrm{MHX,TP}} = \left[\frac{\ell_{\mathrm{MHX}}}{k_{\mathrm{MHX}} A_{\mathrm{INS}}} + \frac{1}{h_{\mathrm{MHX,TP}} \eta_{\mathrm{TP}} (A_f + A_b)} \right] \left[\frac{1}{F_{\mathrm{MHX}}} \right] \tag{20}$$

$$R_{\mathrm{MHX,SP}} = \left[\frac{\ell_{\mathrm{MHX}}}{k_{\mathrm{MHX}} A_{\mathrm{INS}}} + \frac{1}{h_{\mathrm{MHX,SP}} \eta_{\mathrm{SP}} (A_f + A_b)} \right] \left[\frac{1}{1 - F_{\mathrm{MHX}}} \right] \tag{21}$$

where F_{MHX} is equal to $(1-x)\dot{m}h_{\mathrm{fg}}/q_t$ and is an expression of the area of the MHX associated with two-phase heat transfer, ℓ_{MHX} is the thickness of the top plate of the MHX, k_{MHX} is the thermal conductivity of the MHX material (stainless steel), A_{INS} is the surface area of the bottom of the insert, $h_{\mathrm{MHX,TP}}$ is the two-phase heat transfer coefficient in the MHX, $h_{\mathrm{MHX,SP}}$ is the single-phase gaseous heat transfer coefficient in the MHX, A_f is the total area of the fins, and A_b is the total area of the exposed base. The factor η is expressed as

$$\eta = 1 - \frac{A_f}{A_f + A_b}(1 - \eta_f) \tag{22}$$

where η_f is the fin efficiency calculated assuming an adiabatic fin tip using the appropriate heat transfer coefficients in the two-phase and single-phase regions. Notably, this approach assumes that the heat flux is uniformly distributed over the surface of the MHX and that axial conduction in the MHX is negligible.

To calculate $h_{\mathrm{MHX,TP}}$, it was assumed that the working fluid was two-phase, cryogenic nitrogen (LN_2). The CHF for nucleate boiling for LN_2 is about 0.19–0.24 $\mathrm{MW/m^2}$ [25]. For a forced convection flow corresponding to the test conditions, CHF can reach as high as about 1.5 $\mathrm{MW/m^2}$ inside a small tube (~1 mm in diameter) [26]. For boiling, heat fluxes above CHF are in a regime known as film boiling, where the rate of vapor generation is so high that an insulating vapor layer is formed between the surface and the liquid cryogen. This vapor layer prevents direct contact between the liquid and the surface; thus, heat transfer rates are

dramatically reduced.

A spreadsheet model was setup to estimate the heat transfer coefficients for a two-phase, cryogenic nitrogen flow at the conditions of interest for the ICS (saturated flow, 151.6 kPa). To calculate $h_{MHX,TP}$, the Shah correlation as modified by Kandlikar [27] for nucleate flow boiling was used. As an initial estimate, it was assumed that the vapor quality at the inlet to the MHX was 0.5 and that the flow rate was 0.04 l/min (0.52 g/s of pure, saturated liquid nitrogen at 151.6 kPa), resulting in an $h_{MHX,TP}$ value of 6.8×10^5 W/m^2 K. With such high heat transfer coefficients, the temperature differences between the wall and the cryogenic flow are small. If the heat flux exceeds CHF, the heat transfer coefficients will reduce dramatically to about 500–2000 W/m^2 K in the film boiling regime, and wall temperatures will be more than 100 K higher than the nitrogen flow. The MHX geometry was designed to maximize the heat transfer while minimizing the overall pressure drop. The total heat transfer area is about 376 mm^2 on the current MHX. The heat flux on the heat transfer surface will exceed the critical value of about 0.5 MW/m^2 if the heat load is higher than 190 W. In that case, the wall could be blanketed by a continuous vapor film and the temperatures on the wall can be more than 100 K higher than the liquid nitrogen flow. Because the heat loads were well below this limit, it is not believed that film boiling occurred in the MHX. The single-phase heat transfer coefficient $h_{MHX,SP}$ was evaluated using standard correlations for laminar, fully-developed flow in a pipe or channel [20].

For $q_t > (1-x)\dot{m}h_{fg}$, the tool-chip interface temperature for of the was calculated as

$$T_{ct} = [(1-x)\dot{m}h_{fg}(R_{SPR} + R_{MHX,TP}) + T_{CRYO}] + [(q_t - (1-x)\dot{m}h_{fg}) \times (R_{SPR} + R_{MHX,SP}) + \overline{T_{SP}}] \quad (23)$$

where T_{CRYO} is the saturation temperature of the cryogen ($\sim$80 K) and $\overline{T_{SP}}$ is the mean temperature of the gas flow in the single-phase region.

For $q_t < (1-x)\dot{m}h_{fg}$, F_{MHX} is unity and the tool-chip interface temperature for of the ICS approach was calculated as

$$T_{ct} = \lfloor q_t(R_{SPR} + R_{MHX,TP}) + T_{CRYO} \rfloor \quad (24)$$

Using the computed values of the tool-chip interface temperature T_{ct}, predictions for the tool wear for the ICS approach will be compared with measured values and used to illustrate other cooling approaches. Next, the design and fabrication of the ICS is described.

3 ICS Design and Fabrication

The ICS tool holder consists of two main components, the MHX module and the cryogen transport and distribution hardware. Each of these is discussed in more detail below.

3.1 MHX Module Design. The MHX module consisted of the MHX itself and a base plate. A separate manifold was designed to route the working fluid in and out of the heat exchanger module. The base plate captured the MHX, enabled electron-beam welding, and interfaced with the manifold. The MHX slots were machined with a precision carbide saw blade. The MHX and a view of the base plate in the brazed tool holder are shown in Fig. 3. To evaluate the mechanical robustness of the design, the pressure distribution beneath the cutting tool insert was measured using a pressure sensitive film. It was found that the majority of the pressure was below the clamp on the top of the insert. Pressures in this region exceeded 10.3 MPa and were used to design the assembly with appropriate safety factors.

3.2 Tool Holder Design. Using mock-ups, it was determined that the best path for the working fluid was to transport it through a tube within a channel machined into the bottom of the tool holder. To achieve this, a layer was machined from the bottom of the tool holder and a passage was milled down its length. Within this passage, a thin-walled stainless steel tube was mounted that transported the cryogenic working fluid down the length of the tool holder. This tube was brazed to the manifold near the tip of the tool, which routes the cryogen from the tube exit to the heat exchanger module and to a vacuum-interface on the back of the tool. Thus, a vacuum space could be created between the transport tube wall and the channel within the tool holder. Small ceramic spacers were placed in various locations along the tube length to preclude tube-wall contact, which would act as a thermal short. The MHX manifold was needed due to the restricted geometry of the system. The entire assembly was vacuum-brazed. The completed tool holder is shown in the photograph of Fig. 3.

3.3 System-Level Design and Testing. A portable cart was designed and built to supply the cryogenic fluid to the tool holder. The main functions of the cart were to store the working fluid, provide a convenient means to control the flow rate, and monitor the amount of fluid left in the commercially available dewar. To transport the cryogen from the cart to the tool holder, a commercially available, vacuum-jacketed transfer line was purchased. This flexible line enabled the transport of the working fluid with a minimum of heat leak. A small test facility was built to evaluate the heat leak and the pressure drop in a preliminary version of the ICS and its support system as a function of the cryogenic fluid flow rate. The facility was instrumented with pressure transducers and thermocouples to quantify the heat leak to the ICS and the pressure drop within the internally mounted tube within the cutting tool.

The system heat leak was quantified by measuring the temperatures at the inlet and outlet of the tube. At high flow rates, the flow through the tube was saturated (vapor or vapor-liquid) as indicated by the temperature measurements. As the flow rate was decreased during the test, the inlet to the test section remained saturated until a critical flow rate value was reached. At this critical flow rate, the temperature at the tube inlet just began to rise above saturation. Using this critical flow rate and the known thermodynamic properties of cryogenic nitrogen, the heat leak into the system was quantified. In addition, the vacuum-jacketed transfer line was removed for one test, enabling the heat leak of the other components to be isolated. Based on our initial tests, approximately 77% of the total heat leak was in the dewar withdrawal system. For this reason, a custom withdrawal device was designed and installed in the dewar to reduce this heat leak. Also, the system was redesigned to minimize the number of valves and to upgrade the connections between sections to thermally insulating bayonet connections. As a result, the vapor quality at the inlet to the tool holder (Fig. 4) and the pressure drop through the internal tube mounted in the tool holder (Fig. 5) were substantially reduced. The pressure drop predictions are based on the correlation for the two-phase multiplier given by Friedel [27].

4 Results and Discussion

In this section, the results from the machining tests will be discussed first. Second, the model validation will be described.

4.1 Machining Tests. Table 2 illustrates the test conditions for the 416 stainless steel parts that were machined for the validation of the ICS performance. For each test condition, three samples were machined with three separate inserts. Each insert was then examined using an optical microscope with a digital measuring stage for average flank wear, maximum flank wear, and notch wear consistent with ISO 3685. Typical flank wear on the insert for the 100 m/min condition is shown in Fig. 6 for conventional cooling with 5 l/min of conventional flood coolant compared with the ICS approach with 0.04 l/min of cryogenic nitrogen. One of the three inserts was then used for extended wear testing to determine the shape of the tool wear curve with time, which is nonlinear. After ensuring that the data at each experimen-

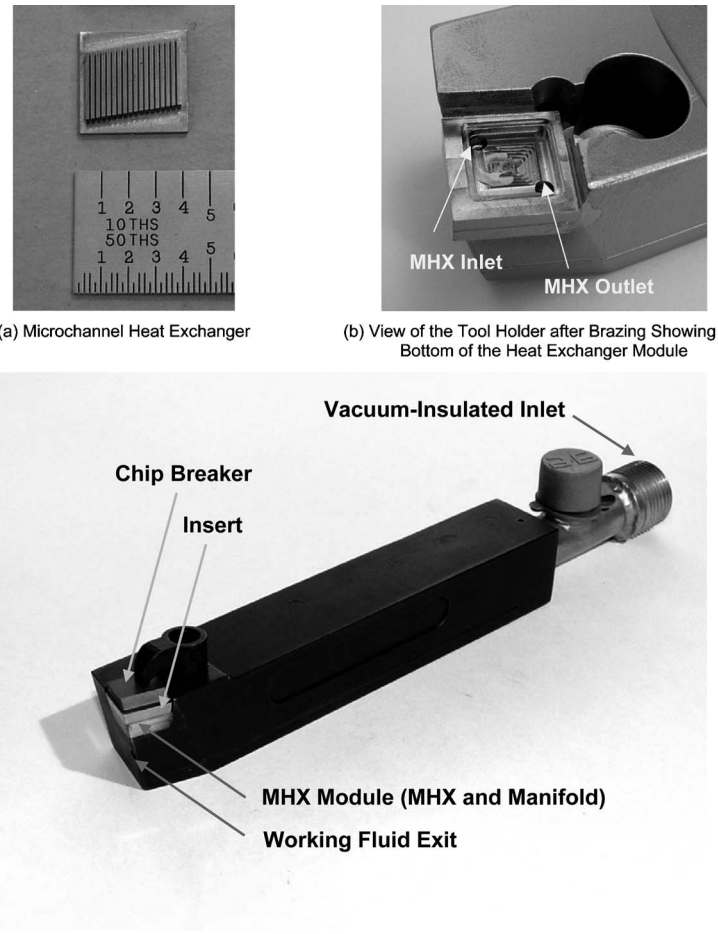

(a) Microchannel Heat Exchanger

(b) View of the Tool Holder after Brazing Showing the Bottom of the Heat Exchanger Module

(c) The Completed Tool Holder

Fig. 3 The (*a*) MHX, the (*b*) heat exchanger module, and the (*c*) fabricated tool holder

tal condition were consistent and reasonable, the tool life based on the average flank wear was computed. The experimental results are illustrated in Fig. 7.

Each data point shown is the result of 32 machining experiments of the type described in Table 2 and approximately 16 h of actual metal cutting. This figure clearly illustrates that the use of the ICS increases tool life compared with conventional synthetic coolants, which translates directly to machining cost reductions. As expected, increasing the cutting speed increases the overall heat transfer rate to the cutting tool, reducing its benefit relative to conventional flood cooling. At 200 m/min, the tool wear of both

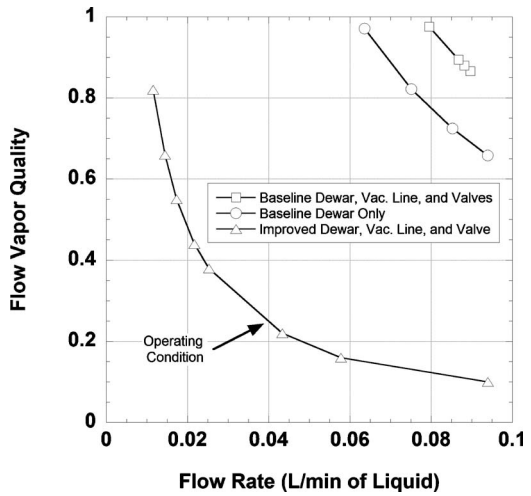

Fig. 4 Working fluid flow vapor quality at the tool holder inlet as a function of flow rate

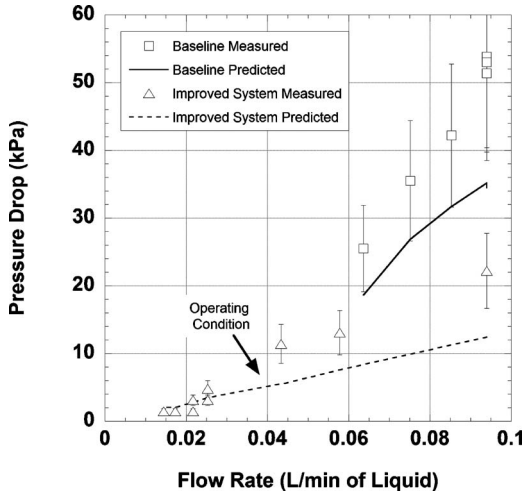

Fig. 5 Pressure drop measurements and predictions as a function of flow rate for the internal transport tube in the tool holder

Table 2 Test conditions

Variable	Value
Material	416 stainless steel
Insert geometry	SPG 422
Insert grade	KC720
Feed rate (mm/rev)	0.33
Cutting speeds (m/min)	85.3 to 200
Depth of cut (mm)	1
Length of cut (mm)	230
No. of cuts in one test (mm)	15
Flow rate of standard coolant if used (l/min)	5
Flow rate of liquid nitrogen for ICS (l/min)	0.04

systems is identical. In this case, the calculated heat transfer rate to the is in the range of 80 W, whereas the available latent heat transfer in the MHX $(1-x)\dot{m}h_{fg}$ is about 69 W. At this condition, the MHX performance is marginal and significant sensible heating of the exiting gas flow occurred. Further increases in the overall heat transfer rate into the cutting tool would need to be accompanied by an increased nitrogen flow rate to increase tool life relative to conventional flood cooling.

4.2 Model Validation. In this section, predictions the model developed in Sec. 2.2 will be compared with the experimental results and used to evaluate other tool cooling options. First, the flood cooling results will be used to establish the empirical constants present in the model. Second, the performance of the model for the ICS will be described. Third, the model will be used to evaluate other cooling options including a single-phase gaseous coolant through the MHX and an increased cryogenic nitrogen flow through the ICS such that no vaporization occurs. Each of these is discussed in more detail below.

Using the results from Fig. 7 for flood cooling, a simple curve fit was used to determine the empirical constants C and n from Eq. (12) as 0.714 and 3.90, as illustrated in Fig. 8. As described earlier, these constants only depend upon the material being machined, the tool material, and the tool geometry; thus, these constants should not be influenced by the cooling approach used to remove thermal energy from the machining operation. The constants above were then used to predict the performance of the ICS. The latent heat capacity of the ICS was approximately 69 W using the measured inlet quality to the MHX. To complete the predictions, Eq. (12) was combined with Eqs. (23) and (24) to complete the model for the ICS, expressed as

$$\overline{TL} = 0.714\left\{\frac{1}{T_m}[q_t(R_{SPR}+R_{MHX,TP})+T_{CRYO}]\right\}^{-3.90} \quad q_t < (1-x)\dot{m}h_{fg}$$

$$\overline{TL} = 0.714\left\{\frac{1}{T_m}[(1-x)\dot{m}h_{fg}(R_{SPR}+R_{MHX,TP})+T_{CRYO}+(q_t-(1-x)\dot{m}h_{fg})(R_{SPR}+R_{MHX,SP})+\overline{T}_{SP}]\right\}^{-3.90} \quad q_t > (1-x)\dot{m}h_{fg} \tag{25}$$

The results of this model are compared with the experimental results as illustrated in Fig. 9.

The agreement between the predicted and measured tool life is reasonable; however, the model somewhat underpredicts the tool life at low cutting speeds. This may be due to a simplification when evaluating the flow boiling heat transfer coefficient within the MHX. In Fig. 3, the MHX inlet is located perpendicular to the MHX; thus, the inlet two-phase mixture is similar to an impinging jet on the upper (unfinned) surface that may result in a significant local heat transfer enhancement that was neglected in the analysis. Near the cutting speed associated with the latent heat capacity of the MHX ($\sim$180 m/min), the predicted tool life departs from the linear region at lower cutting speeds and this trend is reasonably consistent with the experimental results. This effect is due to the increased overall thermal resistance associated with the single-phase region in the MHX, whose extent increases as the surface speed increases above 180 m/min.

In Fig. 10, the model was used to compare different tool cooling approaches using the ICS. As a baseline, the predictions for the simple flood cooling approach as described in this paper are shown. If the ICS has sufficient latent heat capacity to retain the two-phase flow throughout MHX, the tool life is substantially increased at all surface speeds. The high heat transfer coefficient and low cryogen temperature provide an efficient, effective means to remove thermal energy from the tool-chip interface. At the other extreme, if the vapor quality is near unity when the nitrogen flow enters the MHX, the heat transfer and the ICS performance are negatively impacted such that conventional flood cooling is a reasonable alternative. Interestingly, the ICS with single-phase gas flow has a slightly higher predicted tool life at low speeds and a lower tool life at higher speeds relative to flood cooling. This behavior is likely due to the fact that as the single-phase gas proceeds through the MHX, its temperature increases; hence, the mean temperature $\overline{T}_{SP}$ is near 80 K near the inlet and steadily increases through the MHX. If the latent heat capacity of the ICS is reduced to 50 W ($x=0.5$), the MHX will be in fully two-phase region at low speeds. As the surface speed is increased to a value beyond the latent heat capacity, the heat transfer within the MHX will be partially two-phase and partially single-phase after which the fraction of the overall heat transfer in the single-phase region increases as the speed increases. This is evident in Fig. 10 as the predicted tool life rapidly decreases relative to the fully two-phase system. This decrease in predicted tool life continues until the

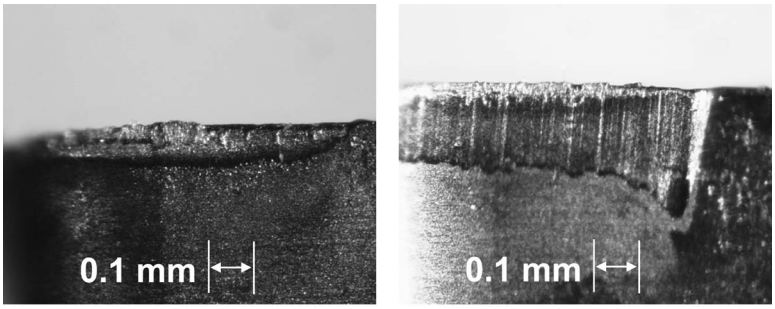

(a) Indirect Cooling System (0.04 L/min) (b) Conventional Flood Coolant (5 L/min)

Fig. 6 Photographs of the tool flank wear region for 416 stainless steel after 60 min of machining at a surface speed (cutting speed) of 100 m/min

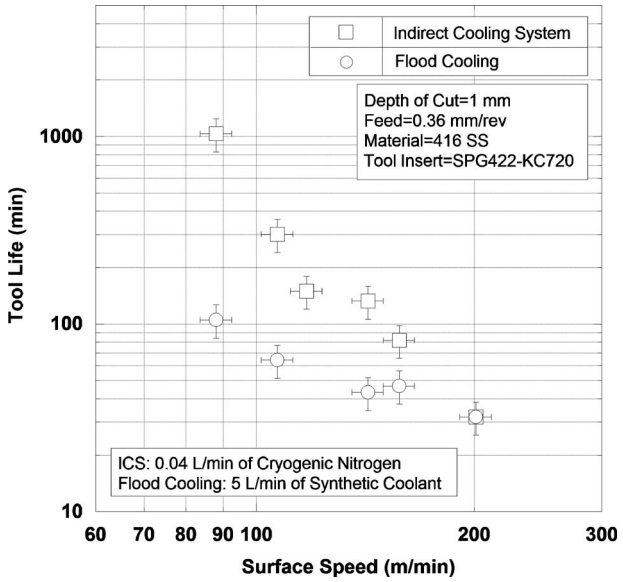

Fig. 7 Tool life test results for 416 stainless steel for flood cooling and the ICS

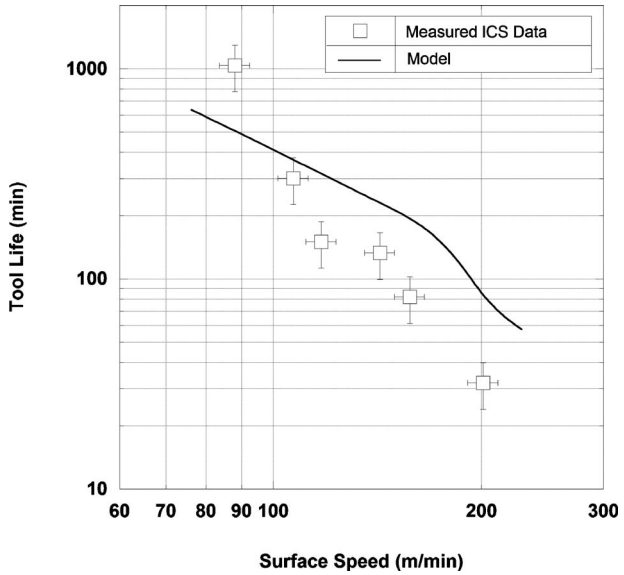

Fig. 9 Comparison of measured and predicted ICS performance

curve asymptotes to a value just above the full single-phase ICS due to the decreased value of $\overline{T}_{SP}$ relative to the fully single-phase gaseous case. Comparing the results of 69 W ($x=0.3$) latent heat capacity of the ICS with flood cooling repeats the experimental conditions (Fig. 7) with the analytical model. The model captures the rapid decrease in tool life after the latent heat capacity is exceeded such that the tool life for ICS and flood cooling at 200 m/min are approaching an identical value. This result demonstrates that the model is consistent with the experimental trends. If single-phase liquid water is used in the ICS, the performance is poorer than conventional flood cooling. Thus, to utilize the ICS to reduce the tool-chip interface temperature and extend tool life, the use of a cryogenic working fluid is absolutely essential.

5 Conclusions

An ICS was designed with a small flow rate of cryogenic nitrogen ($\sim$0.04 l/min) to replace a high flow rate of a conventional flood coolant or an external cryogen ($\sim$5 l/min) for effective cooling of a cutting tool. The ICS and the associated MHX module were developed to integrate with a commercial tool holder and system-level testing confirmed that the heat leak and pressure drop were minimized. Additionally, a model was developed to relate the predicted tool-chip interface temperature to the tool life. Performance testing confirmed that the ICS approach can significantly improve the tool life relative to conventional flood cooling, enabling processing cost reductions by improving processing speed or by preserving tooling. Reasonable agreement was obtained between the predictive model developed for tool life and the experimental results; thus, using the empirical constants from flood cooling tests to evaluate a wide range of tool cooling options

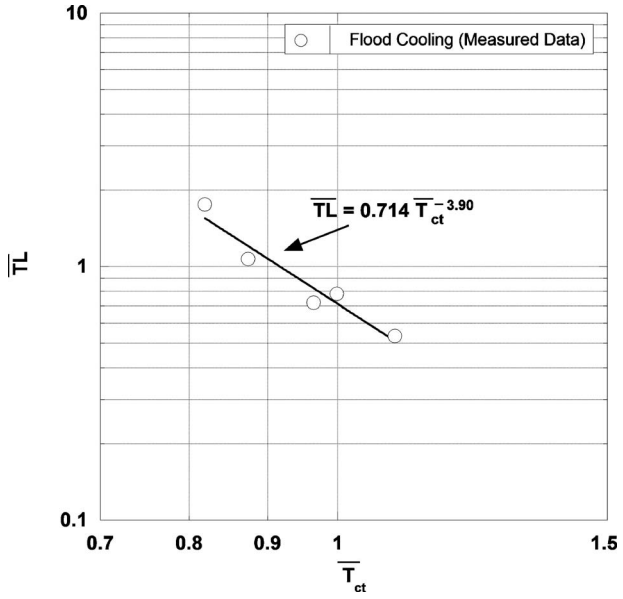

Fig. 8 Determination of constants *C* and *n* in Eq. (12) using the tool life measurements for flood cooling

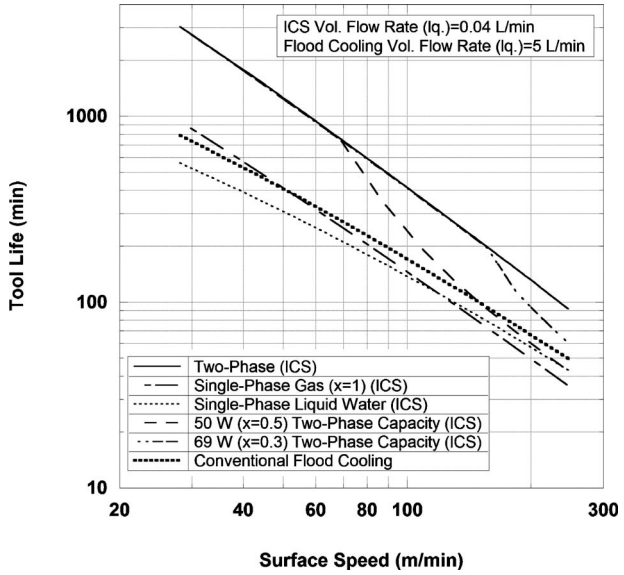

Fig. 10 Comparison of various cooling approaches for the tool geometry and machining conditions corresponding to the experiments

is a viable approach. The model was used to evaluate various cooling approaches and it was shown that to achieve a significant tool life improvement at all speeds, the latent heat capacity of the MHX must exceed the maximum expected heat input to the tool. The model also showed that to achieve significant increases in tool life with the ICS, the use of a cryogenic working fluid is critical. Eventual integration of the ICS onto the manufacturing floor will greatly enhance the environmental friendliness of manufacturing operations in small and medium sized shops while extending their manufacturing capability and reducing costs. Recently, the ICS approach has been extended to milling and drilling operations for advanced materials, including titanium and ceramic matrix composites, and will be the subject of future publications. These operations are the most prevalent machining operations in the industry and will result in a wide application of the ICS.

Acknowledgment

We gratefully acknowledge the support of the U.S. Environmental Protection Agency SBIR Program through Contract Nos. 68-D-02-016 and 68-D-03-042 and the U.S. Army Armament Research and Development Center (ARDEC) through Contract No. DAAE30-03-D-1009-2. We would also like to acknowledge the support of our commercialization partner, MAG Industrial Automation Systems (MAG IAS).

Nomenclature

- A = area (m^2)
- $\overline{A}$ = tool dependent geometric factor
- c_p = specific heat (J/kg K)
- d = depth of cut (m)
- q''' = heat generation rate (W/m^3)
- V = volume (m^3), velocity (m/s)
- F = cutting force (N)
- h = combined length of sticking and sliding regions (m), heat transfer coefficient (W/m^2 K)
- h_1 = length of sticking region (m)
- h_2 = length of sliding region (m)
- h_{fg} = latent heat of vaporization (J/kg)
- k = thermal conductivity (W/m K)
- ℓ_{MHX} = thickness of the top plate of the MHX (m)
- $\dot{m}$ = mass flow rate (kg/s)
- q = heat transfer rate (W)
- R = thermal resistance (K/W)
- TL = tool life (min)
- t = thickness (m)
- u = specific cutting energy (J/mm^3)
- w = width (m)
- x = vapor quality at MHX inlet

Greek Symbols

- α = thermal diffusivity (m^2/s)
- β = friction angle (rad)
- $\dot{\varepsilon}$ = strain rate (s^{-1})
- ϕ = shear plane angle (rad)
- η = dimensionless factor, efficiency
- μ = friction coefficient
- $\overline{\sigma}$ = material flow stress (N/m^2)
- τ = shear stress (N/m^2)
- ξ = fraction of thermal energy generated at tool-chip interface that remains with the chip
- ψ = fraction of machining energy dissipated as heat
- ζ = tool dependent geometric factor

Subscripts

- b = exposed base
- c = chip
- COAT = coating
- CONT = contact
- CONV = convection
- ct = tool-chip interface
- eff = effective
- f = fin
- FLOOD = flood cooling
- INS = insert
- m = melting
- MHX = microchannel heat exchanger
- o = reference
- s = shear plane
- SH = tool shank
- SP = single-phase
- SPR = spreading
- t = tool
- TP = two-phase
- w = workpiece

References

[1] Taylor, G. I., and Quinney, H., 1934, "The Latent Energy Remaining in a Metal After Cold Working," Proc. R. Soc. London, Ser. A, **143**, pp. 307–326.
[2] Taylor, G. I., and Quinney, H., 1937, "The Emission of Latent Energy Due to Previous Cold Working When a Metal Is Heated," Proc. R. Soc. London, Ser. A, **163**, pp. 157–181.
[3] El Wakil, S., 1989, *Processes and Design for Manufacturing*, Prentice-Hall, Englewood Cliffs, NJ.
[4] Saada, J., 1990, "Take a Bite Out of Titanium," Cutting Tool Engineering, **42**(7), pp. 45–50.
[5] Sutherland, J., 2000, "Cutting Fluid Issues," www.mfg.mtu.edu/marc/research
[6] López de Lacalle, L. N., Pérez-Bilbatua, J., Sánchez, J. A., Llorente, J. I., Gutiérrez, A., and Albóniga, J., 2000, "Using High Pressure Coolant in the Drilling and Turning of Low Machinability Alloys," Int. J. Adv. Manuf. Technol., **16**, pp. 85–91.
[7] Hong, S. Y., and Ding, Y., 2001, "Cooling Approaches and Cutting Temperatures in Cryogenic Machining of Ti–6A1–4V," Int. J. Mach. Tools Manuf., **41**, pp. 1417–1437.
[8] Hong, S. Y., Markus, I., and Jeong, W.-C., 2001, "New Cooling Approach and Tool Life Improvement in Cryogenic Machining of Titanium Alloy Ti–6A1–4V," Int. J. Mach. Tools Manuf., **41**, pp. 2245–2260.
[9] Hong, S. Y., Ding, Y., and Jeong, W., 2001, "Friction and Cutting Forces in Cryogenic Machining of Ti–6A1–4V," Int. J. Mach. Tools Manuf., **41**, pp. 2271–2285.
[10] Dhar, N. R., Paul, S., and Chattopadhyay, A. B., 2002, "Role of Cryogenic Cooling on Cutting Temperature in Turning Steel," ASME J. Manuf. Sci. Eng., **124**(1), pp. 146–154.
[11] Paul, S., and Chattopadhyay, A. B., 1995, "Effects of Cryogenic Cooling by Liquid Nitrogen Jet on Forces, Temperature and Surface Residual Stresses in Grinding Steels," Cryogenics, **35**, pp. 515–523.
[12] Liu, J., and Chou, Y. K., 2007, "Cutting Tool Temperature Analysis in Heat-Pipe Assisted Composite Machining," ASME J. Manuf. Sci. Eng., **129**(5), pp. 902–910.
[13] Nishiwaki, N., Takeyama, H., and Hori, S., 1981, "A Method for Improving the Thermal Behaviour of Machine Tools With Heat Pipes," Bull. Jpn. Soc. Precis. Eng., **15**(4), pp. 249–250.
[14] Jeffries, N. P., and Zerkle, R. D., 1970, "Thermal Analysis of an Internally-Cooled Metal-Cutting Tool," Int. J. Mach. Tools Manuf., **10**, pp. 381–399.
[15] Lowen, E., and Shaw, M., 1954, "On the Analysis of Cutting-Tool Temperatures," Trans. ASME, **76**, pp. 217–231.
[16] Ernst, H., and Merchant, M. E., 1940, *Chip Formation, Friction, and High Quality Machined Surfaces*, Surface Treatment of Metals, Cleveland, OH, pp. 299–378.
[17] Lee, E. H., and Schaffer, B. W., 1951, "The Theory of Plasticity Applied to a Problem of Machining," J. Appl. Phys., **18**(4), pp. 405.
[18] Green, R. E., ed., 1996, *Machinery's Handbook*, 25th ed., Industrial, p. 994.
[19] Boothroyd, G., and Knight, W. A., 2006, *Fundamentals of Machining and Machine Tools*, Taylor and Francis, New York.
[20] Incropera, F. P., and DeWitt, D. P., 1990, *Fundamentals of Heat and Mass Transfer*, Wiley, New York.
[21] Kuo, C. J., and Peles, Y., 2009, "Flow Boiling of Coolant (HFE-7000) Inside Structured and Plain Wall Microchannels," ASME J. Heat Transfer, **131**, p. 121011.
[22] Cheng, P., Wang, G., and Quan, X., 2009, "Recent Work on Boiling and Condensation in Microchannels," ASME J. Heat Transfer, **131**, p. 043211.
[23] Liu, D., and Garimella, S. V., 2007, "Flow Boiling Heat Transfer in Microchannels," ASME J. Heat Transfer, **129**, pp. 1321–1332.

[24] Turner, S. E., Asako, Y., and Faghri, M., 2007, "Convection Heat Transfer in Microchannels With High Speed Gas Flow," ASME J. Heat Transfer, **129**, pp. 319–328.
[25] Frost, W., 1975, *Heat Transfer at Low Temperatures*, Plenum, New York.
[26] Verkhman, S. N., 1969, "Critical Heat Fluxes in Boiling of Liquid Nitrogen Underheated to Saturation Point in Forced-Flow Conditions," J. Appl. Mech. Tech. Phys., **10**(1), pp. 85–88.
[27] Rohsenow, W. M. , Hartnett, J. P. , and Cho, Y. I. , eds., 1998, *Handbook of Heat Transfer*, 3rd ed., McGraw-Hill, New York.

Modeling of the Off-Axis High Power Diode Laser Cladding Process

Shaoyi Wen
Graduate Research Assistant

Yung C. Shin
Professor
Mem. ASME

Center for Laser-based Manufacturing,
School of Mechanical Engineering,
Purdue University,
West Lafayette, IN 47907

Off-axis high power diode laser (HPDL) cladding is commonly used for surface quality enhancement such as coating, part repairing, etc. Although some laser cladding models are available in literature, little has been reported on the modeling of powder flow and molten pool for a rectangular beam with side powder injection. In this article, a custom-designed flat nozzle delivers the powder material into a distinct molten pool formed by a HPDL with a rectangular beam. A powder model is first presented to reveal the powder flow behavior below the flat nozzle. Key parameters such as nozzle inclination angle, rectangular beam profile, shielding gas flow rates, and powder feed rate are incorporated so that spatial powder density, powder velocity, and temperature distribution are distinctly investigated. Then in order to describe thermal and fluidic behaviors around the molten pool formed by the rectangular beam, a three-dimensional self-consistent cladding model is developed with the incorporation of the distributed powder properties as input. The level set method is adopted to track the complex free surface evolution. Temperature fields and fluid motion in the molten pool area resulting from the profile of rectangular beam are distinctly revealed. The effect of continuous mass addition is also embedded into the governing equations, making the model more accurate. A HPDL cladding with little dilution is formed and the simulated results agree well with the experiment. [DOI: 10.1115/1.4002447]

Keywords: HPDL, laser cladding, level set, track geometry

1 Introduction

Laser cladding with blown powder is widely used in the industry as an efficient method for surface quality enhancement. Basically, one or more metallic or nonmetallic layers are selectively deposited on the workpiece to improve the surface wear or corrosion resistance characteristics. The clad is formed by feeding powder coaxially or off-axis into a molten pool region caused by the localized laser beam. A high power diode laser (HPDL) with a wide rectangular beam spot provides great potential in efficiently producing wide clad tracks with flatter profiles than coaxial nozzles. Due to short wavelength (in the order of 808 nm), HPDL offers good metal coupling characteristics compared with other lasers, providing an increase of beam absorption by a factor of 2.5 over CO_2 wavelength [1–3]. Other advantages of HPDL include flexible beam shaping, increased beam quality, longer service time, and lower investment cost, etc. [3,4]. With these advantageous characteristics, HPDL cladding processes have been experimentally investigated [1,4–6]. Well bonded clad tracks with limited dilution and fine metallurgical structure have been produced [1,4–6], which indicates the effectiveness and versatility of the HPDL cladding process.

In order to understand the complex phenomena and mechanisms associated with laser cladding, it is essential to develop mathematical models to guide the process. Although some laser cladding models [7–17] have been presented in literature, the modeling of off-axis HPDL cladding processes has been seldom addressed. Jouvard et al. [7] presented an analytical model to evaluate two power thresholds, the first one of which is required for melting the substrate and the second one is for melting powder during flight. Due to complex track shape evolution, simplified assumptions such as predefined clad height [8,9] or flat surface [10] in the absence of powder were made to calculate the molten pool when coupling the powder flow. Simply assuming the molten pool profile as a part of circle, Kumar and Roy [11] developed a two-dimensional model for the blown-powder laser cladding process to study the influence of the Marangoni–Benard and Rayleigh–Benard convection on the process parameters. A volume of fluid algorithm was used by Choi et al. [12] to obtain the free surface shape in a two-dimensional mathematical model incorporating melting, solidification, and evaporation phenomena. Toyserkani et al. [13] developed a three-dimensional cladding model with a track development method by adding tiny objects on the previous domain in the melt pool with an assumption that the powder and melt pool are decoupled. A modified thermal conductivity was used to take into account the thermocapillary phenomena of the liquid metal without calculating the fluid flow. Huang et al. [14] developed a three-dimensional transient numerical model for the process of laser cladding in which fluid flow and heat transfer in solid-liquid phase change system were simulated. However, they used a simple flag variable method to update free surface shape and did not consider the effect of fluid motion and capillary force on the free surface geometry.

Recently, the level set method has been adopted in the modeling [15–17] for accurate prediction of free surface shape. Based on the semi-implicit finite-difference approximation method, Han et al. [15] presented a comprehensive two-dimensional model for the coaxial laser cladding process while considering the powder injection effect on melt pool flow pattern and penetration. Using a controlled-volume finite-difference method, Qi et al. [16] and He and Mazumder [17] developed a self-consistent three-dimensional model for direct metal deposition with coaxial powder injection. However, in all these previous studies, the effect of continual addition of mass and energy due to deposited powder was not rigorously considered. In this article, additional source terms responsible for the effect of continual addition of mass are incorporated, making the model more physically complete. An improved

Manuscript received June 18, 2009; final manuscript received January 11, 2010; published online November 16, 2010. Assoc. Editor: Wilson K. S. Chiu.

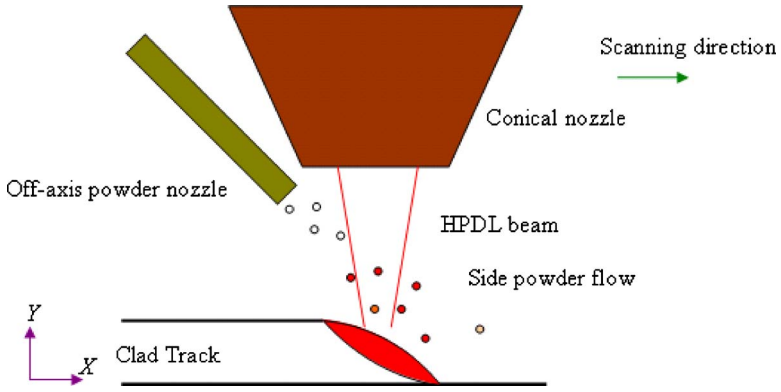

Fig. 1 Schematic HPDL cladding process

level set equation, which considers mass and energy conservation, is also proposed so that the whole set of governing equations are implicitly solved using a finite volume method.

As seen from the above discussion, current cladding models are not comprehensive yet and almost all involved lasers are of circular beam [7–17]. The distinct powder flow and molten pool created by a rectangular beam with side powder injection have not been reported to date. In this article, a custom-designed flat nozzle delivers the powder material into a distinct molten pool formed by a HPDL with a rectangular beam. A powder model is first presented to reveal the powder flow behavior below the flat nozzle. Key parameters, such as the nozzle inclination angle, the rectangular beam profile, shielding gas flow rates, and powder feed rate, are incorporated so that spatial powder density, powder velocity, and temperature distribution are distinctly investigated. Then in order to describe thermal and fluidic behavior around the molten pool formed by the rectangular beam, a three-dimensional self-consistent cladding model is developed with the incorporation of the distributed powder properties as input.

2 Mathematical Model

A schematic of the off-axis HPDL cladding process is shown in Fig. 1. An off-axis head (the powder flow nozzle and the optics) moves in X direction at a certain scanning speed over the surface of a stationary substrate. In the cladding process, the powders, whose feed rate is precisely controlled by a powder feeder, are fed into the laser spot region via a flat powder nozzle as seen in Fig. 1. During their flight, the particles travel through the laser irradiation zone in which the particles will be rapidly heated up as illustrated in Fig. 1. Collision between each two particles is not considered and laser attenuation is ignored due to low powder density and short laser powder interaction distance.

A molten pool is created by intense laser heating of the surface of the substrate and the current track layer. With laser scanning, the melt solidifies very quickly due to the high attendant cooling rate and a clad track is formed. The liquid motion in the molten pool is assumed to be incompressible and laminar. Powders falling in the region of the molten pool are assumed to get melted immediately while others falling outside the molten pool are considered lost. The effect of shielding gas pressure on the molten pool has been ignored.

The model in this paper consists of two parts. A powder model is first introduced in Sec. 2.1 to reveal the distinct powder flow behavior below the flat nozzle. Then a three-dimensional self-consistent cladding model, which is discussed in Sec. 2.2, is developed with the incorporation of the distributed powder properties and rectangular laser profile as input to address multiphysics such as mass addition, heat transfer, fluid flow, melting, and solidification during the off-axis HPDL cladding process.

2.1 Off-Axis Powder Flow

2.1.1 Calculation Domain. Figure 2 describes the three-dimensional calculation domain used in the powder flow model. The dimensions of the conical nozzle and flat powder nozzle and their relative positions are from the real configurations. The diameter of the conical nozzle is 47.00 mm and the flat nozzle slot opening is 4×14 mm^2. The nozzle angle in Fig. 2 is set at 38 deg from the horizontal plane. The ambient space below the nozzle is

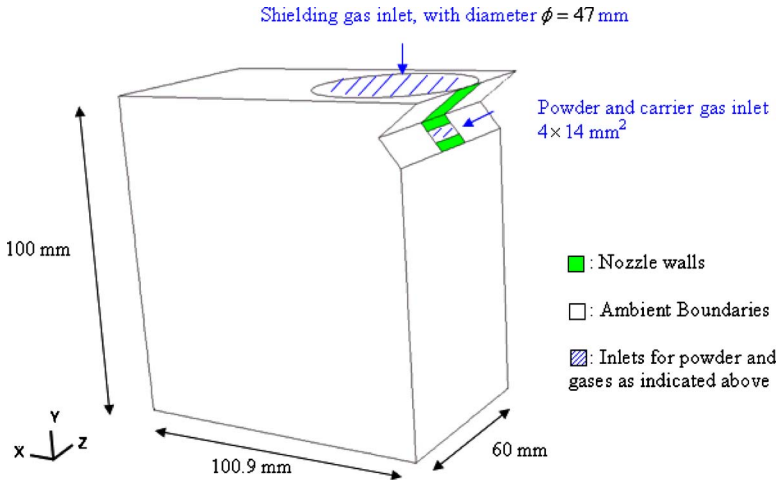

Fig. 2 Schematic 3D calculation domain for powder flow model

Table 1 Turbulent gas flow governing equation parameters

Equation	Φ	Γ	$\dot{S}_\Phi$
Mass	1	0	0
x-momentum	u	μ	$-\frac{\partial p}{\partial x}+\nabla\cdot\left(\mu\frac{\partial \mathbf{V}}{\partial x}\right)+\Psi_x$
y-momentum	v	μ	$-\frac{\partial p}{\partial y}+\nabla\cdot\left(\mu\frac{\partial \mathbf{V}}{\partial y}\right)+\Psi_y$
z-momentum	w	μ	$-\frac{\partial p}{\partial z}+\nabla\cdot\left(\mu\frac{\partial \mathbf{V}}{\partial z}\right)+\Psi_z$
k-equation	k	$\mu_l+\frac{\mu_t}{\sigma_k}$	$\rho(G_k-\varepsilon)$
ε-equation	ε	$\mu_l+\frac{\mu_t}{\sigma_\varepsilon}$	$\frac{\varepsilon}{k}(C_1\rho G_k-C_2\rho\varepsilon)$

chosen to be $100\times100.9\times60$ mm^3, which is large enough to make the boundaries not affected by the powder stream. The grid system is designed using tetrahedral meshes to fit the irregular shape domain except in the laser spot region, where fine cubic meshes were used to resolve the strong beam intensity for accurate calculation in the laser material interaction area.

In this paper, the gas phase is treated as continuum while the particle flow is simulated as a discrete phase that consists of particles dispersed in the continuum phase. The behavior of continuous gas phase is modeled by solving the time-averaged Navier–Stokes equations while the dispersed phase is solved in a Lagrangian frame of reference by tracking a certain number of particles through the calculated flow field. As powders flow through the gas, they interact with the laser beam. A unique user-defined function [18] is incorporated to solve the thermal behavior of the particle phase as calculation continues. The Lagrangian approach of the discrete phase model (DPM) in FLUENT has been used to solve each particle's dynamic behavior.

2.1.2 Modeling of Turbulent Flow. The steady turbulent gas flow in the powder stream is described by a general equation [19]

$$\nabla\cdot(\rho\mathbf{V}\Phi)=\nabla\cdot(\Gamma\nabla\Phi)+\dot{S}_\Phi \tag{1}$$

where ρ is the gas density, Φ is the dependent variable, Γ is the diffusivity, and $\dot{S}_\Phi$ represents any source terms associated with variable Φ. The momentum equations together with the two $k-\varepsilon$ equations [20,21] can be obtained by appropriate assignment of Φ, Γ, and source term $\dot{S}_\Phi$. A list of the terms in the Cartesian coordinate system is given in Table 1, where $\Psi_i(i=x,y,z)$ is the source term representing the coupled momentum transport from the particle phase [18,21]

$$\Psi_i=\frac{1}{V_C}\sum_{j=1}^{n_c}\frac{3\mu C_D\mathrm{Re}}{4\rho_p d_p^2}(u_{p,i}-u_i)\dot{m}_p^j\Delta t^j \tag{2}$$

where $\dot{m}_p^j$ is the particle mass rate for the jth trajectory passing through a cell C; V_C is the volume of the cell; Δt^j is the time that a particle on the jth trajectory takes to pass through the cell; n_C is the total number of particle trajectories passing through the cell; Re and C_D are Reynolds number and the drag coefficient of a particle expressed in Eqs. (6) and (7); ρ_p, d_p, and $u_{p,i}$ are the density, diameter, and velocity in i direction of a particle, respectively; μ_l and μ_t are laminar and turbulent viscosity, respectively, $(\mu=\mu_l+\mu_t)$, $\mu_t=\rho C_\mu k^2/\varepsilon$, and G_k represents the rate of production of kinetic energy, which is expressed by

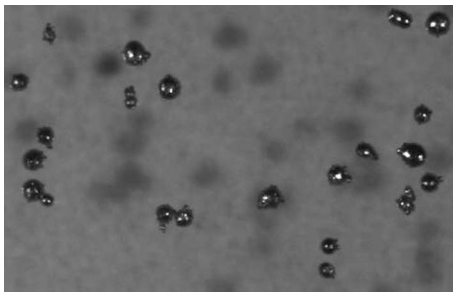

Fig. 3 Nonspherical (satelliting) particles

$$G_k=\frac{\mu_t}{\rho}\left(2\left[\left(\frac{\partial u}{\partial x}\right)^2+\left(\frac{\partial v}{\partial y}\right)^2+\left(\frac{\partial w}{\partial z}\right)^2\right]+\left(\frac{\partial u}{\partial y}+\frac{\partial v}{\partial x}\right)^2+\left(\frac{\partial u}{\partial z}+\frac{\partial w}{\partial x}\right)^2+\left(\frac{\partial v}{\partial z}+\frac{\partial w}{\partial y}\right)^2\right) \tag{3}$$

The above equations contain four empirical constants, which are selected as follows [22]: $C_1=1.44$, $C_2=1.92$, $C_\mu=0.09$, $\sigma_k=1.0$, and $\sigma_\varepsilon=1.30$. The commercial computational fluid dynamics (CFD) code, FLUENT, is used to solve the set of momentum and turbulence equations.

2.1.3 Modeling of Powder Dynamic and Thermal Behavior. Immersed in the surrounding gas, each particle is treated by the Lagrangian approach. The powder dynamic equations [21,23] are given by

$$\frac{d\mathbf{x}}{dt}=u_p \tag{4}$$

$$\frac{du_p}{dt}=\frac{18\mu}{\rho_p d_p^2}\frac{C_D\mathrm{Re}}{24}(u-u_p)+\frac{g(\rho_p-\rho)}{\rho_p} \tag{5}$$

$$\mathrm{Re}=\frac{\rho d_p|u-u_p|}{\mu} \tag{6}$$

$$C_D=\frac{24}{\mathrm{Re}}(1+a_1\mathrm{Re}^{a_2})+\frac{a_3\mathrm{Re}}{a_4+\mathrm{Re}} \tag{7}$$

$$a_1=\exp(2.3288-6.4581\varphi+2.4486\varphi^2)$$

$$a_2=0.0964+0.5565\varphi$$

$$a_3=\exp(4.905-13.8944\varphi+18.4222\varphi^2-10.2599\varphi^3)$$

$$a_4=\exp(1.4681+12.2584\varphi-20.7322\varphi^2+15.8855\varphi^3) \tag{8}$$

where ρ_p, d_p, and u_p are the density, diameter, and velocity of each particle, respectively. Basically, the particles are driven by the forces of gas flow drag and gravity. φ is the shape factor for nonspherical particles. As shown in Fig. 3, the powder has a satelliting shape and a shape factor value of 0.8 is chosen [18,24].

Particle temperature is governed by the laser heating, ambient gas convection, and latent heat of its phase change rate, and is described by [18]

$$m_p c_p\frac{dT_p}{dt}=h_c A_p(T_\infty-T_p)+\eta I\frac{A_p}{4}-m_p L_f\frac{df}{dt} \tag{9}$$

$$\mathrm{Nu}=\frac{h_c d_p}{\lambda}=2+0.6\ \mathrm{Re}^{0.5}\ \mathrm{Pr}^{0.33} \tag{10}$$

where λ is the thermal conductivity of the surrounding gases and $\mathrm{Pr}(=c_p\mu/\lambda)$ is the Prandtl number. f is the liquid fraction, which is expressed as

$$f = \frac{m_l}{m_p} = \begin{cases} 0 & T_p \le T_{\text{sol}} \\ \dfrac{T_p - T_{\text{sol}}}{T_{\text{liq}} - T_{\text{sol}}} & T_{\text{sol}} < T_p < T_{\text{liq}} \\ 1 & T_p \ge T_{\text{liq}} \end{cases} \quad (0 \le f \le 1) \tag{11}$$

The iteration form of particle temperature can be derived as [18]

$$T_p^{i+1} = \alpha_p + (T_p^i - \alpha_p)\exp(-\beta_p \Delta t) \tag{12}$$

where

$$\alpha_p = T_\infty + \frac{\eta I}{4h_c}$$

$$\beta_p = \frac{h_c A_p}{m_p c_p + \dfrac{\varsigma m_p L_f}{T_{\text{liq}} - T_{\text{sol}}}} \tag{13}$$

where m_p is the total mass of a particle, c_p is the specific heat capacity, A_p is the particle surface area, and T_p and T_∞ are the temperatures of the particle and surrounding gas, respectively. I is the laser intensity on the particles, η is the particle absorptivity of laser power, and L_f is the latent heat of the particle material. h_c is the convection coefficient and T_{sol} and T_{liq} are solidus and liquidus temperatures for the alloy particles, respectively. For stellite 6 powder used in this study, the solidus temperature is 1533 K, and liquidus temperature is 1630 K. Powder density, specific heat, latent heat, and absorption coefficient for diode laser are 8380 kg/m^3, 421 J/kg K, 2.92×10^5 J/kg, and 0.7, respectively. m_l is the mass of liquid part of a particle during its phase change. ς is equal to one when a particle is experiencing phase change; otherwise, it is zero. During particle melting, f increases from 0 to 1, that is, from completely solid to totally liquid.

2.1.4 HPDL Rectangular Beam. A 4.0 kW Nuvonyx ISL-4000L HPDL operating at 808 nm was used in this study. Optical elements focus the laser beam into a 12 mm by 0.5 mm rectangle [6]. The divergence angles for the fast axis and slow axis are 19 deg and 23 deg, respectively. Because the HPDL beam profile plays a critical role in determining final product qualities [25], it is important to incorporate the unique spatial rectangular beam profile into the model. The data provided by the laser manufacturer [6] show a Gaussian profile in fast axis plane while it shows a trapezoidal shape one in the slow axis plane. Laser cladding utilizes the scanning of the beam perpendicular to the slow axis.

Corresponding equations describing the spatial laser intensity distribution are given by

$$I = I_0 \exp\left(-\frac{6(x-x_c)^2}{d^2}\right) \quad \text{for} \quad |z| \le 0.26w$$

$$I = I_0 \exp\left(-\frac{6(x-x_c)^2}{d^2}\right)\left(0.3 + \frac{1-0.3}{0.24w}(0.5w - |z|)\right) \quad \text{for} \quad 0.26w < |z| \le 0.5w$$

$$I = 0 \quad \text{for} \quad |z| > 0.5w \tag{14}$$

where x_c is the center position of the laser beam in x direction. d and w are the depth and width of the laser beam, respectively. I_0 is the peak laser intensity at the beam center. The laser focus spot is located at about 28 mm away from the conical nozzle. The laser intensity value defined in Eq. (14) is numerically stored in the user-defined memory of a local cell [18]. In this way, the spatial laser intensity field value can be assigned to each cell in the calculation domain. As calculation continues, the simulation of the particle heating process is accomplished via the iteration form given in Eq. (12) by retrieving the stored value in a cell into the variable I as the particle travels through the cell [18].

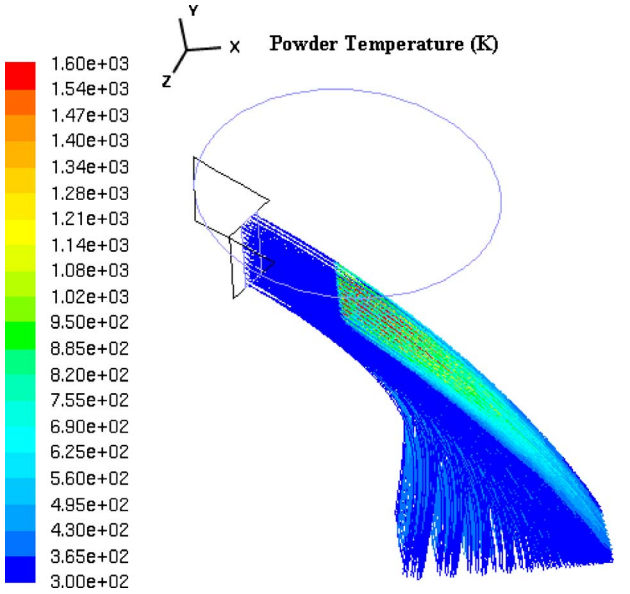

Fig. 4 Off-axis HPDL powder flow with temperature profile, laser power 2400 W, beam spot 12×0.5 mm^2, stellite 6 powder flow rate 35 g/min, shielding gas (argon) flow rate 0.8 SCFM, and carrier gas (argon) flow rate 10 SCFH

The powder flow with the temperature profile has been predicted as in Fig. 4. As seen in Fig. 4, the powder stream, which is injected from the flat nozzle, flows toward the laser focus area. Due to gravity, the powder stream spreads when x distance increases. In the laser irradiation zone, particles are quickly heated up from ambient temperature to around a maximum of 2000 K, indicating that some particles are melted. After passing through the laser beam, the powders cool down due to convection to the surrounding gases. As seen from Fig. 4, the powder temperatures tend to be uniform in the middle of the powder stream along z direction, which is reasonable because of the uniform laser beam intensity there. It is worth to note that the particle trajectory is critical to determining the particle temperature history because it determines the laser particle interaction time and the laser intensity that the particle experiences, thus influencing the powder temperature distribution [18].

Particle dynamic analysis (PDA) technique was used to measure the particle velocity profile in the powder stream to validate the powder dynamic model. The comparison results are shown in Fig. 5. As seen in Fig. 5, the simulated powder velocities match well with the experimental ones. Powder velocities are nearly uniform across the width of the nozzle, fulfilling the goal of the original design.

2.2 HPDL Cladding Process

2.2.1 Governing Equations. To accurately model mass transfer, melt fluid motion, melting and solidification, and free surface evolution during the HPDL cladding process, a unique set of governing equations are established as follows.

Mass equation

$$\frac{\partial}{\partial t}(\rho) + \nabla \cdot (\rho \boldsymbol{V}) = \dot{S}_{\text{mass}} \tag{15}$$

Momentum equations

$$\frac{\partial(\rho u)}{\partial t} + \nabla \cdot (\rho \boldsymbol{V} u) = \nabla \cdot (\mu \nabla u) + \dot{S}_{\text{xmom}} \tag{16}$$

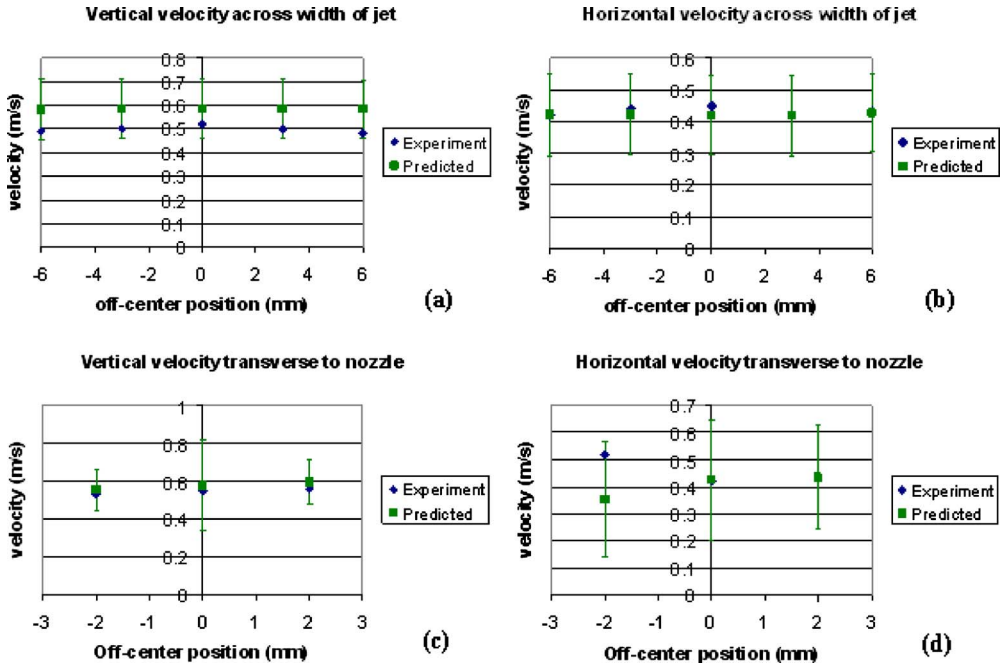

Fig. 5 Comparison between predicted and experimental (*a*) vertical velocity, (*b*) horizontal velocity across width of jet with powder feedrate 35 g/min, (*c*) vertical velocity, and (*d*) horizontal velocity transverse to nozzle with powder feedrate 25 g/min. All measured at 6 mm above laser spot, carrier gas 5 SCFH, shielding gas 1.6 SCFM, and nozzle angle 41 deg from horizontal plane.

$$\frac{\partial(\rho v)}{\partial t} + \nabla \cdot (\rho \boldsymbol{V} v) = \nabla \cdot (\mu \nabla v) + \dot{S}_{\text{ymom}} \tag{17}$$

$$\frac{\partial(\rho w)}{\partial t} + \nabla \cdot (\rho \boldsymbol{V} w) = \nabla \cdot (\mu \nabla w) + \dot{S}_{\text{zmom}} \tag{18}$$

Energy equation

$$\frac{\partial(\rho h)}{\partial t} + \nabla \cdot (\rho \boldsymbol{V} h) = \nabla \cdot (k \nabla T) + \dot{S}_{\text{enthalpy}} \tag{19}$$

Level set equation

$$\frac{\partial(\rho \varphi)}{\partial t} + \nabla \cdot (\rho \boldsymbol{V} \varphi) = \dot{S}_{\text{levelset}} \tag{20}$$

All the source terms in Eqs. (15)–(20) are given in Table 2.

The physical meaning of $\dot{S}_{\text{mass}}$ is the rate that the gas phase in a certain control volume is being replaced by the deposited material due to the moving metal/air interface. Similarly, the last term of $\dot{S}_{\text{imom}}$ $(i=x,y,z)$ and $\dot{S}_{\text{enthalpy}}$ represents the additional momentum and enthalpy associated with the moving interface. This mass conservation aspect has been incorporated into the governing equations, making the model more physically complete and accurate than those in literature [15–17]. H is the Heaviside function, which is used to smooth the properties across the interface and defined as [15,26]

$$H_{\xi}(\varphi) = \begin{cases} 0 & \text{if } \varphi < -\xi \\ 0.5\left[1 + \dfrac{\varphi}{\xi} + \dfrac{1}{\pi}\sin\left(\dfrac{\pi\varphi}{\xi}\right)\right] & \text{if } |\varphi| \le \xi \\ 1 & \text{if } \varphi > \xi \end{cases} \tag{21}$$

where φ is the level set function and ξ is half interface thickness.

The second term of $\dot{S}_{\text{imom}}$ is a Darcy term, representing the damping force when the fluid passes through a porous media (mushy zone). μ_m is the liquid metal viscosity and K is the isotropic permeability and expressed by the Kozeny–Carman equation [27]. The third term of $\dot{S}_{\text{imom}}$ contains two forces at the free surface: the capillary and Marangoni forces [16,17]. The capillary force acts in the normal direction due to the interface curvature κ and surface tension γ. $\boldsymbol{n}$ is the normal vector of the free surface. The Marangoni force acts in the tangential direction of the free surface and is caused by the surface temperature gradient. ∇_s denotes the gradient in the tangent plane. The fourth term of $\dot{S}_{\text{ymom}}$ is buoyancy force (Boussinesq model), in which ρ_r is the reference density at a reference temperature T_r. β is the thermal expansion coefficient and g is gravity acceleration.

The first term of $\dot{S}_{\text{enthalpy}}$ accounts for energy transfer due to relative phase motion in the mush zone [28] while the second term

Table 2 Source terms for the governing equations

Equation	Source term
Mass	$\dot{S}_{\text{mass}} = \dfrac{\partial \rho}{\partial H}\dfrac{\partial H}{\partial t}$
x-momentum	$\dot{S}_{\text{xmom}} = -\dfrac{\partial p}{\partial x} - \dfrac{\mu_m}{K}u - e_x \cdot (\gamma \boldsymbol{n}\kappa - \nabla_s \gamma)\delta(\phi) + \dfrac{\partial(\rho u)}{\partial H}\dfrac{\partial H}{\partial t}$
y-momentum	$\dot{S}_{\text{ymom}} = -\dfrac{\partial p}{\partial y} - \dfrac{\mu_m}{K}v - e_y \cdot (\gamma \boldsymbol{n}\kappa - \nabla_s \gamma)\delta(\phi) + \rho_r g\beta(T - T_r) + \dfrac{\partial(\rho v)}{\partial H}\dfrac{\partial H}{\partial t}$
z-momentum	$\dot{S}_{\text{zmom}} = -\dfrac{\partial p}{\partial z} - \dfrac{\mu_m}{K}w - e_z \cdot (\gamma \boldsymbol{n}\kappa - \nabla_s \gamma)\delta(\phi) + \dfrac{\partial(\rho w)}{\partial H}\dfrac{\partial H}{\partial t}$
Energy	$\dot{S}_{\text{enthalpy}} = -\nabla \cdot (\rho f_s (h_l - h_s)\boldsymbol{V}) + [q_l'' + q_p'' - A_h(T - T_\infty) - \sigma\varepsilon(T^4 - T_\infty^4)]\delta(\phi) + \dfrac{\partial(\rho h)}{\partial H}\dfrac{\partial H}{\partial t}$
Level set	$\dot{S}_{\text{levelset}} = -\rho F_p \lvert\nabla \phi\rvert + \dot{S}_{\text{mass}}\phi$

includes heat flux exchanges on the interface in which q_l'' represents the absorbed heat flux of the HPDL intensity profile defined in Eq. (14) and q_p'' represents the extra energy from the powder, which is small and can be neglected. The rest two denote heat loss terms through convection and radiation, respectively. A_h is the heat transfer coefficient of forced convection, σ and ε denote the Stefan–Boltzmann constant and the material emissivity, respectively, and T_∞ is ambient temperature. $\delta(\varphi)$ is the derivative of the Heaviside function [15,26] given by

$$\delta(\varphi) = \begin{cases} 0 & \text{if } |\varphi| > \xi \\ \dfrac{1}{2\xi} + \dfrac{1}{2\xi}\cos\left(\dfrac{\pi\varphi}{\xi}\right) & \text{if } |\varphi| \le \xi \end{cases} \tag{22}$$

Through $\delta(\varphi)$, the surface forces and energy are successfully incorporated into the source terms.

The level set method [26] is adopted to track the evolution of the complex free surface shape. In this study, a new conservative form is proposed. In the source term $\dot{S}_{\text{levelset}}$, F_p is the free surface growth velocity due to the powder addition given by

$$F_P = \frac{M(x,y,z)}{\rho_p} v_p \tag{23}$$

in which $M(x,y,z)$ is the mass concentration profile of powder flow when reaching the melt pool, which is obtained from the output of the aforementioned powder flow model, v_p is the powder impinging velocity, and ρ_p is the powder density.

The properties, such as density ρ, enthalpy h, thermal conductivity k, and dynamic viscosity μ in the metal/air transition region, are expressed as

$$\rho = (1-H)\rho_m + H\rho_g \tag{24}$$

$$h = (1-H)h_m + Hh_g \tag{25}$$

$$k = (1-H)k_m + Hk_g \tag{26}$$

$$\mu = (1-H)\mu_m + H\mu_g \tag{27}$$

in which subscripts m and g represent metal and gas, respectively.

The solid-liquid region (metal region) is characterized by three separate phases: pure solid, pure liquid and solid-liquid mixture (mush zone). The corresponding mush zone properties are defined as

$$\rho_m = g_s\rho_s + g_l\rho_l \tag{28}$$

$$h_m = f_s h_s + f_l h_l \tag{29}$$

$$c_{pm} = f_s c_{ps} + f_l c_{pl} \tag{30}$$

$$k_m = \left(\frac{g_s}{k_s} + \frac{g_l}{k_l}\right)^{-1} \tag{31}$$

$$\mu_m = \mu_l \frac{\rho_m}{\rho_l} \tag{32}$$

where subscripts s and l represent solid and liquid, respectively. c_{ps} and c_{pl} are solid and liquid metal heat capacity, respectively, and g_s and g_l are the solid and liquid volume fraction of material respectively. Solid, liquid, and mixture metal enthalpies are expressed as [15–17,28]

$$h_s = c_{ps}T, \quad h_l = c_{pl}T + \Delta\ell, \quad h_m = c_{pm}T + f_l\Delta\ell \tag{33}$$

where $\Delta\ell$ is a modified latent heat

$$\Delta\ell = (c_{ps} - c_{pl})T_s + L_m \tag{34}$$

in which L_m is the latent heat. Phase change (melting or solidification) is indicated by the variation of the liquid fraction value. The liquid mass fraction of material $f_l(=1-f_s)$ is defined as

Table 3 Main material properties for powder and substrate [8,9,29]

Property, symbol (unit)	Stellite 6	Mild steel (1018)
Density, ρ_s or ρ_l (kg/m^3)	8380	7800
Specific heat, c_{ps} or c_{pl} (J/kg K)	421	610
Solid conductivity, k_s (W/m K)	14.8	50.0
Liquid conductivity, k_l (W/m K)	48.8	35.0
Latent heat, L_m (J/kg)	2.92×10^5	2.46×10^5
Liquidus temperature, T_l (K)	1630	1803
Solidus temperature, T_s (K)	1533	1766
Dynamic liquid viscosity, μ_l (Pa s)	5.96×10^{-3}	6.10×10^{-3}
Surface tension coefficient (N/m K)	-1.12×10^{-4}	-4.90×10^{-4}

$$f_l = \begin{cases} 1, & T > T \\ \dfrac{T - T_s}{T_l - T_s}, & T_s \le T \le T_l \\ 0, & T < T_s \end{cases} \tag{35}$$

in which T_s and T_l are solidus and liquidus temperatures, respectively.

3 Numerical Solution

In order to accurately calculate the strong liquid motion, free surface motion, and local high temperature gradient, fine meshes were designed around the molten pool region. In the area where a track is going to be deposited, the minimum grid spacing is about 83.3 μm in Y direction. The overall calculation domain is $25\times12\times20$ mm^3 in X, Y, and Z directions with a nonuniform grid of $147\times40\times46$. Initially, the computation domain is composed of gas (above the substrate) and solid phase (substrate). The whole set of governing equations are solved using a finite volume method with an upwind scheme to treat the advection fluxes. Stored on the collocated grid system, main variables such as pressure, velocities, temperature, and level set function are calculated using a coupled solver. In each time step, the convergence was checked through residuals of calculated variables. Once it converges, physical properties are updated and the next time step calculation begins. The time step value was chosen such that the maximum displacement of the free surface at one time step is less than the minimum grid spacing [16,17].

4 Result and Discussion

In this study, a continuous 4.0 kW Nuvonyx ISL-4000L HPDL with a rectangular beam spot size of 12×0.5 mm^2 was considered. The powder material is Stellite 6 and the substrate material is mild steel 1018. The main properties of materials are listed in Table 3. Due to the natural convection on the sides of the substrate, an adiabatic boundary condition is applied to each side except for the surface where clad forms. The initial temperature was set to be 300 K.

A sequential three-dimensional track evolution in a 1.8 s period during the process is illustrated in Fig. 6. As seen in Fig. 6, a distinct, wide, rectangular molten pool is generated at the front of the track with the moving beam. The melt solidifies very quickly due to the high attendant cooling rate and forms a track after the laser moves away. A wide track with a height about 0.4 mm and little dilution is being formed. Corresponding cross sections along the scanning direction are also displayed. It can be seen that the molten pool peak temperature can be as high as around 1795 K at $t=1.8$ s and the fluid motion velocity is about 0.01 m/s under the conditions of this study. The molten pool free surface is deformed due to strong fluid motion. To better examine the fluid motion in the molten pool and mush zone, sequential velocity fields in cross sections along the scanning direction are separately shown in Fig. 7. As seen in Fig. 7, two vortexes (one strong top vortex and a

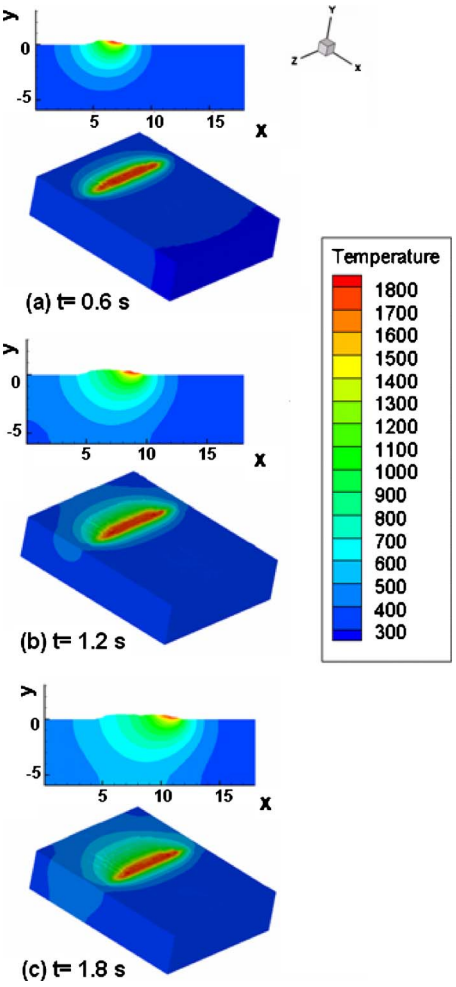

Fig. 6 Sequential 3D off-axis HPDL deposition profile and temperature distribution with cross sections, laser power 2100 W, beam spot 12×0.5 mm² with 6.35 mm defocus down, stellite 6 powder flow rate 35 g/min, and scanning speed 3.33 mm/s

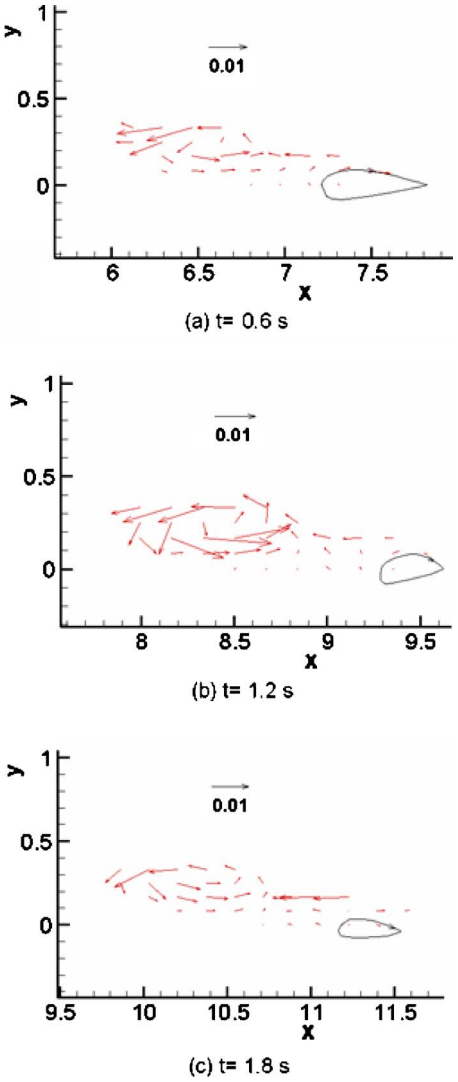

Fig. 7 Sequential fluid motion velocity fields in the molten pool in cross sections along the laser scanning direction, laser power 2100 W, beam spot 12×0.5 mm² with 6.35 mm defocus down, Stellite 6 powder flow rate 35 g/min, and scanning speed 3.33 mm/s, weak vortex is shown by a stream line

weak corner vortex) form in the molten pool. The fluid velocity decreases when the melt flows through the mush zone, where a damping effect in the porous media occurs.

To validate the model, off-axis HPDL cladding experiments have been carried out using three sets of processing parameters as listed in Table 4. The clad heights, widths, and cross section profile are compared between simulated and experimental results as shown in Figs 8–10. As seen in Figs. 8–10, wide tracks with large width-to-thickness aspect ratio and little dilution have been produced. The clad heights, widths, and clad shape match each other well. The simulated molten pool depths are very limited within the track with little dilution, which agrees well with experimental ones.

5 Conclusion

The off-axis HPDL cladding process with distinct powder flow and molten pool has been completely modeled. Key parameters such as nozzle inclination angle, rectangular beam profile, shielding gas flow rates, and powder feed rate were incorporated in a powder model so that spatial powder density, powder velocity, and temperature distribution could be accurately accounted for. The thermal and fluidic behaviors around the molten pool formed by the unique rectangular beam were revealed through a three-dimensional self-consistent cladding model with the incorporation of the distributed powder properties as input. The effect of continuous mass addition has been rigorously considered, thus making the model more accurate. All HPDL cladding experiments in this study produced well-bonded tracks with little dilution. Simulated track heights, widths, and profiles together with molten pool depth agree well with experimental ones. The models addressed in this paper provide a means in optimizing processing parameters in HPDL cladding processes.

Table 4 Processing parameters of three cases

Parameters	Case a	Case b	Case c
Laser power (W)	2100	2400	2400
Scanning speed (mm/s)	3.33	3.33	3.00
Powder feed rate (g/min)	35	35	35
Distance from conical nozzle (mm)	34.35	24.00	30.00
Nozzle angle from horizontal (deg)	49	38	38
Shielding gas flow rate (SCFM)	1.7	0.8	1.2
Carrier gas flow rate (SCFH)	3	10	4

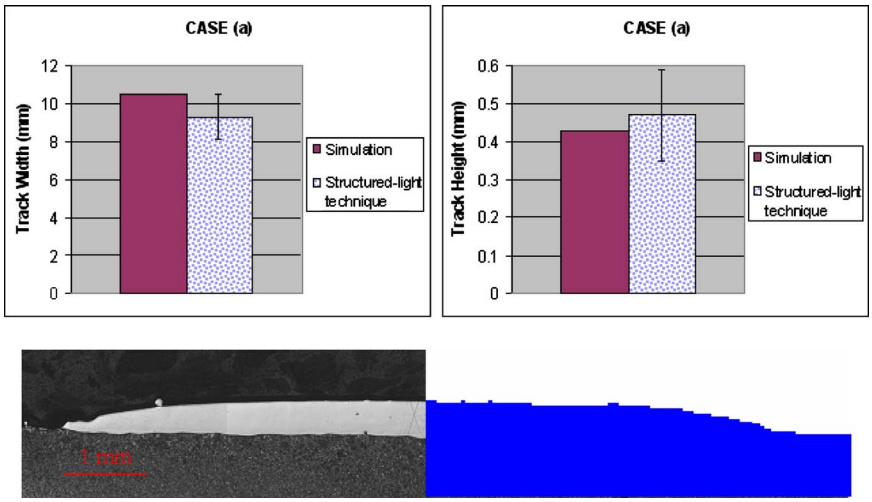

Fig. 8 Comparison of track height, width, and profile between simulated and experimental results, laser power 2100 W, beam spot 12×0.5 mm² with 6.35 mm below focus, stellite 6 powder flow rate 35 g/min, and scanning speed 3.33 mm/s

Acknowledgment

The authors wish to gratefully acknowledge the financial support provided for this study by the National Science Foundation (Grant Nos. 0538786-IIP and 0917936-IIP), the State of Indiana through the 21st Century R&T Fund, and the Industrial Consortium members of the Center for Laser-based Manufacturing.

Nomenclature

A = area

A_h = convection coefficient for metal

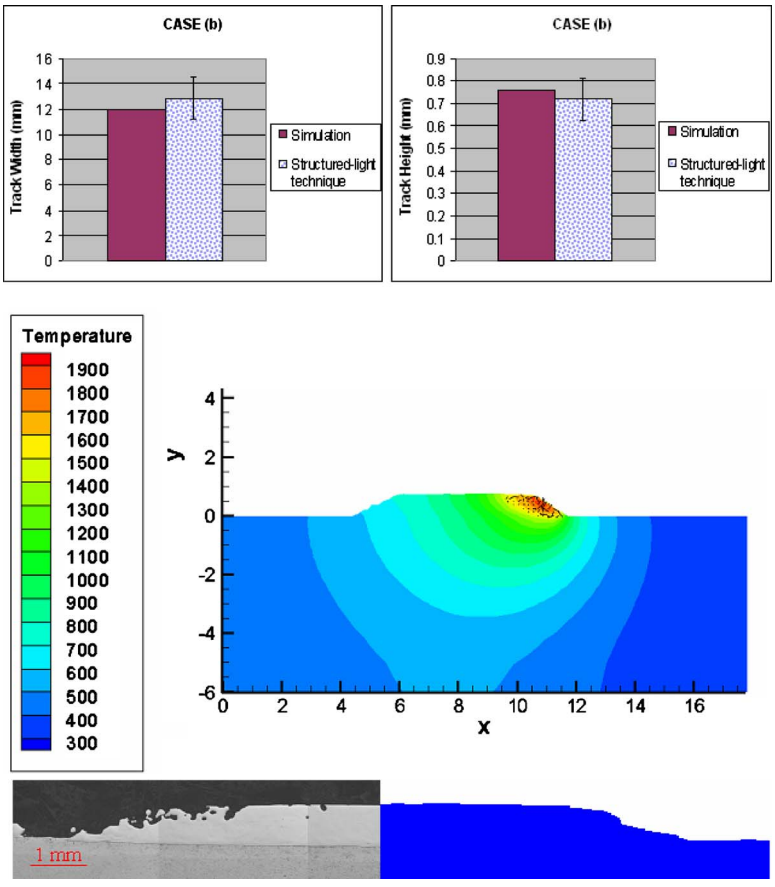

Fig. 9 Comparison of track height, width, and profile between simulated and experimental results, laser power 2400 W, beam spot 12×0.5 mm² with 4.00 mm above focus, stellite 6 powder flow rate 35 g/min, and scanning speed 3.33 mm/s

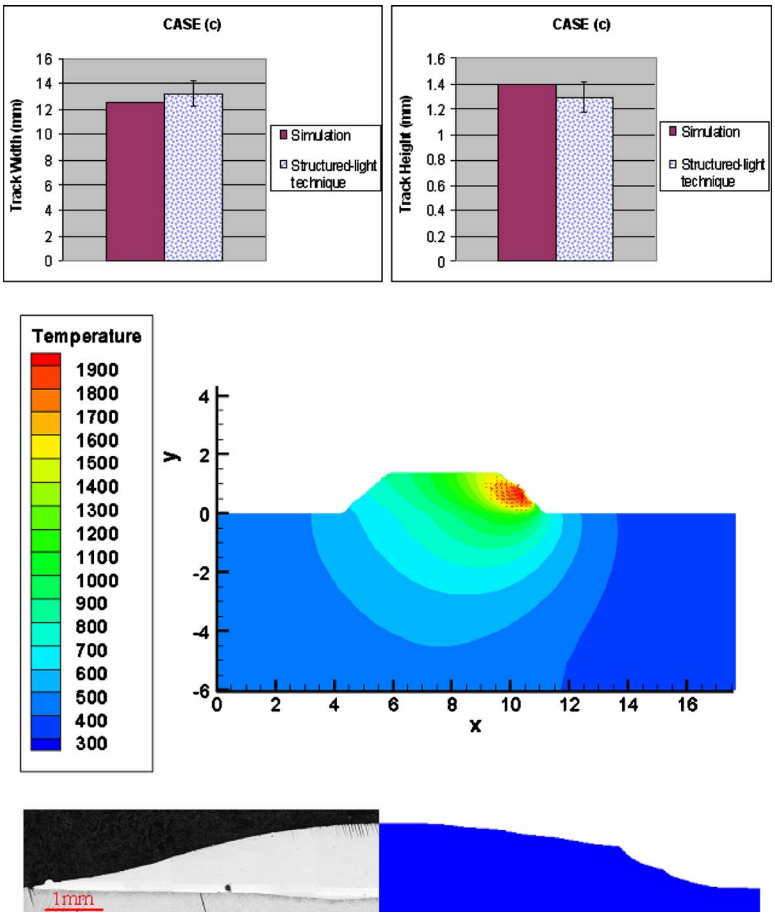

Fig. 10 Comparison of track height, width, and profile between simulated and experimental results, laser power 2400 W, beam spot 12×0.5 mm² with 2.00 mm below focus, stellite 6 powder flow rate 35 g/min, and scanning speed 3.00 mm/s

a_1, a_2, a_3, a_4 = constants
C_D = drag coefficient
C_1, C_2, C_μ = coefficients in turbulent transport equations
c_p = heat capacity
d = diameter
e_x, e_y, e_z = direction vector
F = free surface growth velocity
f = mass fraction
G_k = rate of production of kinetic energy
g = gravitational acceleration
g = volume fraction
H = Heaviside function
h_c = convection coefficient for powder
h = enthalpy
I = laser intensity
K = isotropic permeability
k = kinetic energy of turbulence
k = thermal conductivity of metal
L = latent heat
M = mass concentration of powder
m = mass
$\dot{m}$ = mass flow rate
Nu = Nusselt number
n = number of particle trajectories
$\boldsymbol{n}$ = normal vector of free surface
P = laser power
Pr = Prandtl number
p = pressure
q'' = heat flux
Re = Reynolds number
$\dot{S}$ = source term
T = temperature
T_∞ = ambient temperature
t = time
Δt = time interval
u, v, w = velocity
V = volume
$\boldsymbol{V}$ = velocity vector
x, y, z = coordinates
$\boldsymbol{x}$ = position vector

Greek Symbols

ρ = density
γ = surface tension
ε = rate of dissipation of turbulence energy
ε = radiation emissivity
Φ = variable
Ψ = source term from powder
λ = thermal conductivity of gas
η = absorptivity
ξ = half interface thickness
ϕ = level set function
φ = shape factor
μ = dynamic viscosity
α, β = parameter
ς = parameter

β = thermal expansion coefficient
κ = interface curvature
σ = Stefan–Boltzmann constant
$\sigma_k, \sigma_\varepsilon$ = coefficients in turbulent transport equations
δ = delta function

Subscripts

b = laser beam
C = cell
enthalpy = energy equation
f = fusion
i = iteration level or direction
j = number
l = laminar
l = liquid
liq = liquidus
m = metal
m = melting
mass = continuity equation
mom = momentum equation
p = powder
r = reference
s = solid
sol = solidus
t = turbulent

Superscript

j = powder trajectory number

References

[1] Barnes, S., Timms, N., Bryden, B., and Pashby, I., 2003, "High Power Diode Laser Cladding," J. Mater. Process. Technol., **138**, pp. 411–416.
[2] Nowotny, S., Richter, A., and Beyer, E., 1998, "Laser Cladding Using High-Power Diode Lasers," ICALEO'98 Proceedings, 85G, pp. 68–74.
[3] Li, L., 2000, "The Advances and Characteristics of High-Power Diode Laser Materials Processing," Opt. Lasers Eng., **34**, pp. 231–253.
[4] Bachmann, F., 2000, "High Power Diode Laser Technology and Applications," Proc. SPIE, **3888**, pp. 394–403.
[5] Tuominen, J., Hayhurst, P., Eronen, V., Vuoristo, P., and Mantyla, T., 2003, "Comparison of Muti-Feed and Off-Axis High Power Diode Laser (HPDL) Cladding," Proc. SPIE, **4973**, pp. 116–127.
[6] Schoeffel, K. C., and Shin, Y. C., 2007, "Laser Cladding of Two Hardfacing Alloys Onto Cylindrical Low Alloy Steel Substrates With a High Power Direct Diode Laser," ASME Paper No. MSEC2007-31112.
[7] Jouvard, J. M., Grevey, D. F., Lemoine, F., and Vannes, A. B., 1997, "Continuous Wave Nd:YAG Laser Cladding Modeling: A Physical Study of Track Creation During Low Power Processing," J. Laser Appl., **9**(1), pp. 43–50.
[8] Picasso, M., Marsden, C. F., Wagniere, J. D., Frenk, A., and Rappaz, M., 1994, "A Simple but Realistic Model for Laser Cladding," Metall. Mater. Trans., B, **25B**, pp. 281–291.
[9] Hoadley, A. F. A., and Rappaz, M., 1992, "A Thermal Model of Laser Cladding by Powder Injection," Metall. Trans. B, **23**(5), pp. 631–642.
[10] Kaplan, A. F. H., and Groboth, G., 2001, "Process Analysis of Laser Beam Cladding," ASME J. Manuf. Sci. Eng., **123**, pp. 609–614.
[11] Kumar, S., and Roy, S., 2006, "The Effect of Marangoni–Rayleigh–Benard Convection on the Process Parameters in Blown-Powder Laser Cladding Process—A Numerical Investigation," Numer. Heat Transfer, Part A, **50**, pp. 689–704.
[12] Choi, J., Han, L., and Hua, Y., 2005, "Modeling and Experiments of Laser Cladding With Droplet Injection," ASME J. Heat Transfer, **127**, pp. 978–986.
[13] Toyserkani, E., Khajepour, A., and Corbin, S., 2003, "Three-Dimensional Finite Element Modeling of Laser Cladding by Powder Injection: Effects of Powder Federate and Travel Speed on the Process," J. Laser Appl., **15**(3), pp. 153–160.
[14] Huang, Y. L., Liang, G. Y., and Su, J. Y., 2004, "3-D Transient Numerical Simulation on the Process of Laser Cladding by Powder Feeding," J. Univ. Sci. Technol. Beijing, **11**(1), pp. 13–17.
[15] Han, L., Liou, F. W., and Phatak, K. M., 2004, "Modeling of Laser Cladding With Powder Injection," Metall. Mater. Trans. B, **35**, pp. 1139–1150.
[16] Qi, H., Mazumder, J., and Ki, H., 2006, "Numerical Simulation of Heat Transfer and Fluid Flow in Coaxial Laser Cladding Process for Direct Metal Deposition," J. Appl. Physiol., **100**, p. 024903.
[17] He, X., and Mazumder, J., 2007, "Transport Phenomena During Direct Metal Deposition," J. Appl. Physiol., **101**, p. 053113.
[18] Wen, S., Shin, Y. C., Murthy, J. Y., and Sojka, P. E., 2009, "Modeling of Coaxial Powder Flow for the Laser Direct Deposition Process," Int. J. Heat Mass Transfer, **52**, pp. 5867–5877.
[19] Patankar, S. V., 1980, *Numerical Heat Transfer and Fluid Flow*, Hemisphere, Washington.
[20] Serag-Eldin, M. A., and Spalding, D. B., 1979, "Computations of Three-Dimensional Gas Turbine Combustion Chamber," J. Eng. Power, **101**, pp. 327–336.
[21] Fluent, Inc., 2006, FLUENT 6.3 User Manual, Canonsburg, Pennsylvania.
[22] Launder, B. E., and Spalding, D. B., 1972, *Lectures in Mathematical Models of Turbulence*, Academic, London, UK.
[23] Haider, A., and Levenspiel, O., 1989, "Drag Coefficient and Terminal Velocity of Spherical and Nonspherical Particles," Powder Technol., **58**, pp. 63–70.
[24] Pan, H., Sparks, T., Thakar, Y. D., and Liou, F., 2006, "The Investigation of Gravity Driven Metal Powder Flow in Coaxial Nozzle for Laser-Aided Direct Metal Deposition Process," ASME J. Manuf. Sci. Eng., **128**(2), pp. 541–553.
[25] Pinkerton, A. J., and Li, L., 2005, "An Experimental and Numerical Study of the Influence of Diode Laser Beam Shape on Thin Wall Direct Metal Deposition," J. Laser Appl., **17**(1), pp. 47–56.
[26] Osher, S., and Fedkiw, R., 2003, *Level Set Methods and Dynamic Implicit Surfaces*, Springer, New York.
[27] Asai, S., and Muchi, I., 1978, "Theoretical Analysis and Model Experiments on the Formation Mechanism of Channel-Type Segregation," Trans. Iron Steel Inst. Jpn., **18**, pp. 90–98.
[28] Bennon, W. D., and Incropera, F. P., 1987, "A Continuum Model for Momentum, Heat and Species Transport in Binary Solid-Liquid Phase Change Systems—I. Model Formulation," Int. J. Heat Mass Transfer, **30**(10), pp. 2167–2170.
[29] Huang, Y. L., Yang, Y. Q., Wei, G. Q., Shi, W. Q., and Li, Y. B., 2008, "Boundary Coupled Dual-Equation on Mass Transfer in the Process of Laser Cladding," Chin. Opt. Lett., **6**(5), pp. 356–360.

Theoretical Analysis of Microwave Heating of Dielectric Materials Filled in a Rectangular Waveguide With Various Resonator Distances

Phadungsak Rattanadecho
e-mail: ratphadu@engr.tu.ac.th

Waraporn Klinbun

Research Center of Microwave Utilization in Engineering (RCME),
Department of Mechanical Engineering,
Faculty of Engineering,
Thammasat University (Rangsit Campus),
Pathumthani 12120, Thailand

This paper proposes mathematical models of the microwave heating process of dielectric materials filled in a rectangular waveguide with a resonator. A microwave system supplies a monochromatic wave in a fundamental mode (TE_{10} mode). A convection exchange at the upper surface of the sample is considered. The effects of resonator distance and operating frequency on distributions of electromagnetic fields inside the waveguide, temperature profile, and flow pattern within the sample are investigated. The finite-difference time-domain method is used to determine the electromagnetic field distribution in a microwave cavity by solving the transient Maxwell equations. The finite control volume method based on the SIMPLE algorithm is used to predict the heat transfer and fluid flow model. Two dielectric materials, saturated porous medium and water, are chosen to display microwave heating phenomena. The simulation results agree well with the experimental data. Based on the results obtained, the inserted resonator has a strong effect on the uniformity of temperature distributions, depending on the penetration depth of microwave. The optimum distances of the resonator depend greatly on the operating frequencies. [DOI: 10.1115/1.4002628]

Keywords: microwave heating, rectangular waveguide, TE_{10} mode, porous medium, resonator

1 Introduction

Microwave is a form of electromagnetic wave with wavelengths ranging from 1 m down to 1 mm, with frequencies between 0.3 GHz and 300 GHz. Microwave is applied in many industry and household as a source of thermal energy. It is used in the drying of textile, paper, photographic film, and leather. Other uses include vulcanization, casting, and cross-linking polymers. Perhaps, the largest consumer of microwave power is the food industry, where it is used for cooking, thawing, freeze drying, sterilization, pasteurization, etc. This is the result of the energy carried by the microwave that is converted to thermal energy within the material and a very rapid temperature increase throughout the material that may lead to less by-products and decomposition products. In addition, microwave heating has several advantages, such as high speed startup, selective energy absorption, instantaneous electric control, nonpollution, high energy efficiency, and high product quality.

In order to maintain product quality, uniform distribution of heat is of paramount importance in these processes. The factors that influence the uniformity of heat are load factors and microwave system factors. For example, dielectric properties, volume, shape, and mixture ratio are load factors [1]. Microwave system factors are turntable, operating frequency, placement inside the oven, oven size, and geometry [2]. Knowledge of several parameters is required for an accurate account of all phenomena that occur in a dielectric heated by microwaves. This includes a description of electromagnetic field distribution, power absorbed, temperature, and velocity field. For this reason, we need to solve Maxwell's equation, momentum, and energy equation. Since the complexity and number of the equations are involved, a numerical method is the only approach to conduct realistic process simulations.

The computational study interactions between electromagnetic field and dielectric materials have been investigated in a variety of microwave applicator, such as a multimode cavity (Datta et al. [3], Jia and Bialkowski [4], Lui et al. [5], Ayappa et al. [6], Zhang et al. [7], Clemens and Saltiel [8], Chatterjee et al. [9], and Zhu et al. [10–13]) and a rectangular waveguide (Ratanedecho et al. [14–16], Rattanedecho [17], Curet et al. [18], and Tada et al. [19]). The dielectric materials, such as food, liquid, and a saturated porous packed bed, are chosen for investigating microwave heating phenomena. Ratanedecho et al. [15] investigated, both numerically and experimentally, the microwave heating of a liquid sample in a rectangular waveguide. Microwave was operated in TE_{10} mode at a frequency of 2.45 GHz. The movement of liquid induced by microwave energy was taken into account. Coupled electromagnetic, flow field, and thermal profile were simulated in two-dimensional. Their work showed the effects of liquid electric conductivity and microwave power level on the degree of penetration and rate of heat generation within a liquid layer. Results showed that the heating kinetic strongly depends on the dielectric properties. Ratanedecho et al. [16] investigated the heating of multilayered materials by microwave heating with a rectangular waveguide. They found that when a layer of lower dielectric material is attached in front of a sample, the microwave energy absorbed and the distribution of temperature within the sample are enhanced. Basak et al. [20] studied the efficient microwave heating of porous dielectrics. The results showed that the average power absorption of the samples (b/a and b/o) was enhanced in the presence of Al_2O_3 support. Thermal runaway heating was ob-

Contributed by the Heat Transfer Division of ASME for publication in the JOURNAL OF HEAT TRANSFER. Manuscript received September 14, 2010; final manuscript received September 26, 2010; published online November 16, 2010. Editor: Jogesh Jaluria.

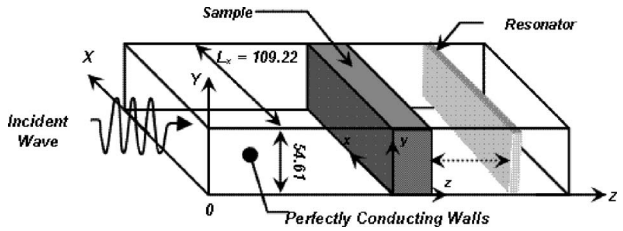

Fig. 1 Schematic of microwave system

served at the face that was not attached with support for the b/a sample and the intensity of thermal runaway increase with porosity, whereas lower thermal runaway was observed for b/o samples at all porosity values. The last, one side incidence may correspond to the largest heating rates, whereas distributed sources may correspond to smaller thermal runaway for both samples.

Many parameters, such as dielectric properties, sample volume, microwave power level, turntable, and operating frequency, were studied in detail. Rattanadecho [17] developed two-dimensional models to predict the electromagnetic fields (TE_{10} mode) inside a guide and the power and temperature distributions within a wood located in a rectangular waveguide. His simulations were performed showing the influence of irradiation times, working frequencies, and sample size. Chatterjee et al. [9] numerically investigated the heating of containerized liquid using microwave radiation. The effects of turntable rotation, natural convection, power source, and aspect ratio of container on the temperature profile were studied, and they presented detailed results of temperature profiles, stream functions, and time evolution of flow field. Results indicated that turntable rotation did not aid in achieving uniform heating in the case of a symmetric heat source. Zhu et al. [10,11] presented a numerical model to study heat transfer in liquids that flowed continuously in a circular duct that was subjected to microwave heating. The results showed that the heating pattern strongly depends on the dielectric properties of the fluid in the duct and on the geometry of the microwave heating system.

However, the effects of the operating frequency and resonator distance on microwave phenomena in the case of using a rectangular waveguide with a resonator have not been clearly studied yet. The present study concerns with a microwave heating of the dielectric materials subjected to a monochromatic wave (TE_{10} mode). The objective of this study can be summarized by the following items: (i) A two-dimensional microwave heating model is carried out to predict the distribution of electromagnetic fields, temperatures, and velocities. (ii) Simulation results are compared and validated with the experimental results in previous works. (iii) The effects of resonator, resonator distances (0 mm, 50 mm, 100 mm, and 200 mm), operating frequencies (1.5 GHz, 2.45 GHz, and 5.8 GHz), and dielectric properties microwave heating phenomena are studied.

2 Problem Description

Figure 1 depicts the physical model of the problem. It is a microwave system supplying a monochromatic wave in the fundamental mode (TE_{10} mode). Microwave energy is transmitted along the *Z*-direction of a rectangular waveguide (cross section area of 109.2×54.6 mm^2) with microwave power input of 300 W. The walls of the guide are thermally insulated and are perfect electric conductors. A resonator inserted at the end of the guide is used to reflect a transmitted wave, and resonator distances are referred to distances between the bottom surface of the sample and the surface of the resonator. The sample (cross section area of 109.2×54.6 mm^2) fills the guide. The upper surface of the sample is exposed for a convection exchange with ambient temperature. The samples are saturated porous medium and water. A saturated porous medium is a packed bed consisting of single sized glass beads with voids filled with water. The porosity of the medium is 0.385 everywhere. The coordinate system designated by *XYZ* is used to describe electromagnetic fields, and the system, *xyz*, is designated for describing the temperature and flow fields.

3 Modeling of Microwave Heating

3.1 Modeling of Electromagnetic Fields. The electromagnetic field is solved according to the theory of Maxwell's equations. In this study, we consider in a fundamental mode (TE_{10}), therefore, Maxwell's equations in terms of the electric and magnetic intensities given by Ratanedecho et al. [15],

$$\varepsilon\frac{\partial E_Y}{\partial t}=\frac{\partial H_X}{\partial Z}-\frac{\partial H_Z}{\partial X}-\sigma E_Y \tag{1}$$

$$\mu\frac{\partial H_Z}{\partial t}=-\frac{\partial E_Y}{\partial X} \tag{2}$$

$$\mu\frac{\partial H_X}{\partial t}=\frac{\partial E_Y}{\partial Z} \tag{3}$$

where

$$\varepsilon=\varepsilon_0\varepsilon_r,\quad \mu=\mu_0\mu_r,\quad \sigma=2\pi f\varepsilon\tan\delta \tag{4}$$

ε is the complex permittivity, σ is the electrical conductivity, and μ is the magnetic permeability. In addition, if magnetic effects are negligible, which is proven to be a valid assumption for most dielectric materials used in microwave heating applications, the magnetic permeability (μ) is well approximated by its value (μ_0) in the free space. $\tan\delta$ is the loss tangent coefficient.

In this study, dielectric properties of samples depend on temperature as follows:

$$\varepsilon_r(T)=\varepsilon_r'(T)-j\varepsilon_r''(T) \tag{5}$$

where

$$\varepsilon_r'(T)=\phi\varepsilon_{rw}'(T)+(1-\phi)\varepsilon_{rp}'(T) \tag{6}$$

$$\varepsilon_r''(T)=\phi\varepsilon_{rw}''(T)+(1-\phi)\varepsilon_{rp}''(T) \tag{7}$$

ϕ is the porosity, thus, a case of water $\phi=1$,

$$\tan\delta=\frac{\varepsilon_r''(T)}{\varepsilon_r'(T)} \tag{8}$$

From the Poynting vector, the volumetric power absorbed (Q) by a dielectric material can be calculated from the local electric fields [15]:

$$Q=2\pi f\varepsilon_0\varepsilon_r'(\tan\delta)\cdot E_Y^2 \tag{9}$$

3.2 Boundary Conditions. The upper surface of the sample is partially received incident electromagnetic wave and the sidewalls of the waveguide are perfect electric conductors.

1. *Perfectly conducting boundary*: Boundary conditions on the inner wall surface of waveguide and at resonator are given by Faraday's law and Gauss's theorem [15]:

$$E_t=0,\quad H_n=0 \tag{10}$$

   where *t* and *n* denote tangential and normal components, respectively.
2. *Continuity boundary condition*: Boundary conditions along the interface between the sample and air are given by Ampere's law and Gauss's theorem [15]:

$$E_t=E_t',\quad H_t=H_t'$$

$$D_n=D_n',\quad B_n=B_b' \tag{11}$$

3. *Absorbing boundary condition*: At both ends of rectangular

waveguide, the first-order absorbing conditions are applied [15]:

$$\frac{\partial E_Y}{\partial t} = \pm \upsilon \frac{\partial E_Y}{\partial Z} \tag{12}$$

where $\pm$ is represented as the forward and backward directions and υ is the velocity of wave propagation.

4. *Oscillation of the electric and magnetic intensities by magnetron*: An incident wave due to magnetron is given by Ratanedecho et al. [15],

$$E_Y = E_{Yin} \sin\left(\frac{\pi X}{L_X}\right) \sin(2\pi f t) \tag{13}$$

$$H_X = \frac{E_{Yin}}{Z_H} \sin\left(\frac{\pi X}{L_X}\right) \sin(2\pi f t) \tag{14}$$

where E_{Yin} is the input value of electric fields intensity, L_X is the length of the rectangular waveguide in the X-direction, and Z_H is the wave impedance defined as follows:

$$Z_H = \frac{\lambda_g Z_l}{\lambda} = \frac{\lambda_g}{\lambda}\sqrt{\frac{\mu}{\varepsilon}} \tag{15}$$

Here, Z_l is the intrinsic impedance depending on the properties of the material, and λ and λ_g are the wavelengths of microwave in free space and rectangular waveguide, respectively.

3.3 Modeling of Heat Transfer and Fluid Flow. To reduce the complexity of the problem, the following assumptions have been introduced into energy and fluid flow equations, particularly in the case of the saturated porous packed bed sample:

1. The saturated fluid within the medium is in a local thermodynamic equilibrium with the solid matrix.
2. The saturated porous packed bed is rigid and no chemical reactions occur.
3. The fluid flow is unsteady, laminar, and incompressible.
4. The pressure work and viscous dissipation are all assumed negligible.
5. The solid matrix is made of spherical particles while the porosity and permeability of the medium are assumed to be uniform throughout the saturated porous packed bed.
6. There is no phase change for the liquid and solid phases.
7. The samples are homogeneous and isotropic.

Heat equation: For saturated porous packed bed and water layer, as follows [21]:

$$\Phi \frac{\partial T}{\partial t} + u\frac{\partial T}{\partial x} + w\frac{\partial T}{\partial z} = \alpha\left(\frac{\partial^2 T}{\partial x^2} + \frac{\partial^2 T}{\partial z^2}\right) + \frac{Q}{(\rho C_p)_w} \tag{16}$$

$\Phi = [\phi(\rho C_p)_w + (1-\phi)(\rho C_p)_p]/(\rho C_p)_w$ is the heat capacity ratio. If the sample is water, the heat capacity ratio has a value of 1. Q is the volumetric power absorbed, which is calculated from Eq. (9).

Continuity equation:

$$\frac{\partial u}{\partial x} + \frac{\partial w}{\partial z} = 0 \tag{17}$$

Momentum equations:

1. For water layer [15]:

$$\frac{\partial u}{\partial t} + \frac{\partial (u\cdot u)}{\partial x} + \frac{\partial (w\cdot u)}{\partial z} = -\frac{1}{\rho_w}\frac{\partial P}{\partial x} + \nu\left(\frac{\partial^2 u}{\partial x^2} + \frac{\partial^2 u}{\partial z^2}\right) \tag{18}$$

$$\frac{\partial w}{\partial t} + \frac{\partial (u\cdot w)}{\partial x} + \frac{\partial (w\cdot w)}{\partial z} = -\frac{1}{\rho_w}\frac{\partial P}{\partial z} + \nu\left(\frac{\partial^2 w}{\partial x^2} + \frac{\partial^2 w}{\partial z^2}\right) + g\beta(T - T_\infty) \tag{19}$$

2. For saturated porous packed bed [21]:

$$\frac{1}{\phi}\frac{\partial u}{\partial t} + \frac{1}{\phi^2}\frac{\partial (u\cdot u)}{\partial x} + \frac{1}{\phi^2}\frac{\partial (w\cdot u)}{\partial z} = -\frac{1}{\rho_w}\frac{\partial P}{\partial x} + \frac{\nu}{\phi}\left(\frac{\partial^2 u}{\partial x^2} + \frac{\partial^2 u}{\partial z^2}\right) - \frac{\gamma u}{\rho_w \mathrm{K}} \tag{20}$$

$$\frac{1}{\phi}\frac{\partial w}{\partial t} + \frac{1}{\phi^2}\frac{\partial (u\cdot w)}{\partial x} + \frac{1}{\phi^2}\frac{\partial (w\cdot w)}{\partial z} = -\frac{1}{\rho_w}\frac{\partial P}{\partial z} + \frac{\nu}{\phi}\left(\frac{\partial^2 w}{\partial x^2} + \frac{\partial^2 w}{\partial z^2}\right) - \frac{\gamma w}{\rho_w \mathrm{K}} + g\beta(T - T_\infty) \tag{21}$$

The momentum equations for the saturated porous packed bed consist of the Brinkmann term, which describes viscous effects due to the presence of a solid body. This form of momentum equations is known as the Brinkmann-extended Darcy model [21], where γ is the dynamic viscosity, K is the medium permeability, β is the thermal expansion coefficient, α is the effective thermal diffusivity of the saturated porous packed bed, and ν is the kinematic viscosity of the fluid.

3.4 Initial and Boundary Conditions.

1. At the interface between the sample and the walls, zero slip boundary conditions are used for the momentum equations,

$$u = w = 0 \tag{22}$$

No heat exchange takes place:

$$\frac{\partial T}{\partial x} = \frac{\partial T}{\partial z} = 0 \tag{23}$$

2. The upper surface of sample exchanges with surrounding where the boundary conditions are given by

- Heat is lost from the surface via natural convection,

$$-\lambda\frac{\partial T}{\partial z} = h_c(T - T_\infty) \tag{24}$$

where h_c is the local heat transfer coefficient.

- In order to capture the real flow phenomenon, the influence of Marangoni flow is included in analyzing model where the velocity in the normal direction (w) and shear stress in the horizontal direction are assumed to be zero [15],

$$\eta\frac{\partial u}{\partial z} = -\frac{d\xi}{dT}\frac{\partial T}{\partial x} \tag{25}$$

where η and ξ are the absolute viscosity and surface tension of liquid layer, respectively.

The initial condition of the sample is defined as follows:

$$T = T_0 \quad \text{at } t = 0 \tag{26}$$

4 Numerical Procedure

Maxwell's equations (Eqs. (1)–(6)) are solved using the finite-difference time-domain (FDTD) method. The electric field components (E) are stored halfway between the basic nodes, while the magnetic field components (H) are stored at the center. So, they are calculated at alternating half-time steps. E and H field components are discretized by a central difference method (second-order accurate) in both spatial and time domains. The energy and fluid flow equations (Eqs. (17)–(21)) are solved numerically by using the finite control volume (FCV) method along with the

Table 1 Thermal and dielectric properties used in the computations [14]

Properties	Air	Water	Glass bead
C_p(J/kg^{-1} K^{-1})	1007	4186	800
λ(W m^{-1} K^{-1})	0.0262	0.609	1.4
ρ(kg/m^{-3})	1.205	1000	2500
μ_r	1.0	1.0	1.0
ε_r	1.0	$88.15-0.414T+(0.131\times10^{-2})T^2-(0.046\times10^{-4})T^3$	5.1
tan δ	0.0	$0.323-(9.499\times10^{-3})T+(1.27\times10^{-4})T^2-(6.13\times10^{-7})T^3$	0.01

SIMPLE algorithm developed by Patankar [22]. These equations are coupled to Maxwell's equations by Eq. (9). Because the dielectric properties of most liquids depend on temperature, it is necessary to consider the coupling between the E field and the temperature distribution. For this reason, the iteration scheme (reference from Ratanedecho et al. [15]) is used to resolve the nonlinear coupling of Maxwell's equations, momentum, and energy equations. Spatial and temporal resolutions are selected to ensure stability and accuracy. To ensure stability of the time-stepping algorithm, Δt is chosen to satisfy the courant stability condition [15]:

$$\Delta t \leq \frac{\sqrt{(\Delta x)^2+(\Delta z)^2}}{v} \tag{27}$$

The spatial resolution of each cell is defined as follows:

$$\Delta x, \Delta z \leq \frac{\lambda_g}{10\sqrt{\varepsilon_r}} \tag{28}$$

The calculation conditions that correspond to Eqs. (27) and (28) are as follows:

1. Grid size: $\Delta x=1.0922$ mm and $\Delta z=1.0000$ mm
2. Time steps: $\Delta t=2\times10^{-12}$ s and $\Delta t=0.01$ s are used corresponding to electromagnetic field and temperature field calculations, respectively.
3. The relative error in the iteration procedures of 10^{-6} is chosen.

5 Results and Discussion

5.1 Physical Properties. Two samples are simulated in order to illustrate microwave heating phenomena using a rectangular waveguide with a resonator. Saturated porous packed bed and water layer are selected for this purpose. Thermal properties and temperature-dependent dielectric properties of the samples are shown in Table 1 [14]. The dielectric properties of samples are assumed independent of the microwave frequency.

The convection heat transfer coefficient $h_c=10$ W m^{-2} K^{-1} is due to natural convection flux at the upper surface of the sample. Initially, the whole calculation domain is assumed to be at a uniform temperature of 301 K.

The penetration depth (D_p) is defined as the distance at which the power density has decreased to 37% of its initial value at the surface [20]:

$$D_p = \frac{1}{\frac{2\pi f}{v}\sqrt{\frac{\varepsilon_r'\left[\sqrt{1+\left(\frac{\varepsilon_r''}{\varepsilon_r'}\right)^2}-1\right]}{2}}} = \frac{1}{\frac{2\pi f}{v}\sqrt{\frac{\varepsilon_r'[\sqrt{1+(\tan\delta)^2}-1]}{2}}} \tag{29}$$

5.2 Numerical Validations. The numerical results have been validated with experimental data of an earlier work (Cha-um et al. [23]). Figures 2(a) and 2(b) show a comparison of the numerical results and experimental data of temperature profiles along x- and z-axes, respectively (Cha-um et al. [23]). It may be noted that the earlier work was investigated without a resonator inside a rectangular waveguide. It was observed that the trends of results are in good agreement. From Fig. 2, the magnitudes of the temperatures predicted within the water layer are all close to the experimental values. Only small discrepancies are noticed. These maybe resulted from keeping some of thermal properties constant during the simulation process. For the saturated porous medium, the experimental data are significantly higher than the computational

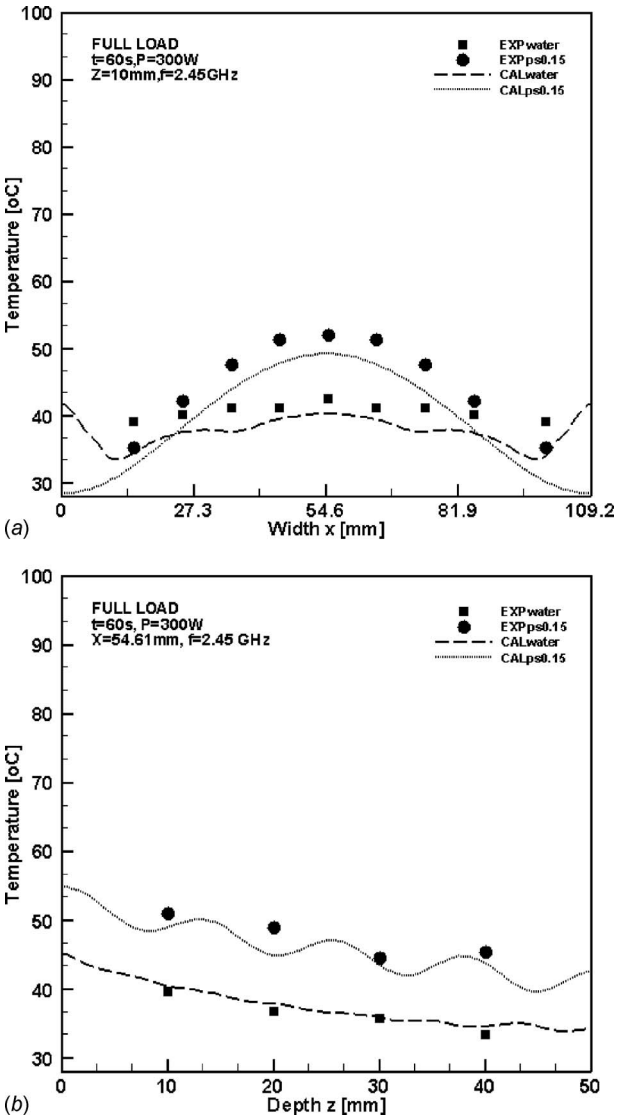

Fig. 2 Comparison of numerical solutions with experimental results of temperature profile: (*a*) along *x*-axis and (*b*) along *z*-axis

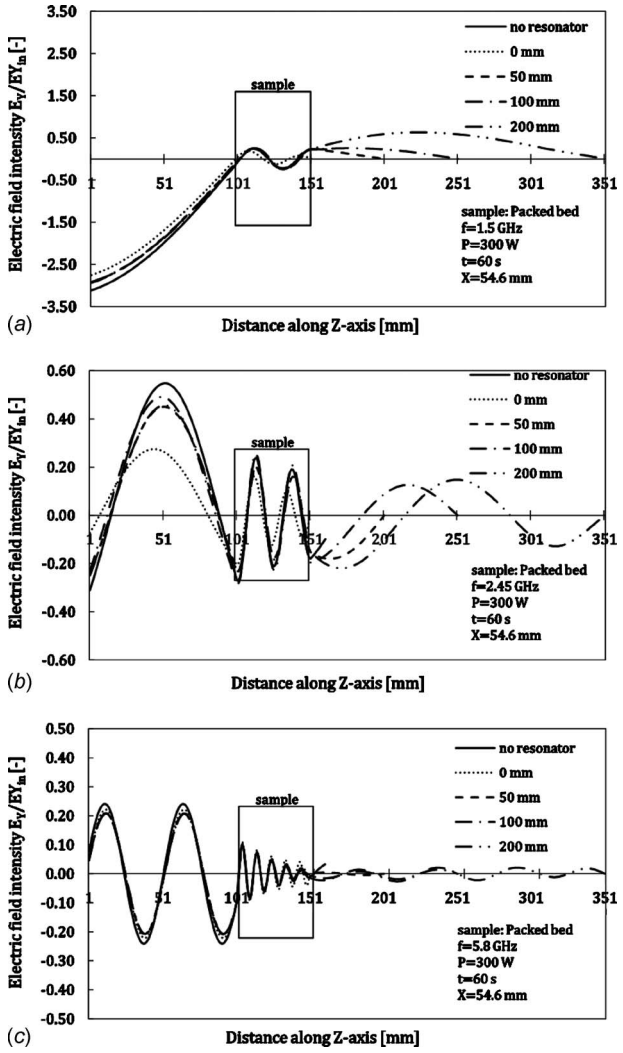

Fig. 3 Distribution of electric field within saturated packed beds filled the guide for various microwave frequencies at t = 60 s: (*a*) 1.5 GHz, (*b*) 2.45 GHz, and (*c*) 5.8 GHz

results, especially along with the X-direction [23]. The discrepancy may be attributed to the uncertainties in some parameter such as porosity, (ϕ), and the thermal and dielectric property database. Further, the uncertainty in temperature measurement might come from the error in the measured microwave power input where the calculated uncertainty associated with temperature was less than 2.65% [23]. From this result, it is clear that the model can be used as a real tool for investigating in detail this particular microwave heating of dielectric materials at a fundamental level.

5.3 Heating Characteristics for Saturated Porous Packed Bed. This section is performed to examine the heating characteristic of a guide loaded with a saturated porous packed bed (cross section area of 109.2×54.6 mm^2) with a thickness of 50 mm.

5.3.1 Electric Field Distribution. Figure 3 illustrates the electric field distribution along the center axis (x=54.6 mm) of a rectangular waveguide at t=60 s for various resonator distances away from the right boundary at the different operating frequencies. In the figure, the vertical axis represents the intensity of the electric fields E_Y, which is normalized to the amplitude of the input electric fields E_{Yin}. In the case without a resonator, all transmitted waves through the sample are absorbed by a fixed water load at the end of the guide. For the cases with a resonator in the waveguide for various distances (0 mm, 50 mm, 100 mm, and 200 mm) and various frequencies (1.5 GHz, 2.45 GHz, and 5.8 GHz), the electric fields with a small amplitude are formed within the saturated porous packed bed, while the stronger standing wave outside the saturated porous packed bed (left-hand side) with a larger amplitude is formed by interference between the forward waves and the reflected waves from the resonator. At 2.45 GHz, the penetration depth of microwave within the saturated porous packed bed is about 110.2 mm (Table 2), which is much greater than the thickness of the saturated porous packed bed, so a large portion of the microwave is able to penetrate through the layer. However, due to the reflections occurring at the air-resonator interface, the standing wave can be formed at the right-hand side, as seen in the figure.

Table 2 Penetration depth of saturated packed bed and water (28°C)

Frequency, f (GHz)	Penetration depth, D_p (mm)	
	Saturated packed bed	Water
1.50	181.0	50.6
2.45	110.2	31.0
5.80	46.8	13.1

5.3.2 Temperature Profiles and Velocity Fields. Figure 4 illustrates the distribution of temperature within a saturated porous packed bed along depth (x=54.6 mm) for t=60 s with various resonator distances and various operating frequencies. It is shown that the highest temperature occurs at the surface and slightly decreases along the depth of the sample according to the penetration depth of microwave. For the operating frequencies of 1.5 GHz and 2.45 GHz, the penetration depths of microwave are 181.0 mm and 110.2 mm, respectively, which are larger than the thickness of a saturated porous packed bed (50 mm). Thus, the microwave can either transmit through or reflect from the resonator. The standing waves are formed and transmitted back into the saturated porous packed bed. During the 1.5 GHz operating frequency, the temperature is much higher for the case of resonator distances corresponding to 0 mm. This result indicates that the waves resonate very well, thereby forming a strong standing wave. During the 2.45 GHz operating frequency, it is interesting that the temperature is greater for the case of resonator distances at about 100 mm, whereas the saturated porous packed bed with resonator distances at 0 mm corresponds to the lowest temperature during microwave heating. While the operating frequency is 5.8 GHz, all cases correspond to lower temperature situations. Since the penetration depth of microwave within a saturated porous packed bed is about 46.8 mm, which is smaller than the thickness of the sample (50 mm), energy dissipates quickly inside the bed. Consequently, a very minimal resonance of standing wave occurs. Refer to the uniformity of temperature within the saturated porous packed bed and the temperature difference between the upper and lower surfaces for each operating frequency in Fig. 4; it is observed that the uniformity does not follow the maximum temperature. For 1.5 GHz and 2.45 GHz, the uniformity in temperature occurs for a case of no resonator and a case with resonator at a distance of about 0 mm, respectively. While the operating frequency is 5.8 GHz, it cannot be indicated because all cases correspond to same situations. Contours of temperature and velocity fields within the sample for the maximum temperature case with various operating frequencies are shown in Figs. 5 and 6, respectively. The temperature distributions qualitatively follow electric field distribution and velocity field. The flow pattern displays circulation patterns, which are characterized by the two symmetrical vortices stemming from the upper corners. The fluid flows as it is driven by the effect of buoyancy. This effect is distributed from the upper corner near the surface where the incident wave propa-

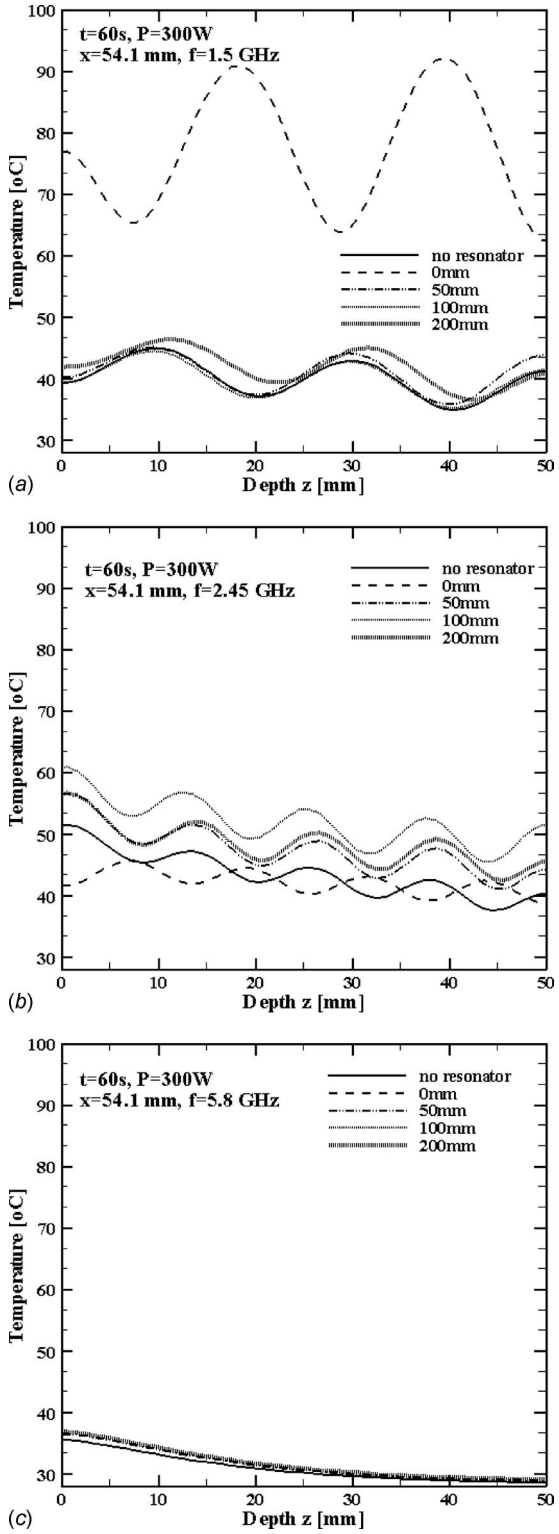

Fig. 4 Temperature profile along *z*-axis within saturated packed beds filled the guide for various microwave frequencies at $t=60$ s: (*a*) 1.5 GHz, (*b*) 2.45 GHz, and (*c*) 5.8 GHz

gates through. The buoyancy effect is associated with the lateral temperature gradient at locations near the top surface. Heated portions of the fluid become lighter than the rest of the fluid and are expanded laterally away from the sides to the center of the sample.

5.4 Heating Characteristics for Water Layer. This section

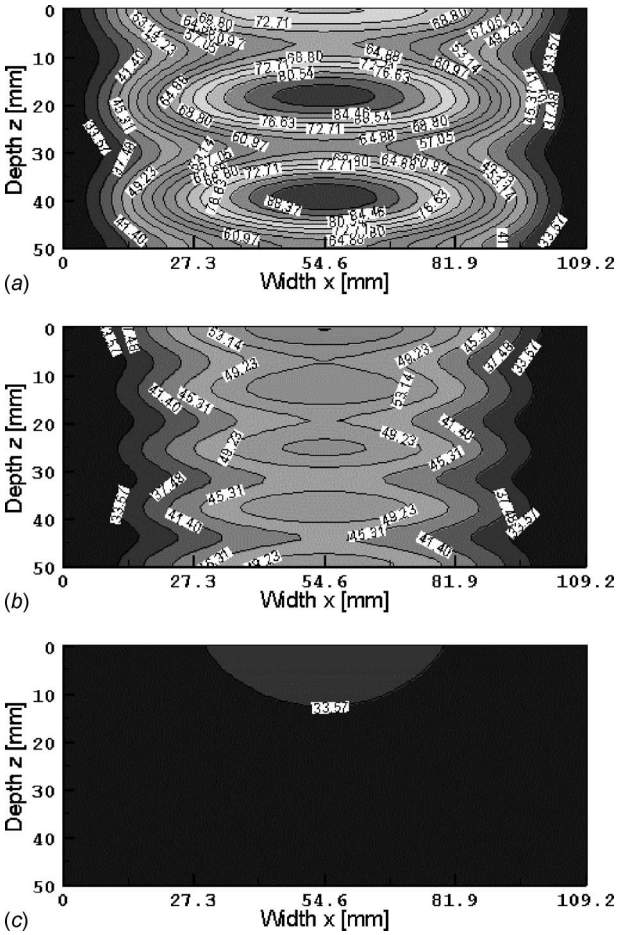

Fig. 5 Temperature contour within packed beds at 60 s: (*a*) 1.5 GHz, 0 mm; (*b*) 2.45 GHz, 100 mm; and (*c*) 5.8 GHz, 200 mm

presents the heating characteristics of a water layer filled in a rectangular waveguide. The sample has a 109.2×54.6 mm^2 cross section area with 30 mm of thickness.

5.4.1 Electric Fields Distribution. Figure 7 illustrates the electric field distribution along the center axis ($x=54.6$ mm) of a rectangular waveguide at $t=60$ s for various resonator distances and operating frequencies. In the figure, the vertical axis represents the intensity of the electric fields E_Y, which is normalized to the amplitude of the input electric fields E_{Yin}. From the figure, the results are similar to cases of a saturated porous packed bed. The amplitude of the electric fields is high over the surface of a water layer (left-hand side) and almost disappears within the water layer. Small amplitude transmitted waves (right-hand side) are reflected from a resonator and are transmitted back into a water layer. Note that the amplitude of electric fields within a water layer is lower than cases of the saturated porous packed bed, but the amplitude of electric fields on the surface (left-hand side) is higher than the case of the saturated porous packed bed. This is because of the small penetration depth and dielectric properties of the water layer (as seen in Tables 1 and 2).

5.4.2 Temperature Profiles and Velocity Fields. Figure 8 illustrates the distribution of temperature within a water layer along the depth ($x=54.6$ mm) for $t=60$ s with various resonator distances and various operating frequencies. It shows no significant temperature difference between surface and inside the water layer for a variety of resonator distances because the small penetration depth and convection play an important role in smoothing out the temperature profile. For 1.5 GHz and 2.45 GHz of operating fre-

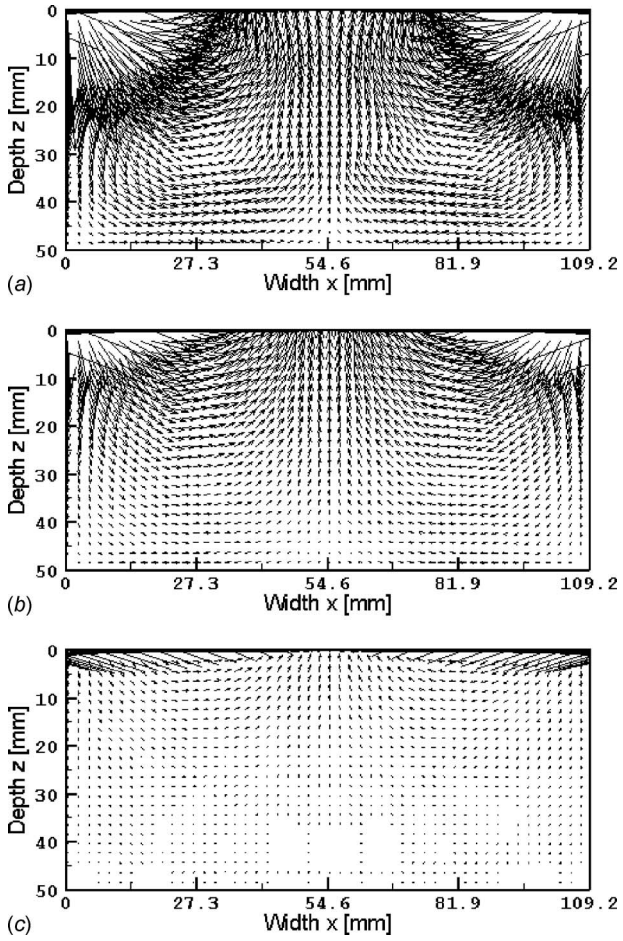

Fig. 6 Velocity field within packed beds at 60 s: (*a*) 1.5 GHz, 0 mm; (*b*) 2.45 GHz, 100 mm; and (*c*) 5.8 GHz, 200 mm (vector length (relative): 35,900,000 grid units/magnitude)

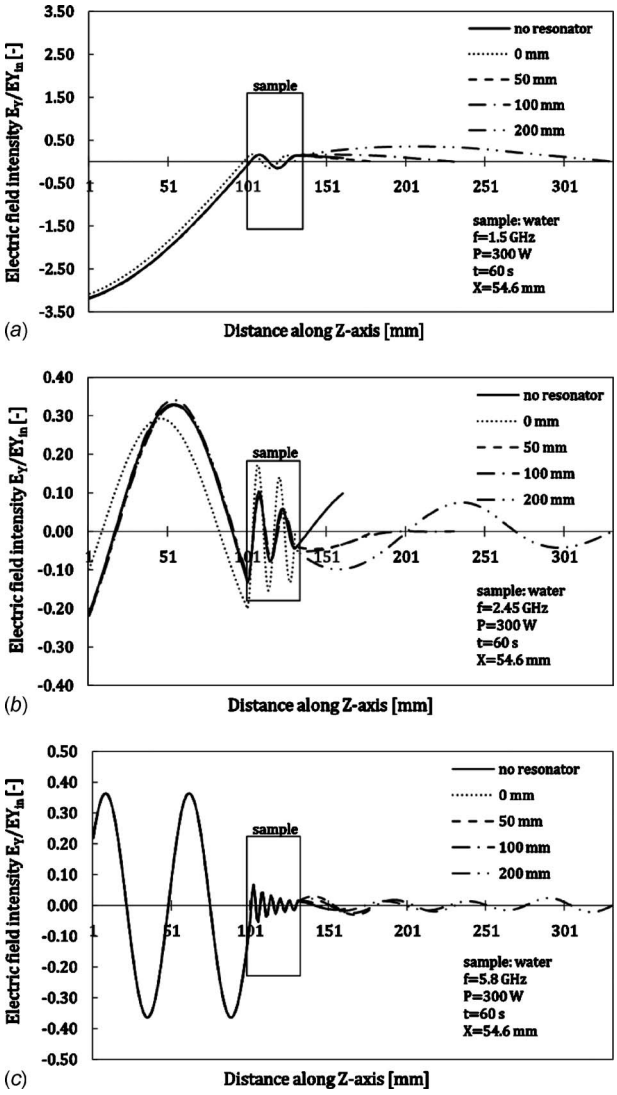

Fig. 7 Distribution of electric field within water filled the guide for various microwave frequencies at $t=60$ s: (*a*) 1.5 GHz, (*b*) 2.45 GHz, and (*c*) 5.8 GHz

quencies, the guide with resonator at a distance of 0 mm corresponds to relatively higher temperature during microwave heating. For a 5.8 GHz operating frequency, the penetration depth of microwave inside the water layer is 13.1 mm (Table 2). It is shorter than the thickness of the water layer, so all cases with and without a resonator are found to be low and give nearly the same temperature. In other words, the resonator does not affect temperature distribution when the penetration depth is lower than the thickness of the water layer since the electric field is rapidly converted to thermal energy within the water layer. The result of the uniformity of temperature is not different in each case. Figures 9 and 10 show the contour of temperature and velocity fields, respectively, within the sample for the maximum temperature case with various times and various operating frequencies. It is interesting to observe that the highest temperature is in the upper region of the heating water layer with the temperature decreasing toward the lower boundary. The velocity fields within the water layer on the *x*-*z* plane correspond to temperature fields in Fig. 9. The effect of conduction plays a greater role than convection at the early stage of heating. As the heating proceeds, the local heating on the surface water layer causes the difference of surface tension on the surface of water layer, which leads to the convective flow of water (Marangoni flow). This causes water to flow from the hot region (higher power absorbed) at the central region of the water layer to the colder region (lower power absorbed) at the sidewall of the container. In the stage of heating ($t=60$ s), the effect of convective flow becomes stronger and plays a more important role, especially at the upper portion of the sidewalls of the container. However, at the bottom region of the walls where the convection flow is small, temperature distributions are primarily governed by the conduction mode.

5.5 Comparison of Heating Characteristics: Saturated Porous Packed Bed Versus Water Layer. In this section, we highlight the microwave heating characteristics of the saturated porous packed bed and the water layer to emphasize the importance of the penetration depth of microwave and the inserted resonator. The electric field distribution, temperature profile, and velocity field show the strong function of the penetration depth of microwave within the samples (water layer (30 mm of thickness) or the saturated porous packed bed (50 mm of thickness)). The dielectric properties are temperature-dependent. Water layer is a high lossy material, but a saturated porous packed bed is a low lossy material. For all cases of operating frequencies for the saturated porous packed bed, temperature distribution is found to be larger than that for the water layer for all cases of resonator distances. For example, the maximum temperature (T) for the saturated porous packed bed with resonator distances at 0 mm is 53°C, corresponding to a 1.5 GHz operating frequency, whereas T for the water layer with resonator distances at 0 mm is 53°C, corresponding to a 1.5 GHz operating frequency ($t=40$ s, $z=30$ mm). It

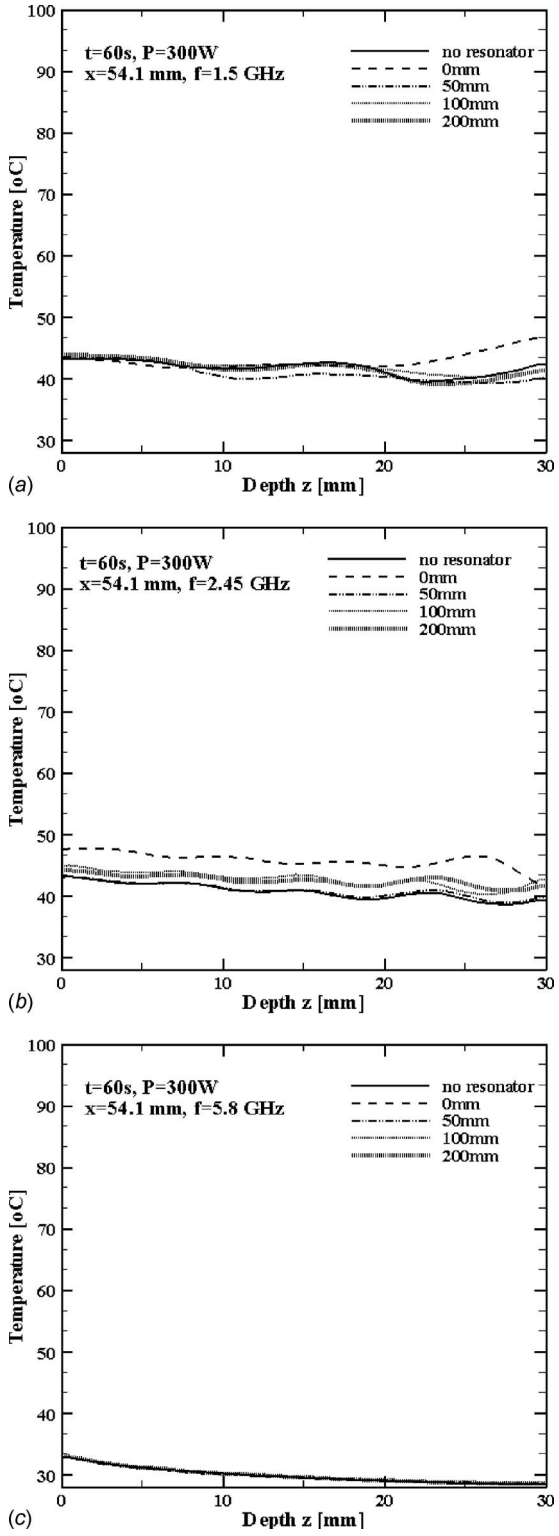

Fig. 8 Temperature profiles within water layer at 60 s: (*a*) 1.5 GHz, (*b*) 2.45 GHz, and (c) 5.8 GHz

may also be noted that greater power absorption occurs within the saturated porous packed bed than within the water layer for all cases. This is because of the standing waves formed by reflected waves from the resonator inside the saturated porous packed bed.

6 Conclusions

This paper presents the simulations of microwave heating of a saturated porous packed bed and a water layer that is filled in the

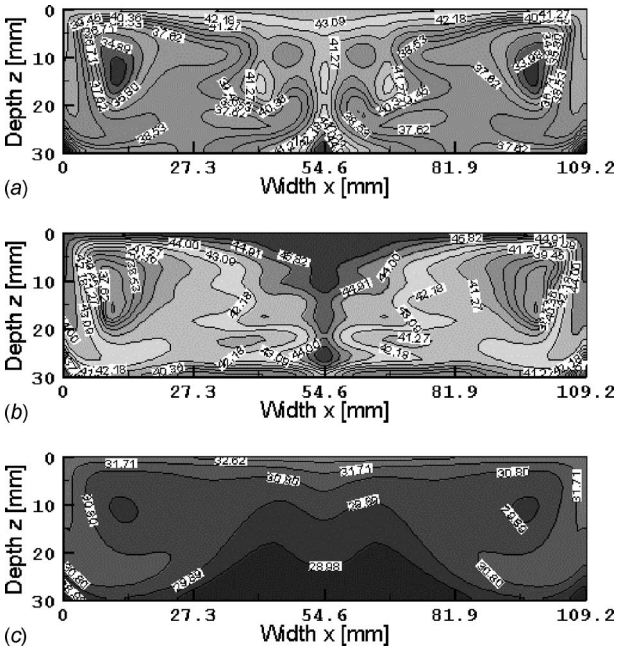

Fig. 9 Temperature contour within water layer at 60 s: (*a*) 1.5 GHz, 0 mm; (*b*) 2.45 GHz, 0 mm; and (*c*) 5.8 GHz, 200 mm

guide with a resonator. The dielectric properties of the sample are found to depend strongly on temperature. The results show an interaction between physical parameters (resonator distances, operating frequencies, and dielectric properties) and microwave heating phenomena. For heating of the saturated porous packed bed, the inserted resonator strongly affects the uniformity of temperature distribution because the penetration depth of microwave is larger than the thickness of the saturated porous packed bed. The microwaves can transmit through the bed and then reflect back in the bed, forming a standing wave within the bed. For heating of water, the inserted resonator does not affect the unifor-

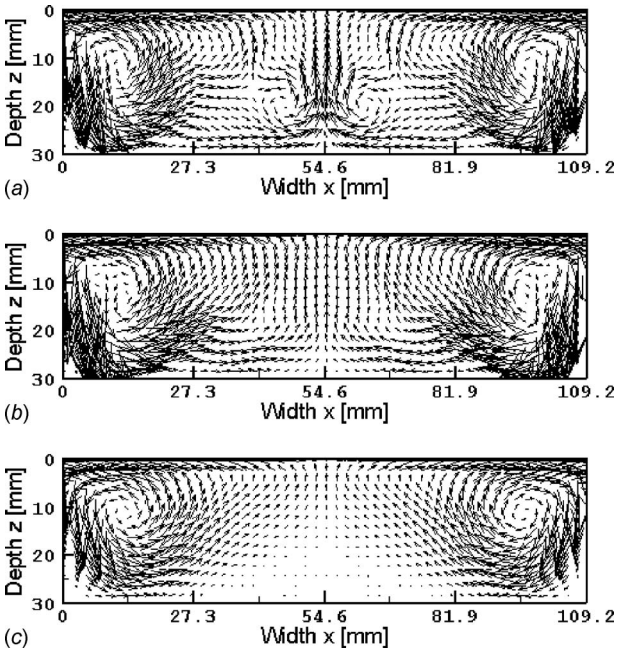

Fig. 10 Velocity field within water layer at 60 s: (*a*) 1.5 GHz, 0 mm; (*b*) 2.45 GHz, 0 mm; and (*c*) 5.8 GHz, 200 mm (vector length (relative): 2500 grid units/magnitude)

Table 3 The generalized heating strategies for saturated packed bed and water layer

Heating strategy (GHz)	Saturated packed bed ($109.2\times54.6\times50$ mm^3)		Water layer ($109.2\times54.6\times30$ mm^3)	
	Maximum temperature (mm)	Uniform temperature (mm)	Maximum temperature (mm)	Uniform temperature (mm)
1.5	0	No resonator	0	Nonsignificant
2.45	100	0	0	Nonsignificant
5.8	200	Nonsignificant	Nonsignificant	Nonsignificant

mity of temperature distribution except for the case of operating frequency at 1.5 GHz because the penetration depth of microwave during 1.5 GHz is larger than the thickness of the water layer. Additionally, the convection mode plays a significant role on heat transfer in the water layer.

Table 3 illustrates the heating characteristics for both the saturated porous packed bed and the water layer for various operating frequencies without a resonator and with a resonator at different distances. It is observed that the case with a resonator distance of 0 mm may be the optimal choice for the high heating rate saturated porous packed bed with 1.5 GHz and for the water layer with 2.45 GHz, while no obvious benefit when using a resonator is observed in the other cases. However, Table 3 provides some useful guidelines for optimal microwave heating of a saturated porous packed bed and a water layer with a resonator inserted in the guide.

Acknowledgment

The authors gratefully acknowledge the financial support provided by The Thailand Research Fund for the simulation facilities described in this paper.

Nomenclature

C_p = specific heat capacity J/(kg K)
E = electric field intensity (V/m)
f = frequency of incident wave (Hz)
g = gravitational constant (m/s^2)
H = magnetic field intensity (A/m)
p = pressure (Pa)
P = power (W)
Q = local electromagnetic heat generation term (W/m^3)
s = Poynting vector (W/m^2)
t = time (s)
T = temperature (°C)
$\tan\delta$ = dielectric loss coefficient
u,w = velocity component (m/s)
Z_H = wave impedance (Ω)
Z_l = intrinsic impedance (Ω)

Greek Letters

α = thermal diffusivity (m^2/s)
β = coefficient of thermal expansion (1/K)
γ = dynamic viscosity (Pa/s)
ε = permittivity (F/m)
η = absolute viscosity (Pa s)
λ = wavelength (m)
μ = magnetic permeability (H/m)
ν = kinematics viscosity (m^2/s)
ξ = surface tension (N/m)
ρ = density (kg/m^3)
σ = electric conductivity (S/m)
υ = velocity of propagation (m/s)
ω = angular frequency (rad/s)

Subscripts

∞ = ambient condition
a = air
j = layer number
in = input
w = water
p = particle

References

[1] Ayappa, K. G., Davis, H. T., Crapiste, G., Davis, E. A., and Gordon, J., 1991, "Microwave Heating: An Evaluation of Power Formulations," Chem. Eng. Sci., **46**(4), pp. 1005–1016.
[2] Ayappa, K. G., Davis, H. T., Davis, E. A., and Gordon, J., 1992, "Two-Dimensional Finite Element Analysis of Microwave Heating," AIChE J., **38**(10), pp. 1577–1592.
[3] Datta, A. K., Prosetya, H., and Hu, W., 1992, "Mathematical Modeling of Batch Heating of Liquids in a Microwave Cavity," J. Microwave Power Electromagn. Energy, **27**, pp. 38–48.
[4] Jia, X., and Bialkowski, M., 1992, "Simulation of Microwave Field and Power Distribution in a Cavity by a Three Dimension Finite Element Method," J. Microwave Power Electromagn. Energy, **27**(1), pp. 11–22.
[5] Liu, F., Turner, I., and Bialowski, M., 1994, "A Finite-Difference Time-Domain Simulation of Power Density Distribution in a Dielectric Loaded Microwave Cavity," J. Microwave Power Electromagn. Energy, **29**(3), pp. 138–147.
[6] Ayappa, K. G., Brandon, S., Derby, J. J., Davis, H. T., and Davis, E. A., 1994, "Microwave Driven Convection in a Square Cavity," AIChE J., **40**(7), pp. 1268–1272.
[7] Zhang, Q., Jackson, T. H., and Ungan, A., 2000, "Numerical Modeling of Microwave Induced Natural Convection," Int. J. Heat Mass Transfer, **43**, pp. 2141–2154.
[8] Clemens, J., and Saltiel, C., 1996, "Numerical Modeling of Materials Processing in Microwave Furnaces," Int. J. Heat Mass Transfer, **39**(8), pp. 1665–1675.
[9] Chatterjee, S., Basak, T., and Das, S. K., 2007, "Microwave Driven Convection in a Rotating Cylindrical Cavity: A Numerical Study," J. Food. Eng., **79**, pp. 1269–1279.
[10] Zhu, J., Kuznetsov, A. V., and Sandeep, K. P., 2007, "Mathematical Modeling of Continuous Flow Microwave Heating of Liquid (Effect of Dielectric Properties and Design Parameters)," Int. J. Therm. Sci., **46**, pp. 328–341.
[11] Zhu, J., Kuznetsov, A. V., and Sandeep, K. P., 2007, "Numerical Simulation of Forced Convection in a Duct Subjected to Microwave Heating," Heat Mass Transfer, **43**, pp. 255–264.
[12] Zhu, J., Kuznetsov, A. V., and Sandeep, K. P., 2008, "Investigation of a Particulate Flow Containing Spherical Particles Subjected to Microwave Heating," Heat and Mass Transfer, **44**, pp. 481–493.
[13] Zhu, J., Kuznetsov, A. V., and Sandeep, K. P., 2007, "Numerical Modeling of a Moving Particle in a Continuous Flow Subjected to Microwave Heating," Numer. Heat Transfer, Part A, **52**, pp. 417–439.
[14] Rattanadecho, P., Aoki, K., and Akahori, M., 2001, "A Numerical and Experimental Study of Microwave Drying Using a Rectangular Waveguide," Drying Technology An International Journal , **19**(9), pp. 2209–2234.
[15] Ratanadecho, P., Aoki, K., and Akahori, M., 2002, "A Numerical and Experimental Investigation of the Modeling of Microwave Heating for Liquid Layers Using a Rectangular Waveguide (Effects of Natural Convection and Dielectric Properties)," Appl. Math. Model., **26**(3), pp. 449–472.
[16] Rattanadecho, P., Aoki, K., and Akahori, M., 2002, "Experimental Validation of a Combined Electromagnetic and Thermal Model for a Microwave Heating of Multi-Layered Materials Using a Rectangular Waveguide," ASME J. Heat Transfer, **124**(5), pp. 992–996.
[17] Rattanadecho, P., 2006, "The Simulation of Microwave Heating of Wood Using a Rectangular Wave Guide: Influence of Frequency and Sample Size," Chem. Eng. Sci., **61**(14), pp. 4798–4811.
[18] Curet, S., Rouaud, O., and Boillereaux, L., 2008, "Microwave Tempering and Heating a Single-Mode Cavity: Numerical and Experimental Investigations," Chem. Eng. Process., **47**, pp. 1656–1665.
[19] Tada, S., Echigo, R., and Yoshida, H., 1998, "Numerical Analysis of Electromagnetic Wave in a Partially Loaded Microwave Applicator," Int. J. Heat

Mass Transfer, **41**, pp. 709–718.
[20] Basak, T., Aparna, K., Meenakshi, A., and Balakrishnan, A. R., 2006, "Effect of Ceramic Supports on Microwave Processing of Porous Food Samples," Int. J. Heat Mass Transfer, **49**, pp. 4325–4339.
[21] Pakdee, W., and Rattanadecho, P., 2006, "Unsteady Effects on Natural Convective Heat Transfer Through Porous Media in Cavity Due to Top Surface Partial Convection," Appl. Therm. Eng., **26**(17–18), pp. 2316–2326.
[22] Patankar, S. V., 1980, *Numerical Heat Transfer and Fluid Flow*, Henisphere, New York.
[23] Cha-um, W., Pakdee, W., and Rattanadecho, P., 2009, "Experimental Analysis of Microwave Heating of Dielectric Materials Using a Rectangular Wave Guide (MODE: TE_{10}) (Case Study: Water Layer and Saturated Porous Medium)," Exp. Therm. Fluid Sci., **33**(3), pp. 472–481.

Single-Phase Thermal Transport of Nanofluids in a Minichannel

Dong Liu[1]
e-mail: dongliu@uh.edu

Leyuan Yu

Department of Mechanical Engineering,
University of Houston,
Houston, TX 77004-4006

Nanofluids have been proposed as a promising candidate for advanced heat transfer fluids in a variety of important engineering applications ranging from energy storage and electronics cooling to thermal processing of materials. In spite of the extensive studies in the literature, a consensus is lacking on if and how the dispersed nanoparticles alter the thermal transport in convective flows. In this work, an experimental investigation was conducted to study single-phase forced convection of Al_2O_3-water nanofluid in a circular minichannel with a 1.09 mm inner diameter. The friction factor and convection heat transfer coefficients were measured for nanofluids of various volume concentrations (up to 5%) and were compared with those of the base fluid. The Reynolds number (Re) varied from 600 to 4500, covering the laminar, transition, and early fully developed turbulent regions. It was found that in the laminar region, the nanofluids exhibit pronounced entrance region behaviors possibly due to the flattening of the velocity profile caused by the flow-induced particle migration. Three new observations were made for nanofluids in the transition and turbulent regions: (1) The onset of transition to turbulence is delayed; (2) both the friction factor and the convective heat transfer coefficient are below those of water at the same Re in the transition flow; and (3) once fully developed turbulence is established, the difference in the flow and heat transfer of nanofluids and water will diminish. A simple scaling analysis was used to show that these behaviors may be attributed to the variation in the relative size of the nanoparticle with respect to the turbulent microscales at different Re. The results from this work suggest that the particle-fluid interaction has a significant impact on the flow physics of nanofluids, especially in the transition and turbulent regions. Consequently, as a heat transfer fluid, nanofluids should be used in either the laminar flow or the fully developed turbulent flow at sufficiently high Re in order to yield enhanced heat transfer performance. [DOI: 10.1115/1.4002462]

Keywords: nanofluids, heat transfer, pressure drop, turbulence, transition

1 Introduction

Nanofluids are engineered colloids that are formulated by dispersing solid nanoparticles of 1–100 nm diameters into a base fluid. Since the early work of Choi in 1995 [1], extensive research efforts have been devoted to exploring the thermal properties and convective transport of nanofluids. The studies prior to 2009 have been summarized in several comprehensive review articles [2–7]. The most dramatic discovery of nanofluids, though still under debate, has been the disproportionate enhancement of thermal conductivity at very low particle concentrations. Consequently, they have been generally considered as a promising candidate for advanced heat transfer fluids. Single-phase forced convection of nanofluids has drawn particular interest due to its direct engineering relevance in a variety of applications ranging from energy storage and electronics cooling to thermal processing of materials [8–25]. It was found that in both laminar and turbulent flows, convective heat transfer is enhanced in nanofluids as compared with the base fluids. Most studies showed that the heat transfer enhancement increases with increasing nanoparticle concentration and Re. Moreover, the enhancement generally surpasses what can be expected from the thermal conductivity enhancement alone. Thus, the applicability of the established heat transfer correlations for predicting the thermal transport of nanofluids has been called into question.

To further investigate the thermal transport mechanism, a few experimental studies on the single-phase pressure drop and convective heat transfer of nanofluids have been reported in the literature since 2009. Some selected ones will be briefly reviewed with the emphasis on assessing the applicability of conventional heat transfer correlations for nanofluids and on exploring the heat transfer enhancement mechanisms in nanofluids. Hwang et al. [26] studied the pressure drop and convective heat transfer of Al_2O_3-water nanofluids in fully developed laminar flow ($Re < 800$). The measured friction factor is in good agreement with the prediction from the Hagen–Poiseuille equation, but the substantial enhancement in convective heat transfer coefficient cannot be correlated by the Shah equation. Using a scaling analysis, it was shown that the heat transfer enhancement should be attributed to the modification of the velocity profile due to Brownian diffusion and thermophoresis, rather than the enhanced thermal conductivity and the direct energy transfer by the nanoparticle dispersion. Anoop et al. [27] conducted convective heat transfer experiments in the laminar developing region ($300 < Re < 2200$) using Al_2O_3-water nanofluids with two nanoparticle sizes. The nanofluid with smaller nanoparticles exhibits a higher heat transfer coefficient. The heat transfer enhancement in the entrance region exceeds that in the nearly developed region. It was postulated that these observations are caused by the property change in the developing region as well as the particle migration. Lai et al. [28] presented an experimental study of convective heat transfer of Al_2O_3-water nanofluids in both the developing and fully developed laminar regions. The results show that the heat transfer coefficient increases with the flow rate and the nanoparticle volume concentration. The heat transfer enhancement is greater in the developing region and decreases along the axial locations, owing in part to the thinning of the thermal boundary layer in the nanofluids. The heat transfer enhancement in the fully developed region was attributed to the flattening of the velocity profile due to the shear-induced particle migration [11,29]. Sharma et al. [30] studied the convective heat transfer of Al_2O_3-water nanofluids in

[1]Corresponding author.

Manuscript received February 15, 2010; final manuscript received May 6, 2010; published online November 16, 2010. Assoc. Editor: Wilson K. S. Chiu.

the transition flow region ($3500 < Re < 9000$) in a tube with and without twisted tape inserts. Buongiorno and co-workers [16,31] investigated the convective heat transfer of Al_2O_3-water and ZrO_2-water nanofluids in both the laminar ($140 < Re < 1900$) and fully developed turbulent regions ($9000 < Re < 63{,}000$). The pressure drop and Nusselt number were found to be predicted well by conventional models as long as the concentration- and temperature-dependent thermophysical properties were considered for the nanofluids. The authors concluded that the heat transfer enhancement was simply caused by the changes in thermophysical properties, and the nanofluids can be treated as a homogeneous mixture. In their experimental investigation of turbulent convection heat transfer, Torri and Yang [32] observed significant heat transfer enhancement in aqueous suspensions of nanodiamond particles and concluded that the reduced thermal boundary layer thickness, the thermal conduction under dynamic conditions, and the particle migration may be responsible for the heat transfer enhancement. Duangthongsuk and Wongwises [33] experimentally investigated the convective heat transfer of TiO_2-water nanofluids in turbulent flow ($4000 < Re < 16{,}000$). They observed that the heat transfer coefficient decreases with increasing nanoparticle concentration, and at the highest concentration, can drop below that of the base fluid. It was postulated that the effect of increased viscosity may override the enhancement in thermal conductivity, thereby leading to a decrease in the heat transfer performance. Besides the foregoing studies conducted in a single tube configuration, convective heat transfer of nanofluids has also been investigated in microchannel heat sinks. Jung et al. [34] reported the pressure drop and convective heat transfer measurements of nanofluids in a microchannel heat sink under laminar flow conditions ($Re < 300$). The measured Nusselt number was considerably lower than the theoretical prediction for fully developed laminar flow ($Nu = 4.36$) and can be correlated well with a modified Dittus–Boelter correlation. Wu et al. [35] carried out an experimental study on the laminar flow and heat transfer of Al_2O_3-water nanofluids in a silicon microchannel heat sink. It was found that the Nusselt number increases with the increase in the nanoparticle concentration and Re and Prandtl (Pr) numbers.

From the literature survey, it is clear that the mechanisms for convective heat transfer enhancement in nanofluids still remain mysterious. The flow-induced particle migration has been attributed by several groups as a possible key mechanism for the enhanced laminar heat transfer in nanofluids. In this model, the balance of particle fluxes due to the Brownian diffusion and the variations in local shear rate and viscosity is considered in deriving the radial distribution of particles in an originally homogeneous flow field. The resulting nonuniform particle distribution gives rise to modified velocity and thermophysical property profiles in the channel, which serve to enhance the heat transfer. Physically, the particle migration concept is to assume that the nanofluids are a heterogeneous solid-fluid two-phase mixture. Its success in predicting the laminar flow and heat transfer suggests that the particle-fluid interaction missing in the widely used homogeneous mixture model of nanofluids should be explored further to reveal the fundamental mechanisms of thermal transport in nanofluids. Additionally, the previous studies were performed for either laminar flow or fully developed turbulent flow at very high Re, and there is a gap in the knowledge of the convective flow and heat transfer of nanofluids in the transition region ($2200 < Re < 3500$).

This paper presents a thorough experimental investigation of single-phase convection of Al_2O_3-water nanofluids in a circular minichannel. The friction factor and convection heat transfer coefficient were measured for nanofluids of various volume concentrations (up to 5%). The Reynolds number was varied from 600 to 4500 to cover the entire range of laminar, transition, and early stage of fully developed turbulent flows. The objectives are (1) to characterize the pressure drop and heat transfer behaviors of nanofluids with respect to their constituent base fluid, (2) to validate the applicability of established conventional correlations in predicting the flow and heat transfer of nanofluids, and (3) to explore the fundamental mechanisms underlying the convective transport in nanofluids.

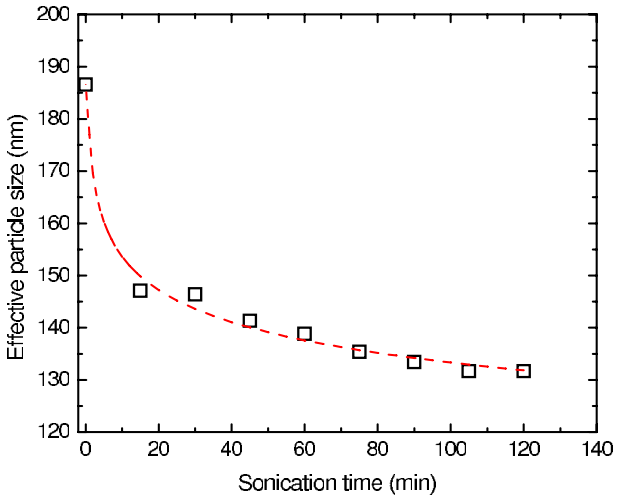

Fig. 1 Effective particle size versus sonication time (0.1% Al_2O_3 nanofluid, pH=3)

2 Formulation of Nanofluids

Nanofluids used in this work were prepared by dispersing commercial γ-phase Al_2O_3 nanoparticles of 40 nm nominal diameter (Alfa Aesar) in deionized water. The volume concentrations investigated were 1%, 2%, 3.5%, and 5%. To stabilize the nanofluids, both physical and chemical dispersion techniques were employed. The normal procedures are as follows. The powderlike nanoparticles were first dispersed in the base fluid with a magnetic stirrer. A trace amount of nitric acid was then added to adjust the pH value of the suspension to 3.0, which creates a repulsive electrostatic interaction between nanoparticles that alleviates the particle aggregation. Following that, the nanofluid sample was homogenized with a high-shear homogenizer (Barnant model 700-5400) for 3 h. As the last step, an ultrasonicator (Biologics 150 VT) was used to further break down the finer nanoparticle aggregates for 2 h.

To assess the efficacy of ultrasonication, the dependence of an effective particle size on the sonication duration was examined using the dynamic light scattering (DLS) technique (Malvern NanoZS). Figure 1 shows the effective particle size measured at 15 min intervals over a period of 2 h. It shows that the particle size decreases rapidly from, initially, 186 nm to 146 nm within the first 30 min and reaches a constant value of 135 nm at the end of ultrasonication. The size distribution of nanoparticles in the nanofluids used in the experiments is shown in Fig. 2. The effective particle size is found to be 135 nm, considerably larger than the nominal diameter (40 nm) specified by the vendor. It indicates that the particle agglomeration cannot be entirely broken even after intensive mechanical and chemical dispersing. Strictly speaking, the effective particle size is slightly outside the upper bound of nanoparticles used in nanofluids (particle size from 1 nm to 100 nm); however, it is still well within the typical particle size range reported in the nanofluid literature. The nanofluid remained stable without any visible sedimentation for several days.

3 Experiments

3.1 Experimental Setup. The experimental apparatus is schematically shown in Fig. 3. A gear pump (IDEX Micropump 67-GA-V21) was used to circulate the nanofluid through the test loop. The flow rate was measured by a turbine flowmeter (Mc-

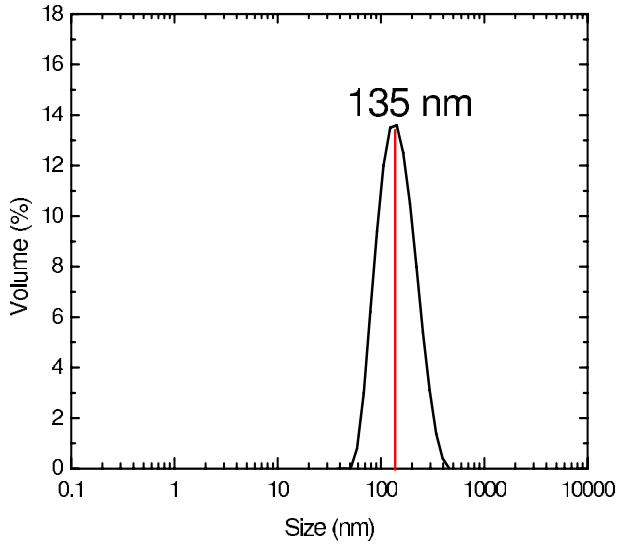

Fig. 2 DLS measurement of effective particle size (0.1% Al_2O_3 nanofluid, pH=3)

Millan G111). A liquid-liquid heat exchanger (Lytron LL520G14) was used in conjunction with an air-cooled chiller (Neslab MERLIN 25) to reduce the temperature of the heated nanofluid to room temperature before it flows back to the reservoir. Readings of the flow rate, temperature, and pressure measurements were collected by a data acquisition system (Agilent 34970A) and were processed in a computer.

The test tube is a circular minichannel made of stainless steel, which measures 1.09 mm in inner diameter and 0.25 mm in wall thickness. The total length is 306 mm (L/D=281). The test tube is resistively heated by passing a dc current through it. For this purpose, it was connected to a dc power supply (Dynatronix CRS12-200) via two copper electrical connectors. The voltage drop across the minichannel was measured directly by the data acquisition system, and the current was obtained using an accurate shunt resistor. Six copper-constantan (T-type) thermocouples (Omega 5TC-TT-T40-36) were attached to the outer wall of the tube at 44 mm axial intervals (TC1–TC6). The temperature readings from these thermocouples were extrapolated to yield the local temperatures at the inner wall. In order to minimize the heat loss to the ambient, the minichannel was wrapped in three layers of thermal insulating materials. The test tube was connected to the flow loop with two Plexiglass connectors, which provide both electrical and thermal isolation from the rest of the loop. Two thermocouple probes (Omega TMT IN-020G-6) were accommodated in the Plexiglass connectors to measure the fluid temperatures at the inlet and outlet of the channel. Two absolute pressure transducers (Omega PX319-050A5V and PX319-030A5V) were installed to measure the pressure drop across the microchannel.

3.2 Test Procedure. Prior to each experiment run, the nanofluid was freshly prepared following the dispersing processes described before. In the pressure drop experiments, the flow rate was adjusted by a control valve. After the flow rate and the pressure signals stabilized, the data were read into the data acquisition system. The flow rate was then increased in small increment, and the procedure was repeated. In the heat transfer experiments, the power input to the test tube was maintained at a constant level. The flow rate was first set to the maximum value and gradually decreased in subsequent experiments. Each steady-state value was calculated as an average of 100 readings for all flow rate, pressure, temperature, and power measurements. The Reynolds number obtained in this work ranges from 600 to 4500.

3.3 Data Reduction

3.3.1 Thermophysical Properties. The effective density and specific heat of nanofluids are estimated as

$$\rho_{\mathrm{nf}}(T) = \phi \cdot \rho_p(T) + (1 - \phi) \cdot \rho_f(T) \tag{1}$$

$$C_{p,\mathrm{nf}}(T) = \frac{\phi \cdot (\rho C_p)_p(T) + (1 - \phi) \cdot (\rho C_p)_f(T)}{\rho_{\mathrm{nf}}(T)} \tag{2}$$

The effective viscosity of nanofluids was measured at 25°C using a capillary viscometer (Cannon-Ubbelohde 9721-R53). The normalized results with reference to the viscosity of pure water are presented in Fig. 4. It is seen that the effective viscosity exceeds that of water and increases with the nanoparticle volume concentration. Nonetheless, the viscosity increment is moderate and can be well predicted by the Batchelor correlation [36],

$$\mu_{\mathrm{nf}} = \mu_f(T)(1 + 2.5\phi + 6.2\phi^2) \tag{3}$$

which reduces to the Einstein correlation ($\mu_{\mathrm{nf}}/\mu_{\mathrm{f}}=1+2.5\phi$) at very low particle concentrations.

The effective thermal conductivity of nanofluids was characterized using a thermal property analyzer (KD2 Pro). A sample measurement in Fig. 5 shows that the thermal conductivity of nanofluids is enhanced as compared with that of water and can be reasonably correlated by the Buongiono model [16] over the temperature range measured,

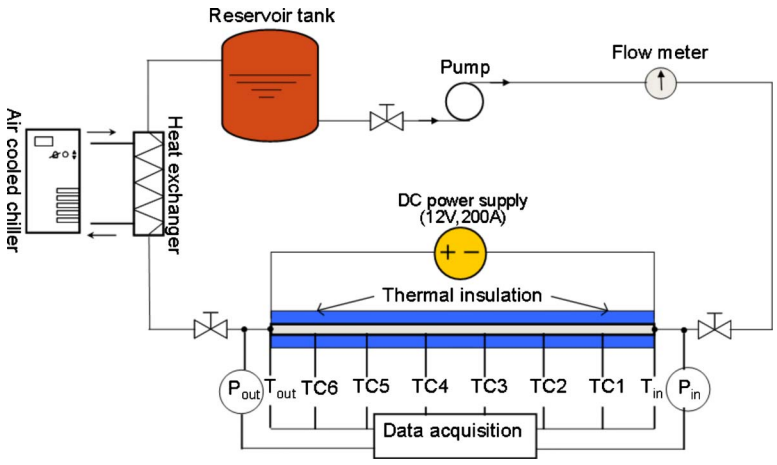

Fig. 3 Schematic of the experimental apparatus

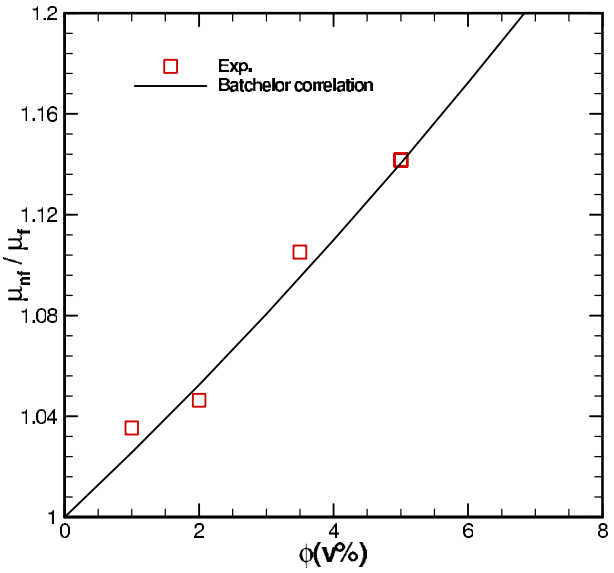

Fig. 4 Effective viscosity of nanofluid at various volume concentrations at 25°C

$$k_{nf} = k_f(T)(1 + 4.5503\phi) \tag{4}$$

It is noted that in Eqs. (1)–(4), the temperature dependence has been considered in the thermophysical properties of the nanofluids [27,37].

3.3.2 Pressure Drop. The pressure drop and flow rate were measured to obtain Re and the Darcy friction factor f, which are defined as

$$\mathrm{Re} = \rho u D/\mu \tag{5}$$

$$f = \frac{(\Delta P/L)D}{\rho u^2/2} \tag{6}$$

It is noted that ΔP in Eq. (6) is the pressure drop across the channel length and is calculated by subtracting the inlet and outlet pressure losses from the measured overall pressure drop [38,39].

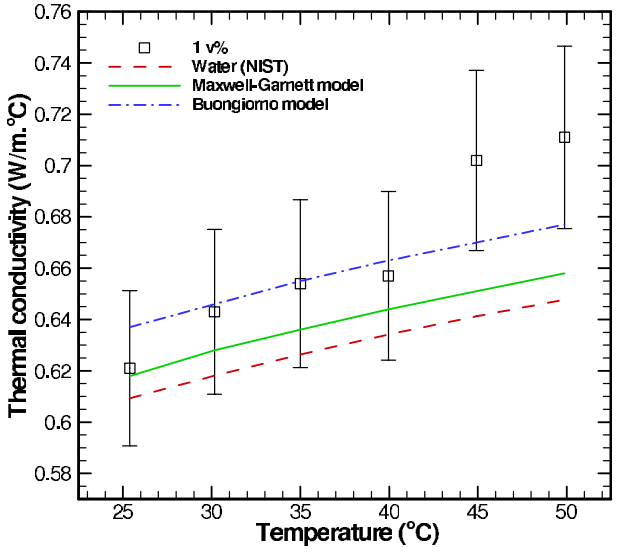

Fig. 5 Effective thermal conductivity of nanofluid at various temperatures (error bar ±5%)

3.3.3 Heat Transfer. It is reasonable to assume a constant heat flux boundary condition on the channel wall since the resistive heating method is used in this work. The wall heat flux can be calculated from the sensible heat gain by the fluid,

$$q'' = \rho_f Q c_p (T_{f,\mathrm{out}} - T_{f,\mathrm{in}})/A \tag{7}$$

where the fluid properties are evaluated at the mean temperature,

$$\overline{T_f} = (T_{f,\mathrm{in}} + T_{f,\mathrm{out}})/2 \tag{8}$$

The local convective heat transfer coefficient is defined as

$$h(x) = q''/[T_w(x) - T_f(x)] \tag{9}$$

where the local wall temperature T_w is extrapolated from the temperature reading of $T_{w,o}$ obtained at the outer wall of the minichannel following [40]

$$T_w(x) = T_{w,o}(x) + \frac{\rho_f Q C_p (T_{f,\mathrm{out}} - T_{f,\mathrm{in}})}{4\pi k_w L} - \frac{\rho_f Q C_p (T_{f,\mathrm{out}} - T_{f,\mathrm{in}}) D_o^2}{2\pi k_w (D_o^2 - D^2) L} \ln\frac{D_o}{D} \tag{10}$$

Assuming that the local fluid temperature follows a linear profile along the channel length, T_f can be calculated from the energy conservation,

$$T_f(x) = T_{f,\mathrm{in}} + q''\pi D x/(\rho_f Q C_p) \tag{11}$$

Similarly, the average heat transfer coefficient is determined from

$$\overline{h} = q''/[\overline{T_w} - \overline{T_f}] \tag{12}$$

where the average wall temperature is $\overline{T_w} = (1/5)\Sigma_{i=1}^{5} T_w(i)$ and the fluid temperature is calculated from Eq. (8).

The Nusselt number can be calculated as

$$\mathrm{Nu} = \frac{h \cdot D}{k} \tag{13}$$

This definition applies for both the local and average Nusselt numbers, and the thermal conductivity is evaluated at the corresponding fluid temperatures.

3.4 Measurement Uncertainties. The temperature measurement uncertainty was ±0.3°C. The uncertainty in the flow rate measurements was 1%. The error associated with the pressure transducers was 2%. A standard error analysis [41] revealed that the uncertainties in the reported Reynolds number, friction factor, and heat transfer coefficient were in the ranges of 3.3–7.0%, 5.8–28.9%, and 2.2–9.6%, respectively. It is noted that the maximum uncertainties are for the lowest Re (~600). As the Re increases, the measurement uncertainties quickly drop to their lower bound.

4 Results and Discussion

4.1 Experiments With Water. Control experiments were first performed with the base fluid (water) to verify the integrity of the experimental facility and the test procedures. The results also provide the baseline information of the single-phase thermal transport of nanofluids in a circular minichannel.

4.1.1 Pressure Drop. The friction factor measurements were compared with predictions from the conventional theory for fluid flow in a circular channel. In the laminar region, the Hagen–Poiseuille equation [40] was used for the hydrodynamically fully developed flow condition,

$$f \cdot \mathrm{Re} = 64 \tag{14}$$

and the Shah equation [42] was used to account for the developing length effect,

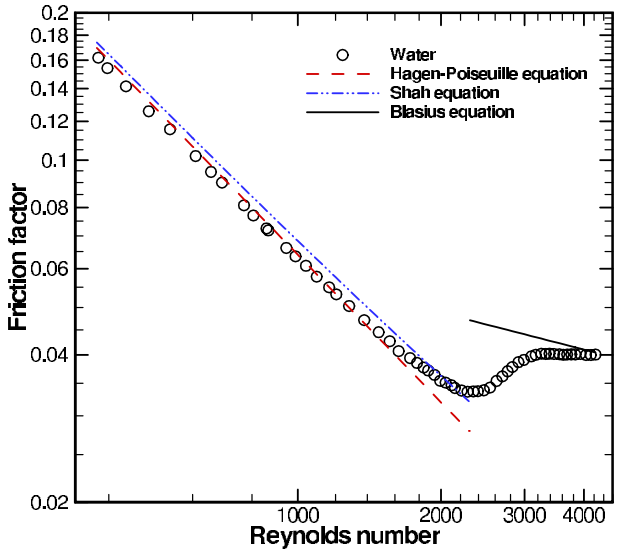

Fig. 6 Friction factor versus Reynolds number (water)

$$f_{app}\mathrm{Re} \approx 4\left(\frac{3.44}{\sqrt{\varsigma}} + \frac{16 + 0.3125\varsigma - 3.44/\sqrt{\varsigma}}{1 + 2.12 \times 10^{-4}/\varsigma^2}\right) \tag{15}$$

where $\varsigma = (x/D)/\mathrm{Re}$. For fully developed turbulent flow, the predictions were obtained from the Blasius solution [40],

$$f = 0.316/\mathrm{Re}^{0.25} \quad (\mathrm{Re} < 2 \times 10^4) \tag{16}$$

Figure 6 shows the measured friction factor of water as a variation in Re. At relatively low Re (<1000), the hydrodynamic entrance length ($L^+ = 0.056\mathrm{Re}\cdot D$) is only a small fraction of the total channel length ($L^+/L < 0.20$), and the entrance region effect is minor. Hence, the experimental data agree excellently with the Hagen–Poiseuille equation. Once Re exceeds 1500, the entrance region effect can no longer be neglected ($L^+/L \sim 0.30$). Consequently, the friction factor starts to deviate from the fully developed flow and gradually approaches the hydrodynamically developing flow described by Eq. (15). Further, Fig. 6 shows that the transition from laminar to turbulent flow occurs at $\mathrm{Re}_{cr} \approx 2300$ and the transition region persists to $\mathrm{Re} \approx 3200$ where the fully developed turbulent flow begins to establish.

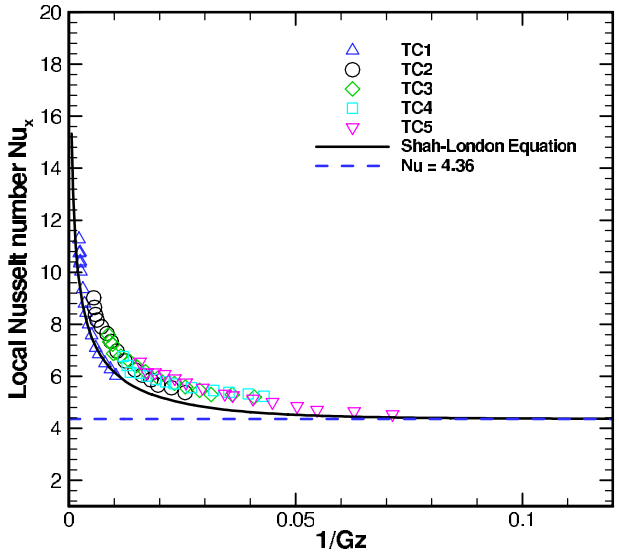

Fig. 7 Local Nusselt number versus the inverse of Graetz number (water, heat flux $q'' = 6.5$ kW/m^2)

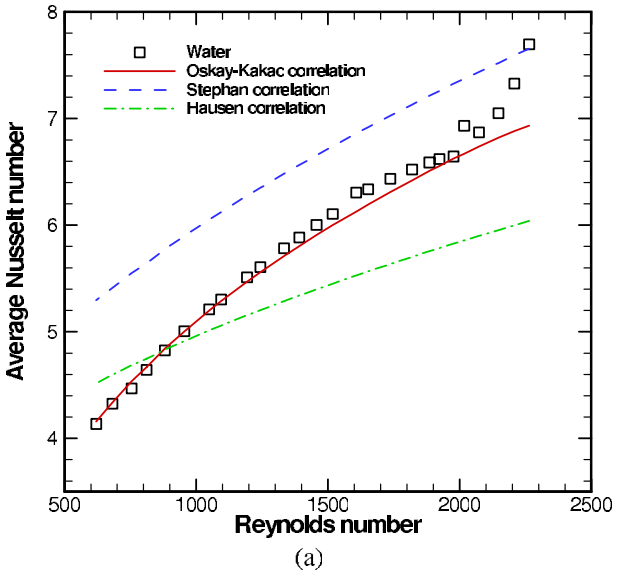

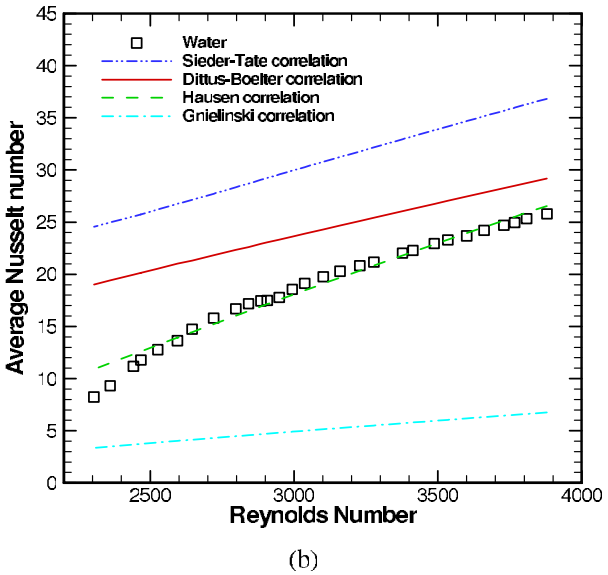

Fig. 8 Average Nusselt number versus Reynolds number (water, heat flux $q'' = 6.5$ kW/m^2)

4.1.2 Heat Transfer. The local Nusselt number measurements are depicted in Fig. 7 as a function of the inverse of Graetz number ($\mathrm{Gz} = (D/x)\mathrm{Re}\cdot\mathrm{Pr}$). The entrance region behavior can be clearly identified. Nusselt numbers are, in principle, infinite at $1/\mathrm{Gz} = 0$ and rapidly decay to their asymptotical (fully developed) value, i.e., $\mathrm{Nu} = 4.36$. The experimental data can be reasonably represented by the Shah–London correlation [43],

$$\mathrm{Nu}_x = \begin{cases} 1.302/(\mathrm{Gz})^{1/3} - 1 & \text{for } 1/\mathrm{Gz} \le 0.00005 \\ 1.302/(\mathrm{Gz})^{1/3} - 0.5 & \text{for } 0.0005 \le 1/\mathrm{Gz} \le 0.0015 \\ 4.364 + 8.68/(1000\mathrm{Gz})^{0.506}e^{-41/\mathrm{Gz}} & \text{for } 1/\mathrm{Gz} \ge 0.0015 \end{cases} \tag{17}$$

Figure 8 presents the measured average Nusselt number as a function of Re. Predictions from some established heat transfer correlations for convective flow in a circular channel are also included for comparison purposes. The heat transfer correlations

Table 1 Selected conventional heat transfer correlations from the literature

Correlation	Conditions	Range of validity
	Laminar heat transfer	
Hausen correlation [40], $\mathrm{Nu} = 3.66 + \frac{0.19(\mathrm{RePr}D/L)^{0.8}}{1+0.117(\mathrm{RePr}D/L)^{0.467}}$	Thermally developing (constant wall temperature)	$\mathrm{Re} < 2200$
Stephan correlation [44], $\mathrm{Nu} = 4.364 + \frac{0.086(\mathrm{RePr}D/L)^{1.33}}{1+0.1\mathrm{Pr}(\mathrm{Re}D/L)^{0.83}}$	Simultaneously developing (constant wall heat flux)	$0.7 < \mathrm{Pr} < 7$ or $\mathrm{RePr}D/L < 33$ for $\mathrm{Pr} > 7$
Oskay–Kakac correlation [45], $\mathrm{Nu} = 1.86(\mathrm{RePr}D/L)^{1/3}\left(\frac{\mu_f}{\mu_w}\right)^{0.152}$	Thermally developing (constant wall heat flux)	$800 < \mathrm{Re} < 2200$, $\mathrm{T_w/T_f} < 3$
	Turbulent heat transfer	
Dittus–Boelter correlation [46], $\mathrm{Nu} = 0.023\mathrm{Re}^{0.8}\mathrm{Pr}^{1/3}$	Fully developed turbulent	$0.6 < \mathrm{Pr} < 160$, $\mathrm{Re} > 10{,}000$, $\mathrm{L/D} > 10$
Hausen correlation [47], $\mathrm{Nu} = 0.116(\mathrm{Re}^{2/3} - 125)\mathrm{Pr}^{1/3}[1 + (D/L)]^{2/3}\left(\frac{\mu_f}{\mu_w}\right)^{0.14}$	Thermally developing turbulent	$0.7 < \mathrm{Pr} < 3$, $2200 < \mathrm{Re} < 10{,}000$
Gnielinski correlation [48], $\mathrm{Nu} = \frac{(f/8)(\mathrm{Re}-1000)\mathrm{Pr}}{1+12.7(f/8)^{1/2}(\mathrm{Pr}^{2/3}-1)}$, $f = \frac{1}{(1.82\ln(\mathrm{Re})-1.64)^2}$	Transitional and fully developed turbulent	$3000 < \mathrm{Re} < 5 \times 10^4$
Sieder–Tate correlation [49], $\mathrm{Nu} = 0.027\mathrm{Re}^{0.8}\mathrm{Pr}^{1/3}\left(\frac{\mu_f}{\mu_w}\right)^{0.14}$	Fully developed turbulent	$0.7 < \mathrm{Pr} < 16{,}700$, $\mathrm{Re} > 10{,}000$, $\mathrm{L/D} > 10$

are enumerated in Table 1, together with their corresponding hydrodynamic and thermal conditions and the applicable range. Figure 8(*a*) shows that in the laminar region, the measured data of Nusselt number are in good agreement with the predication from the Oskay–Kakac correlation, while the other laminar heat transfer correlations provide a much less satisfactory prediction of the experimental data. The transition to turbulent flow at $\mathrm{Re_{cr}} \approx 2300$ can also be found in Fig. 8(*a*). Figure 8(*b*) demonstrates that, among the turbulent heat transfer correlations, the Hausen correlation for thermally developing turbulent flow is the best in predicting the experimental data. The successes of the Oskay–Kakac and Hausen correlations can be attributed to the close match between their founding conditions and those of the present experiments.

4.2 Experiments With Nanofluids. Following similar test procedures, the pressure drop and convective heat transfer experiments were conducted for Al_2O_3-water nanofluids with volume concentrations of 1%, 2%, 3.5%, and 5%.

4.2.1 Pressure Drop. Figure 9 shows the measured friction factor for nanofluids as a function of Re. Several interesting features can be observed. First, in the laminar region, the friction factor of nanofluids shows an increasing trend with the volume concentration and is generally higher than that of pure water at the same Re. Second, at low Re where the flow field would be fully developed if water were the working fluid, the Shah equation for developing flows (Eq. (15)) outperforms the Hagen–Poiseuille equation (Eq. (14)) in predicting the friction factor of nanofluids. It suggests that the entrance region in nanofluids is prolonged, or, equivalently, the development of the velocity boundary layer is retarded in nanofluids. Third, the onset of transition to turbulence is delayed in nanofluids. The transition occurs as the result of the amplified perturbations in the flow field that eventually trigger instability. While no strict theoretical limit exists for the critical Re, it is generally agreed that the onset of turbulence can occur at $\mathrm{Re_{cr}} = 2100-2300$ in a channel flow, unless special measures are taken to suppress the perturbations. Figure 9 shows that while $\mathrm{Re_{cr}}$ is almost exactly 2300 for water, it shifts toward a higher value as the nanofluid volume concentration increases. From the inset in Fig. 9, $\mathrm{Re_{cr}}$ reaches 2500 for the 5% nanofluid. Thus, the laminar flow behavior of nanofluids extends into the otherwise transition region for water ($2300 < \mathrm{Re} < 2500$), where the friction factor of nanofluids actually falls below that of water. The region with a reduced friction factor further persists until fully developed turbulence begins to establish at $\mathrm{Re} \approx 3200$. Afterward, the data for both nanofluids and water collapse together and become difficult to distinguish, indicating the vanishing influence of nanoparticles on the flow dynamics at high Re.

The prolonged entrance region in the laminar flow in nanofluids has been discussed in the literature [22,50,51] and has been attrib-

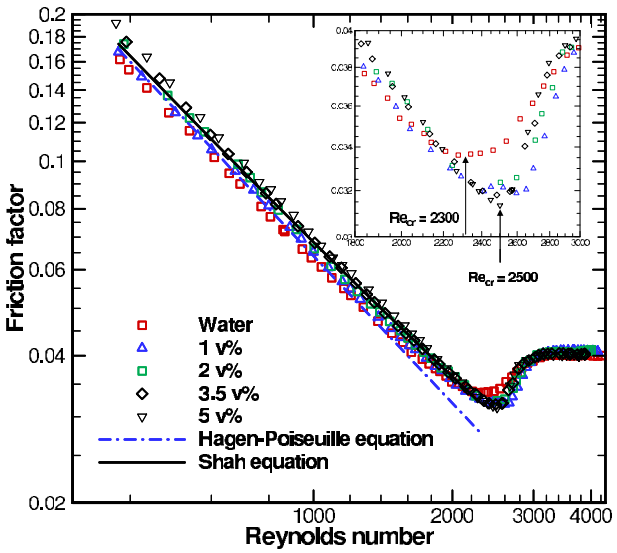

Fig. 9 Friction factor versus Reynolds number for nanofluids at various volume concentrations

uted to the shear-induced nanoparticle migration, which results in a nonuniform distribution of particles along the radial direction of the channel; i.e., the concentration is at its maximum at the centerline and decreases toward the channel wall. According to Eq. (3), the local visocity of the nanofluid will be greater in the centerline region than in the near-wall region. As a consequence, the velocity profile will be no longer parabolic even when the flow is fully developed but flattened in the center with a steeper gradient near the wall. Since this is a representative feature of laminar developing flows, it is interpreted as a prolonged entrance region effect in nanofluids. While the postulated particle migration model yields useful information for the laminar flow of nanofluids, it is insufficient to explain the delayed transition to turbulence and the subsequent flow behavior under early fully developed turbulent conditions, as previously discussed. A different mechanism must, therefore, be sought to provide insight into the flow physics of nanofluids in the transition and turbulent regions.

In the study of particle-laden turbulent flows, it has long been known that addition of small particles can modify the turbulence structures by changing the turbulent kinetic energy of the carrier fluid [52–55]. In particular, the changes in turbulent structure depend on the size of the particles relative to the length scale of turbulence, i.e., the Kolmogorov microscale, η [56–58]. Gore and Crowe [59] defined a critical parameter, $d_p/\eta \approx 0.1$, for gas-solid flows, above which turbulence intensity is enhanced and below which it is attenuated. Hetsroni [60] also proposed that "small" particles suppress turbulence by acting as an additional source of dissipation, and "large" particles enhance turbulence due to wake shedding. Noticing the similarity between the friction factor results of nanofluids in Fig. 9 and the results obtained in particle-laden turbulent flows, it is interesting to examine, using a simple scaling analysis, the effect of the interaction between nanoparticles and the base fluid on the transition and turbulent flow behaviors.

The Kolmogorov microscale represents the finest structure in turbulence at which the kinetic energy is dissipated by viscosity and can be estimated as

$$\eta \approx \frac{\nu}{u_\tau^2} \tag{18}$$

where the wall shear velocity u_τ is defined as $u_\tau = (\tau_w/\rho_f)^{1/2}$. The wall shear stress τ_w can be obtained from the definition of the Darcy friction factor $f = 8\tau_w/(\rho_f u^2)$, in conjunction with the Blasius equation (Eq. (16)). Now, consider the experimental conditions in this study, $D = 1.09$ mm, $d_p = 135$ nm, and $\nu = 8.6 \times 10^{-7}$ m^2/s for water, the relative sizes of d_p/η are found to be 0.003 and 0.005 for Re = 2550 and 3200, respectively. It is noted that while $d_p/\eta \approx 0.1$ was originally proposed to determine the enhancement or attenuation of turbulence by particles in gas-solid flows, a smaller critical value can be expected for liquid-solid flows where the interaction between the liquid and solid particles is much more intensive. Nevertheless, the above scaling analysis shows that the nanoparticles should be considered small as compared with the length scale of turbulence ($d_p/\eta \ll 0.1$) at Re < 3200, and the particle-fluid interaction will damp the instability and reduce the turbulence intensity and Reynolds stress in the flow. Consequently, the transition to turbulence is delayed and the friction factor is reduced to below that of the base fluid. As Re further increases, the Kolmogorov microscale will decrease, as suggested by Eq. (18), and d_p/η will increase and eventually exceed the critical value. In that case, the nanoparticles become large with respect to the turbulence structures, and the turbulent flow will be intensified. Due to the limit of the Re range in the present study, the intensified turbulence was not observed in Fig. 9; however, the recovery trend in the nanofluid data to that of the base fluid supports the arguments from the above analysis.

4.2.2 Heat Transfer. The local heat transfer coefficients measured for nanofluids at five axial locations (TC1–TC5) are presented in Fig. 10 for Re = 870 and 1230. It can be found that convective heat transfer in nanofluids is enhanced and that the increment increases in proportion to Re and the nanoparticle concentration. The heat transfer enhancement is more significant in the entrance region than at downstream locations. In Fig. 10(*a*), the enhancement in heat transfer coefficient for the 5% nanofluid is 19% near the entrance and decreases to less than 9% near the channel exit. This trend also strengthens with increasing nanoparticle concentration and Re. The thermally developing flow shown in Fig. 10 is consistent with the pronounced hydrodynamic entrance region effect observed in Fig. 9.

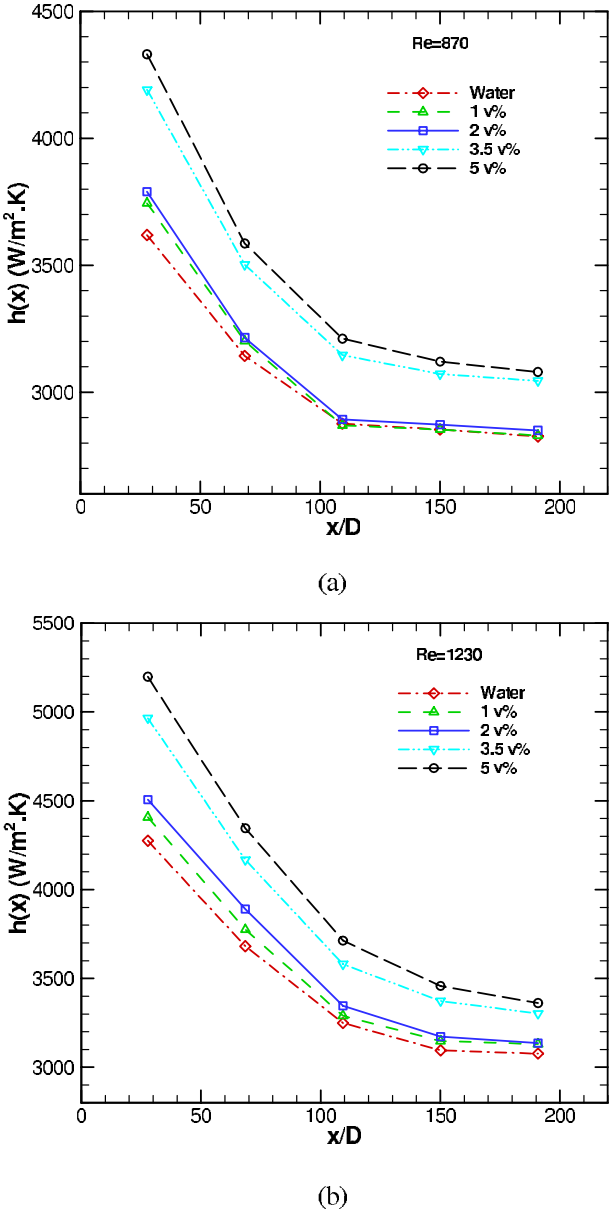

Fig. 10 Local convective heat transfer of nanofluids (heat flux $q'' = 6.5$ kW/m^2)

Figure 11 shows the average Nusselt number for the nanofluids in the laminar region. The experimental data are bounded by predictions from the Oskay–Kakac correlation and the Stephan correlation, whereas the Hausen equation for laminar flow almost always underpredicts the measured data. Since the Oskay–Kakac correlation works well for the base fluid, its role as the lower bound in Fig. 11 for the measured nanofluid results again proves the heat transfer enhancement in nanofluids. As the nanoparticle

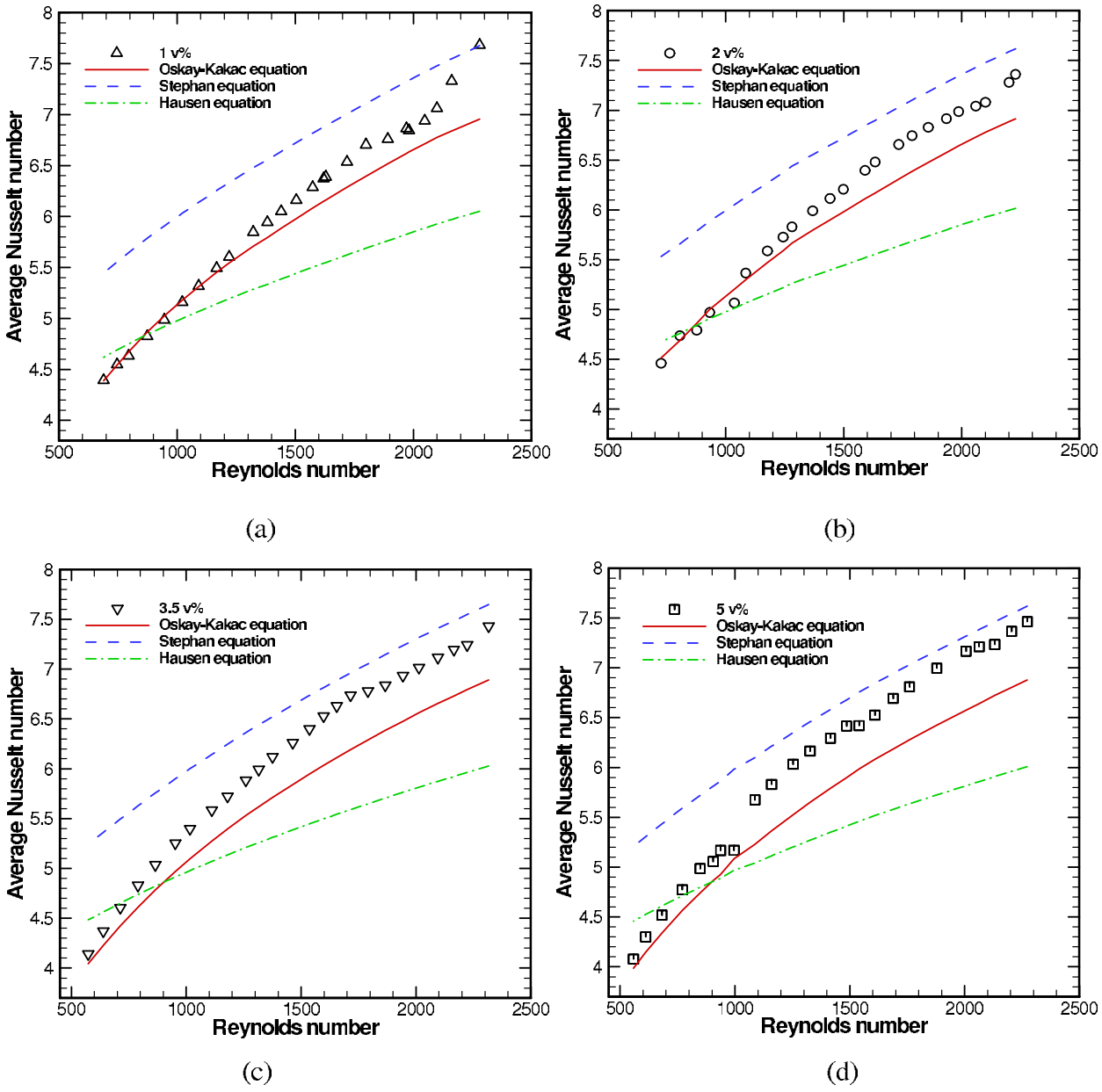

Fig. 11 Average Nusselt number versus Reynolds number in the laminar flow region (nanofluids, heat flux q'' = 6.5 kW/m^2)

concentration and Re increase, the convection in nanofluids becomes more hydrodynamically and thermally developing, as manifested in Figs. 9 and 10. It is thus not surprising that the experimental data move toward the theoretical prediction from the Stephan correlation, which was developed for simultaneously developing flow conditions.

The average Nusselt numbers measured for the nanofluids in the transition and turbulent regions are presented in Fig. 12. As Re increases, there are two locations where the slope of the experimental data changes. The first one corresponds to the onset of transition to turbulence, and the second one is associated with the initial establishment of fully developed turbulent heat transfer. It can be observed that the delayed transition occurs at $Re_{cr} \approx 2800$. Throughout the transition and the early stage of fully developed turbulent regions (Re up to 4500), the measured Nusselt number falls short of the prediction from the Hausen equation, which represents the data of water well. Furthermore, the heat transfer reduction worsens as the nanoparticle concentration increases, as shown in Figs. 12(*a*)–12(*d*). It can be deduced that, rather than enhancing convective heat transfer, the presence of nanoparticles causes deterioration of heat transfer in the transition and the early stage of fully developed turbulent flows. This observation can be qualitatively understood as the natural consequence of the suppressed turbulence discussed before. It is noted that, however, the heat transfer reduction observed in this work is not necessarily in conflict with the enhancement of turbulent heat transfer reported in the literature, which was experimented at much higher Re in the fully developed turbulent region. Using the same argument, it can be expected that the size ratio d_p/η will surpass the critical value and that the nanoparticles will become large enough to intensify the turbulent heat transfer.

Figure 13 provides an overview of the comparison of the average Nusselt number measured for nanofluids and the base fluid over the entire range of Re studied in the present work. It shows clearly that nanofluids enhance convective heat transfer modestly in laminar flow; however, they cause significant heat transfer de-

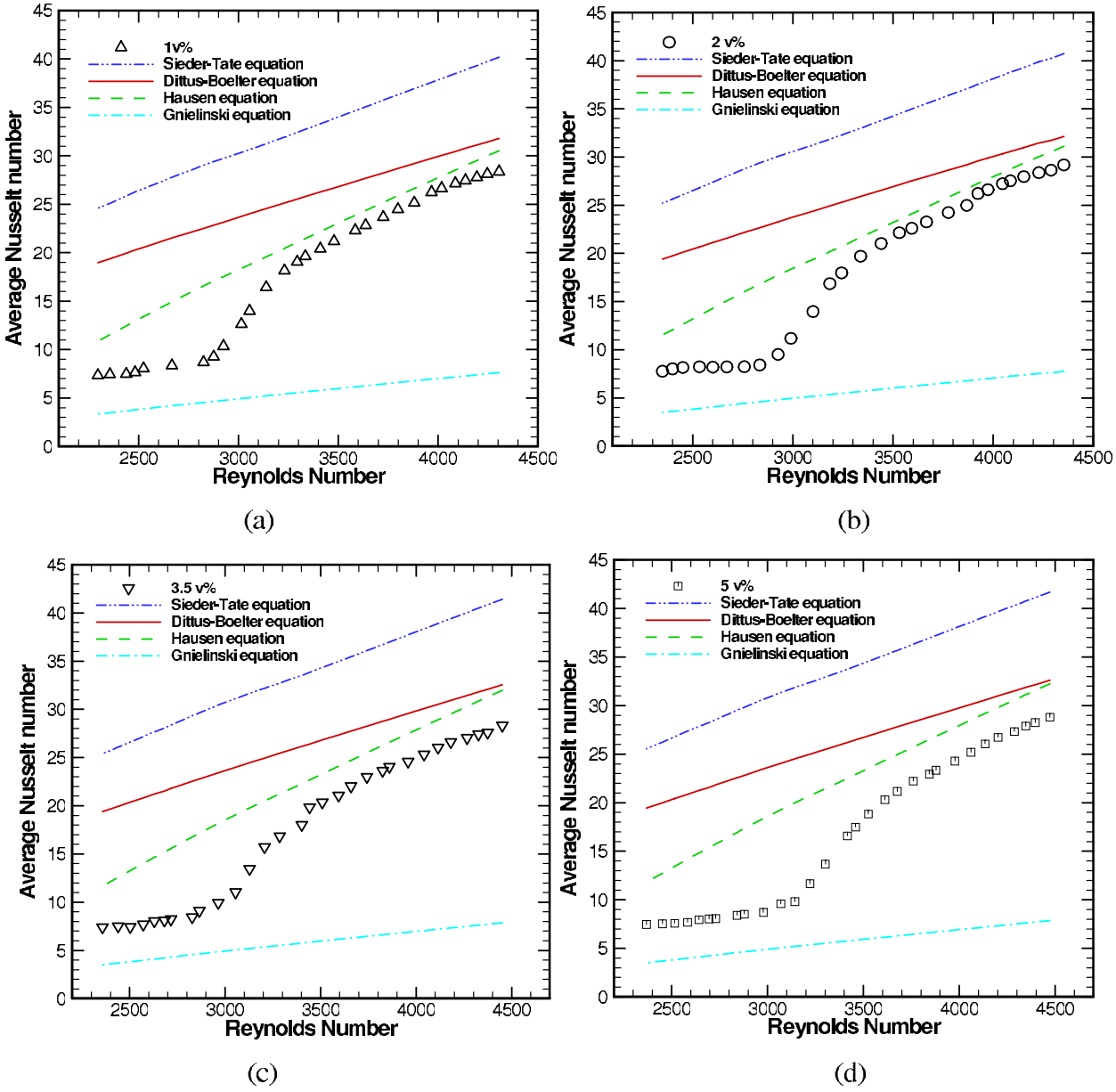

Fig. 12 Average Nusselt number versus Reynolds number in the transition and turbulent flow regions (nanofluids, heat flux $q''=6.5$ kW/m^2)

terioration in the transition and the early stage of fully developed turbulent regions. Both the enhancement and deterioration are seen to increase with the nanoparticle concentration. The delayed transition to turbulent heat transfer in nanofluids can also be identified in Fig. 13. Further, once the flow becomes fully turbulent, the difference in the measured Nusselt number between nanofluids and water tends to diminish as a result of the alleviated suppression of turbulence. Lastly, a piece of useful information may be deduced from Fig. 13 as a design guideline for utilizing nanofluids as an advanced heat transfer fluid: Nanofluids should be operated in either the laminar region or the fully developed turbulent region with sufficiently high Re for the sake of enhanced heat transfer performance.

5 Conclusions

An experimental investigation was conducted to study the single-phase convective heat transfer of Al_2O_3-water nanofluids in a circular minichannel. Both the pressure drop and the heat transfer coefficient were measured over a wide range of Re, covering the laminar, transition, and early stage of fully developed turbulent flows. The key findings can be summarized as follows.

(1) Nanofluids exhibit pronounced entrance region behaviors, both hydrodynamically and thermally, in the laminar region. The convective heat transfer of nanofluids is enhanced in the laminar flow with the penalty of increased pressure drop. The increments in both heat transfer and pressure drop are proportional to the nanoparticle volume concentration. No dramatic heat transfer enhancement as reported in the early literature was observed in the nanoparticle concentration range considered in this work.

(2) The critical Re at which the onset of transition to turbulence occurs is delayed in nanofluids due to the particle-fluid interaction, which damps the instabilities in the flow. The suppression of turbulence is alleviated as the flow becomes fully developed turbulent. Correspondingly, the convective heat transfer of nanofluids deteriorates in the transition and the early stage of fully developed turbulent

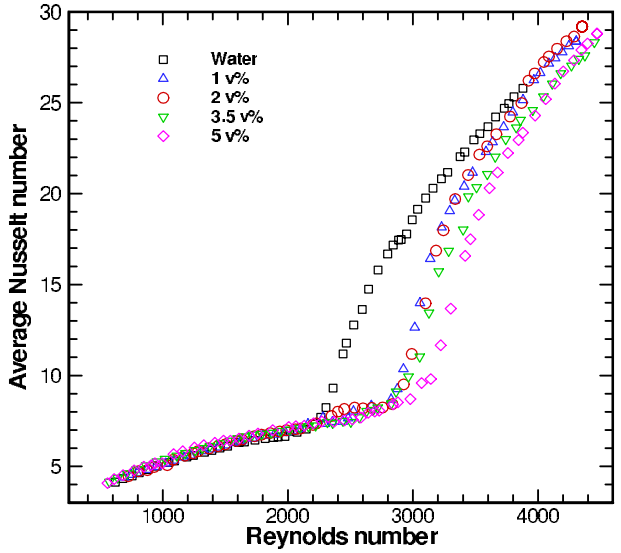

Fig. 13 Average Nusselt number versus Reynolds number over the entire flow range (nanofluids, heat flux q'' = 6.5 kW/m^2)

regions and gradually recovers after the fully developed turbulence is intensified.

(3) Established conventional correlations cannot fully predict the single-phase pressure drop and heat transfer of nanofluids, particularly in the transition and turbulent regions, even when the effective thermophysical properties are taken into consideration.

(4) Nanofluids should be used in either the laminar flow or the fully developed turbulent flow with sufficiently high Re in order to yield enhanced heat transfer performance for engineering applications.

Acknowledgment

The authors are grateful to Dr. Suresh Garimella and Dr. Brian Iverson for insightful discussions. They also thank Dr. Hollingsworth for sharing with them the dc power supply and the ultrasonicator. Finally, they acknowledge the financial support from the Cooling Technologies Research Center (a National Science Foundation Industry/University Cooperative Research Center) at Purdue University and from the National Science Foundation (Grant No. 0927340).

Nomenclature

f = friction factor
Gz = Graetz number
h = heat transfer coefficient, W/m^2 K
k = thermal conductivity, W/m K
L = length of test tube, m
D = channel diameter, m
C_p = specific heat, kJ/kg K
P = pressure, Pa
Pr = Prandtl number
q'' = heat flux, W/m^2
Q = volumetric flow rate, m^3/s
Re = Reynolds number
T = temperature, °C
u = velocity, m/s

Greek Symbols

ϕ = volume concentration
η = Kolmogorov microscale, μm
μ = viscosity, N s/m^2
ρ = density, kg/m^3
τ = shear stress, N/m^2

Subscripts

cr = critical
f = base fluid
nf = nanofluids
p = particle
x = local
w = wall

References

[1] Choi, S. U. S., 1995, "Enhancing Thermal Conductivity of Fluids With Nanoparticles," *Developments and Applications of Non-Newtonian Flows*, ASME, New York, pp. 99–105.
[2] Choi, S. U. S., Zhang, Z. G., and Keblinski, P., 2004, *Nanofluids in Encyclopedia of Nanoscience and Nanotechnology*, American Scientific, Los Angeles, CA, Vol. 6, p. 757.
[3] Eastman, J. A., Phillpot, S. R., Choi, S. U. S., and Keblinski, P., 2004, "Thermal Transport in Nanofluids," Annu. Rev. Mater. Res., **34**, pp. 219–246.
[4] Keblinski, P., Eastman, J. A., and Cahill, D. G., 2005, "Nanofluids for Thermal Transport," Mater. Today, **8**(6), pp. 36–44.
[5] Das, S. K., Choi, S. U. S., and Patel, H. E., 2006, "Heat Transfer in Nanofluids—A Review," Heat Transfer Eng., **27**, pp. 3–19.
[6] Yu, W., France, D. M., Routbort, J. L., and Choi, S. U. S., 2008, "Review and Comparison of Nanofluid Thermal Conductivity and Heat Transfer Enhancements," Heat Transfer Eng., **29**, pp. 432–460.
[7] Cheng, L. X., Filho, E. P. B., and Thome, J. R., 2008, "Nanofluid Two-Phase Flow and Thermal Physics: A New Research Frontier of Nanotechnology and Challenges," J. Nanosci. Nanotechnol., **8**, pp. 3315–3332.
[8] Li, Q., and Xuan, Y., 2002, "Convective Heat Transfer and Flow Characteristics of Cu-Water Nanofluid," Sci. China, Ser. E: Technol. Sci., **45**, pp. 408–416.
[9] Xuan, Y., and Li, Q., 2003, "Investigation on Convective Heat Transfer and Flow Features of Nanofluids," ASME J. Heat Transfer, **125**, pp. 151–156.
[10] Yang, Y., Zhang, Z., Grulke, E. A., Anderson, W. B., and Wu, G., 2005, "Heat Transfer Properties of Nanoparticle-in-Fluid Dispersions (Nanofluids) in Laminar Flow," Int. J. Heat Mass Transfer, **48**, pp. 1107–1116.
[11] Wen, D. S., and Ding, Y. L., 2004, "Experimental Investigation Into Convective Heat Transfer of Nanofluids at Entrance Region Under Laminar Flow Condition," Int. J. Heat Mass Transfer, **47**, pp. 5181–5188.
[12] Ding, Y. L., Alias, H., Wen, D. S., and Williams, R. A., 2006, "Heat Transfer of Aqueous Suspensions of Carbon Nanotubes (CNT Nanofluids)," Int. J. Heat Mass Transfer, **49**, pp. 240–250.
[13] He, Y. R., Jin, Y., Chen, H. S., Ding, Y. L., Can, D. Q., and Lu, H. L., 2007, "Heat Transfer and Flow Behavior of Aqueous Suspensions of TiO_2 Nanoparticles (Nanofluids) Flowing Upward Through a Vertical Pipe," Int. J. Heat Mass Transfer, **50**, pp. 2272–2281.
[14] Heris, S. Z., Esfahany, M. N., and Etemad, S. Gh., 2007, "Experimental Investigation of Convective Heat Transfer of Al_2O_3/Water Nanofluid in Circular Tube," Int. J. Heat Fluid Flow, **28**, pp. 203–210.
[15] Chen, H., Yang, W., He, Y., Ding, Y. L., Zhang, L., Tan, C., Lapkin, A. A., and Bavykin, D. V., 2008, "Heat Transfer and Flow Behavior of Aqueous Suspensions of Titanate Nanotubes," Powder Technol., **183**, pp. 63–72.
[16] Williams, W., Buongiorno, J., and Hu, L. W., 2008, "Experimental Investigation of Turbulent Convective Heat Transfer and Pressure Loss of Alumina/Water and Zirconia/Water Nanoparticle Colloids in Horizontal Tubes," ASME J. Heat Transfer, **130**, p. 042412.
[17] Putra, N., Roetzel, W., and Das, S. K., 2003, "Natural Convection of Nano-Fluids," Heat Mass Transfer, **39**, pp. 775–784.
[18] Duangthongsuk, W., and Wongwises, S., 2008, "Effect of Thermophysical Properties Models on the Predicting of the Convective Heat Transfer Coefficient for Low Concentration Nanofluid," Int. Commun. Heat Mass Transfer, **35**, pp. 1320–1326.
[19] Wen, D. S., and Ding, Y. L., 2005, "Formulation of Nanofluids for Natural Convective Heat Transfer Applications," Int. J. Heat Fluid Flow, **26**, pp. 855–864.
[20] Nnanna, A. G., 2007, "Experimental Model of Temperature-Driven Nanofluid," ASME J. Heat Transfer, **129**, pp. 697–704.
[21] Khanafer, K., Vafai, K., and Lightstone, M., 2003, "Buoyancy-Driven Heat Transfer Enhancement in a Two-Dimensional Enclosure Utilizing Nanofluids," Int. J. Heat Mass Transfer, **46**, pp. 3639–3653.
[22] Wen, D. S., and Ding, Y. L., 2005, "Effect of Particle Migration on Heat Transfer in Suspensions of Nanoparticles Flowing Through Minichannels," Microfluid. Nanofluid., **1**, pp. 183–189.
[23] Mansour, R. B., Galanis, N., and Nguyen, C. T., 2007, "Effect of Uncertainties in Physical Properties on Forced Convection Heat Transfer With Nanofluids," Appl. Therm. Eng., **27**, pp. 240–249.
[24] Kim, J., Kang, Y. T., and Choi, C. K., 2004, "Analysis of Convective Instability and Heat Transfer Characteristics of Nanofluids," Phys. Fluids, **16**, pp. 2395–2401.
[25] Hwang, K. S., Lee, J. H., and Jang, S. P., 2007, "Buoyancy-Driven Heat Transfer of Water-Based Al_2O_3 Nanofluids in a Rectangular Cavity," Int. J.

Heat Mass Transfer, **50**, pp. 4003–4010.
[26] Hwang, K. S., Jang, S. P., and Choi, S. U. S., 2009, "Flow and Convective Heat Transfer Characteristics of Water-Based Al_2O_3 Nanofluids in Fully Developed Flow Regime," Int. J. Heat Mass Transfer, **52**, pp. 193–199.
[27] Anoop, K. B., Sundararajan, T., and Das, S. K., 2009, "Effect of Particle Size on the Convective Heat Transfer in Nanofluid in Developing Region," Int. J. Heat Mass Transfer, **52**, pp. 2189–2195.
[28] Lai, W. Y., Vind, S., Phelan, P. E., and Prasher, R., 2009, "Convective Heat Transfer for Water-Based Alumina Nanofluids in a Single 1.02-mm Tube," ASME J. Heat Transfer, **131**, p. 112401.
[29] Mills, P., and Snabre, P., 1995, "Rheology and Structure of Concentrated Suspensions of Hard Sphere, Shear Induced Particle Migration," J. Phys. II, **5**, pp. 1597–1608.
[30] Sharma, K. V., Sundar, L. S., and Sharma, P. K., 2009, "Estimation of Heat Transfer Coefficient and Friction Factor in the Transition Flow With Low Volume Concentration of Al_2O_3 Nanofluid Flowing in a Circular Tube and With Twisted Tape Insert," Int. Commun. Heat Mass Transfer, **36**, pp. 503–507.
[31] Rea, U., McKrell, T., Hu, L. W., and Buongiorno, J., 2009, "Laminar Convective Heat Transfer and Viscous Pressure Loss of Alumina-Water and Zirconia-Water Nanofluids," Int. J. Heat Mass Transfer, **52**, pp. 2042–2048.
[32] Torii, S., and Yang, W.-J., 2009, "Heat Transfer Augmentation of Aqueous Suspensions of Nanodiamonds in Turbulent Pipe Flow," ASME J. Heat Transfer, **131**, p. 043203.
[33] Duangthongsuk, W., and Wongwises, S., 2010, "An Experimental Study on the Heat Transfer Performance and Pressure Drop of TiO_2-Water Nanofluids Flowing Under a Turbulent Flow Regime," Int. J. Heat Mass Transfer, **53**, pp. 334–344.
[34] Jung, J. Y., Oh, H. S., and Kwak, H. Y., 2009, "Forced Convective Heat Transfer of Nanofluids in Microchannels," Int. J. Heat Mass Transfer, **52**, pp. 466–472.
[35] Wu, X., Wu, H., and Cheng, P., 2009, "Pressure Drop and Heat Transfer of Al_2O_3 Nanofluids Through Silicon Microchannels," J. Micromech. Microeng., **19**, p. 105020.
[36] Batchelor, G. K., 1977, "The Effect of Brownian Motion on the Bulk Stress in a Suspension of Spherical Particles," J. Fluid Mech., **83**, pp. 97–117.
[37] Pak, B. C., and Ho, Y. I., 1998, "Hydrodynamic and Heat Transfer Study of Dispersed Fluids With Submicron Metallic Oxide Particles," Exp. Heat Transfer, **11**, pp. 151–170.
[38] Liu, D., and Garimella, S. V., 2004, "Investigation of Liquid Flow in Microchannels," J. Thermophys. Heat Transfer, **18**, pp. 65–72.
[39] Blevins, R. D., 1992, *Applied Fluid Dynamics Handbook*, Krieger, Malabar, FL.
[40] Incropera, F. P., and DeWitt, D. P., 1996, *Fundamentals of Heat and Mass Transfer*, Wiley, New York.
[41] Taylor, J. R., 1997, *An Introduction to Error Analysis*, University Science Books, Sausalito, California.
[42] White, F. M., 1991, *Viscous Fluid Flow*, McGraw-Hill, New York.
[43] Shah, R. K., and London, A. L., 1978, "Laminar Flow Forced Convection in Ducts," *Advances in Heat Transfer*, Academic, New York, Suppl. 1.
[44] Stephan, K., and Preuber, P., 1979, "Warmeubergang und Maximale Warmestromdichte Beim Behaltersieden Binarer und Ternarer Flussigkeitsgemische," Chem.-Ing.-Tech., **51**, p. 37.
[45] Kakac, S., Shah, R. K., and Aung, W., 1987, *Handbook of Single-Phase Convective Heat Transfer*, Wiley, New York.
[46] Dittus, F. W., and Boelter, L. M. K., 1930, *Heat Transfer in Automobile Radiators of the Tubular Type*, Vol. 2, University of California, Berkeley, pp. 443–461.
[47] Hausen, H., 1959, "Neue Gleichungen fur die Wameiibertragung bei Freier oder Erzwungerner Stromung," Allg. Warmetchn., **9**, pp. 75–79.
[48] Gnielinkski, V., 1976, "New Equations for Heat and Mass Transfer in Turbulent Pipe and Channel Flow," Int. Chem. Eng., **16**, pp. 359–367.
[49] Sieder, E. N., and Tate, G. E., 1936, "Heat Transfer and Pressure Drop of Liquids in Tubes," Ind. Eng. Chem., **28**, pp. 1429–1435.
[50] Leighton, D., and Acrivos, A., 1987, "The Shear-Induced Migration of Particles in Concentrated Suspensions," J. Fluid Mech., **181**, pp. 415–439.
[51] Phillips, R. J., Armstrong, R. C., Brown, R. A., Graham, A. L., and Abbott, J. R., 1992, "A Constitutive Equation for Concentrated Suspensions That Accounts for Shear-Induced Particle Migration," Phys. Fluids A, **4**, pp. 30–40.
[52] Bhadani, M. M., and Ludlow, N. G. T., 1961, "Precipitation of Sub-Micron Dust in Still Air by Cloud-Size Water Droplets," Nature (London), **190**, pp. 974–976.
[53] Hetsroni, G., and Sokolov, M., 1971, "Distribution of Mass, Velocity, and Intensity of Turbulence in a Two-Phase Turbulent Jet," ASME J. Appl. Mech., **38**, pp. 315–327.
[54] Rogers, C. B., and Eaton, J. K., 1991, "The Effect of Small Particles on Fluid Turbulence in a Flat-Plate, Turbulent Boundary in Air," Phys. Fluids A, **3**, pp. 928–937.
[55] Kulick, J. D., Fessler, J. R., and Eaton, J. K., 1994, "Particle Response and Turbulence Modification in Fully Developed Channel Flow," J. Fluid Mech., **277**, pp. 109–134.
[56] Pan, Y., and Banerjee, S., 1996, "Numerical Simulation of Particle Interactions With Wall Turbulence," Phys. Fluids, **8**, pp. 2733–2755.
[57] Elghobashi, S. E., and Abou-Arab, T. W., 1983, "A Two-Equation Turbulence Model for Two-Phase Flows," Phys. Fluids, **26**, pp. 931–938.
[58] Rizk, M. A., and Elghobashi, S. E., 1985, "The Motion of a Spherical Particle Suspended in a Turbulent Flow Near a Plane Wall," Phys. Fluids, **28**, pp. 806–817.
[59] Gore, R. A., and Crowe, C. T., 1989, "Effect of Particle Size on Modulating Turbulent Intensity," Int. J. Multiphase Flow, **15**, pp. 279–285.
[60] Hetsroni, G., 1989, "Particle-Turbulence Interaction," Int. J. Multiphase Flow, **15**, pp. 735–746.

Modeling Transport in Porous Media With Phase Change: Applications to Food Processing

Amit Halder[1]
Graduate Research Assistant
e-mail: ah333@cornell.edu

Ashish Dhall[1]
Graduate Research Assistant
e-mail: ad333@cornell.edu

Ashim K. Datta[2]
Professor
e-mail: akd1@cornell.edu

Department of Biological and Environmental Engineering,
Cornell University,
Ithaca, NY 14853

Fundamental, physics-based modeling of complex food processes is still in the developmental stages. This lack of development can be attributed to complexities in both the material and transport processes. Society has a critical need for automating food processes (both in industry and at home) while improving quality and making food safe. Product, process, and equipment designs in food manufacturing require a more detailed understanding of food processes that is possible only through physics-based modeling. The objectives of this paper are (1) to develop a general multicomponent and multiphase modeling framework that can be used for different thermal food processes and can be implemented in commercially available software (for wider use) and (2) to apply the model to the simulation of deep-fat frying and hamburger cooking processes and validate the results. Treating food material as a porous medium, heat and mass transfer inside such material during its thermal processing is described using equations for mass and energy conservation that include binary diffusion, capillary and convective modes of transport, and physicochemical changes in the solid matrix that include phase changes such as melting of fat and water and evaporation/condensation of water. Evaporation/condensation is considered to be distributed throughout the domain and is described by a novel nonequilibrium formulation whose parameters have been discussed in detail. Two complex food processes, deep-fat frying and contact heating of a hamburger patty, representing a large group of common food thermal processes with similar physics have been implemented using the modeling framework. The predictions are validated with experimental results from the literature. As the food (a porous hygroscopic material) is heated from the surface, a zone of evaporation moves from the surface to the interior. Mass transfer due to the pressure gradient (from evaporation) is significant. As temperature rises, the properties of the solid matrix change and the phases of frozen water and fat become transportable, thus affecting the transport processes significantly. Because the modeling framework is general and formulated in a manner that makes it implementable in commercial software, it can be very useful in computer-aided food manufacturing. Beyond its immediate applicability in food processing, such a comprehensive model can be useful in medicine (for thermal therapies such as laser surgery), soil remediation, nuclear waste treatment, and other fields where heat and mass transfer takes place in porous media with significant evaporation and other phase changes.
[DOI: 10.1115/1.4002463]

1 Introduction

Mathematical modeling has not been able to contribute as much to the development of food processing industries as it has with respect to the mechanical and chemical industries. The primary reason for this is that food are complex and nonhomogeneous, and the physics that could explain what happens during processing is still not clearly established. The time and cost involved limit the number of experiments that can be done to achieve this. Looking at recent trends toward the automation of food processes and production of minimally processed healthier foods, it can be said that there is a need to develop accurate mathematical models of these food processes, which can be extensively used for equipment design or to ensure food safety. The development of fundamental physics-based models of food processes is not trivial as it requires physical as well as mathematical insight into the material and the process.

In food systems, an enormous range of thermal processes can be viewed as involving transport of energy, moisture, and, in some cases, fat through a hygroscopic porous medium. Examples include extraction, drying, deep-fat frying, microwave heating, meat roasting, and rehydration. In the vast majority of food systems, proteins or carbohydrates form a porous skeleton, which has water and/or fat physically and chemically bound to it. During heating, water and fat can transport inside the solid matrix or can be released into the pore space and then transported through the porous medium. Other important phenomena that can occur are rapid evaporation due to intensive heating and the melting of ice or fat during the processing of frozen food and shrinkage due to physicochemical changes in the porous matrix. There is no single model that considers all of these physics together and that can also be implemented in a software application for wide usage.

The existing models of thermal processes can be broadly divided into four groups. The first group consists of totally lumped models for heat and mass transport that do not include any important physics [1–5]. Such models are based entirely on empirical data, are suited for a specified product and processing condition, and, therefore, cannot be used for even a slightly different situation. The second group consists of slightly improved models that assume conductive heat transfer for energy and diffusive transport for moisture, solving a transient diffusion equation using experi-

[1]Co-authors Amit Halder and Ashish Dhall contributed equally to this work.
[2]Corresponding author.
Contributed by the Heat Transfer Division of ASME for publication in the JOURNAL OF HEAT TRANSFER. Manuscript received February 13, 2009; final manuscript received May 5, 2010; published online November 16, 2010. Assoc. Editor: Wilson K. S. Chiu.

mentally determined effective diffusivity [6–10]. Lumping together all modes of water transport as diffusion cannot be justified under all situations, especially when other phenomena such as pressure-driven flow due to intensive heating or transport due to physicochemical changes in the porous medium become important. Also, the use of effective diffusivity does not yield insights into the prevalent transport mechanisms. These models might provide good matches with experimental results, but they cannot be generalized to other conditions.

The third group of models, with a significantly improved formulation compared with those of simple diffusion models, assumes a sharp moving boundary separating the dry and wet regions (e.g., deep-fat frying models [11–13]). This assumption is analogous to that made in freezing and thawing models of a pure material [14], where a sharp front separates the frozen and unfrozen regions. In contrast to sharp boundary models, distributed evaporation models assume that evaporation occurs over a zone rather than at an interface [15–17]. In a given situation, it is possible that the real evaporation zone is very narrow, closer to the sharp interface, and that a distributed evaporation formulation will, in fact, predict such narrow evaporation zone.

Evaporation of water in intensive heating food processes, such as deep-fat frying and baking, has usually been implemented using an equilibrium formulation wherein liquid water present in the food is always assumed to be in equilibrium with water vapor present in the pore space [15,16,18]. There is no detailed study of this equilibrium assumption for hygroscopic materials such as food. Only a qualitative description of the conditions under which either equilibrium or nonequilibrium assumptions can hold is available [19]. As will be explained later, a nonequilibrium formulation that can also be used to enforce equilibrium is a more general approach and appears to be the obvious alternative. Furthermore, significant effort is required to implement the equations resulting from an equilibrium formulation in the framework of most commercial software, whereas implementation of a nonequilibrium formulation is straightforward.

Overall, accurate models of food processes, which include all the physics, still do not exist. Multiphase porous media models have been used with success in other fields and applications to describe physics that is similar to that involved in food processing. A multiphase porous media approach with conservation equations for relevant components, appropriately including the effect of various phenomena particular to food, has been developed for some food applications [18,20–22]. However, none of these models is general enough to be applied to many different processes. Moreover, these models have been formulated in such a way that they are very difficult to manipulate and implement in commercial software and have been solved by user-developed codes. These codes are either publicly unavailable, have limited capabilities, or are difficult to use by anyone other than the creator. A general framework applicable to the majority of food processes, which is implementable in commercial software, has not been developed yet. This development is not trivial and requires significant reformulations or in some cases developing a new model altogether. The present study aims to do this.

Some of the physics involved in food processes can be seen in other applications such as geoscience [23], nuclear waste storage and management [24], groundwater contamination [25,26], and thermal treatment of tumors or drug delivery in biomedical engineering [27]. However, food processing applications, involving thermal treatment of heterogeneous materials, are extremely complex. A fundamental physics-based model developed for food processes, which accounts for all the relevant phenomena, can be applied to other fields with simplifications.

The objectives of this study are (1) to develop a general multiphase model for hygroscopic biological materials that can be used for various thermal processes and can be implemented in commercially available software and (2) to apply the model to simulate deep-fat frying and hamburger cooking processes and validate the results.

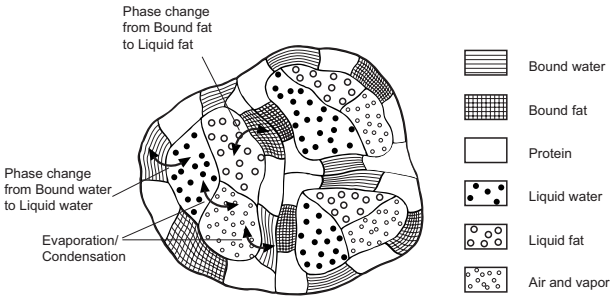

Fig. 1 Schematic of a porous food material showing mass transfer between various phases

The outline of the paper is as follows: A comprehensive mathematical model, which can be used to simulate a large number of thermal processes, is presented first, followed by a detailed discussion of a nonequilibrium approach to implementing evaporation/condensation phase change. Two food processes, deep-fat frying of a restructured potato slab and contact heating of a hamburger patty, are modeled using the set of equations developed to show the model's effectiveness in solving different types of thermal food processes. The paper concludes with a discussion of the importance of this comprehensive modeling framework in food processing.

2 Mathematical Model

A multiphase porous media model is developed, which describes heat and mass transfer inside a food material during thermal processing. Mass and energy conservation equations are developed, which, depending on the process, may include binary diffusion, capillary and convective modes of transport, effects of physicochemical changes in the solid matrix on transport, and phase changes such as melting and evaporation-condensation. Evaporation/condensation is assumed to be distributed throughout the domain.

2.1 Problem Description. The schematic description of a meat matrix as a porous medium is shown in Fig. 1. The material is assumed to be homogeneous. The first and most important step is to identify the distinct phases that are important and significantly affect transport. There can be three types of such phases: solid, liquid, and gas. The solid phase in food materials comprises a carbohydrate or protein matrix with water and, possibly, fat physically and chemically bound to it. So, in all, there can be three components in the solid phase, i.e., the solid matrix, bound water, and bound fat. The solid matrix is nontransportable. However, the bound water and fat can transport inside the matrix, even while remaining bound to the solid. In food, the capacity of the solid matrix to hold water or fat (known as water (or fat) holding capacity in the food science literature) changes with temperature. Usually, as temperature rises, water (or fat) is gradually released from the matrix into the pore space. Thus, water (or fat) undergoes an interphase mass transfer from the solid phase to the pore liquid phase. Therefore, the mass balance of the solid phase is important where the phase change from solid to liquid is significant; otherwise, it can be ignored. In the pores, all immiscible liquids, such as fat and water, can be considered as separate liquid phases. The third and last type of phase is the gas phase. There cannot be more than one gas phase as gases are miscible and occupy the total available gas volume available to them. In most food applications, a gas phase is a mixture of air and water vapor.

2.2 Assumptions. The assumptions made while formulating this multiphase framework are as follows: (1) All the phases

(solid, liquids, and gas) are in continuum. (2) Local thermal equilibrium exists throughout the material between all phases. (3) Pressure is shared by all phases as the effects of capillary pressure have been included as diffusion terms [17,28]. (4) There can be nonequilibrium between water in solid and water vapor in gas phase; i.e., their concentrations are not given by the moisture isotherms. (5) Deformation of the material during processing is not considered.

2.3 Governing Equations. The mathematical model consists of conservation equations for all the phases and components discussed above. For the sake of generalization, we assume that there are n phases in all. Of these, there is one solid phase, one gas phase, and $n-2$ liquid phases. There are b components inside the solid phase and two (vapor and air) inside the gas phase.

2.3.1 Mass Balance Equations. Porosity, ϕ, is defined as the fraction of the total volume occupied by pores, given by

$$\phi = \frac{V_g + \sum_{i=1}^{n-2} V_i}{V} \tag{1}$$

where V_i is the volume occupied by the ith liquid phase in an elemental volume V. If, during a process, the solid matrix loses a bound fluid, such as water, then porosity, ϕ, does not remain constant. As the solid matrix loses water, the porosity increases. In such cases, porosity can be estimated as

$$\phi = 1 - \frac{V_s}{V} = 1 - \sum_{j=1}^{b} \frac{V_j}{V} = 1 - \sum_{j=1}^{b} \frac{c_j}{\rho_j} \tag{2}$$

where b is the number of components in the solid phase, and c_j and ρ_j are the concentration and density of the jth solid component, respectively. Here, it is assumed that the total volume of the solid can be estimated as the sum of the individual volumes of the solid phase components, with each component retaining its pure state density.

Saturation of a transportable phase is defined as the fraction of pore volume occupied by that particular phase:

$$S_i = \frac{V_i}{\phi V}$$

$$S_g = \frac{V_g}{\phi V} \tag{3}$$

where i stands for any liquid phase. The summation of saturation of all transportable phases should lead to unity (Eq. (5)).

The mass balance equation for a phase solves for the saturation of the phase. There are $n-2$ liquid phases and one gas phase. So, $n-2$ mass balance equations (Eq. (4)) are solved to obtain the saturation (S_i) of each individual liquid phase. The saturation of gas, S_g, is calculated from Eq. (5):

$$\frac{\partial}{\partial t}(\phi \rho_i S_i) + \nabla \cdot \mathbf{n_i} = -\dot{R}_{i,j} - \dot{I} \tag{4}$$

$$S_g + \sum_{i=1}^{n-2} S_i = 1 \tag{5}$$

where $\dot{R}_{i,j}$ denotes interphase mass transfer from the ith liquid phase to the jth solid component. Similarly, $\dot{I}$ denotes the phase change from liquid water to water vapor.

The total flux of the liquid phase, $\mathbf{n_i}$, is due to the liquid pressure, $P - p_{i,\text{cap}}$, which is the difference between gas pressure and capillary pressure. This total flux term is given by Darcy's law [28] as

$$\mathbf{n_i} = -\rho_i \frac{k^p_{\text{in},i} k^p_{r,i}}{\mu_i} \nabla (P - p_{i,\text{cap}}) = -\rho_i \frac{k^p_{\text{in},i} k^p_{r,i}}{\mu_i} \nabla P + \rho_i \frac{k^p_{\text{in},i} k^p_{r,i}}{\mu_i} \left(\frac{\partial p_{i,\text{cap}}}{\partial c_i} \nabla c_i + \frac{\partial p_{i,\text{cap}}}{\partial T} \nabla T \right) \tag{6}$$

The first term in the right-hand side of the above equation represents flow due to gradients in gas pressure and is significant only in the case of intensive heating of food materials such as microwave heating, deep-fat frying, and contact heating at high temperature. The second and third terms can be rewritten in terms of capillary diffusivity, $D_{i,\text{cap}}$, and diffusivity due to thermal gradients, $D_{i,T}$, given by

$$D_{i,\text{cap}} = -\rho_i \frac{k^p_{\text{in},i} k^p_{r,i}}{\mu_i} \frac{\partial p_{i,\text{cap}}}{\partial c_i} \tag{7}$$

$$D_{i,T} = -\rho_i \frac{k^p_{\text{in},i} k^p_{r,i}}{\mu_i} \frac{\partial p_{i,\text{cap}}}{\partial T} \tag{8}$$

In most of the cases, the gas phase is a mixture of water vapor and air. Spatial variations in the concentration of these components during processing are obtained by solving the respective mass conservation equations in terms of their mass fractions, ω_v and ω_a, with binary diffusion [29]:

$$\frac{\partial(\phi \rho_g S_g \omega_v)}{\partial t} + \nabla \cdot (u_g \rho_g \omega_v) = \nabla \cdot \left(\phi S_g \frac{C_g^2}{\rho_g} M_a M_v D_{\text{eff},g} \nabla x_v \right) + \dot{I} \tag{9}$$

$$\omega_v + \omega_a = 1 \tag{10}$$

The concentration of components in the solid phase is determined by solving the mass conservation equation for each:

$$\frac{\partial c_j}{\partial t} = \nabla(D_{j,\text{cap}} \nabla c_j) + \nabla(D_{j,T} \nabla T) + \dot{R}_{i,j} \tag{11}$$

where $R_{i,j}$ is the rate of mass transfer from the liquid phase to component j in the solid phase, $D_{j,\text{cap}}$ is the diffusivity due to concentration gradients, and $D_{j,T}$ is the diffusivity due to temperature gradients. Details of $R_{i,j}$ are discussed later in the section in the discussion of phase change.

Therefore, the $n-2$ number of Eq. (4) and the b number of Eq. (11), along with Eqs. (5), (9), and (10), constitute the set of $n+b+1$ equations from which the concentration variables $c_1, c_2, \ldots, c_b, S_1, S_2, \ldots, S_{n-2}, S_g$, ω_v, and ω_a can be found. Temperature and pressure at every point inside the material are determined by invoking gas phase mass conservation and energy conservation equations, as discussed later. Note, however, that there are additional unknowns in these equations for which auxiliary equations will be needed, as discussed later (Eq. (37) for the evaporation rate, $\dot{I}$, and Eq. (38) for the solid phase change rate, $\dot{R}$).

2.3.2 Momentum Balance. The momentum balance equation for a phase solves for the velocity of that phase. In a porous medium with low permeabilities, Darcy flow is valid [28]. Therefore, Darcy's equation for each phase in porous media replaces the standard momentum conservation (Navier–Stokes) equation. However, some software applications do not support Darcy's law (Eq. (6)) directly and instead solve the modified Navier–Stokes equation (Eq. (12)), which includes Darcy's term, for momentum balance:

$$\frac{\partial((\phi S_i)\rho_i \mathbf{u_i})}{\partial t} + \nabla \cdot ((\phi S_i)^2 \rho_i \mathbf{u_i} \mathbf{u_i}) = -(\nabla P - \rho_i \mathbf{g}) - (\phi S_i) \frac{\mu_i}{k^p_{r,i} k^p_{\text{in},i}} \mathbf{u_i} \tag{12}$$

Although Eq. (6) is different from Eq. (12) due to the additional terms, the inertial terms are shown to be negligible for low-

permeability systems [28,30], and Eq. (12) reduces to Eq. (6) for such systems. Solving Eq. (12) for each phase may involve numerous convergence issues as well as large computation times and should be avoided when addressing low-permeability porous media problems. When there is no option in the software but to solve the Navier–Stokes equation, numerical complications can be reduced by assuming that all the transportable phases share the same pressure and velocity, thereby solving only one equation for the mixture. This is a simplified approach and may lead to erroneous results depending on the problem complexities.

2.3.3 Continuity Equation to Solve for Pressure. The gas pressure, P, is calculated by solving the overall mass balance equation for the gas phase,

$$\frac{\partial}{\partial t}(\phi S_g \rho_g) + \nabla \cdot \mathbf{n_g} = \dot{I} \tag{13}$$

where

$$\mathbf{n_g} = -\rho_g \frac{k_{r,g}^p k_{\text{in},g}^p}{\mu_g} \nabla P \tag{14}$$

The ideal gas law is used to relate gas phase density and pressure:

$$\rho_g = \frac{PM_g}{RT} \tag{15}$$

Pressure, P, is shared by all the phases (the capillary pressures of liquid phases have been included as diffusion). However, Eq. (13) cannot be used if saturation of the gas phase goes to zero in any region as pressure cannot be determined in the region—thus leading to the failure of the numerical solution (discussion follows). The gas phase can go to zero under various conditions, such as high condensation rate in a low porosity region or the accumulation of liquids due to favorable pressure gradients. One way to deal with the above problem is to prevent the gas phase from going to zero by forcing the gas phase saturation to a small value such that it does not affect the solution and at the same time does not require any further reformulations. The gas phase can be prevented from going to zero by introducing residual gas saturation or by giving high liquid capillary diffusivity values at low gas saturations [31]. Another method is to drop Eq. (13) from the system of equations and solve for pressure using the conservation equation for water. The latter is difficult to implement and used only in specialized porous media codes (e.g., TOUGH2 [32]).

2.3.4 Energy Equation. Since thermal equilibrium is assumed to exist across all phases (e.g., all phases in a representative elemental volume have the same temperature), the energy balance equation of the mixture (Eq. (16)) is solved to calculate T:

$$\rho_{\text{eff}} c_{p,\text{eff}} \frac{\partial T}{\partial t} + (c_p \mathbf{n})_{\text{fluid}} \cdot \nabla T = \nabla \cdot (k_{\text{eff}} \nabla T) - \lambda \dot{I} \tag{16}$$

The properties of the mixture are obtained by averaging those of the pure components, weighted by their mass or volume fractions (volume fraction is also referred to as saturation in this manuscript) as appropriate:

$$\rho_{\text{eff}} = \sum_{j=1}^{b} c_j + \phi \left(\sum_{i=1}^{n-2} S_i \rho_i + S_g \rho_g \right) \tag{17}$$

$$c_{p,\text{eff}} = m_g(\omega_v c_{p,v} + \omega_a c_{p,a}) + \sum_{i=1}^{n-2} m_i c_{p,i} + \sum_{j=1}^{b} m_j c_{p,j} \tag{18}$$

$$(c_p \mathbf{n})_{\text{fluid}} = \sum_{i=1}^{n-2} \mathbf{n_i} c_{p,i} + \rho_g \mathbf{u_g} (\omega_v c_{p,v} + \omega_a c_{p,a}) \tag{19}$$

$$k_{\text{eff}} = \left(\sum_{j=1}^{b} \frac{c_j}{\rho_j} k_j \right) + \phi \left(\sum_{i=1}^{n-2} S_i k_i + S_g(\omega_v k_v + \omega_a k_a) \right) \tag{20}$$

Note that in the energy equation, the melting of ice and fat is handled using the apparent specific heat method [33], in which the latent heat of fusion is incorporated by modifying the specific heat in the temperature range of melting.

2.4 Boundary Conditions. Pressure at the boundary (which is open to the outside environment) in most food processes is the ambient pressure; hence, the boundary condition (BC) for the continuity equation (Eq. (13)) can be expressed as

$$P_{\text{surf}} = P_{\text{amb}} \tag{21}$$

The flux at the boundary for any transportable phase can be due to a combination of phenomenon such as blowing or suction, surface evaporation, and convection outside the surface. By blowing or suction, it is meant that the phases have a normal velocity component at the surface, and they either flow out (blowing) or flow into (suction) the porous medium.

If there is an insignificant pressure gradient at the boundary, then vapor can leave the surface by surface convection only. The total vapor flux from a hypothetical surface, with $\phi = 1$ (no solid phase) and only gas phase present, can be written as

$$n_{v,\text{tot,surf}} = h_m(\rho_{g,\text{surf}} \omega_{v,\text{surf}} - \rho_{v,\text{amb}}) \tag{22}$$

where h_m is the mass transfer coefficient.

In a multiphase problem, the vapor flux due to surface convection will have contribution from evaporation from liquid water, evaporation from bound water in solid phase, and water vapor already present at the surface. Also, only a part of the surface contributes to the vapor flux (e.g., nonwater phases will not contribute to the vapor flux). Therefore, the above expression (Eq. (22)) is multiplied by the ratio of the contributing surface area to the total surface area to get the total vapor flux. The total vapor flux leaving the surface will have the following expression:

$$n_{v,\text{tot,surf}} = h_m \left(\frac{V_w + V_g + V_{bw}}{V} \right) (\rho_{g,\text{surf}} \omega_{v,\text{surf}} - \rho_{v,\text{amb}}) \tag{23}$$

Equation (23) gives the total vapor flux for the present problem (multiphase problem) assuming that volume fraction is equal to the surface area fraction.

When there is an insignificant pressure gradient at the boundary, flux for other liquid phases such as fat and cooking oil, which do not undergo phase change at the boundary, will be zero.

The other extreme can be the case when blowing at the surface dominates over other factors and boundary pressure is specified, in which case flux at the boundary for any ith component will simply be

$$n_{i,\text{surf}} = -\rho_i \frac{k_{\text{in},i}^p k_{r,i}^p}{\mu_i} \nabla (P - p_{i,\text{cap}})|_{\text{surf}} = -\rho_i \frac{k_{\text{in},i}^p k_{r,i}^p}{\mu_i} \nabla P|_{\text{surf}} - D_{i,\text{cap}} (\nabla \phi \rho_{l,i} S_{l,i})|_{\text{surf}} - D_{i,T} \nabla T|_{\text{surf}} \tag{24}$$

For a gas phase component, such as water vapor, the second and third terms in the above Eq. (24) are zero.

However, if neither blowing nor convection at the boundary is dominating, then both phenomena contribute to the mass transfer at the boundary, and the total flux of vapor going out is given by

$$n_{v,\text{surf}} = -\rho_v \frac{k_{\text{in},g}^p k_{r,g}^p}{\mu_g} \nabla P|_{\text{surf}} + h_m \left(\frac{V_g}{V_{\text{tot}}} \right) (\rho_{g,\text{surf}} \omega_{v,\text{surf}} - \rho_{v,\text{amb}}) \tag{25}$$

Similarly, for liquid water, if neither blowing nor surface evaporation is dominating, then both contribute to the mass transfer at the boundary, and the flux of water going out is given by

$$n_{w,\text{surf}} = -\rho_w \frac{k^p_{\text{in},w} k^p_{r,w}}{\mu_w} \nabla (P - p_{w,\text{cap}})|_{\text{surf}} + h_m \left(\frac{V_w}{V_{\text{tot}}} \right) (\rho_{g,\text{surf}} \omega_{v,\text{surf}} - \rho_{v,\text{amb}}) \quad (26)$$

Note that the blowing phenomenon for any water phase becomes significant under conditions of large pressure-driven flow when surface evaporation is insufficient to take away all the liquid coming out of the boundary [15,34]. Ni and Datta [15] used $S_w = 1$ as the condition at which blowing occurs, whereas Constant et al. [34] used $P - p_{cw} > P_{\text{atm}}$ in the cell adjacent to the boundary.

In simulating the frying process (discussed later) [17] for vapor transport at the boundary, neither blowing nor convective transfer at the surface was dominating throughout the process. No single boundary condition will work for the whole process. During the initial phase of the frying process, blowing is dominant, but convection at the surface eventually takes over. So, a single lumped mass transfer coefficient was used to account for both blowing and convection at the surface. In that case, the boundary condition at the surface was given by Eqs. (25) and (26), but the equations resembled Eq. (23) with the mass transfer coefficient as a lumped value of blowing and diffusion instead of diffusion only. These factors eventually lead to a changing mass transfer coefficient.

In the case of other liquids such as fat or cooking oil, there is no evaporation and therefore only blowing, and Eq. (24) gives the flux. For the energy equation, there is energy going out due to bulk flow, heat lost due to surface evaporation, and convective heat transfer with hot air or oil or a heated plate:

$$q_{\text{surf}} = h(T_{\text{amb}} - T_{\text{surf}}) - T \sum_{i=1}^{n-1} (c_{p,i} n_{i,\text{surf}}) + \lambda h_m \left(\frac{V_w + V_{bw}}{V_{\text{tot}}} \right) \times (\rho_{g,\text{surf}} \omega_{v,\text{surf}} - \rho_{v,\text{amb}}) \quad (27)$$

2.5 Initial Conditions. Typical initial conditions (ICs) are

$$\text{IC for Eq. (13): } P = P_{\text{amb}} \quad (28)$$

$$\text{IC for Eq. (16): } T = T_{\text{amb}} \quad (29)$$

$$\text{IC for Eq. (4): } S_i = S_{0,i} \quad (30)$$

$$\text{IC for Eq. (9): } \omega_v = \omega_{0,v} \quad (31)$$

$$\text{IC for Eq. (11): } c_j = c_{0,i} \quad (32)$$

Initially, the food material is at ambient pressure and temperature conditions. Depending on the composition of the food material, the initial phase saturation of the liquids ($S_{0,i}$) is estimated. The water vapor in air is in equilibrium with liquid water initially. Using a moisture sorption isotherm (Eqs. (34) and (35)), equilibrium water vapor pressure at ambient temperature is calculated. For example, the mass fraction of vapor in the gas phase, ω_v at 25°C, is calculated as 0.02.

2.6 Phase Change. The evaporation rate, distributed spatially and over time, is a complex function of food material and process parameters. Phase change can be formulated in two ways, equilibrium and nonequilibrium.

2.6.1 Equilibrium Formulation. In the equilibrium formulation of evaporation that is the most common in the literature [15,16], vapor is always assumed to be in equilibrium with the water in the solid matrix:

$$p_v = p_{v,\text{eq}} \quad (33)$$

where $p_{v,\text{eq}}$ is the equilibrium vapor pressure at a particular temperature and moisture content and is given by the moisture isotherm equation,

$$\ln \frac{p_{v,\text{eq}}}{p_{\text{sat}}(T)} = f(S_w, T) \quad (34)$$

where $p_{v,\text{eq}}$ is the equilibrium vapor pressure and $p_{\text{sat}}(T)$ is the vapor pressure of pure water at temperature T and is given by the Clausius–Clapeyron equation:

$$\ln \frac{p_{\text{sat}}(T)}{p_0} = \frac{\Delta \overline{H}_{\text{vap}}}{R} \frac{(T - T_0)}{T T_0} \quad (35)$$

The relationship $f(S_w, T)$ is generally obtained from experiments, and much data exist in the literature. As shown already in Eq. (33), in the equilibrium formulation, p_v is always equal to $p_{v,\text{eq}}$ and the vapor concentration, ω_v, can be calculated using this relationship. Therefore, the evaporation rate, $\dot{I}$, comes out of the solution as all the terms on the left-hand side of the mass balance equation of the vapor (Eq. (9)) are known.

2.6.2 Nonequilibrium Formulation. In a nonequilibrium formulation, Eq. (33) is not used and is replaced by an explicit expression for the evaporation rate, $\dot{I}$, as discussed in this section. To understand this, consider a beaker half filled with liquid water and half with pure nitrogen (with no water vapor). There is a partition between the two halves, which prevents any mixing. At time $t = 0$, the partition between liquid water and nitrogen is removed, and the system is allowed to come to equilibrium. The whole system comes to equilibrium after time Δt. This Δt depends on the distance that the vapor has to diffuse and the diffusion rate. For this system, during the time Δt, the average evaporation rate over space and time is given as

$$\dot{I} = \frac{(\rho_{v,f} - \rho_{v,i})}{\Delta t} = \frac{M_v}{RT} \frac{(p_{v,f} - p_{v,i})}{\Delta t} \quad (36)$$

where $\rho_{v,f}$ is the final vapor density after the equilibration time and is equal to the equilibrium vapor density, and $\rho_{v,i}$ is the initial vapor density. The same concept can be applied in the case of evaporation in the pores inside the food. A representative elemental volume, shown in Fig. 1, may consist of a number of pores and comes to equilibrium after time Δt and the evaporation rate is given by Eq. (36). Equation (36) is identical to the nonequilibrium evaporation rate expression in porous hygroscopic solids used for the modeling of phase change [35,36] given by

$$\dot{I} = K(\rho_{v,\text{eq}} - \rho_v) S_g \phi \quad (37)$$

where $\rho_v = \rho_g \omega_v$ is the vapor density at a location that comes from solution. Here, K is a material and process-dependent parameter signifying the rate constant of evaporation and is the reciprocal of equilibration time Δt.

2.6.2.1 Choice of equilibration time. The equilibration time, Δt, depends on the ratio of the gas phase volume in the pore in which vapor has to diffuse and the surface area available for evaporation. For a simple cylindrical pore, this ratio scales as the radius of the pore. It has been shown that the time taken for a molecule to make a transition from liquid water to water vapor is 10^{-14} s [37]. Using this condition and pure diffusion of vapor from the evaporating surface, the time to equilibrium at one mean free path (1 μm) away from the liquid surface is less than 10^{-6} s, and that 25 μm away is around 10^{-5} s. The time-scale analysis, shown in the Appendix, concludes that all the transport time scales within a pore are greater than the equilibration time scale for food materials with a maximum pore size smaller than 25 μm (e.g., potato, meat, etc.). In that case, the nonequilibrium phenomenon is insignificant, and an equilibration time that is one order of magnitude below the smallest transport time scale ensures equilibrium. But if pore sizes are on the order of 100 μm (e.g., bread), then the nonequilibrium phenomenon becomes significant and a reasonable value of K should be used. Estimation of precise values of K, by pore scale analysis or otherwise, can be a study in

itself. However, high precision in K is not expected to significantly improve the model prediction [38], and, therefore, the value calculated from the pure diffusion approach is reasonable for the model.

2.6.2.2 Relationship of equilibration time to time step choice. In Halder et al. [38], it is also shown that as the equilibration time is decreased, the dependence of the solution on the equilibration time decreases, such that decreasing the equilibration time from 10^{-3} s to 10^{-4} s caused a negligible change in the solution. This is because if the temperature and moisture transport time scales are orders of magnitude higher, it is not necessary to use the accurate range of the equilibration time. Using a higher equilibration time than the actual value, but one still smaller than the transport scales, there is a negligible change in the solution, but the time elapsed to solve the problem is reduced significantly. For accuracy, the time step of the numerical solution should be smaller than the equilibration and transport time scales.

Coincidentally, an equilibrium formulation is difficult to implement in commercial software. Typically, commercial software application requires the source term (evaporation rate, $\dot{I}$, in the conservation equations) to be explicitly stated in terms of dependent variables in the model. A nonequilibrium formulation, given by Eq. (37), allows precisely this, i.e., the explicit expression of the evaporation rate, and therefore would be preferred in commercial software application and is therefore used in our model. For infinitely large K, corresponding to the instantaneously occurring phase change, Eq. (37) reverts back to Eq. (33), the equilibrium assumption, making it possible to simulate the equilibrium formulation as well.

2.6.3 Other Phase Changes. Analogous to the evaporation rate that relates water release from the liquid to the vapor phase, the release of liquids such as fat and liquid water from the solid matrix to the transportable phase, as temperature increases, can also be written in terms of rate expressions, similar to Eq. (37), given by

$$\dot{R}_{i,j} = K_{i,j}(c_{s,j} - c_{s,j,\mathrm{eq}}) \tag{38}$$

The holding capacity co-relation, $c_{s,j,\mathrm{eq}}$, is experimentally determined [39]. It is assumed that the concentrations in the solid phase always remain at equilibrium. Large values of $K_{i,j}$ were selected so that equilibrium is satisfied at each time step, similar to the use of large K to force equilibrium in the nonequilibrium formulation for evaporation discussed above.

3 Model Implementation and Validation

In the following section, the model developed is applied to two food processes, the frying of a restructured potato slab (made from dried potato flakes) and contact heating of a hamburger patty, to demonstrate its effectiveness in describing different processes. The model is validated in each case using experimental results.

3.1 Deep-Fat Frying of Restructured Potato. Deep-fat frying can be defined as a process for cooking foods by immersing them in edible oil at a temperature above the boiling point of water, usually between 150°C and 200°C.

3.1.1 Problem Formulation. A schematic of the problem description is shown in Fig. 2. The restructured potato slab is assumed to be a porous medium. There are four phases: solid, liquid water, oil, and gas. The gas phase is a mixture of air and water vapor. Shrinkage during frying and the effects of gravity are ignored. To simulate a 1D heat and mass transfer, no flux conditions for mass species and energy are specified at boundaries other than $x=0$. The problem is considered to be symmetric with $x=L$ as the line of symmetry. The left boundary ($x=0$) is the frying surface where heat and mass exchange with the environment takes place. In a restructured potato, water in the solid matrix is negligible (as all the water is in the pore space), so interphase mass transfer from solid to liquid is ignored (it cannot be ignored in the case of contact heating of meat as shown later). This simplifies the overall model, as porosity can be assumed to be constant with time and mass balance of the solid is not required.

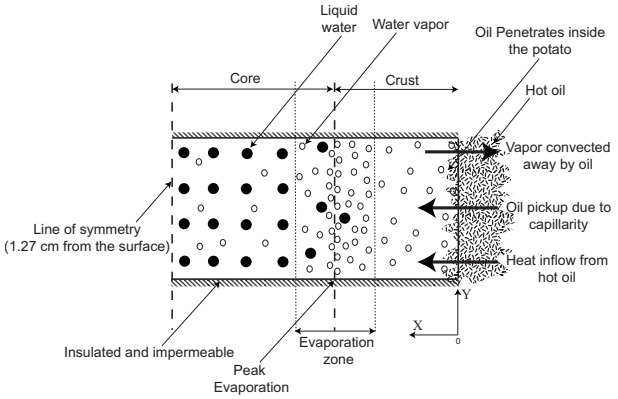

Fig. 2 Schematic showing computational domain and boundary conditions. Two-dimensional geometry was implemented with the above boundary conditions to simulate an effective one-dimensional problem. For computation, the dimension in the y-direction was chosen to be 0.08 cm.

3.1.2 Mass Balance Equation. Saturation of liquid water and oil is calculated by solving the mass balance equations of the phases (Eq. (4)). Saturation of gas is calculated from Eq. (5). The gas phase is a mixture of water vapor and air, so the mass balance equation of water vapor is solved using Eq. (9) and the mass fraction of air is calculated from Eq. (10).

3.1.3 Energy Balance Equation. Local thermal equilibrium exists between all the phases, and, therefore, the energy balance equation for a mixture (Eq. (16)) is solved to get the temperature, T.

3.1.4 Continuity and Momentum Equation. The continuity equation of the gas phase (Eq. (13)) is solved to give the pressure, P. During frying, the gas phase never goes to zero, so solving Eq. (13) does not lead to numerical difficulties (discussion in Sec. 2.3.2). Darcy's law is assumed to be valid and gives the velocities of each phase (liquid water, oil, and gas).

3.1.5 Boundary Conditions and Initial Conditions. Boundary conditions at $x=0$ are given as

$$\text{BC for Eq. (13): } P_{\mathrm{surf}} = P_{\mathrm{amb}} \tag{39}$$

$$\text{BC for Eq. (16): } q_{\mathrm{surf}} = h(T_{\mathrm{amb}} - T_{\mathrm{surf}}) - (\lambda + c_{p,w}T)n_{w,\mathrm{surf}} - c_{p,v}Tn_{v,\mathrm{surf}} - c_{p,o}T_{\mathrm{amb}}n_{o,\mathrm{surf}} \tag{40}$$

$$\text{BC for Eq. (4): } n_{w,\mathrm{surf}} = h_m S_w(\rho_{g,\mathrm{surf}}\omega_{v,\mathrm{surf}} - \rho_{v,\mathrm{amb}}) \tag{41}$$

$$S_{o,\mathrm{surf}} = S_{o1} \tag{42}$$

$$\text{BC for Eq. (9): } n_{v,\mathrm{surf}} = h_m S_g(\rho_{g,\mathrm{surf}}\omega_{v,\mathrm{surf}} - \rho_{v,\mathrm{amb}}) \tag{43}$$

Initial conditions inside the potato before frying are

$$\text{IC for Eq. (13): } P = P_{\mathrm{amb}} \tag{44}$$

$$\text{IC for Eq. (16): } T = T_{\mathrm{amb}} \tag{45}$$

$$\text{IC for Eq. (4): } S_w = 0.3 \tag{46}$$

$$S_o = 0 \tag{47}$$

Table 1 Input parameters used in the simulations of deep-fat frying

Parameter	Symbol	Value	Units	Source
Density				
Water	ρ_w	998	kg/m^3	
Vapor	ρ_v	Ideal gas	kg/m^3	
Air	ρ_a	Ideal gas	kg/m^3	
Oil	ρ_o	879	kg/m^3	[42]
Solid	ρ_s	1528	kg/m^3	[20]
Specific heat capacity				
Water	c_{pw}	4178	J/kg K	[43]
Vapor	c_{pv}	2062	J/kg K	[43]
Air	c_{pa}	1006	J/kg K	[43]
Oil	c_{po}	2223	J/kg K	[43]
Solid	c_{ps}	1650	J/kg K	[43]
Thermal conductivity				
Water	k_w	0.57	W/m K	[43]
Vapor	k_v	0.026	W/m K	[43]
Air	k_a	0.026	W/m K	[43]
Oil (corn)	k_o	0.17	W/m K	[44]
Solid	k_s	0.21	W/m K	[43]
Intrinsic permeability				
Water	$k^p_{\text{in},w}$	5×10^{-14}	m^2	[15]
Air and vapor	$k^p_{\text{in},g}$	10×10^{-14}	m^2	[15]
Oil	$k^p_{\text{in},o}$	5×10^{-14}	m^2	[15]
Relative permeability				
Water	$k^p_{r,w}$	$((S_w-0.08)/0.92)^3$		[45]
Air and vapor	$k^p_{r,g}$	$(1-S_w-S_f)/0.92$		[45]
Oil	$k^p_{r,o}$	$((S_f-0.08)/0.92)^3$		[15]
Capillary diffusivity				
Water	$D_{w,\text{cap}}$	$10^{-8}\exp(-2.8+2M)$		[15]
Oil	$D_{o,\text{cap}}$	$10^{-8}\exp(-2.8+2M_o)$		[15]
Viscosity				
Water	μ_w	0.988×10^{-3}	Pa s	
Air and vapor	μ_g	1.8×10^{-5}	Pa s	
Oil	μ_o	$5.05\times10^{-6}\exp(2725/T)$	Pa s	[42]
Heat transfer coefficient				
Frying	h	Graph	W/m^2 K	[17]
Post-frying cooling	h	20	W/m^2 K	[46]
Mass transfer coefficient	h_m	Graph	m/s	[17]
Latent heat of vaporization	λ	2.26×10^6	J/kg	
Porosity	ϕ	0.928		[20]
Vapor diffusivity in air	$D_{\text{eff},g}$	2.6×10^{-6}	m^2/s	
Oil temperature	T_{oil}	180	°C	
Ambient pressure	P_{amb}	101325	Pa	
Surface oil saturation	S_{o1}	0.11 (frying)		[16]
		0.28 (cooling)		[16]

$$\text{IC for Eq. (9): } \omega_v = 0.02 \tag{48}$$

Further details and explanations of boundary and initial conditions are given elsewhere [17].

3.1.6 Input Parameters and Numerical Solution. Input parameters and other auxiliary equations used in this frying simulation are given in Table 1. A commercially available finite element software, COMSOL Multiphysics (Comsol Inc., Burlington, MA), was used to solve these equations. The computational domain, shown in Fig. 2, is 0.0127×0.0008 m^2 and has a mesh consisting of 127×3 quadrilateral elements. Simulating 16 min of heating took approximately 6 h of CPU time for a time step size of 0.01 s on a Pentium 3.4 GHz PC with 2 Gbyte random access memory (RAM).

3.1.7 Results and Validation. The simulation results are compared with the experimental data of Farkas and Singh [20], as shown in Fig. 3(*a*). The predicted temperatures at a distance of 0.05 cm from the surface are close to experimental values for the first 2 min, but there is a considerable difference between them for the next 10 min and finally again matching closely for the last 4 min of frying. This difference is due to discrepancies in the temperature measurement technique for the depth of 0.05 cm, as discussed in Halder et al. [38]. The temperature predictions for locations 0.42 cm and 0.85 cm from the frying surface compare well with the experimental measurements.

As shown in Fig. 3(*b*), the moisture content (dry basis) of the potato slab dropped from its initial value of 2.50 to 1.56 after 16 min of heating. Our model prediction, with improved boundary

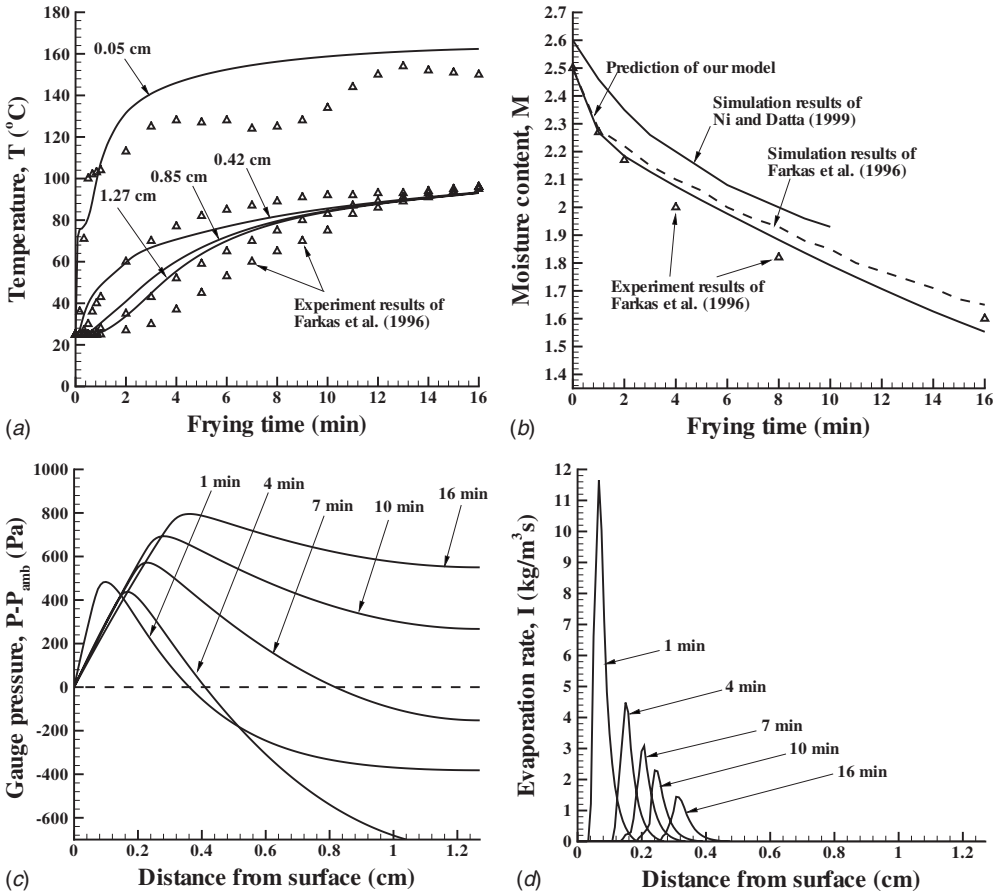

Fig. 3 Comparison of model predictions for deep-fat frying with experimental data from literature for (*a*) temperature and (*b*) moisture content (dry basis). The spatial pressure and evaporation profiles during different times of frying are shown in (*c*) and (*d*), respectively [38].

conditions and evaporation formulation, matches very closely with the experimental results [20], making a better match than in other studies [15,20]. Such close agreement between experimental measurements and model prediction confirms the effectiveness of the model and serves to validate it.

As can be seen in Figs. 3(*c*) and 3(*d*), the peak pressure occurs where the evaporation rate is maximum. The evaporation rate is distributed over a narrow zone near the surface, thus validating our assumption that evaporation does not occur at an interface (sharp boundary) but is distributed over a thin zone. In the region where rapid evaporation takes place, the pressure is always above that of the ambient pressure. Initially, there is condensation in the core region, due to which the pressure falls below ambient pressure. This negative gauge pressure occurs because the gas phase has a negative rate of accumulation in the core—the air present in the core is driven out due to binary diffusion, and vapor reaching the core is condensed. As temperature rises and evaporation (and not condensation) starts to occur in the core region, the pressure starts rising and finally reaches around 600 Pa after 16 min of frying.

3.2 Contact Heating of a Hamburger Patty. Meat can be processed and cooked in a variety of ways. For the purpose of this study, double-sided contact heating of hamburger patties [40] is selected, as shown in the schematic of Fig. 4. A frozen hamburger patty of cylindrical shape (diameter of 10 cm and height of 1 cm), initially stored at −22 °C, is placed between two hot plates. The gap between the top and bottom heating plates is kept fixed at 1

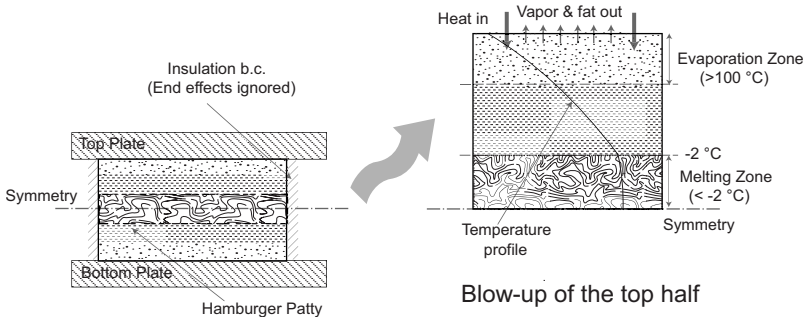

Fig. 4 Schematic showing computational domain and boundary in the case of contact heating of a hamburger patty

cm. As temperature rises, water and fat melt but are still held strongly by the solid matrix. With further rise in temperature, denaturation of muscle proteins occurs, which causes the release of bound water and fat, making both liquids transportable. Mass transfer can also occur between water and vapor in the gas phase due to vaporization and condensation. Gradually, the region near the hot plates loses all the water due to evaporation, and a dried crust region develops. The variables of interest for predicting quality and safety aspects of meat cooking are temperature, moisture content, fat content, evaporation rate, and their histories.

3.2.1 Problem Details. A schematic of the problem description is shown in Fig. 4. To simulate a 1D heat and mass transfer in a cylindrical patty, it is assumed that the exchange of heat and mass with the outside environment takes place through the top and bottom surfaces of the patty only, and the sides are insulated (i.e., radial transport is ignored so gradients are present only in the axial directions). Since the effect of gravity is small, and the top and the bottom plates are at the same temperature, symmetry is assumed at the centerline. The patty is assumed to comprise three transportable fluid phases—liquid water, liquid fat, and gas (mixture of air and water vapor)—and a solid phase comprising of protein, frozen water, and fat.

3.2.2 Mass Balance Equation. As in frying, the saturations of the water and fat phases are calculated by solving the mass balance equations of the phases (Eq. (4)). Saturation of gas is calculated from Eq. (5). The gas phase is a mixture of water vapor and air, so the mass balance equation of water vapor is solved using Eq. (9), and the mass fraction of air is calculated from Eq. (10). In meat cooking, where the solid releases water and fat, there are three additional mass balance equations for each component of the solid phase (Eq. (11)).

3.2.3 Energy Balance Equation. Thermal equilibrium exists between all the phases, and, therefore, the energy balance equation for a mixture (Eq. (16)) is solved to get the temperature, T.

3.2.4 Continuity and Momentum Equation. Similar to frying, Eq. (13) is solved to obtain pressure, P, and Darcy's law provides the velocities of each phase.

3.2.5 Boundary and Initial Conditions. In the case of contact heating of meat, the heat transfer coefficient is very high (>1000 W/m^2). This leads to high evaporation rates and thus large pressure gradients close to the heated surface. Under such conditions, blowing can be significant. Therefore, the boundary flux for water vapor is given by Eq. (25). Following Ni et al. [21], $S_w=1$ was used as the condition to kick in blowing for liquid water. However, this condition was never satisfied during 150 s of heating, and liquid water left the patty by surface evaporation only. The time-dependent heat transfer coefficient and plate temperature data are taken from Pan et al. [40].

Initially frozen at -22°C, the patty is composed of 60 wt % water, 24 wt % fat, and 16 wt % protein, and all are assumed to be in solid phase. The porosity of frozen patties is taken as 2% [41]. From these data, the initial concentrations for all the components can be calculated. Note that at the initial temperature, all water and fat are assumed to be in the solid matrix, and therefore concentrations of both bulk water and fat are zero. Initially, air is assumed to be saturated with vapor. The equilibrium mass fraction of vapor in the gas phase, ω_v, at -22°C is 0.0015.

3.2.6 Input Parameters and Numerical Solution. Input parameters used in the hamburger patty cooking simulation are given in Table 2. A commercially available finite element software, COMSOL Multiphysics (Comsol Inc., Burlington, MA), was used to solve these equations. The computational domain is 0.005 m in length and has a mesh consisting of 500 elements. Simulation of 150 s of heating took approximately 6 h of CPU time for a time step size of 0.01 s on a Pentium 3.4 GHz PC with 2 Gbyte RAM.

3.2.7 Results and Validation. Predicted temperature history is compared with the experimental data from Ref. [40], as shown in Fig. 5(*a*). The temperatures at the core of the patty, i.e., the coldest point, follow the experimental results for around 100 s. After that, the predicted heating rate is slightly lower than the experimentally observed value. The coldest-point temperature is around 70°C after 150 s, whereas the measured temperature is 85°C. The experimentally observed total weight losses (water and fat) are about 10%, 12%, 16%, and 22% (of the initial weight) after 60 s, 80 s, 100 s, and 120 s of heating, respectively (Fig. 5(*b*)). The difference between the loss predicted by the simulation and the experimental observed loss is less than 2% (of the initial patty weight) at 60 s, 80 s, and 100 s and about 5% at 120 s.

Once the ice is completely melted, the Biot number for the process is 250 (the heat transfer coefficient is greater than 1000 W/m^2 K, the patty thickness is 1 cm, and the thermal conductivity is around 0.4 W/m^2 K, which means that the heat transfer is internally limited). We compared our thermal conductivity values (estimated by volume averaging) with the values experimentally measured in Pan and Singh and found that there is a difference of about 10%. The averaging correlations for transport property estimation may have an error of $\pm 10\%$ [43], which affects the results in the case of internally limited processes, in this case leading to lower heating rates and lower weight losses.

An absolute comparison is difficult to achieve due to limitations in the property estimation correlations. However, the close results validate the more fundamental approach toward the modeling of food cooking. Following this approach, thermal processing of meat products can be simulated by applying the multiphase transport model. This has advanced the existing approach for modeling the meat-cooking process, under which bulk thermal properties of meat (such as enthalpy and thermal conductivity) are measured as functions of temperature, and then, a simple conduction equation is used to fit the data.

Figures 5(*c*) and 5(*d*) show the spatial profiles of the pressure and evaporation rates, respectively, at different times. The evaporation rate and, therefore, the pressure are maximum near the heated surface. The interior of the patty has negative pressures due to the diffusion, followed by the condensation, of vapor from the surface to the relatively cooler interior. Gradually, as the surface dries up, the evaporation and peak pressure zones are expected to move from the surface to the core, as was shown earlier (in Fig. 3) for deep-fat frying.

4 Similarity in Fundamental Physics

As shown in deep-fat frying and contact heating of hamburger patties (Figs. 3 and 5), the fundamental physics involved in different thermal food processes are similar. As the food (porous hygroscopic material) is heated from the boundary, the temperature inside rises. The rise in temperature causes a phase change, which in turn causes a rise in pressure. The pressure gradient causes the flow of phases toward the boundary where mass transfer takes place. If there is a fluid component absorbed in the solid, then with a rise in temperature and subsequent changes in solid matrix properties it changes into a transportable phase. Therefore, a single model is able to solve distinct modes of cooking or processing where the physics is similar and distinct modes of heating are handled by distinct boundary conditions (e.g., frying, baking, etc.) or in some cases by source terms (e.g., microwave heating).

5 Conclusion

The aim of this paper is to show that transport for many of the thermal processes in food (e.g., frying, baking, meat cooking, and microwave heating) can be modeled using the comprehensive framework developed. The developed model includes all the important physics encountered in cooking or food processing (e.g., melting, bound phase, phase change, pressure-driven flow, capillary flow, and binary diffusion). Depending on the food processing situation, this comprehensive model can be simplified by ignoring

Table 2 Input parameters used in the simulations of contact heating of a hamburger patty

Parameter	Symbol	Value	Units	Source
Patty dimensions				
Height		10	mm	[40]
Initial conditions				
Mass fractions				
Water	x_{fw}	0.6	–	[40]
Fat	x_f	0.24	–	[40]
Protein	x_{pr}	0.16	–	[40]
Porosity	ϕ	0.02	–	[41]
Temperature	T_{ini}	−22	°C	[40]
Pressure	P_{ini}	101,325	Pa	–
Properties				
Water activity	a_w	–	–	[47]
Density				
Water	ρ_w	997.2	kg/m^3	[43]
Ice	ρ_i	917	kg/m^3	[43]
Gas	ρ_v	Ideal gas	kg/m^3	[43]
Fat	ρ_f	925.6	kg/m^3	[43]
Protein	ρ_{pr}	1330	kg/m^3	[43]
Specific heat capacity				
Water	$c_{p,w}$	4178	J/kg K	[43]
Ice	$c_{p,i}$	2062	J/kg K	[43]
Gas	$c_{p,g}$	1006	J/kg K	[43]
Fat	$c_{p,f}$	1984	J/kg K	[43]
Protein	$c_{p,\mathrm{pr}}$	2008	J/kg K	[43]
Thermal conductivity				
Water	k_w	0.57	W/m K	[43]
Ice	k_w	2.22	W/m K	[43]
Gas	k_g	0.025	W/m K	[43]
Fat	k_f	0.18	W/m K	[43]
Protein	k_{pr}	0.18	W/m K	[43]
Intrinsic permeability				
Water	$k^p_{\mathrm{in},w}$	5×10^{-16}	m^2	[48]
Fat	$k^p_{\mathrm{in},f}$	1×10^{-15}	m^2	[48]
Gas	$k^p_{\mathrm{in},g}$	5×10^{-16}	m^2	Same as fat
Relative permeability				
Water	$k^p_{r,w}$	$((S_w-0.08)/0.92)^3$	–	[45]
Fat	$k^p_{r,f}$	$((S_f-0.08)/0.92)^3$	–	Same as water
Gas	$k^p_{r,g}$	$(1-S_w-S_f)/0.92$	–	[45]
Capillary diffusivity				
Water	$D_{w,\mathrm{cap}}$	$10^{-10}\exp(-2.8+10S_w)$	m^2/s	[47]
Fat	$D_{f,\mathrm{cap}}$	$10^{-10}\exp(-2.8+10S_f)$	m^2/s	[47]
Viscosity				
Water	μ_w	0.988×10^{-3}	Pa s	
Gas	μ_g	1.8×10^{-5}	Pa s	
Fat	μ_f	0.02	Pa s	[49]
Holding capacities				
Water	$c_{bw,\mathrm{eq}}$	$c_{bw,\mathrm{ini}}\exp(-0.0132(T-303))$	kg/m^3	[39]
Fat	$c_{bf,\mathrm{eq}}$	$c_{bf,\mathrm{ini}}\exp(-0.0159(T-303))$	kg/m^3	[39]
Heat transfer coefficient	h	–	W/m^2 K	[40]
Mass transfer coefficient	h_m	0.015	m/s	[15]
Latent heat of vaporization	λ	2.26×10^6	J/kg	
Latent heat of fusion				
Water		3.34×10^5	J/kg	
Fat		1.5×10^5	J/kg	
Vapor diffusivity in air	$D_{\mathrm{eff},g}$	2.6×10^{-5}	m^2/s	
Grill temperature	T_{surf}	–	°C	[40]
Ambient pressure	P_{amb}	101,325	Pa	

some physics that are irrelevant for that process and material. For example, in frying restructured potato, it is assumed that there is no bound water and all the water is available for transport, thus largely reducing complexities. In meat cooking, all of the physics is necessary, and, therefore, it results in the most complex model. The two food processes, the frying of potato and the contact heating of hamburger patty, modeled in this paper demonstrate the effectiveness of the framework in solving different types of thermal processes.

Though meat and potato are completely different in terms of composition, and frying and contact cooking are completely different modes of cooking, transport in the case of frying of potato

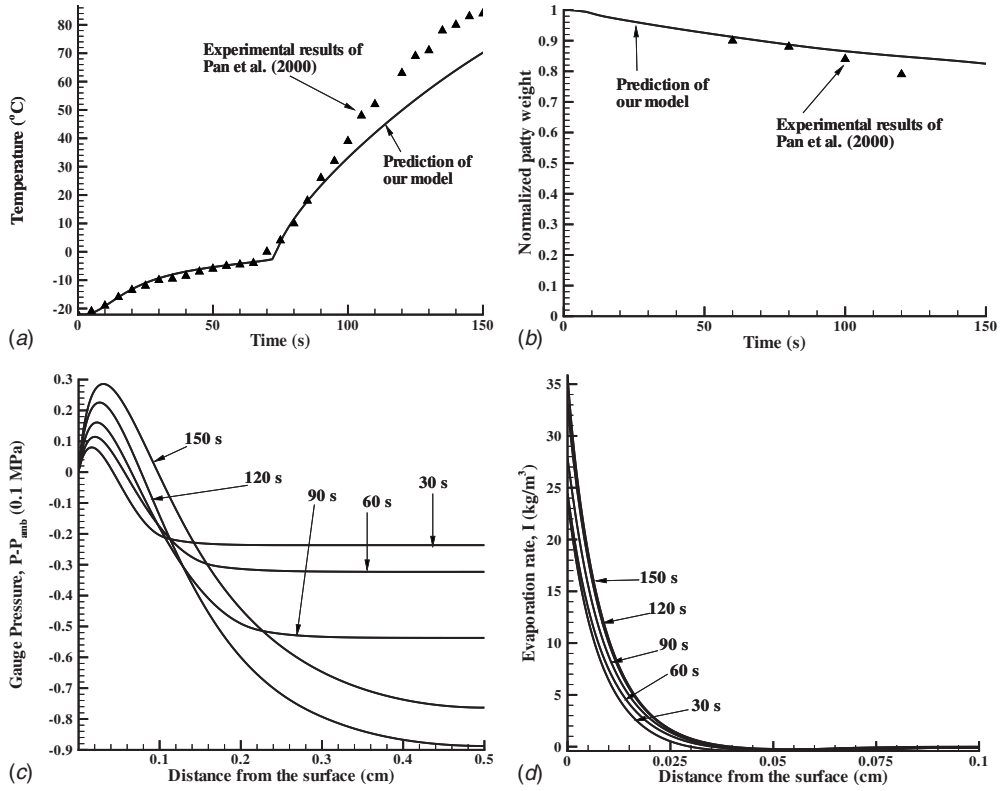

Fig. 5 (*a*) **Temperature at the center point,** (*b*) **average moisture content,** (*c*) **spatial pressure, and** (*d*) **spatial evaporation rate profiles for contact heating of a hamburger patty at different times**

and meat cooking can be solved by the same model. This is because the developed model is not based on empirical relationships but is a fundamental-based model, which can be generalized over a wide range of hygroscopic porous materials and different types of thermal processes. The input parameters required to solve the problem have a physical meaning and are inherent properties of either the process or the food material and can be determined experimentally.

A novel nonequilibrium evaporation formulation is used in the model to describe the evaporation and condensation processes. The nonequilibrium evaporation constant, K, is the reciprocal of the equilibration time and has been investigated in detail in this paper. Further, the same nonequilibrium formulation can be used to implement equilibrium by using a very large value of K. A time-scale analysis shows that the transport scales are much larger than the evaporation time scale for a typical food material. Therefore, a higher value for the equilibration time can be used in a simulation without affecting the solution.

The comprehensive model developed here can also simulate transport in other hygroscopic porous materials. Although the immediate applications shown here are to food processes, the model has applications in many different fields, for example, fuel cells, drug delivery through tissues, and nuclear waste treatment. For example, in fuel-cell simulation, there are two different phases (liquid and gas) that experience pressure-driven flow in porous media. There is a chemical reaction in fuel cells between liquid phases to form gaseous phase, which is analogous to evaporation in frying and meat cooking.

Another unique feature of the modeling framework is that it can be easily implemented in some general purpose CFD software. Most commercial software requires the evaporation rate to be explicitly expressed in terms of dependent variables of the model, and the nonequilibrium formulation presented here allows precisely this, unlike the implicit evaporation formulations of the past. Use of the direct Darcy law over the Navier–Stokes analog of the Darcy flow reduces unnecessary numerical complexities. Because the model is versatile and easily implementable, it can be very useful in product, process, and equipment designs in the food sector and similar applications in other fields.

Acknowledgment

This research was partially supported by the U.S. Department of Agriculture Regional Project No. NC 1023 and the U.S. Department of Agriculture National Integrated Food Safety Project No. 2004-51110-02167.

Nomenclature

b = number of components in the solid phase
c = concentration, kg m^{-3}
c_p = specific heat capacity, J kg^{-1} K^{-1}
C_g = molar density, kmol m^{-3}
$D_{\text{eff},g}$ = effective gas diffusivity, m^2 s^{-1}
D = diffusivity, m^2 s^{-1}
$\mathbf{g}$ = acceleration due to gravity, kg m^{-3}
h = heat transfer coefficient, W m^{-2} K^{-1}
h_m = mass transfer coefficient of vapor, m s^{-1}
$\dot{I}$ = volumetric evaporation rate, kg m^{-3} s^{-1}
k = thermal conductivity, W m^{-2} K^{-1}
k^p = permeability, m^2
K = nonequilibrium evaporation constant, s^{-1}
$K_{i,j}$ = nonequilibrium constant for interphase mass transfer from i to j, s^{-1}
L = length scale, m
m = overall mass fraction
M_a, M_v = molecular weight of air and vapor
n = total number of phases
$\mathbf{n}$ = total flux, kg m^{-2} s^{-1}
P = gas pressure, Pa

p_v = vapor pressure, Pa
$\mathbf{q}$ = heat flux, J m^{-2} s^{-1}
R = universal gas constant, J kmol^{-1} K^{-1}
$R_{i,j}$ = rate of mass transfer from i to j, kg m^{-3} s^{-1}
S = saturation
t = time, s
T = temperature
u = velocity, m s^{-1}
V = volume, m^3
x = mole fraction
ρ = density, kg m^{-3}
λ = latent heat of vaporization, J kg^{-1}
ω_v, ω_a = mass fraction of vapor and air in relation to total gas
ϕ = porosity
μ = dynamic viscosity, Pa s
amb = ambient
a, g, o, s, v, w = air, gas, oil, solid, vapor, water
bw, bf = water, fat in solid phase
cap = capillary
eff = effective
eq = equilibrium
f = final
i = ith liquid phase, initial
in = intrinsic
ini = initial
j = jth component in the solid phase
0 = at time $t=0$
r = relative, residual
sat = saturation
surf = surface
T = temperature
tot = total 2

Appendix: Transport Time-Scale Analysis

The minimum length scale (L) of significance for typical food materials is assumed to be 0.1 mm:

$$L \sim 10^{-4}\ \text{m} \tag{A1}$$

The time scale for capillary diffusion (t_{cap}):

$$t_{\text{cap}} \sim \frac{L^2}{D_{\text{cap}}} = \frac{10^{-8}\ \text{m}^2}{10^{-6}\ \text{m}^2/\text{s}} = 10^{-2}\ \text{s} \tag{A2}$$

Note that a low value for the length scale and the highest possible value of D_{cap} is used to obtain the minimum relevant diffusion time scale.

The time scale for binary diffusion (t_g):

$$t_g \sim \frac{L^2}{D_{\text{eff},g}} = \frac{10^{-8}\ \text{m}^2}{10^{-5}\ \text{m}^2/\text{s}} = 10^{-3}\ \text{s} \tag{A3}$$

The time scale for pressure-driven flow (t_p):

$$v \sim \frac{k}{\mu}\frac{\Delta P}{L} = \frac{10^{-15}\ \text{m}^2}{10^{-3}\ \text{Pa s}}\frac{10^{5}\ \text{Pa}}{10^{-4}\ \text{m}} = 10^{-3}\ \text{m/s}$$

$$t_p \sim \frac{L}{v} = \frac{10^{-4}\ \text{m}}{10^{-3}\ \text{m/s}} = 10^{-1}\ \text{s} \tag{A4}$$

The time scale for heat flow (t_h):

$$t_h \sim \frac{L^2}{\dfrac{k_{\text{eff}}}{\rho_{\text{eff}} c_{p,\text{eff}}}} = \frac{10^{-8}\ \text{m}^2}{10^{-7}\ \text{m}^2/\text{s}} = 10^{-1}\ \text{s} \tag{A5}$$

Therefore, it can be seen that all the transport time scales are larger than the evaporation equilibrium time scale, which is 10^{-5} s for 25 μm sized pores [37].

References

[1] Ateba, P., and Mittal, G. S., 1994, "Modeling the Deep-Fat Frying of Beef Meatballs," Int. J. Food Sci. Technol., **29**(4), pp. 429–440.
[2] Ikediala, J. N., Correia, L. R., Fenton, G. A., and Ben-Abdallah, N., 1996, "Finite Element Modeling of Heat Transfer in Meat Patties During Single-Sided Pan-Frying," J. Food Sci., **61**(4), pp. 796–802.
[3] Bengtsson, N. E., Jakobsson, B., and Dagerskog Sik, M., 1976, "Cooking of Beef by Oven Roasting—Study of Heat and Mass-Transfer," J. Food Sci., **41**(5), pp. 1047–1053.
[4] Chau, K. V., and Snyder, G. V., 1988, "Mathematical-Model for Temperature Distribution of Thermally Processed Shrimp," Trans. ASAE, **31**(2), pp. 608–612.
[5] Fowler, A. J., and Bejan, A., 1991, "The Effect of Shrinkage on the Cooking of Meat," Int. J. Heat Fluid Flow, **12**(4), pp. 375–383.
[6] Dincer, I., and Yildiz, M., 1996, "Modelling of Thermal and Moisture Diffusions in Cylindrically Shaped Sausages During Frying," J. Food Eng., **28**(1), pp. 35–44.
[7] Williams, R., and Mittal, G. S., 1999, "Low-Fat Fried Foods With Edible Coatings: Modeling and Simulation," J. Food Sci., **64**(2), pp. 317–322.
[8] Shilton, N., Mallikarjunan, P., and Sheridan, P., 2002, "Modeling of Heat Transfer and Evaporative Mass Losses During the Cooking of Beef Patties Using Far-Infrared Radiation," J. Food Eng., **55**(3), pp. 217–222.
[9] Wang, L., and Singh, R. P., 2004, "Finite Element Modeling and Sensitivity Analysis of Double-Sided Contact-Heating of Initially Frozen Hamburger Patty," Trans. ASAE, **47**(1), pp. 147–157.
[10] Kondjoyan, A., Rouaud, O., McCann, M. S., Havet, M., Foster, A., Swain, M., and Daudin, J. D., 2006, "Modelling Coupled Heat-Water Transfers During a Decontamination Treatment of the Surface of Solid Food Products by a Jet of Hot Air. I. Sensitivity Analysis of the Model and First Validations of Product Surface Temperature Under Constant Air Temperature Conditions," J. Food Eng., **76**(1), pp. 53–62.
[11] Farkas, B. E., Singh, R. P., and Rumsey, T. R., 1996, "Modeling Heat and Mass Transfer in Immersion Frying. 1. Model Development," J. Food Eng., **29**(2), pp. 211–226.
[12] Farid, M. M., and Chen, X. D., 1998, "The Analysis of Heat and Mass Transfer During Frying of Food Using a Moving Boundary Solution Procedure," Heat Mass Transfer, **34**(1), pp. 69–77.
[13] Bouchon, P., and Pyle, D. L., 2005, "Modelling Oil Absorption During Post-Frying Cooling—I: Model Development," Food Bioprod. Process., **83**(C4), pp. 253–260.
[14] Mascarenhas, W. J., Akay, H. U., and Pikal, M. J., 1997, "A Computational Model for Finite Element Analysis of the Freeze-Drying Process," Comput. Methods Appl. Mech. Eng., **148**(1–2), pp. 105–124.
[15] Ni, H., and Datta, A. K., 1999, "Moisture, Oil and Energy Transport During Deep-Fat Frying of Food Materials," Food Bioprod. Process., **77**(C3), pp. 194–204.
[16] Yamsaengsung, R., and Moreira, R. G., 2002, "Modeling the Transport Phenomena and Structural Changes During Deep Fat Frying—Part 1: Model Development," J. Food Eng., **53**(1), pp. 1–10.
[17] Halder, A., Dhall, A., and Datta, A. K., 2007, "An Improved, Easily Implementable, Porous Media Based Model for Deep-Fat Frying—Part I: Model Development and Input Parameters," Food Bioprod. Process., **85**(C3), pp. 209–219.
[18] Zhang, J., Datta, A. K., and Mukherjee, S., 2005, "Transport Processes and Large Deformation During Baking of Bread," AIChE J., **51**(9), pp. 2569–2580.
[19] Zhang, J., Datta, A. K., and Rakesh, V., 2005, "Investigation of Non-Equilibrium in Water Evaporation," Third Inter-American Drying Conference, Montreal, Canada.
[20] Farkas, B. E., Singh, R. P., and Rumsey, T. R., 1996, "Modeling Heat and Mass Transfer in Immersion Frying. 2. Model Solution and Verification," J. Food Eng., **29**(2), pp. 227–248.
[21] Ni, H., Datta, A. K., and Torrance, K. E., 1999, "Moisture Transport in Intensive Microwave Heating of Biomaterials: A Multiphase Porous Media Model," Int. J. Heat Mass Transfer, **42**(8), pp. 1501–1512.
[22] Yamsaengsung, R., and Moreira, R. G., 2002, "Modeling the Transport Phenomena and Structural Changes During Deep Fat Frying—Part II: Model Solution and Validation," J. Food Eng., **53**(1), pp. 11–25.
[23] Rutqvist, J., Wu, Y. S., Tsang, C. F., and Bodvarsson, G., 2002, "A Modeling Approach for Analysis of Coupled Multiphase Fluid Flow, Heat Transfer, and Deformation in Fractured Porous Rock," Int. J. Rock Mech. Min. Sci., **39**(4), pp. 429–442.
[24] Buscheck, T. A., and Nitao, J. J., 1993, "Repository-Heat-Driven Hydrothermal Flow at Yucca Mountain.1. Modeling and Analysis," Nucl. Technol., **104**(3), pp. 418–448.
[25] Abriola, L. M., and Pinder, G. F., 1985, "A Multiphase Approach to the Modeling of Porous-Media Contamination by Organic-Compounds. 1. Equation Development," Water Resour. Res., **21**(1), pp. 11–18.
[26] Arbogast, T., Bryant, S., Dawson, C., Saaf, F., Wang, C., and Wheeler, M., 1996, "Computational Methods for Multiphase Flow and Reactive Transport Problems Arising in Subsurface Contaminant Remediation," J. Comput. Appl. Math., **74**(1–2), pp. 19–32.
[27] Khanafer, K., and Vafai, K., 2006, "The Role of Porous Media in Biomedical Engineering as Related to Magnetic Resonance Imaging and Drug Delivery," Heat Mass Transfer, **42**(10), pp. 939–953.
[28] Datta, A. K., 2007, "Porous Media Approaches to Studying Simultaneous Heat

and Mass Transfer in Food Processes. I: Problem Formulations," J. Food Eng., **80**(1), pp. 80–95.
[29] Curtiss, C. F., and Bird, R. B., 2001, "Multicomponent Diffusion," Ind. Eng. Chem. Res., **40**(7), p. 1791.
[30] Vafai, K., and Tien, C. L., 1981, "Boundary and Inertia Effects on Flow and Heat-Transfer in Porous-Media," Int. J. Heat Mass Transfer, **24**(2), pp. 195–203.
[31] Perre, P., and Moyne, C., 1991, "Processes Related to Drying. 2. Use of the Same Model to Solve Transfers Both in Saturated and Unsaturated Porous-Media," Drying Technol., **9**(5), pp. 1153–1179.
[32] Pruess, K., 2004, "The TOUGH Codes—A Family of Simulation Tools for Multiphase Flow and Transport Processes in Permeable Media," Vadose Zone J., **3**, pp. 738–746.
[33] Pham, Q. T., 1995, "Comparison of General-Purpose Finite-Element Methods for the Stefan Problem," Numer. Heat Transfer, Part B, **27**(4), pp. 417–435.
[34] Constant, T., Moyne, C., and Perre, P., 1996, "Drying With Internal Heat Generation: Theoretical Aspects and Application to Microwave Heating," AIChE J., **42**(2), pp. 359–368.
[35] Le, C. V., Ly, N. G., and Postle, R., 1995, "Heat and Mass-Transfer in the Condensing Flow of Steam Through an Absorbing Fibrous Medium," Int. J. Heat Mass Transfer, **38**(1), pp. 81–89.
[36] Scarpa, F., and Milano, G., 2002, "The Role of Adsorption and Phase Change Phenomena in the Thermophysical Characterization of Moist Porous Materials," Int. J. Thermophys., **23**(4), pp. 1033–1046.
[37] Ward, C. A., and Fang, G., 1999, "Expression for Predicting Liquid Evaporation Flux: Statistical Rate Theory Approach," Phys. Rev. E, **59**(1), pp. 429–440.
[38] Halder, A., Dhall, A., and Datta, A. K., 2007, "An Improved, Easily Implementable, Porous Media Based Model for Deep-Fat Frying—Part II: Results, Validation and Sensitivity Analysis," Food Bioprod. Process., **85**(C3), pp. 220–230.
[39] Pan, Z., and Singh, R. P., 2001, "Physical and Thermal Properties of Ground Beef During Cooking," Lebensm.-Wiss. Technol., **34**(7), pp. 437–444.
[40] Pan, Z., Singh, R. P., and Rumsey, T. R., 2000, "Predictive Modeling of Contact-Heating Process for Cooking a Hamburger Patty," J. Food Eng., **46**(1), pp. 9–19.
[41] Boukouvalas, C. J., Krokida, M. K., Maroulis, Z. B., and Marinos-Kouris, D., 2006, "Density and Porosity: Literature Data Compilation for Foodstuffs," Int. J. Food Prop., **9**(4), pp. 715–746.
[42] Tseng, Y. C., Moreira, R., and Sun, X., 1996, "Total Frying-Use Time Effects on Soybean-Oil Deterioration and on Tortilla Chip Quality," Int. J. Food Sci. Technol., **31**, pp. 287–294.
[43] Choi, Y., and Okos, M. R., 1986, "Thermal Properties of Liquid Foods—Review," *Physical and Chemical Properties of Food*, M. R. Okos, ed., American Society of Agricultural Engineers, St Joseph, MI, pp. 35–77.
[44] Lewis, M. J., 1987, *Physical Properties of Foods and Food Processing Systems*, VCH, Deerfield Beach, FL.
[45] Bear, J., 1972, *Dynamics of Fluids in Porous Media*, Elsevier, New York.
[46] Hanreich, G., and Nicolics, J., 2001, "Measuring the Natural Convective Heat Transfer Coefficient at the Surface of Electronic Components," IEEE Instrumentation and Measurement Technology Conference, pp. 1045–1050.
[47] Hallstrom, B., 1990, "Mass Transport of Water in Foods a Consideration of the Engineering Aspects," J. Food Eng., **12**(1), pp. 45–52.
[48] Oroszvári, B. K., Rocha, C. S., Sjöholm, I., and Tornberg, E., 2006, "Permeability and Mass Transfer as a Function of the Cooking Temperature During the Frying of Beefburgers," J. Food Eng., **74**(1), pp. 1–12.
[49] Goodrum, J. W., Geller, D. P., and Adams, T. T., 2002, "Rheological Characterization of Yellow Grease and Poultry Fat," J. Am. Oil Chem. Soc., **79**(10), pp. 961–964.

Thermal Processing of Tissue Engineering Scaffolds

Alisa Morss Clyne
Department of Mechanical Engineering and Mechanics,
School of Biomedical Engineering, Science, and
Health Systems,
Drexel University,
3141 Chestnut Street,
Philadelphia, PA 19104
e-mail: asm67@drexel.edu

Tissue engineering requires complex three-dimensional scaffolds that mimic natural extracellular matrix function. A wide variety of techniques have been developed to create both fibrous and porous scaffolds out of polymers, ceramics, metals, and composite materials. Existing techniques include fiber bonding, electrospinning, emulsion freeze drying, solvent casting/particulate leaching, gas foaming/particulate leaching, high pressure processing, and thermally induced phase separation. Critical scaffold properties, including pore size, porosity, pore interconnectivity, and mechanical integrity, are determined by thermal processing parameters in many of these techniques. In this review, each tissue engineering scaffold preparation method is discussed, including recent advancements as well as advantages and disadvantages of the technique, with a particular emphasis placed on thermal parameters. Improvements on these existing techniques, as well as new thermal processing methods for tissue engineering scaffolds, will be needed to provide tissue engineers with finer control over tissue and organ development. [DOI: 10.1115/1.4002464]

Keywords: tissue engineering, scaffolds, thermal processing, porosity, fiber bonding, electrospinning, emulsion freeze drying, solvent casting/particulate leaching, gas foaming/particulate leaching, high pressure processing, thermally induced phase separations

1 Introduction

Tissue engineering was defined in the late 1980s as "the application of principles and methods of engineering and life sciences toward fundamental understanding of structure-function relationships in normal and pathological mammalian tissues and the development of biological substitutes to restore, maintain, or improve tissue functions" [1]. Tissue engineering has made progress in developing organs with a relatively simple architecture, including cartilage, skin, bladder, and heart valves [2–5]. However, the promise of generating an abundant supply of tissues and organs to replace those lost to disease, aging, and trauma remains unfulfilled. For this reason and because tissue engineering has potential to revolutionize drug discovery and expand our understanding of complex cell behavior, tissue engineering was redefined in 2007. The Multi-Agency Tissue Engineering Science (MATES) Interagency Working Group expanded the name to tissue science and engineering and the definition to "the use of physical, chemical, biological, and engineering processes to control and direct the aggregate behavior of cells" [6].

The MATES strategic plan identified biomaterial scaffold development as an overarching goal for tissue science and engineering. In vivo, cells are supported both structurally and biochemically by the extracellular matrix, a nanoscale fibrous protein mesh. To engineer complex three-dimensional tissues in vitro, cells are seeded into scaffolds that mimic extracellular matrix functions. Scaffolds must have the appropriate three-dimensional architecture for the tissue to be created, including the desired volume, shape, and mechanical properties. Scaffolds must be highly porous with excellent pore interconnectivity to allow high cell density, tissue in-growth, and essential nutrient diffusion [7]. The base material, leachable components, and degradation products of scaffolds must be nontoxic to cells and produce minimal immune response. Finally, scaffolds should actively guide tissue regeneration through incorporation of bioactive components [8].

Tissue engineering scaffolds are made from a wide variety of materials. The material is selected based on whether the scaffold should degrade or remain a permanent part of the tissue as it grows and also based on the desired tissue's mechanical properties. Metals, including stainless steel, cobalt-based alloys, and titanium-based alloys, were traditionally used for orthopedic implants; however, they are difficult to process and are not biodegradable [9]. For bone tissue engineering, ceramics such as calcium phosphate, silica, alumina, zirconia, bioglass, hydroxyapatite, and titanium dioxide are often used alone or as a component in a composite [10]. Polymers are widely used because of their diverse composition, ease of bioactive factor conjugation, and ability to control both their mechanical properties and degradation rate. Natural polymers used in tissue engineering include fibrin, collagen, gelatin, chitosan, alginate, hyaluronic acid, glycosaminoglycan, starch, and chitin [11]. An equally wide range of synthetic polymers are employed in scaffold construction such as polylactide (PLA), polyglycolide (PGA), poly(lactide-co-glycolide) (PLGA), polyanhydrides, and polyorthoesters [12,13]. Many natural and synthetic polymers swell in water to form hydrogels. A wide variety of functions can be designed into the hydrogel, including sensitivity to a specific stimulus, controlled degradability, and self assembly [14,15]. Scaffolds are often functionalized to induce a specific biological function by physically adsorbing or chemically conjugating bioactive factors such as adhesion molecules and growth factors to the scaffold surface.

Thermal processing parameters are critical to many of the techniques developed for scaffold fabrication. Often, the scaffold structure and morphology can be manipulated by changing thermodynamic and heat transfer variables in the manufacturing procedure. In this review, we present methods of fibrous and porous scaffold fabrication that involve thermal processing. advantages and disadvantages for each method are summarized in Table 1. Detailed discussions of scaffold fabrication by rapid prototyping methods and cell-laden scaffold deposition can be found elsewhere [16,17].

2 Fibrous Scaffolds

The natural extracellular matrix is a nanoscale fibrous mesh; therefore, a natural choice for tissue engineered scaffolds is replication of the natural topography. Fibrous scaffolds have a large surface area for cell attachment, and they are highly porous for rapid nutrient diffusion. Studies suggest that many cell types respond to fibrous material nanoscale topography [18]. A disadvantage of these scaffolds is the lack of structural stability and mechanical integrity, in particular, for load bearing tissues . While the original fibrous scaffolds were woven felts, newer techniques such as fiber bonding and electrospinning have advanced fibrous scaffold development.

2.1 Fiber Bonding. Fiber bonding was initiated to enhance the structural stability of existing polymer meshes, which showed positive results in tissue engineering [19]. In this method, fibers are joined at their crosspoints either by sintering the fibers themselves or by melting a secondary polymer to join fibers together. Thermal parameters during the annealing phase are critical since the temperature must be high enough to allow bonding but low enough to maintain fiber shape, diameter, and scaffold porosity.

Manuscript received August 14, 2009; final manuscript received October 26, 2009; published online November 16, 2010. Assoc. Editor: Wilson K. S. Chiu.

Table 1 Advantages and disadvantages of thermal processing methods for tissue engineering scaffolds

Processing method	Advantages	Disadvantages
Fiber bonding	• Fibrous scaffolds are more similar to native extracellular matrix • Better mechanical properties than electrospun or mesh scaffolds • High porosity	• Still not highly mechanically stable • Porosity varies greatly with processing parameters • Limited polymers and solvents available for use • Solvents may have toxic effects
Electrospinning	• Fibrous scaffolds are more similar to native extracellular matrix • Nanoscale fibers can be created from synthetic and natural polymers • High surface area and porosity	• Low mechanical integrity • Pore sizes may be too small for cell infiltration and migration
Emulsion freeze drying	• Highly porous with large pore sizes • Safe for protein and bioactive factor incorporation into the scaffold	• Pore size can be difficult to control • Emulsion may need to be stabilized using surfactant
Solvent casting/particulate leaching	• Defined pore size, high porosity • Independent control of pore size and porosity • Can be used to make porous ceramics	• Scaffold thickness limited to ~3 mm • Nonporous skin layer • Solvent or residual particles can be toxic • Hard to control pore shape and interconnectivity
Gas foaming/particulate leaching	• No skin layer • High porosity	• Solvent or residual particles can be toxic • Hard to control pore shape and interconnectivity
High pressure processing	• Does not require solvents so biomolecules can be incorporated • Many polymers can be processed • Relatively uniform pore distribution	• Creates a nonporous surface • Poor pore interconnectivity • Pore sizes are generally small • Long manufacturing time
Thermally induced phase separation	• Biomolecules can be incorporated • Temperature gradients can be used to create oriented pores	• Solvents can be toxic • Phase separation mechanism must be tightly controlled • Solvent extraction can be time-consuming

While this method can be used to create fibrous scaffolds with enhanced mechanical properties, the scaffold porosity ranges from 50% to 81% and is difficult to control. Limited polymer and solvent choices exist, and the use of harsh solvents might prevent incorporation of bioactive factors or leave residual solvent that could harm cells in the scaffold [9,11].

Fiber bonding was initially developed by Mikos et al. [20] in 1993. The PGA meshes they were using were difficult to form into desired tissue structures and failed to provide a firm substrate for cell adhesion and growth. In their experiments, PGA meshes were cast in poly(L-lactic acid) (PLLA) dissolved in methylene chloride, which then solidified after the solvent evaporated. The composite was heated first to 195°C to melt the PLLA and then to 235°C to sinter the PGA, followed by cooling in liquid nitrogen. PLLA was dissolved in methylene chloride, leaving ~10 μm diameter PGA fibers bonded at their crosspoints without changing polymer surface or bulk properties or fiber diameter. The PLLA matrix, which filled the pores in the PGA as it melted, played a critical role in maintaining PGA fiber shape. In cell studies, hepatocytes bound to fibers and survived within the scaffold for at least one week [20].

Fiber bonding has since been expanded by other groups. While in the original study, PLLA was used as a melted matrix to maintain PGA fiber shape; later experiments used PLLA as the bonding agent [21]. PGA fiber matrices were sprayed with atomized PLLA and annealed at 195°C, which is above the melting point of PLLA but below the melting point of PGA. The PLLA melted and condensed at the PGA fiber crosspoints. Extensive fiber bonding increased scaffold compressive modulus, slowed degradation, improved cell interaction, and prevented matrix contraction with seeded cells. Fiber bonding was also used to create a natural-synthetic polymer blend scaffold [22,23]. Melt-spun fibers (~180 μm diameter) of starch blended with poly(ε-caprolactone) (PCL) were cut and sintered to make scaffolds of varying porosity. Fiber bonding was most recently applied to enhance the structural integrity of electrospun scaffolds. In this study, 0.57–1.35 μm diameter electrospun PCL fibers were bonded at 55°C in Pluronic F127, a difunctional block copolymer surfactant composed of polyoxyethylene-polyoxypropylene copolymers terminating in primary hydroxyl groups [24]. Fibers bonded at crosspoints while maintaining fiber diameter and pore area. Scaffold mechanical properties such as shrinkage, ultimate tensile strength, and burst pressure improved.

2.2 Electrospinning. Electrospinning is the most widely used method for fabricating nanofiber nonwoven matrices. While the method was developed and patented in the early 20th century, it was largely used for textile and filter creation. Electrospinning was applied to tissue engineering scaffolds only after it was demonstrated at the end of the 20th century that organic polymers could be electrospun. Electrospinning occurs by drawing a polymer solution (melt) from a nozzle (spinneret) using a combination of gravity or mechanical pressure and a high voltage electric field (10–20 kV). When the applied electric field surpasses a critical value, the electrostatic force exceeds surface tension and a polymer jet is ejected from the nozzle. The polymer jet then moves toward the collecting plate, which can either be static to collect randomly oriented fibers or rotating to collect aligned fibers. The polymer strands in the jet separate due to charge repulsion, which produces fibers of nanometer scale diameter. Fiber morphology is determined by polymer viscosity, conductivity, surface tension, molecular weight, flow rate, tip to collector distance, and nozzle tip design among others [25]. Thermal electrospinning parameters can help determine polymer properties and, therefore, fiber morphology, and since melt temperatures tend to be low, large and complex molecules (perhaps even bioactive) can be used. Pore sizes range from 2 μm to 200 μm, with porosities reaching as high as 96%. While electrospinning produces a high surface area scaffold similar to native extracellular matrix, the small pore size may not be sufficient for cell seeding and infiltration, and me-

chanical integrity tends to be low.

Synthetic polymers were electrospun using polymer dissolved in a solvent. PLGA, one of the most commonly used biodegradable polymers in tissue engineering, was electrospun at 18 kV with 20 cm between the needle tip and the static copper collecting plate. Fibers had diameters ranging from 500 nm to 800 nm. The scaffold was highly porous, yet had over 300 MPa tensile modulus and supported fibroblast proliferation [26]. Using similar methods, PCL was electrospun at 13 kV to produce fibers ranging in diameter from 20 nm to 5 μm, with an average diameter of 400 nm. Cells migrated into the scaffold and formed mineralized tissue (similar to bone) within 4 weeks [27]. Additional studies with electrospun PCL scaffolds suggested that mesenchymal stem cell differentiation may be directed within these structures [28]. While PLGA and PCL have been widely used as biodegradable scaffolds, Kenawy et al. electrospun nonbiodegradable poly(ethylene-co-vinyl alcohol) (EVOH). Fiber size, which ranged from 0.2 μm to 80 μm, depended on solution concentration. The fibrous mats supported proliferation of both smooth muscle cells and fibroblasts [29].

In addition to synthetic polymers, many natural polymers have been electrospun. Fibrinogen, a soluble protein in blood plasma that plays a key role in wound healing, was electrospun at 22 kV to create fibers with an average diameter of 80 nm [30]. Dissolved silk, electrospun at 15 kV, produced circular, smooth fibers that ranged from 30 nm to 120 nm in diameter [31]. Electrospun collagen and gelatin produced fibers of slightly larger diameter (200–500 nm), whereas elastin fibers were several micrometers in diameter [28,32]. Other natural polymers that have been electrospun include chitin and alginate [33,34]. Each of the electrospun scaffolds produced from natural polymers successfully supported cell attachment, spreading, and/or proliferation [28,31,32]. Li et al. [35] later electrospun synthetic and natural polymer blends, which enhanced scaffold mechanical properties while maintaining cell affinity.

Melt electrospinning eliminates the need for harsh organic solvents in the electrospinning process, which is more environmentally benign and can be used to increase production rate. Zhou et al. [36] showed that PLA could be melted and then electrospun and that both nozzle and spinning region temperatures were critical to fiber size. When spinning temperature was below the glass transition temperature, fast solidification in the spinning region led to a larger jet diameter. Both polyethylene glycol (PEG) and PCL were melt electrospun at temperatures between 60°C and 90°C. Adequate fiber cooling along the path from the nozzle to the collector was critical to producing continuous constant diameter fibers [37]. While polymer degradation did not occur, even these relatively low temperatures would prevent most bioactive factors from being incorporated into fibers during production. Melt-spun fibers tend to be larger (micrometer size range), but adequate solvent evaporation between the nozzle and the collector is not a problem [38].

More recently, new electrospinning techniques were developed to produce functional scaffolds. Electrospun polymers were aligned in the scaffold by mechanical drawing. Aligned scaffolds can induce alignment in cells that require a three-dimensional tissue architecture such as smooth muscle cells and cardiac myocytes [39,40]. Sun et al. [41] produced a surface modified nanofiber by spinning an ultrafine core within the shell of another polymer material. This method could protect bioactive components in the core during the scaffold fabrication process. In multilayer electrospinning, different polymers are sequentially electrospun, whereas in mixed electrospinning, different polymers are simultaneously electrospun using separate nozzles [42]. Electrospinning has also been combined with methods to create porous scaffolds, which are detailed later in this review. Micro- or nano-sized pores were created within electrospun scaffolds by depositing salt particles during the electrospinning process. After the scaffold was created, salt particles were leached out to create a dual-porosity scaffold [43,44]. Park et al. [45] used a combination of direct polymer melt deposition and electrospinning to create a mixed microfiber and nanofiber PCL scaffold. Post-fabrication surface modification significantly enhanced electrospun scaffold biological performance, for example, by grafting a cell-specific ligand or gelatin to the formed scaffold [46,47].

3 Porous Scaffolds

Highly porous scaffolds are desired in tissue engineering because a large surface area promotes cell attachment and growth, and a large porous volume can deliver the required cell mass for tissue regeneration. Scaffold porosity and pore interconnectivity are critical for nutrient diffusion and tissue in-growth. In fact, the optimum pore size for tissue growth varies with tissue type [48]. Many techniques have been developed to create porous scaffolds, including emulsion freeze drying, solvent casting, gas foaming, high pressure processing, and thermally induced phase separation. Thermal processing parameters can determine the scaffold porosity in these techniques and are therefore important to understand and control to create the desired three-dimensional tissue engineering scaffold architecture.

3.1 Emulsion Freeze Drying. Emulsion freeze drying creates highly porous scaffolds with larger pore sizes, which could allow protein-based bioactive factor incorporation. An emulsion is created by homogenization of two immiscible phases: a dispersed water phase and a continuous polymer-solvent phase. The sample is then freeze-dried to create a porous scaffold with pore size and interconnectivity depending on processing parameters. While the emulsion characteristics are largely determined by polymer weight percentage, molecular weight, and dispersed phase volume fraction, the freezing temperature and rate must be sufficient to preserve the emulsion structure. Pore sizes ranging from 20 μm to 200 μm can be created with porosities higher than 90%.

Whang et al. [49] first developed emulsion freeze drying for tissue engineering scaffolds. A polymer-methylene chloride solution of PLA or PLGA was homogenized with water at various volume fractions. After homogenization, samples were poured into a copper mold, placed in a secondary container maintained at −196°C, and, finally, freeze-dried at −55°C to remove water and solvent. Increasing polymer volume fraction increased porosity and pore area, whereas increasing polymer viscosity increased pore size. Scaffolds with median pore size less than 50 μm showed improved bone defect healing, perhaps by stabilizing the injury-induced hematoma and its vital growth factors [50]. Bioactive components, such as bovine serum albumin, were also successfully incorporated into scaffolds as a drug delivery model [51]. The albumin concentration in the water phase during emulsion formation heavily affected pore size. For this case, the scaffold was quenched and freeze-dried at 106°C with a slow increase to room temperature to speed solvent sublimation.

Emulsion freeze drying has recently been expanded. Baker et al. [52] produced PLGA and PLA scaffolds by emulsion freeze drying using Span 80, a nonionized detergent, as a surfactant to stabilize the emulsion. Scaffold pore size ranged from 20 μm to 50 μm, and scaffold mechanical properties varied by a factor of 2. Urinary tract stromal cells showed increased proliferation on the PCL scaffolds with a modulus similar to a native bladder. Composite poly(hydroxybutyrate-co-valerate) (PHBV) polymer and hydroxyapatite (HA) ceramic scaffolds were produced by emulsion freeze drying [53]. Increasing water percentage increased the scaffold porosity, and the pores ranged from several micrometers to 300 μm and showed good interconnectivity. The HA nanoparticles were distributed throughout the scaffold and adhered well within the scaffold, as long as HA content was kept below 10%. Composite scaffolds had higher strength, making them more suitable for hard tissue engineering. In addition to polymers and polymer-ceramic composites, emulsion freeze drying was applied to create hydrogels with an interconnected pore

structure. A mixture of poly(vinyl alcohol) (PVA) and poly(vinyl pyrrolidone) (PVP) was added to a PLGA emulsion and stirred to create a homogeneous distribution of PLGA microparticles in the PVA-PVP hydrogel. The composite was exposed to six freezing cycles and then submerged in water to remove solvents. The final hydrogel had mechanical properties similar to native cartilage, and encapsulated PLGA microparticles could be used for drug release and to enhance scaffold porosity as they degraded [54].

3.2 Solvent Casting/Particulate Leaching. Solvent casting/particulate leaching can be used to create scaffolds of defined pore size. A polymer is cast with either mineral or organic particles dispersed in the solution. The solvent is evaporated out, sometimes by freeze drying, and the particles are dissolved or leached out to create a porous matrix. While this method is generally used for polymers, porous ceramic materials can also be produced using either salt or polymeric particles as porogens [10]. The scaffold pore size and porosity can be modulated independently by changing particulate diameter and concentration, respectively. Pore sizes range from 100 μm to 600 μm with porosities greater than 90%. However, this method can only produce thin membranes (up to 3 mm thick) with a dense surface skin layer, and the pore shape and interconnectivity can be difficult to control [9]. Any residual particulates may impact cell viability. Thermal processing parameters come into play in these scaffolds in determining the polymer form (amorphous or semicrystalline). Particulate leaching can also be combined with thermal fabrication methods, such as melt extrusion, and particulates can be sintered together to create interconnected pores in the final scaffold.

Mikos et al. [55] developed the solvent casting/particulate leaching method in the early 1990s. PLLA was dissolved in a solvent with sodium chloride, sodium tartrate, or sodium citrate particles of various sizes. After the solvent evaporated, samples were heated to 195°C (15°C above the PLLA melting temperature) to remove polymer crystallites. The melted PLLA membranes were either annealed (slowly cooled) or quenched in liquid nitrogen (rapidly cooled) to produce semicrystalline or amorphous membranes, respectively. Membranes produced without heat treatment were semicrystalline. Sodium particles were finally leached out with water. Polymer with 70–90 wt % salt produced homogeneous membranes with interconnected pores. While porosity was independent of salt type, porosity did increase with salt weight fraction and median pore diameter increased with salt particle size. Since membrane thickness was generally only several millimeters, the membranes were laminated together chemically or by annealing to form shaped three-dimensional scaffolds [56,57]. Solvent casting/particulate leaching has been used with a variety of other polymers, including PLGA, PCL, and PLGA-PEG blends, as well as other porogens, including sugar, gelatin, and paraffin [58–63].

The solvent casting/particulate leaching method was modified to promote cell adhesion, create composites, increase pore interconnectivity, remove the nonporous skin, and build three-dimensional scaffolds. Ultrathin (3–7 μm thick) PCL films were prepared by combining solvent casting/particulate leaching with biaxial stretching. Collagen was immobilized on the PCL surface using carbodiimide chemistry. The collagen-modified surfaces were more hydrophilic and showed improved cell attachment and proliferation [59]. A nanocomposite of hydroxyapatite nanoparticles in PLGA with sucrose as the porogen was created to enhance scaffold mechanical and chemical properties for bone formation [64]. Pore interconnectivity was improved by fusing salt particles together via a 95% humidity treatment prior to adding the polymer [65]. Paraffin spheres were similarly used as the porogen with a heated step to fuse adjacent spheres [66]. A scaffold with spherical interconnected pores was created by spherolizing salt or sugar particles by pouring crystals through a temperature controlled flame. The particles were compressed in a mold, a polymer solution was cast in the mold, and the particles were removed with water after the polymer solidified [61,67]. Membranes without skin were created by packing the polymer/salt solution into syringes, drying to remove the solvent, and cutting the rigid polymer/salt structure into slices [68]. Solvent casting/particulate leaching can also be combined with other fabrication methods to improve scaffold porosity. Widmer et al. [69] combined solvent casting with extrusion to create porous tubular conduits. Either PLLA or PLGA was solvent cast with salt, and the composite wafers were then heated to 200–275°C and extruded at 10 mm/s. The high extrusion temperature did not change porosity, but it did decrease pore diameter. This may be related to decreased polymer viscosity at high temperature, allowing greater polymer penetration into the gaps surrounding the salt particles.

3.3 Gas Foaming/Particulate Leaching. Gas foaming/particulate leaching is similar to solvent casting/particulate leaching; however, an effervescent salt is used as the porogen. The effervescent salt produces gas as it is leached out of the polymer, creating 100–500 μm pores with high interconnectivity. The process is quick, and the fabricated scaffolds do not have a skin layer, as occurs with solvent casting. Porosity (greater than 90%) and mechanical stretch can be controlled by adjusting the gas evolution reaction. Both polymer and ceramic scaffolds can be formed using this method with some variations. Thermal processing parameters are important for the particulate effervescence, which depends on both solvent and temperature.

To create a porous polymer scaffold using gas foaming/particulate leaching, Nam et al. [70] mixed PLLA with ammonium bicarbonate and cast the polymer mixture in a mold. Gas foaming was achieved either by drying the sample under vacuum or by immersing it in 90°C water. Ammonium bicarbonate then evolved into ammonia and carbon dioxide gas. While the vacuum method produced 200–300 μm interconnected pores, there was also a dense skin layer. The water method produced pores ranging from 200 μm to 500 μm with no skin layer. Scaffolds were successfully seeded with hepatocytes. In later work, it was shown in a PLGA polymer that porosity could be controlled by varying citric acid concentration in the water [71]. These scaffolds were modified to promote chondrocyte adhesion, either with hyaluronic acid or acrylic acid [72,73]. Porous microspheres, which could be used to directly inject a cell suspension into the body, were created by emulsifying PLGA with ammonium bicarbonate [74].

In addition to polymers, gas foaming/particulate leaching was used for ceramics. A tricalcium phosphate cement paste was mixed with an aqueous hydrogen peroxide solution, poured into a mold, and maintained at 60°C for 2 h. At this temperature, hydrogen peroxide decomposed into water and oxygen gas, which produce the foaming. Porosity and pore size could be controlled by varying hydrogen peroxide concentration. This provided a low processing temperature method to create bioactive ceramic scaffolds with an interconnected macroporous structure [75]. An injectable, biodegradable foaming polymer was also created for use in orthopedic applications such as injection into vertebrae. Poly(propylene fumarate) (PPF) with dry carbonate salts ($NaHCO_3$ or $CaCO_3$) was mixed with concentrated citric acid and injected into a Teflon mold. Foaming occurred almost immediately after citric acid addition through carbon dioxide gas generation and the injectable scaffold increased roughly threefold in volume [76].

3.4 High Pressure Processing. High pressure processing, also known as supercritical fluid technology, is similar to gas foaming in that it forms scaffold pores by expanding gas bubbles. However, in high pressure processing, a gas such as carbon dioxide is applied to a dry polymer at high pressure until the polymer is saturated in the supercritical fluid. Pressure is then rapidly reduced to create thermodynamic instability of the dissolved gas. Bubble nucleation and growth generate pores within the polymer matrix [11]. Most importantly, gas saturation suppresses the polymer glass transition temperature. As the supercritical fluid leaves the polymer, the polymer glass transition temperature increases. When the glass transition temperature is higher than the foaming

temperature, the porous scaffold structure is set. Thus, the driving force for bubble growth is still transition temperature, but this is controlled by varying glass transition temperature via gas pressure rather than by polymer heating. High pressure processing does not use harsh organic solvents nor does it include a heating phase, so biomolecules can be incorporated during scaffold fabrication. A wide range of polymers can be foamed, and the porous structure is relatively uniform since the gas is homogeneously dissolved in the polymer. Pore sizes are typically less than 100 μm, but new methods have created pores up to 350 μm with porosities as high as 93%. The method can be limited by insufficient pore interconnectivity, a nonporous surface layer, as well as the long manufacturing time required to equilibrate the polymer in the high pressure gas [9]. Thermal process parameters determine polymer-gas saturation and pore morphology, and high pressure processing can be combined with other thermal processing techniques such as melt extrusion.

Goel and Beckman [77] generated micropores in poly(methyl methacrylate) (PMMA) by saturating the polymer with carbon dioxide at 25–35 MPa for 24 h. The polymer was rapidly quenched to atmospheric pressure over several minutes and cooled to room temperature. Carbon dioxide is known to be a plasticizer for amorphous polymers, such as PMMA, and the PMMA glass transition temperature drops to nearly room temperature at 12–15 wt % carbon dioxide. Changing the saturation temperature between 40°C and 80°C had nearly no effect on the scaffold porous structure. Porosity did increase with carbon dioxide pressure and saturation time. However, these structures had a microcellular core surrounded by a nonporous skin and pores were not well interconnected [78,79]. Gas molecules near the sample edge may have diffused out faster than they could join bubble nuclei. This created a depletion surface layer where gas concentration was too low to achieve bubble nucleation and pore growth. Since these initial studies, porous scaffolds have been created by high pressure processing from polymers such as PLGA, PCL, PLA, and fibrous polymer blends [79–81].

High pressure processing parameters help determine scaffold morphology. The efficacy of different gases as supercritical fluids was compared, including carbon dioxide, nitrogen, and helium. Carbon dioxide proved to be the most effective agent, perhaps due to interaction between carbon dioxide and polymer carbonyl groups [82]. Barry et al. [83] created 85% porous scaffolds with interconnected pores by altering carbon dioxide venting rate using a backpressure regulator. A 30 s venting time resulted in a pore size around 100 μm, a 15 min venting time resulted in a pore size around 350 μm, and a 60 min venting time created a mix of very large and smaller pores. The longer vent rates allowed nucleation sites to grow into pores while also coalescing pores to increase pore size and interconnectivity. Cooling temperature during depressurization also changed pore morphology. Temperature was increased along with pressure in the saturation phase, which significantly decreased saturation time and enhanced carbon dioxide solubility in the polymer. During foaming, both depressurization and cooling rates were controlled since pressure and temperature decreased together. The temperature decrease increases polymer viscosity and solidifies the scaffold. Rapid cooling may fix small closed pores, whereas slow cooling may collapse the structure since it does not freeze [84].

Particulate leaching has been combined with high pressure processing to alleviate the nonporous exterior skin and improve pore interconnectivity. Salt or gelatin microparticles were added to the polymer solution and then removed with water after high pressure processing [85]. Scaffolds produced using this combination approach proved stronger than scaffolds fabricated using solvent casting/particulate leaching [86]. An inverse high pressure processing technique was used along with the water soluble polymer poly(ethylene oxide) (PEO) as the porogen. Aronin et al. [87] extruded 50:50 PCL/PEO blends at 100°C and then decreased pressure to 10–20 mm Hg to nucleate and grow gas bubbles. The scaffold was cooled and agitated in water to leach out PEO. This foaming process increased scaffold pore size and improved pore size distribution when compared with annealing alone. Finally, the high pressure gas itself can leach unwanted components from fabricated tissue engineering scaffolds. Supercritical carbon dioxide was shown to extract residual unreacted monomer and initiator from scaffolds made by the rapid prototyping technique laser stereolithography, which increased cell attachment and proliferation [88].

Since high pressure processing is free of harsh solvents and heating, this method has been used to create bioactive scaffolds. Bone morphogenic protein-2 was adsorbed onto PLA powder, or vascular endothelial growth factor onto PCL, both of which were then foamed using supercritical carbon dioxide [89,90]. Functionalized scaffolds showed improved induction of promyoblast cells into an osteogenic cell line and increased angiogenesis, showing that the bioactive proteins retained their function throughout the processing. High pressure gases can also be used to functionalize scaffolds after they have been formed. Chitosan scaffolds prepared by freeze drying were impregnated with dexamethasone, which directs stem cell differentiation toward an osteogenic line, at pressures from 8 MPa to 14 MPa and temperatures from 35°C to 55°C. Maximum drug loading was achieved at the lowest temperature and pressures but at the highest exposure time [91]. In contrast, when high pressure carbon dioxide was used to enhance lysozyme adsorption onto PLGA scaffolds, increasing pressure also increased protein in the scaffold [92]. For bone tissue engineering, polymer scaffolds of PLA or PLGA were mixed with hydroxyapatite, β-tricalcium phosphate, or phosphate glass to create composites. After high pressure processing, with or without salt particulate leaching, these composite scaffolds showed good ceramic material incorporation, enhanced cell differentiation toward an osteoblastic line, and improved bone regeneration [93–95].

Recently, acoustic techniques were used both to create and monitor porous scaffolds made by high pressure processing. Wang and Li [96] used ultrasound to assist in foaming PMMA with carbon dioxide. After gas was dissolved in the polymer at high pressure, the material was treated with high intensity focused ultrasound. The heating and implosion from the ultrasound made the polymer-gas mixture thermodynamically unstable, allowing pore nucleation and growth. The porosity and pore size could be controlled through ultrasound scanning speed, power, and gas concentration. An ultrasonic pulse-echo reflectometer was also used for noninvasive monitoring of supercritical scaffold fabrication. Acoustic impedance changes suggested different foaming rates [97]. These methods may allow for better control and nondestructive monitoring of high pressure scaffold fabrication.

3.5 Thermally Induced Phase Separation. Thermally induced phase separation is based on thermodynamic demixing of a polymer-solvent solution into a polymer-rich phase and polymer-poor phase. The polymer is dissolved in a solvent, such as dioxane, dimethyl sulfoxide, or molten naphthalene. The temperature is reduced below the bimodal solubility curve to induce phase separation, and then the solidified solvent-rich phase is removed by sublimation or freeze drying to leave a porous polymer scaffold. This method produces scaffolds with either microporous (1–10 μm) or macroporous (greater than 100 μm) structures with varying degree of interconnectivity. The porosity (up to 90%) and pore morphology can be tuned by adjusting thermodynamic parameters. In particular, solid-liquid phase separation and liquid-liquid phase separation produce different scaffold morphologies, as does whether the phase separation mechanism is binodal demixing or spinodal decomposition. Bioactive molecules can also be included in the scaffold without decreased activity since the fabrication environment does not contain harsh chemical or thermal conditions.

A porous PLLA scaffold was prepared by dissolving polymer in molten naphthalene (80°C), rapidly quenching the material on a

25°C mold, and then removing the naphthalene by sublimation. The resulting porous scaffold had relatively uniform open pores with less than 0.2 wt % naphthalene remaining in the polymer. The PLLA foams supported cell growth equally well as unprocessed PLLA [98]. poly(ester urethane) urea (PEUU) and PLGA porous scaffolds were created with dimethyl sulfoxide and dioxane as solvents. Lower quenching temperature produced smaller size pores, and a temperature gradient could be used to orient the pores [99–101].

Several studies examined the importance of process parameters on scaffold structure. Schugens et al. [102] looked in particular at solid-liquid phase separation versus liquid-liquid phase separation. PLA was dissolved in dioxane (solid-liquid) or 87:13 dioxane:water mixture (liquid-liquid). The polymer solution was rapidly immersed in liquid nitrogen (−196°C) or a dry ice bath (−78°C or −20°C) for 2 h then warmed to 0°C and connected to a vacuum line to completely sublimate the dioxane. For solid-liquid phase separation, channels formed in the scaffold with pore diameter of 100 μm and oriented in the cooling direction due to solvent crystallization forward progress. Lower quenching temperatures produced lower porosity scaffolds. When water was added to dioxane to induce liquid-liquid phase separation, isotropic interconnected pores formed in the scaffold [103]. Similar oriented versus isotropic pores were observed with solid-liquid and liquid-liquid phase separation in PLLA and PLGA [104]. In these studies, a surfactant (Pluronic) was also shown to increase pore size. Scaffold morphological variations could be exploited for different tissue applications, such as using tubes for directed nerve regeneration.

While pore morphology in solid-liquid phase separation is a function of solvent crystallization, pore morphology in liquid-liquid phase separation is a function of the polymer thermodynamic state prior to quenching [104]. If the polymer state lies in the metastable region between the binodal and spinodal phase diagram curves, binodal demixing occurs. Binodal demixing is dominated by pore nucleation and growth, which only occurs when there is a large composition change from the mixture average. The scaffold, therefore, has a poorly interconnected beadlike structure. If the polymer state is in the unstable region below the spinodal curve, spinodal decomposition occurs. In spinodal decomposition, phase separation occurs near the mixed phase composition. This results in a scaffold with well-interconnected open pores. Polymer concentration may change the phase separation mechanism, and temperature and time of phase separation affect porosity and pore size [103,105]. While the final freeze drying step is needed for solvent removal without loss of porous structure, freeze drying is time-consuming and may result in a nonporous surface skin. By immersing the frozen polymer in a −20°C ethanol solution instead of freeze drying, solvent was extracted in a timely manner with improved porosity throughout the scaffold [106].

Polymer-ceramic composites were successfully formed by thermally induced phase separation. Zhang and Ma [107] created PLLA and PLGA scaffolds with hydroxyapatite using dioxane as the solvent for solid-liquid phase separation. Hydroxyapatite disturbed solvent crystallization, making irregular crystals that decreased porosity and formed isotropic pores instead of channels. However, composite scaffolds had improved mechanical properties. Solid-liquid and liquid-liquid phase separations were compared in polymer-hydroxyapatite scaffolds. Liquid-liquid phase separation decreased average pore size from 100 μm to 10 μm and a random pore structure was formed with fibrous wall texture [108]. A chitosan-alginate scaffold was created with water as the solvent. Natural materials have desirable cell interactions and bioactive proteins could be incorporated since processing parameters were not harsh [109]. In contrast, when alkaline phosphatase was incorporated into a scaffold prepared with dioxane and lower phase separation temperatures, 30% of its bioactivity was lost [98].

Thermally induced phase separation was combined with other methods to improve scaffold properties. Paraffin microspheres, pressed and heated together to form a mold, were used as a porogen for PLLA or gelatin scaffolds [110,111]. Shaped scaffolds were created by thermally induced phase separation in negative molds made by solid freeform fabrication [112]. Thus, shaped features could be created on multiple size scales. Ao et al. [113] combined two thermally induced phase separation processes to create hollow nerve conduits filled with biodegradable matrix. A chitosan hollow tube was initially made using a tube shaped mold. The chitosan tube was then filled with a chitosan-acetic acid solution and directionally frozen to produce oriented tubes.

4 Conclusions

While many of the fundamental techniques to make fibrous and porous scaffolds have existed for a long time, these techniques are continuously being improved to create finer control over scaffold properties. Thermal processing parameters are integral to many of these methods and are particularly important since cells and bioactive molecules have limited resistance to higher temperatures. Tissue engineers continue to learn how different cell types respond to varied scaffold morphology; therefore, new fabrication methods are needed to create and control scaffold architecture. Three-dimensional and rapid prototyping techniques show promise with controlling shape on the macroscale, but more advanced techniques are needed to control nanoscale cell-scaffold interactions [17,114]. Furthermore, thermal processing is critical to the relatively unexplored field of tissue engineered structure storage. As suggested by the MATES Interagency Working Group, the future success of tissue engineering will require integrated collaborative efforts across the spectrum of disciplines.

References

[1] Skalak, R., and Fox, C. F., 1988, Tissue Engineering: Proceedings of a Workshop, Granlibakken, Lake Tahoe, CA, Feb. 26–29.

[2] Marcacci, M., Berruto, M., Brocchetta, D., Delcogliano, A., Ghinelli, D., Gobbi, A., Kon, E., Pederzini, L., Rosa, D., Sacchetti, G. L., Stefani, G., and Zanasi, S., 2005, "Articular Cartilage Engineering With Hyalograft (R) C—3-Year Clinical Results," Clin. Orthop. Relat. Res., **435**, pp. 96–105.

[3] MacNeil, S., 2007, "Progress and Opportunities for Tissue-Engineered Skin," Nature (London), **445**(7130), pp. 874–880.

[4] Atala, A., Bauer, S. B., Soker, S., Yoo, J. J., and Retik, A. B., 2006, "Tissue-Engineered Autologous Bladders for Patients Needing Cystoplasty," Lancet, **367**(9518), pp. 1241–1246.

[5] Sacks, M. S., Schoen, F. J., and Mayer, J. E., 2009, "Bioengineering Challenges for Heart Valve Tissue Engineering," Annu. Rev. Biomed. Eng., **11**, pp. 289–313.

[6] National Science and Technology Council, 2007, "Advancing Tissue Science and Engineering: A Multi-Agency Strategic Plan."

[7] Karageorgiou, V., and Kaplan, D., 2005, "Porosity of 3D Biomaterial Scaffolds and Osteogenesis," Biomaterials, **26**(27), pp. 5474–5491.

[8] Langer, R., and Vacanti, J. P., 1993, "Tissue Engineering," Science, **260**(5110), pp. 920–926.

[9] Yang, S., Leong, K.-F., Du, Z., and Chua, C.-K., 2001, "The Design of Scaffolds for Use in Tissue Engineering. Part I. Traditional Factors," Tissue Eng., **7**(6), pp. 679–689.

[10] Habraken, W. J. E. M., Wolke, J. G. C., and Jansen, J. A., 2007, "Ceramic Composites as Matrices and Scaffolds for Drug Delivery in Tissue Engineering," Adv. Drug Delivery Rev., **59**(4–5), pp. 234–248.

[11] Chung, H. J., and Park, T. G., 2007, "Surface Engineered and Drug Releasing Pre-Fabricated Scaffolds for Tissue Engineering," Adv. Drug Delivery Rev., **59**(4–5), pp. 249–262.

[12] Tuzlakoglu, K., and Reis, R. L., 2009, "Biodegradable Polymeric Fiber Structures in Tissue Engineering," Tissue Eng. Part B Rev., **15**(1), pp. 17–27.

[13] Weigel, T., Schinkel, G., and Lendlein, A., 2006, "Design and Preparation of Polymeric Scaffolds for Tissue Engineering," Expert Review of Medical Devices, **3**(6), pp. 835–851.

[14] Drury, J. L., and Mooney, D. J., 2003, "Hydrogels for Tissue Engineering: Scaffold Design Variables and Applications," Biomaterials, **24**(24), pp. 4337–4351.

[15] Kopeček, J., and Yang, J., 2009, "Peptide-Directed Self-Assembly of Hydrogels," Acta Biomater., **5**(3), pp. 805–816.

[16] Sun, W., Darling, A., Starly, B., and Nam, J., 2004, "Computer-Aided Tissue Engineering: Overview, Scope, and Challenges," Biotechnol. Appl. Biochem., **39**, pp. 29–47.

[17] Yang, S., Leong, K.-F., Du, Z., and Chua, C.-K., 2002, "The Design of Scaffolds for Use in Tissue Engineering. Part II. Rapid Prototyping Techniques,"

Tissue Eng., **8**(1), pp. 1–11.
[18] Curtis, A. S., and Wilkinson, C. D., 1998, "Reactions of Cells to Topography," J. Biomater. Sci. Polym. Ed., **9**(12), pp. 1313–1329.
[19] Freed, L. E., Vunjak-Novakovic, G., Biron, R. J., Eagles, D. B., Lesnoy, D. C., Barlow, S. K., and Langer, R., 1994, "Biodegradable Polymer Scaffolds for Tissue Engineering," Biotechnology (N. Y.), **12**(7), pp. 689–693.
[20] Mikos, A. G., Bao, Y., Cima, L. G., Ingber, D. E., Vacanti, J. P., and Langer, R., 1993, "Preparation of Poly(Glycolic Acid) Bonded Fiber Structures for Cell Attachment and Transplantation," J. Biomed. Mater. Res., **27**(2), pp. 183–189.
[21] Kim, B. S., and Mooney, D. J., 1998, "Engineering Smooth Muscle Tissue With a Predefined Structure," J. Biomed. Mater. Res., **41**(2), pp. 322–332.
[22] Gomes, M. E., Holtorf, H. L., Reis, R. L., and Mikos, A. G., 2006, "Influence of the Porosity of Starch-Based Fiber Mesh Scaffolds on the Proliferation and Osteogenic Differentiation of Bone Marrow Stromal Cells Cultured in a Flow Perfusion Bioreactor," Tissue Eng., **12**(4), pp. 801–809.
[23] Gomes, M. E., Sikavitsas, V. I., Behravesh, E., Reis, R. L., and Mikos, A. G., 2003, "Effect of Flow Perfusion on the Osteogenic Differentiation of Bone Marrow Stromal Cells Cultured on Starch-Based Three-Dimensional Scaffolds," J. Biomed. Mater. Res. A, **67**(1), pp. 87–95.
[24] Lee, S. J., Oh, S. H., Liu, J., Soker, S., Atala, A., and Yoo, J. J., 2008, "The Use of Thermal Treatments to Enhance the Mechanical Properties of Electrospun Poly(ε-Caprolactone) Scaffolds," Biomaterials, **29**(10), pp. 1422–1430.
[25] Murugan, R., Huang, Z. M., Yang, F., and Ramakrishna, S., 2007, "Nanofibrous Scaffold Engineering Using Electrospinning," J. Nanosci. Nanotechnol., **7**(12), pp. 4595–4603.
[26] Li, W. J., Laurencin, C. T., Caterson, E. J., Tuan, R. S., and Ko, F. K., 2002, "Electrospun Nanofibrous Structure: A Novel Scaffold for Tissue Engineering," J. Biomed. Mater. Res., **60**(4), pp. 613–621.
[27] Yoshimoto, H., Shin, Y. M., Terai, H., and Vacanti, J. P., 2003, "A Biodegradable Nanofiber Scaffold by Electrospinning and Its Potential for Bone Tissue Engineering," Biomaterials, **24**(12), pp. 2077–2082.
[28] Li, M., Mondrinos, M. J., Gandhi, M. R., Ko, F. K., Weiss, A. S., and Lelkes, P. I., 2005, "Electrospun Protein Fibers as Matrices for Tissue Engineering," Biomaterials, **26**(30), pp. 5999–6008.
[29] Kenawy, E.-R., Layman, J. M., Watkins, J. R., Bowlin, G. L., Matthews, J. A., Simpson, D. G., and Wnek, G. E., 2003, "Electrospinning of Poly(Ethylene-co-Vinyl Alcohol) Fibers," Biomaterials, **24**(6), pp. 907–913.
[30] Wnek, G. E., Carr, M. E., Simpson, D. G., and Bowlin, G. L., 2003, "Electrospinning of Nanofiber Fibrinogen Structures," Nano Lett., **3**(2), pp. 213–216.
[31] Min, B.-M., Lee, G., Kim, S. H., Nam, Y. S., Lee, T. S., and Park, W. H., 2004, "Electrospinning of Silk Fibroin Nanofibers and Its Effect on the Adhesion and Spreading of Normal Human Keratinocytes and Fibroblasts In Vitro," Biomaterials, **25**(7–8), pp. 1289–1297.
[32] Matthews, J. A., Wnek, G. E., Simpson, D. G., and Bowlin, G. L., 2002, "Electrospinning of Collagen Nanofibers," Biomacromolecules, **3**(2), pp. 232–238.
[33] Noh, H. K., Lee, S. W., Kim, J.-M., Oh, J.-E., Kim, K.-H., Chung, C.-P., Choi, S.-C., Park, W. H., and Min, B.-M., 2006, "Electrospinning of Chitin Nanofibers: Degradation Behavior and Cellular Response to Normal Human Keratinocytes and Fibroblasts," Biomaterials, **27**(21), pp. 3934–3944.
[34] Bhattarai, N., Edmondson, D., Veiseh, O., Matsen, F. A., and Zhang, M., 2005, "Electrospun Chitosan-Based Nanofibers and Their Cellular Compatibility," Biomaterials, **26**(31), pp. 6176–6184.
[35] Li, M., Mondrinos, M. J., Chen, X., Gandhi, M. R., Ko, F. K., and Lelkes, P. I., 2006, "Co-Electrospun Poly(Lactide-co-Glycolide), Gelatin, and Elastin Blends for Tissue Engineering Scaffolds," J. Biomed. Mater. Res. Part A, **79**(4), pp. 963–973.
[36] Zhou, H. J., Green, T. B., and Joo, Y. L., 2006, "The Thermal Effects on Electrospinning of Polylactic Acid Melts," Polymer, **47**(21), pp. 7497–7505.
[37] Dalton, P. D., Lleixa Calvet, J., Mourran, A., Klee, D., and Möller, M., 2006, "Melt Electrospinning of Poly-(Ethylene Glycol-Block-Epsilon-Caprolactone)," Biotechnol. J., **1**(9), pp. 998–1006.
[38] Sill, T. J., and von Recum, H. A., 2008, "Electrospinning: Applications in Drug Delivery and Tissue Engineering," Biomaterials, **29**(13), pp. 1989–2006.
[39] Zong, X., Ran, S., Fang, D., Hsiao, B. S., and Chu, B., 2003, "Control of Structure, Morphology, and Property in Electrospun Poly(Glycolide-co-Lactide) Non-Woven Membranes via Post-Draw Treatments," Polymer, **44**(17), pp. 4959–4967.
[40] Xu, C. Y., Inai, R., Kotaki, M., and Ramakrishna, S., 2004, "Aligned Biodegradable Nanofibrous Structure: A Potential Scaffold for Blood Vessel Engineering," Biomaterials, **25**(5), pp. 877–886.
[41] Sun, Z. C., Zussman, E., Yarin, A. L., Wendorff, J. H., and Greiner, A., 2003, "Compound Core-Shell Polymer Nanofibers by Co-Electrospinning," Adv. Mater., **15**(22), pp. 1929–1932.
[42] Kidoaki, S., Kwon, I. K., and Matsuda, T., 2005, "Mesoscopic Spatial Designs of Nano- and Microfiber Meshes for Tissue-Engineering Matrix and Scaffold Based on Newly Devised Multilayering and Mixing Electrospinning Techniques," Biomaterials, **26**(1), pp. 37–46.
[43] Lee, Y. H., Lee, J. H., An, I.-G., Kim, C., Lee, D. S., Lee, Y. K., and Nam, J.-D., 2005, "Electrospun Dual-Porosity Structure and Biodegradation Morphology of Montmorillonite Reinforced PLLA Nanocomposite Scaffolds," Biomaterials, **26**(16), pp. 3165–3172.
[44] Kim, T. G., Chung, H. J., and Park, T. G., 2008, "Macroporous and Nanofibrous Hyaluronic Acid/Collagen Hybrid Scaffold Fabricated by Concurrent Electrospinning and Deposition/Leaching of Salt Particles," Acta Biomater., **4**(6), pp. 1611–1619.
[45] Park, S. H., Kim, T. G., Kim, H. C., Yang, D.-Y., and Park, T. G., 2008, "Development of Dual Scale Scaffolds via Direct Polymer Melt Deposition and Electrospinning for Applications in Tissue Regeneration," Acta Biomater., **4**(5), pp. 1198–1207.
[46] Chua, K.-N., Lim, W.-S., Zhang, P., Lu, H., Wen, J., Ramakrishna, S., Leong, K. W., and Mao, H.-Q., 2005, "Stable Immobilization of Rat Hepatocyte Spheroids on Galactosylated Nanofiber Scaffold," Biomaterials, **26**(15), pp. 2537–2547.
[47] Ma, Z., Kotaki, M., Yong, T., He, W., and Ramakrishna, S., 2005, "Surface Engineering of Electrospun Polyethylene Terephthalate (PET) Nanofibers Towards Development of a New Material for Blood Vessel Engineering," Biomaterials, **26**(15), pp. 2527–2536.
[48] Cima, L. G., Vacanti, J. P., Vacanti, C., Ingber, D., Mooney, D., and Langer, R., 1991, "Tissue Engineering by Cell Transplantation Using Degradable Polymer Substrates," J. Biomech. Eng., **113**(2), pp. 143–151.
[49] Whang, K., Thomas, C. H., Healy, K. E., and Nuber, G., 1995, "A Novel Method to Fabricate Bioabsorbable Scaffolds," Polymer, **36**(4), pp. 837–842.
[50] Whang, K., Healy, K. E., Elenz, D. R., Nam, E. K., Tsai, D. C., Thomas, C. H., Nuber, G. W., Glorieux, F. H., Travers, R., and Sprague, S. M., 1999, "Engineering Bone Regeneration With Bioabsorbable Scaffolds With Novel Microarchitecture," Tissue Eng., **5**(1), pp. 35–51.
[51] Whang, K., Goldstick, T. K., and Healy, K. E., 2000, "A Biodegradable Polymer Scaffold for Delivery of Osteotropic Factors," Biomaterials, **21**(24), pp. 2545–2551.
[52] Baker, S. C., Rohman, G., Southgate, J., and Cameron, N. R., 2009, "The Relationship Between the Mechanical Properties and Cell Behaviour on PLGA and PCL Scaffolds for Bladder Tissue Engineering," Biomaterials, **30**(7), pp. 1321–1328.
[53] Sultana, N., and Wang, M., 2008, "Fabrication of HA/PHBV Composite Scaffolds Through the Emulsion Freezing/Freeze-Drying Process and Characterisation of the Scaffolds," J. Mater. Sci. Mater. Med., **19**(7), pp. 2555–2561.
[54] Spiller, K. L., Laurencin, S. J., Charlton, D., Maher, S. A., and Lowman, A. M., 2008, "Superporous Hydrogels for Cartilage Repair: Evaluation of the Morphological and Mechanical Properties," Acta Biomater., **4**(1), pp. 17–25.
[55] Mikos, A. G., Thorsen, A. J., Czerwonka, L. A., Bao, Y., Langer, R., Winslow, D. N., and Vacanti, J. P., 1994, "Preparation and Characterization of Poly(L-Lactic Acid) Foams," Polymer, **35**(5), pp. 1068–1077.
[56] Mikos, A. G., Sarakinos, G., Leite, S. M., Vacant, J. P., and Langer, R., 1993, "Laminated Three-Dimensional Biodegradable Foams for Use in Tissue Engineering," Biomaterials, **14**(5), pp. 323–330.
[57] Shin, M., Abukawa, H., Troulis, M. J., and Vacanti, J. P., 2008, "Development of a Biodegradable Scaffold With Interconnected Pores by Heat Fusion and Its Application to Bone Tissue Engineering," J. Biomed. Mater. Res. Part A, **84A**(3), pp. 702–709.
[58] Lu, L., Peter, S. J., Lyman, M. D., Lai, H.-L., Leite, S. M., Tamada, J. A., Uyama, S., Vacanti, J. P., Langer, R., and Mikos, A. G., 2000, "In Vitro and In Vivo Degradation of Porous Poly(DL-Lactic-*co*-Glycolic Acid) Foams," Biomaterials, **21**(18), pp. 1837–1845.
[59] Cheng, Z. Y., and Teoh, S. H., 2004, "Surface Modification of Ultra Thin Poly (Epsilon-Caprolactone) Films Using Acrylic Acid and Collagen," Biomaterials, **25**(11), pp. 1991–2001.
[60] Wake, M. C., Gupta, P. K., and Mikos, A. G., 1996, "Fabrication of Pliable Biodegradable Polymer Foams to Engineer Soft Tissues," Cell Transplant., **5**(4), pp. 465–473.
[61] Vaquette, C., Frochot, C., Rahouadj, R., and Wang, X., 2008, "An Innovative Method to Obtain Porous PLLA Scaffolds With Highly Spherical and Interconnected Pores," J. Biomed. Mater. Res., Part B: Appl. Biomater., **86B**(1), pp. 9–17.
[62] Ma, Z., Gao, C., Gong, Y., and Shen, J., 2003, "Paraffin Spheres as Porogen to Fabricate Poly(L-Lactic Acid) Scaffolds With Improved Cytocompatibility for Cartilage Tissue Engineering," J. Biomed. Mater. Res., Part B: Appl. Biomater., **67B**(1), pp. 610–617.
[63] Thomson, R. C., Yaszemski, M. J., Powers, J. M., and Mikos, A. G., 1996, "Fabrication of Biodegradable Polymer Scaffolds to Engineer Trabecular Bone," J. Biomater. Sci. Polym. Ed., **7**(1), pp. 23–38.
[64] Zhang, P., Hong, Z., Yu, T., Chen, X., and Jing, X., 2009, "*In Vivo* Mineralization and Osteogenesis of Nanocomposite Scaffold of Poly(Lactide-*co*-Glycolide) and Hydroxyapatite Surface-Grafted With Poly(L-Lactide)," Biomaterials, **30**(1), pp. 58–70.
[65] Murphy, W. L., Dennis, R. G., Kileny, J. L., and Mooney, D. J., 2002, "Salt Fusion: An Approach to Improve Pore Interconnectivity Within Tissue Engineering Scaffolds," Tissue Eng., **8**(1), pp. 43–52.
[66] Ma, P. X., and Choi, J. W., 2001, "Biodegradable Polymer Scaffolds With Well-Defined Interconnected Spherical Pore Network," Tissue Eng., **7**(1), pp. 23–33.
[67] Gross, K. A., and Rodriguez-Lorenzo, L. M., 2004, "Biodegradable Composite Scaffolds With an Interconnected Spherical Network for Bone Tissue Engineering," Biomaterials, **25**(20), pp. 4955–4962.
[68] Pamula, E., Filova, E., Bacakova, L., Lisa, V., and Adamczyk, D., 2009, "Resorbable Polymeric Scaffolds for Bone Tissue Engineering: The Influence of Their Microstructure on the Growth of Human Osteoblast-Like Mg 63 Cells," J. Biomed. Mater. Res. Part A, **89A**(2), pp. 432–443.
[69] Widmer, M. S., Gupta, P. K., Lu, L. C., Meszlenyi, R. K., Evans, G. R. D., Brandt, K., Savel, T., Gurlek, A., Patrick, C. W., and Mikos, A. G., 1998, "Manufacture of Porous Biodegradable Polymer Conduits by an Extrusion Process for Guided Tissue Regeneration," Biomaterials, **19**(21), pp. 1945–1955.

[70] Nam, Y. S., Yoon, J. J., and Park, T. G., 2000, "A Novel Fabrication Method of Macroporous Biodegradable Polymer Scaffolds Using Gas Foaming Salt as a Porogen Additive," J. Biomed. Mater. Res., **53**(1), pp. 1–7.
[71] Yoon, J. J., and Park, T. G., 2001, "Degradation Behaviors of Biodegradable Macroporous Scaffolds Prepared by Gas Foaming of Effervescent Salts," J. Biomed. Mater. Res., **55**(3), pp. 401–408.
[72] Yoo, H. S., Lee, E. A., Yoon, J. J., and Park, T. G., 2005, "Hyaluronic Acid Modified Biodegradable Scaffolds for Cartilage Tissue Engineering," Biomaterials, **26**(14), pp. 1925–1933.
[73] Ju, Y. M., Park, K., Son, J. S., Kim, J.-J., Rhie, J.-W., and Han, D. K., 2008, "Beneficial Effect of Hydrophilized Porous Polymer Scaffolds in Tissue-Engineered Cartilage Formation," J. Biomed. Mater. Res., Part B: Appl. Biomater., **85B**(1), pp. 252–260.
[74] Kim, T. K., Yoon, J. J., Lee, D. S., and Park, T. G., 2006, "Gas Foamed Open Porous Biodegradable Polymeric Microspheres," Biomaterials, **27**(2), pp. 152–159.
[75] Almirall, A., Larrecq, G., Delgado, J. A., Martinez, S., Planell, J. A., and Ginebra, M. P., 2004, "Fabrication of Low Temperature Macroporous Hydroxyapatite Scaffolds by Foaming and Hydrolysis of an α-TCP Paste," Biomaterials, **25**(17), pp. 3671–3680.
[76] Kim, C. W., Talac, R., Lu, L., Moore, M. J., Currier, B. L., and Yaszemski, M. J., 2008, "Characterization of Porous Injectable Poly-(Propylene Fumarate)-Based Bone Graft Substitute," J. Biomed. Mater. Res. Part A, **85A**(4), pp. 1114–1119.
[77] Goel, S. K., and Beckman, E. J., 1994, "Generation of Microcellular Polymeric Foams Using Supercritical Carbon Dioxide. I: Effect of Pressure and Temperature on Nucleation," Polym. Eng. Sci., **34**(14), pp. 1137–1147.
[78] Goel, S. K., and Beckman, E. J., 1994, "Generation of Microcellular Polymeric Foams Using Supercritical Carbon Dioxide. II: Cell Growth and Skin Formation," Polym. Eng. Sci., **34**(14), pp. 1148–1156.
[79] Mooney, D. J., Baldwin, D. F., Suh, N. P., Vacanti, J. P., and Langer, R., 1996, "Novel Approach to Fabricate Porous Sponges of Poly(D,L-Lactic-co-Glycolic Acid) Without the Use of Organic Solvents," Biomaterials, **17**(14), pp. 1417–1422.
[80] Singh, L., Kumar, V., and Ratner, B. D., 2004, "Generation of Porous Microcellular 85/15 Poly(DL-Lactide-co-Glycolide) Foams for Biomedical Applications," Biomaterials, **25**(13), pp. 2611–2617.
[81] Vega-González, A., Subra-Paternault, P., López-Periago, A. M., García-González, C. A., and Domingo, C., 2008, "Supercritical CO_2 Antisolvent Precipitation of Polymer Networks of l-PLA, PMMA, and PMMA/PCL Blends for Biomedical Applications," Eur. Polym. J., **44**(4), pp. 1081–1094.
[82] Sheridan, M. H., Shea, L. D., Peters, M. C., and Mooney, D. J., 2000, "Bioadsorbable Polymer Scaffolds for Tissue Engineering Capable of Sustained Growth Factor Delivery," J. Controlled Release, **64**(1–3), pp. 91–102.
[83] Barry, J. J. A., Silva, M. M. C. G., Cartmell, S. H., Guldberg, R. E., Scotchford, C. A., and Howdle, S. M., 2006, "Porous Methacrylate Tissue Engineering Scaffolds: Using Carbon Dioxide to Control Porosity and Interconnectivity," J. Mater. Sci., **41**(13), pp. 4197–4204.
[84] Mathieu, L. M., Mueller, T. L., Bourban, P. E., Pioletti, D. P., Muller, R., and Manson, J. A. E., 2006, "Architecture and Properties of Anisotropic Polymer Composite Scaffolds for Bone Tissue Engineering," Biomaterials, **27**(6), pp. 905–916.
[85] Salerno, A., Netti, P. A., Di Maio, E., and Iannace, S., 2009, "Engineering of Foamed Structures for Biomedical Application," J. Cell. Plast., **45**(2), pp. 103–117.
[86] Harris, L. D., Kim, B. S., and Mooney, D. J., 1998, "Open Pore Biodegradable Matrices Formed With Gas Foaming," J. Biomed. Mater. Res., **42**(3), pp. 396–402.
[87] Petri Aronin, C. E., Cooper, J. A., Sefcik, L. S., Tholpady, S. S., Ogle, R. C., and Botchwey, E. A., 2008, "Osteogenic Differentiation of Dura Mater Stem Cells Cultured In Vitro on Three-Dimensional Porous Scaffolds of Poly(ε-Caprolactone) Fabricated via Co-Extrusion and Gas Foaming," Acta Biomater., **4**(5), pp. 1187–1197.
[88] Barry, J. J. A., Evseev, A. V., Markov, M. A., Upton, C. E., Scotchford, C. A., Popov, V. K., and Howdle, S. M., 2008, "In Vitro Study of Hydroxyapatite-Based Photocurable Polymer Composites Prepared by Laser Stereolithography and Supercritical Fluid Extraction," Acta Biomater., **4**(6), pp. 1603–1610.
[89] Yang, X. B. B., Whitaker, M. J., Sebald, W., Clarke, N., Howdle, S. M., Shakesheff, K. M., and Oreffo, R. O. C., 2004, "Human Osteoprogenitor Bone Formation Using Encapsulated Bone Morphogenetic Protein 2 in Porous Polymer Scaffolds," Tissue Eng., **10**(7–8), pp. 1037–1045.
[90] Kanczler, J. M., Barry, J., Ginty, P., Howdle, S. M., Shakesheff, K. M., and Oreffo, R. O. C., 2007, "Supercritical Carbon Dioxide Generated Vascular Endothelial Growth Factor Encapsulated Poly(DL-Lactic Acid) Scaffolds Induce Angiogenesis In Vitro," Biochem. Biophys. Res. Commun., **352**(1), pp. 135–141.
[91] Duarte, A. R. C., Mano, J. F., and Reis, R. L., 2009, "Preparation of Chitosan Scaffolds Loaded With Dexamethasone for Tissue Engineering Applications Using Supercritical Fluid Technology," Eur. Polym. J., **45**(1), pp. 141–148.
[92] Vezzu, K., Betto, V., and Elvassore, N., 2008, "High-Pressure Gas-Assisted Absorption of Protein Within Biopolymeric Micro-Patterned Membrane," Biochem. Eng. J., **40**(2), pp. 241–248.
[93] Montjovent, M., Mathieu, L., Hinz, B., Applegate, L. L., Bourban, P., Zambelli, P., Manson, J., and Pioletti, D. P., 2005, "Human Fetal Bone Cells Associated With Bioresorbable PLA Composite Scaffolds for Tissue Engineering," Bone, **36**, pp. S278–S279.
[94] Georgiou, G., Mathieu, L., Pioletti, D. P., Bourban, P. E., Manson, J.-A. E., Knowles, J. C., and Nazhat, S. N., 2007, "Polylactic Acid-Phosphate Glass Composite Foams as Scaffolds for Bone Tissue Engineering," J. Biomed. Mater. Res., Part B: Appl. Biomater., **80B**(2), pp. 322–331.
[95] Kim, S. S., Park, M. S., Jeon, O., Choi, C. Y., and Kim, B. S., 2006, "Poly(Lactide-*co*-Glycolide)/Hydroxyapatite Composite Scaffolds for Bone Tissue Engineering," Biomaterials, **27**(8), pp. 1399–1409.
[96] Wang, H., and Li, W., 2008, "Selective Ultrasonic Foaming of Polymer for Biomedical Applications," ASME J. Manuf. Sci. Eng., **130**(2), pp. 021004.
[97] Mather, M. L., Crowe, J. A., Morgan, S. P., White, L. J., Kalashnikov, A. N., Ivchenko, V. G., Howdle, S. M., and Shakesheff, K. M., 2008, "Ultrasonic Monitoring of Foamed Polymeric Tissue Scaffold Fabrication," J. Mater. Sci. Mater. Med., **19**(9), pp. 3071–3080.
[98] Lo, H., Kadiyala, S., Guggino, S. E., and Leong, K. W., 1996, "Poly(L-Lactic Acid) Foams With Cell Seeding and Controlled-Release Capacity," J. Biomed. Mater. Res., **30**(4), pp. 475–484.
[99] Guan, J. J., Fujimoto, K. L., Sacks, M. S., and Wagner, W. R., 2005, "Preparation and Characterization of Highly Porous, Biodegradable Polyurethane Scaffolds for Soft Tissue Applications," Biomaterials, **26**(18), pp. 3961–3971.
[100] Yang, F., Qu, X., Cui, W. J., Bei, J. Z., Yu, F. Y., Lu, S. B., and Wang, S. G., 2006, "Manufacturing and Morphology Structure of Polylactide-Type Microtubules Orientation-Structured Scaffolds," Biomaterials, **27**(28), pp. 4923–4933.
[101] Nam, Y. S., and Park, T. G., 1999, "Porous Biodegradable Polymeric Scaffolds Prepared by Thermally Induced Phase Separation," J. Biomed. Mater. Res., **47**(1), pp. 8–17.
[102] Schugens, Ch., Maquet, V., Grandfils, C., Jerome, R., and Teyssie, Ph., 1996, "Biodegradable and Macroporous Polylactide Implants for Cell Transplantation. 1. Preparation of Macroporous Polylactide Supports by Solid-Liquid Phase Separation," Polymer, **37**(6), pp. 1027–1038.
[103] Schugens, Ch., Maquet, V., Grandfils, Ch., Jerome, R., and Teyssie, Ph., 1996, "Polylactide Macroporous Biodegradable Implants for Cell Transplantation. II. Preparation of Polylactide Foams by Liquid-Liquid Phase Separation," J. Biomed. Mater. Res., **30**(4), pp. 449–461.
[104] Nam, Y. S., and Park, T. G., 1999, "Biodegradable Polymeric Microcellular Foams by Modified Thermally Induced Phase Separation Method," Biomaterials, **20**(19), pp. 1783–1790.
[105] Carfi Pavia, F., La Carrubba, V., Piccarolo, S., and Brucato, V., 2008, "Polymeric Scaffolds Prepared via Thermally Induced Phase Separation: Tuning of Structure and Morphology," J. Biomed. Mater. Res. Part A, **86A**(2), pp. 459–466.
[106] Ho, M.-H., Kuo, P.-Y., Hsieh, H.-J., Hsien, T.-Y., Hou, L.-T., Lai, J.-Y., and Wang, D.-M., 2004, "Preparation of Porous Scaffolds by Using Freeze-Extraction and Freeze-Gelation Methods," Biomaterials, **25**(1), pp. 129–138.
[107] Zhang, R., and Ma, P. X., 1999, "Poly(α-Hydroxyl Acids)/Hydroxyapatite Porous Composites for Bone-Tissue Engineering. I. Preparation and Morphology," J. Biomed. Mater. Res., **44**(4), pp. 446–455.
[108] Wei, G. B., and Ma, P. X., 2004, "Structure and Properties of Nano-Hydroxyapatite/Polymer Composite Scaffolds for Bone Tissue Engineering," Biomaterials, **25**(19), pp. 4749–4757.
[109] Li, Z. S., Ramay, H. R., Hauch, K. D., Xiao, D. M., and Zhang, M. Q., 2005, "Chitosan-Alginate Hybrid Scaffolds for Bone Tissue Engineering," Biomaterials, **26**(18), pp. 3919–3928.
[110] Chen, V. J., and Ma, P. X., 2004, "Nano-Fibrous Poly(L-Lactic Acid) Scaffolds With Interconnected Spherical Macropores," Biomaterials, **25**(11), pp. 2065–2073.
[111] Liu, X., Smith, L. A., Hu, J., and Ma, P. X., 2009, "Biomimetic Nanofibrous Gelatin/Apatite Composite Scaffolds for Bone Tissue Engineering," Biomaterials, **30**(12), pp. 2252–2258.
[112] Chen, V. J., Smith, L. A., and Ma, P. X., 2006, "Bone Regeneration on Computer-Designed Nano-Fibrous Scaffolds," Biomaterials, **27**(21), pp. 3973–3979.
[113] Ao, Q., Wang, A., Cao, W., Zhang, L., Kong, L., He, Q., Gong, Y., and Zhang, X., 2006, "Manufacture of Multimicrotubule Chitosan Nerve Conduits With Novel Molds and Characterization In Vitro," J. Biomed. Mater. Res. Part A, **77A**(1), pp. 11–18.
[114] Tsang, V. L., and Bhatia, S. N., 2004, "Three-Dimensional Tissue Fabrication," Adv. Drug Delivery Rev., **56**(11), pp. 1635–1647.

Titania Nanotubes: Novel Nanostructures for Improved Osseointegration

Nathan Swami
Department of Electrical Engineering,
University of Virginia,
Charlottesville, VA 22904-4743

Zhanwu Cui
Department of Orthopaedic Surgery,
University of Connecticut Health Center,
Farmington, CT 06030

Lakshmi S. Nair[1]
Assistant Professor
Department of Orthopaedic Surgery,
University of Connecticut Health Center,
Farmington, CT 06030;
Department of Chemical, Materials and Biomolecular Engineering,
University of Connecticut,
Storrs, CT 06269
e-mail: nair@uchc.edu

Nanostructured one dimensional titanium oxides such as nanotubes and nanowires have raised interest lately due to their unique electronic and optical properties. These materials also have shown significant potential as biomaterials because of their ability to modulate protein and cellular interactions. In this review, synthesis and modification of titania nanotubes have been discussed with emphasis on electrochemical synthesis and wet chemical synthesis and their heat treatment of resulting titania nanotubes. The biomedical applications of titania nanotubes were subsequently discussed in detail with a focus on osseointegration. The areas discussed are cell responses to titania nanotubes, effects of titania nanotubes on stem cell proliferation and differentiation, titania nanotubes as drug delivery vehicles, surface modification of titania nanotubes, and in vivo studies using titania nanotubes. It is concluded that the in vitro and in vivo study clearly demonstrates the efficacy of titania nanotube in enhancing osseointegration of orthopedic implants and much of the future work is expected to focus on improving implant functions by modulating the physical and chemical properties of the nanotubes and by locally delivering bioactive molecules in a sustained manner.
[DOI: 10.1115/1.4002465]

Keywords: titania nanotube, osseointegration, electrochemical synthesis, wet chemical synthesis

1 Introduction

The advancements in nanobiotechnology are revolutionizing our capability to understand biological intricacies and resolve biological and medical problems by developing subtle biomimetic techniques. Studies have shown that by mimicking the complex hierarchal architecture and functions of natural tissue, ideal tissue substitutes can be engineered [1].

In the native setting, the organization of cells and hence the properties of the tissues are found to be highly dependent on the architecture of the extracellular matrix (ECM), which has a complex hierarchical structure with spatial and temporal levels of organization that span several orders of magnitude (nanometer to centimeter scale). Tissue engineers attempt to develop tissue substitutes that can sustain the functionality during regeneration and eventually integrate into the host tissue [1]. Engineered tissue can be developed either in vivo by stimulating the body's regenerating ability using biomaterials, cells, and growth factors or ex vivo by culturing cells on suitable biomaterials with/without bioactive factors.

Early attempts during the latter half of the 20th century were focused on identifying the most appropriate materials and fabrication techniques to develop porous structures to grow cells in three dimensions for tissue organization [2]. Along with the developments in biomaterial design, synthesis, and fabrication, significant strides have been made in identifying appropriate cell sources including stem cells and the effect of various biological factors on cellular behavior and tissue organization. Even though many of these biomaterial structures showed close resemblances to the macroscopic properties of native tissue, they are far less than optimal to be used for regenerating tissues in an ideal and reproducible manner. In short, most of the current macro- or microfabrication techniques are unable to create sophisticated structures that could mimic the subtleties of the ECM. Recent paradigm shifts from these fabrication techniques to nanoscience enabled techniques have significantly enhanced our ability to design and develop better biomimetic structures [2]. Ample evidence now exists, which show that the nanoscale topography of the biomaterials is a critical role in modulating cell responses [2]. The unique feature of the nanotechnological approach is that it enables the consideration of spatial and temporal levels of organization, thereby forming an excellent technique to develop biomimetic hierarchical structures.

The importance of nanostructures as biomimetic scaffolds for bone regeneration arises from the structure of bone itself. Bone can be considered as a nanostructured composite matrix with an organic phase composed mainly of proteins and an inorganic phase composed of calcium phosphate mineral. The nanostructure of the bone arises from these building blocks: the major protein in bone is type-I collagen ($\sim$90%), a linear molecule 300 nm in length and 0.5 nm in diameter; the inorganic phase is composed of hydroxyapatite crystals, the thickness and length of which can range from 2–5 nm and 20–80 nm, respectively [3]. This unique nanostructure of the bone led to the hypothesis that osteoblast and osteoclast cell responses can be favorably modulated by scaffold surface nanofeatures.

Several biomimetic nanostructured scaffolds have been developed from biodegradable polymers or composites for bone tissue engineering applications. The most extensively studied structure includes nanofibers developed by the process of electrospinning and self-assembly. The techniques to develop these nanostructures and their potential in modulating the cell response have been reviewed [4].

These recent developments have significantly influenced the field of orthopedic and dental implant science, which mainly uses nondegradable metallic load bearing scaffolds for bone replacing/contacting applications. Titanium and its alloys have long been recognized as an ideal orthopedic implant material due to their osteocompatibility and bone bonding ability. The ultimate goal of these orthopedic implants is to obtain a life-long secure anchoring of the implant in the native surrounding bone. This calls for significant osseointegration, which requires the ability of the implant surface to control cell behavior (including osteoblast, osteoclast, and stem cells) in a manner that mimics active cell sensing and remodeling of tissue in vivo. Several crucial challenges still exist to develop completely osseointegrated implants that guarantee long term performance. Recent statistics show that approximately

[1]Corresponding author.

Manuscript received July 7, 2009; final manuscript received April 1, 2010; published online November 16, 2010. Assoc. Editor: Wilson K. S. Chiu.

20% of the hip replacement surgeries performed annually is reversion surgeries [5]. The less than optimal clinical performance of these implants has been attributed to the poor osseointegration leading to aseptic loosening of the implant, fibrous tissue formation at the implant-bone interface, micromotion at the bone-implant interface, and wear debris formation [6]. Implant surface that can promote early implant-bone integration by enhancing osteoblast performance to facilitate bone formation at the interface and thereby allowing a continuous transition from the tissue to implant surface is critical to achieve osseointegration.

A wide range of surface modification approaches has been investigated to improve the osseointegration of titanium based orthopedic implants [7]. These include machining, grinding, polishing, and blasting, chemical methods such as acid and alkali etching and anodization, and biological methods involve coating the surface with various bioactive materials and molecules [8]. The most extensively investigated biological method includes calcium phosphate or hydroxyapatite coating of the implant surface. Despite the proven efficacy of calcium phosphate coatings, the large variability in the biological response of the coating processes is still a major concern [9]. Other biological modifications include coating the implant surface with various bioactive molecules such as proteins, enzymes, and peptides [10].

The developments in nano-/microtechnologies led to a renewed increase in using implant surface nano-/microfeatures for favorably modulating osseointegration. For example, a recent study indicated a 20–30% increase in osteoblast adhesion on nanograined sintered ceramics on alumina or titania large grain size ceramics [11]. Due to the high osteocompatibility of titania, a variety of titania nanostructures are currently been developed as potential nanostructures to modify implant surface for better osseointegration.

The purpose of this review is to consider the recent literature in terms of the altered osseointegration in response to titania nanotubes—a unique nanostructure currently being evaluated for orthopedic and dental applications. Specifically, the effects of the synthesis parameters on the structure of the nanotubes including the crystallinity, length, and diameter of the titania nanotubes, their ability to modulate cellular responses, and in vivo osseointegration have been discussed.

2 Titania Nanotubes

Nanostructured one dimensional titanium oxides such as nanotubes and nanowires have raised interest lately due to their unique electronic and optical properties. Apart from their applications in the fields of solar cells, photocatalysis, photoelectrolysis, and sensors, these nanomaterials have shown significant potential as biomaterials due to their ability to modulate protein and cellular interactions [12].

2.1 Synthesis and Modification of Titania Nanotubes. Several methods are currently been investigated to fabricate titania nanotubes including the assisted-template method [13], the sol-gel method [14], the electrochemical anodic oxidation method [15–17], and hydrothermal treatment [18–21].

For assisted-template method, aluminum oxide nanoporous membrane with uniform diameter and length is usually used as a template. By using different templates, the scale of the titania nanotubes can be controlled. However, this method has the disadvantage that impurities cannot be completely removed [13].

In the sol-gel method, sol-gel-derived fine TiO_2-based powders were treated chemically (e.g., for 20 h at 110°C) with a 5–10*M* NaOH aqueous solution. As a result, needle-shaped TiO_2 crystals (anatase phase) with a diameter of ≈8 nm and a length of ≈100 nm were obtained [14]. Transmission electron microgram confirmed that this needle-shaped product has a tube structure with a large specific surface area of 400 $m^2\ g^{-1}$ [14].

The electrochemical anodic oxidation method is capable of generating highly ordered nanotube arrays and the dimensions of the nanotube can be precisely controlled [15–17]. Electrolyte composition being used in this method plays a critical role in determining the nanotube nanoarchitecture. Electrolyte composition and its pH determine both the rate of nanotube formation and the rate at which the resultant oxide is dissolved.

Regarding hydrothermal treatment method, it is capable of fabricating titania nanotubes with good crystallinity and pure phase structure [18–21]. Although there is still debate on crystal structure of TiO_2-based nanotube, the chemical composition of $Na_xH_{2-x}Ti_3O_7$ and $Na_xH_{2-x}Ti_2O_4(OH)$ groups were more acceptable than other structures. Fabrication factors, such as applied temperature, treatment time, the type of alkali solution, and the Ti precursor, are considered as the predominant factors in titania nanotube fabrication in hydrothermal treatment. More detailed information on electrochemical synthesis and hydrothermal treatment and their heat treatment will be given in the subsequent sections.

2.1.1 Electrochemical Synthesis and Heat Treatment of Titania Nanotubes

2.1.1.1 Electrochemical synthesis of titania nanotubes. Extensive research has gone into developing titania nanotubes of various structures and crystallinity. One of the most extensively investigated fabrication methods to form titania nanotube arrays is the electrochemical anodization method. Anodization is a commonly used surface modification technique to produce protective oxide layers on metals such as titanium. Anodization has also been used to create biocompatible microporous titanium oxide coatings on implant surface for orthopedic and dental applications. Recent studies demonstrate the feasibility of achieving ordered titania nanotube layers with controlled diameters by anodization of titanium in adequate electrolytes [22]. This combined with a hydrothermal treatment can be used to deposit hydroxyapatite on titanium surfaces to improve osseointegration [23].

High-quality nanotubular TiO_2 arrays can be prepared by electrochemical anodization of titanium sheets or films. Controlling electrochemical oxidation versus electrochemical etching of the oxide allows for the formation of nanotubes [24]. The advantages of this approach versus other methods of titania nanostructure synthesis are that nanotubes can be formed by electrochemical anodization over relatively large areas using samples of a variety of shapes, and the morphology of the nanotubes can be controlled through the electrolyte chemistry, voltage, and stirring. Electrolytes include aqueous acidic [25] and neutral fluoride solutions [26], as well as organic solutions [27,28]. Organic electrolytes may perhaps be ideal for biomedical applications, since they permit the growth of longer tubes up to several microns, the close control of wall thickness and the ability to control adhesion among tubes. Figure 1 shows some examples of nanotubes synthesized within our laboratories.

2.1.1.2 Heat treatment of titania nanotubes prepared by electrochemical synthesis. The as-synthesized nanotubes are amorphous, and annealing is required in order to crystallize them. Heat treatment has been shown to affect the crystalline structure of the resulting titania nanotube. Anatase or rutile structures can be obtained by tuning the annealing temperatures. Varghese et al. [16] investigated the stability of the titania nanotube arrays at different temperatures in dry oxygen as well as dry and humid argon environment. The study has shown that regardless of the ambient, the titania nanotubes crystallized in the anatase phase at about 280°C [16]. The anatase phase crystallinities formed in the tube walls can be transformed completely to rutile phase at 570°C in humid argon and at 620°C in a dry environment [16]. Other than the crystallinity, the annealing temperature has also shown to affect nanotube wall thickness and inner diameter. In the same study, it was found that when annealed in dry argon at 580°C for 3 h, the average inner diameter and the wall thickness varied by 10% and 20%. Mor et al. [29] reported the synthesis of highly ordered

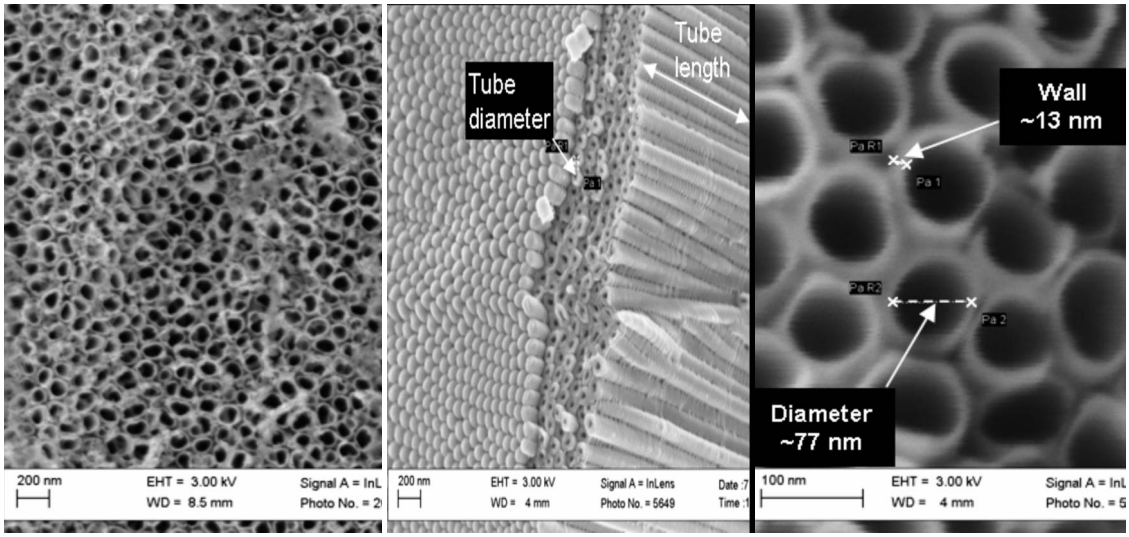

Fig. 1 Titania nanotube structures synthesized in our laboratory. Left: top view of a sample anodized in 1*M* H_2SO_4 +0.15*M* HF at 20 V; center: bottom/side view of a sample anodized in 0.5% NH_4F in glycol ethylene at 30 V; right: top view close up of the sample at center.

titania nanotube arrays by anodization of titanium thin film and found that only anatase phase can be obtained upon annealing at 500°C. However, it has been reported that nanotubes with both rutile and anatase phases can be created on films with a metal layer underneath the nanotubes and annealed above 430°C in an oxygen environment [29]. Apart from these, the anodization bath temperature has been shown to have significant effects on the wall thickness and length of the fabricated titania nanotubes [30]. Recently, a technique has been developed to produce crystalline nanotubes by anodization at 80–120°C, avoiding the postsynthesis annealing, which is claimed to degrade charge transport through the sample substrate [31].

These studies also show that the heat treatment has significant effects on modulating the properties of titania nanotubes and particularly has effects on controlling the crystallinity, length, and wall thickness of the tubes [16,29,30].

2.1.2 Wet Chemical Synthesis and Heat Treatment of Titania Nanotubes

2.1.2.1 Wet chemical synthesis of titania nanotubes. Hydrothermal synthesis of nanotubular titania occurs due to the formation of nanosheets with an increasing tendency of curling, by the reaction between sodium hydroxide and TiO_2 at temperatures between 100°C and 300°C [18]. This method has been applied to grow nanotubes of diameter down to 8 nm with various crystal structures, such as tetragonal anatase, as well as monoclinic and orthorhombic phases of sodium and hydro-titanate phases. While the nanotubes formed by the hydrothermal method are of extremely small size and a diverse range of modifications can be easily achieved, the chief disadvantages include the requirement for long reaction times, the need for sodium hydroxide, which can lead to excessive intercalation, and that the obtained nanotubes are in powder form of random alignment [32].

2.1.3 Heat Treatment of Titania Nanotubes Prepared by Wet Chemical Synthesis. The heat treatment process can influence not only the synthesis of titania nanotube but also the crystallization after synthesis. The morphology, size, and other properties of nanotube TiO_2 formed by the wet chemical method are highly dependent on the temperature, treatment time, the type of alkali solution, and the titanium precursor used during hydrothermal treatment. For instance, studies have established that the amount and length of nanotube TiO_2 gradually increases with applied temperatures (100–200°C), with the synthesis at 150°C giving TiO_2 nanotube of the largest specific surface area and internal nanotube diameter [33]. Poudel et al. [34] reported hydrothermal synthesis of titania nanotube with an outside diameter of 9 nm, wall thickness of about 2.5 nm, and length of about 600 nm and found that the anatase phase is stable for up to 700°C and the rutile phase starts to crystallize at 800°C. The annealing temperature has also shown to affect the morphology and chemical composition of the nanotubes. Thus, the morphology changed from nanotube to nanowire at the annealing temperature of 650°C [34]. If sodium impurities are present, sodium titanate are formed above 600°C [34]. Yoshida et al. investigated the effects of heat treatment on titania nanotube structure fabricated by the hydrothermal method in NaOH, and it was found that the nanotubes are stable below 300°C and around 350°C some nanotubes begin to break into particles of anatase phase, while other nanotubes remain as nanotubes in the presence of excess sodium. This implies that the residual sodium can stabilize the nanostructure. However, at higher temperatures, the particles changed into rutile phase and solid nanorods of $Na_2Ti_6O_{13}$ were formed [35]. Other than the crystallinity, the heat treatment of titania nanotubes also affects other properties, such as the pore volume, and the surface area. Tsai and Teng [36] demonstrated that the surface area of the nanotube increases with the treatment temperature and then decreases with a further temperature increase. The maximum pore volume and surface area for the nanotube TiO_2 occurred at 130°C [37]. Yu et al. [37] reported that the high pore volume and specific surface area of titania nanotube surfaces can be maintained until 600°C, while the pore size of the nanotubes increases to 44.8 nm at 700°C and then decreases to 8.2 nm at 800°C. This has been attributed to the collapse of the nanostructure at higher calcinations temperatures [37]. Further attempts were also made to optimize the crystallization process of the nanotubes using an 86% filling fraction and a 0.1*N* hydrochloric acid wash [35]. The shape of the nanostructures is determined by a variety of factors including sodium hydroxide (NaOH) concentration (which affects sodium intercalation), temperature, and the type of precursors used to synthesize the titania. For instance, nanofiber titania composed of the $H_2Ti_3O_7$ phase was obtained when amorphous. TiO_2 was used as the precursor, whereas nanoribbons assigned to the $H_2Ti_5O_{11}(H_2O)$ phase occurred at the NaOH concentration of 5–15*N* under the temperature range 180–250°C, and nanowires assigned to the $K_2Ti_8O_7$

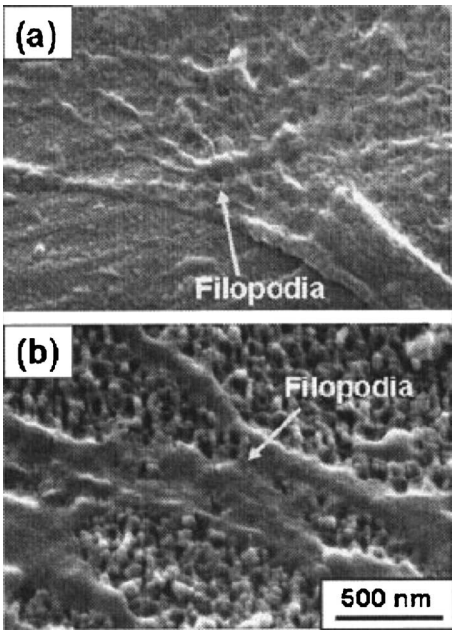

Fig. 2 SEM micrographs showing osteoblast filopodia growth on (*a*) Ti surface (after 12 h) and (*b*) TiO_2 nanotube surface (after 2 h) (reprinted with permission of John Wiley & Sons, Inc.) [42]

phase formed with KOH or LiOH treatments [38]. Following hydrothermal synthesis, thermal post-treatments above 600°C were usually required to form crystalline titania nanostructures [39]. Given the ease of formation of a diverse group of sub-10 nm titania nanostructures by hydrothermal treatments, more systematic studies on correlating synthesis and treatment conditions to formation and functionality are necessary to enable their applications within biomedicine.

2.2 Biomedical Applications of Titania Nanotubes. While a majority of the research involving titania nanotubes has been toward their applications with dye-sensitized solar or photoelectrochemical cells, recent studies suggest their possible biomedical applications. The feasibility of developing biocompatible ordered titania layers with well controllable sizes in the nanometer range makes them potential substrates for studying cell responses to nanoscale features.

2.2.1 Cell Responses to Titania Nanotubes. Earlier studies using substrates fabricated by various micro- and nanofabrication methods have demonstrated the efficacy of surface submicron features in modulating cellular responses [4]. Extensive research has gone toward understanding nano- and microsurface features on musculoskeletal cell responses making nano-/microsurface modification an interesting approach for developing improved implants, as well as scaffolds for musculoskeletal tissue regeneration [4].

The potential of titania nanotube modified surfaces for orthopedic implant application was demonstrated by a series of recent studies. Oh et al. [40] demonstrated significantly accelerated preosteoblast cell growth on aligned nanotubes in comparison to unmodified titanium. The modified surfaces with vertically aligned yet laterally spaced nanotubes were fabricated using the anodization method. The nanotubes have an average outer diameter of about 100 nm and an inner diameter of about 70 nm, wall thickness of about 15 nm, and height of about 250 nm [40]. The study showed that the adhesion and propagation of the osteoblast cells are significantly improved by the presence of nanotube topography. Moreover, as indicated in Fig. 2, the filopodia of the cells grew into the nanotube pores to form an interlocked nanostructure indicating the possibility of developing improved osseointegrated implants via nanotube surface modification [40].

Yao et al. [41] investigated the mechanism of osteoblast adhesion and proliferation on titania nanotube structures and compared the cell responses to unmodified titanium. The nanotube modified surfaces showed ~2.5–4.3-fold increase in surface roughness over unanodized substrates. Using these substrates, the study demonstrated that the increase in surface nanoroughness corresponds to increase in osteoblast adhesion. This has been attributed to several reasons. Nanostructural morphologies of titania nanotube can significantly modulate the hydrophilicity/hydrophobicity of the surface and thereby might modulate protein adsorption and subsequent cell responses [41]. Similarly, the improved performance of osteoblasts on nanotubular titania can also be attributed to its similarity to the nanostructure of bone; the osteoblast cells are accustomed to for optimal performance. As discussed earlier the bone is composed of collagen fibers with unique nanotopography and inorganic mineral with average grain sizes below 100 nm [4]. The higher bioreactivity of the titania nanotubes can also be attributed to the optimal initial protein interactions happening on the anodized titanium. The study also suggested that the favorable cell response on nanotubular titania could lead to improved long term performance of the implants by modulating the cellular response in terms of mineralized matrix synthesis.

Therefore, the effect of anodized titanium surfaces on long term osteoblast functions was evaluated in an effort to understand the potential of this process for implant surface modification [41]. The study investigated the response of human osteoblast cells toward nanoparticulate and nanotubular features. The surfaces having nanofeatures with similar chemical compositions were prepared by anodization using hydrofluoric acid for various time periods. Highest osteoblast functions (in terms of mineralized matrix deposition) were observed on nanotube structures in comparison to nanoparticulate structures, thereby supporting the results of the previous study [41] that nanotube surface modification has the potential to significantly improve the osseointegration of bioimplants.

The ability of titania nanotubes in modulating cell responses was confirmed by recent studies using chondrocytes and endothelial cells [42,43]. As in the case of osteoblasts, the nanotube surface showed significantly increased chondrocyte adhesion. The favorable response of chondrocytes toward titania nanostructures with similar chemistry and crystallinity but with significantly greater nanoscale roughness in comparison to unmodified titanium have been attributed to the fact that chondrocytes like the bone cells are accustomed to the well-organized nanostructured collagen matrix. Brammer et al. [43] investigated the effect of titania nanotubes on primary bovine aortic endothelial cell functions. The study demonstrated the ability of nanotube surface to provide nanocues that affect endothelial cell sensing, spreading, and attachment. Cell migration was significantly affected by the vertically aligned yet laterally spaced nanotube topography showing lamellipodia with organized actin cytoskeletal filaments and locomotive morphologies.

2.2.2 Effects of Titania Nanotubes on Stem Cell Proliferation and Differentiation. Apart from the studies evaluating various primary cell responses toward titania nanotubes, a few studies have investigated the effect of titania nanotubes on mesenchymal stem cell proliferation and differentiation. Popat et al. [44] demonstrated the ability of titania nanotubes to improve short term and long term osseointegration by promoting osteoblast differentiation and matrix production using human mesenchymal stem cells cultured in osteogenic media. The mesenchymal stem cells showed higher adhesion, proliferation, exhibited the osteoblastic phenotype characterized by increased alkaline phosphatase activity and bone matrix deposition when cultured on titania nanotubes [45]. The study demonstrated the suitability of titania nanotubes substrate for stem cell based bone regeneration. The study also evalu-

ated the in vivo biocompatibility of the titania nanotubes using a rat subcutaneous model and demonstrated the absence of chronic inflammation or fibrosis of titania nanotubes showing good in vivo biocompatibility [45].

A study by Park et al. [46] evaluated the effect of titania nanotube diameter on stem cell adhesion, spreading, growth, and differentiation. It has been found that diameters less than 30 nm with a maximum at 15 nm strongly enhanced cellular activities. This unique behavior has been attributed to the fact that the diameter range provided an effective length scale for accelerated integrin clustering/focal contact formation. Following the observation of the unique stem cell behavior on surfaces coated with titania nanotubes of varying diameter, another study was undertaken by the same group to evaluate if the observed phenomenon is a specific characteristic of stem cells or reflects a general trend in cell behavior in the context of orthopedic tissue regeneration [47]. The response of two cells relevant to bone regeneration: Osteoblast and osteoclast toward titania nanotubes of different diameters were investigated to demonstrate the nature of cell response to nanofeatures and if the balance between the bone-forming and bone-resorbing capability will be affected by the nanofeatures. Titanium films were anodized with phosphate-fluoride electrolyte at different voltages to form vertically aligned titania nanotubes on the surface having diameters between 15 nm and 100 nm. Osteoclast differentiation of hematopoietic stem cells (HSCs) follow the same trend as the previous study using MSCs with the highest differentiation observed on titania nanotubes having diameters less than 30 nm. The osteoblasts also showed a similar trend with the highest proliferation, enhanced formation of focal contacts, and mineralization on 15 nm tubes in comparison to surfaces having larger size nanotubes or smooth surfaces. Another important observation was that the mineralization of the human osteoblasts cells was not hampered by coculture with osteoclasts on 15 nm nanotubes, while mineralization was not stimulated in coculture on 100 nm nanotubes. The authors concluded that the unique behavior of nanotube surfaces having lower diameters ($\sim$15 nm) can be attributed to the fact that the nanoscale spacing of 15 nm corresponds approximately the diameter of an integrin extracellular domain, and it represents a universal spacing constant supporting a maximum of cellular responses to surfaces. The coculture study points to the fact that the nanoscale microenvironment plays a crucial role in bone cell differentiation even in the presence of complex cell-cell interactions and growth factors. Even though the results are encouraging, further studies are needed to corroborate the results using a wide range of cell types and culture conditions.

These in vitro studies demonstrate that the small scale lateral spacing environment provided by the titania nanotube surface can favorably modulate cell fate and that the feasibility of using titania nanotube as a localized drug and protein delivery vehicle makes it a potential matrix for a variety of therapeutic indications including developing osseointegrated implant systems.

2.2.3 Titania Nanotubes as Drug Delivery Vehicles. The high osteocompatibility of titania nanotube surface also raise interest in using the nanotubes as local drug depots for the sustained delivery of bioactive molecules at the implant tissue interface. A series of studies demonstrated the efficacy of titania nanotubes as localized drug delivery vehicles. Popat et al. [44] investigated the feasibility of using titania nanotubes as a local antibiotic delivery vehicle. The development of localized antibiotic releasing implants will be highly beneficial for reducing implant associated infections and studies have shown that acute infection or chronic osteomyelitis develops in about 5–33% of implant surgeries [48]. Titania nanotubes with 80 nm diameter and 400 nm length were used for the study. Different amounts of gentamicin (200 μg, 400 μg, and 600 μg) were incorporated within the nanotubes via a freeze drying method. The encapsulation process had high loading efficiency (70–85%). The release kinetics was followed in phosphate buffer solution. A slower and sustained release of drug was obtained from the nanotubes with higher drug loading. The antibacterial effect of the gentamicin loaded nanotubes was evaluated after challenging the unmodified and modified films with bacteria. The study showed that the bacterial colonies on titanium and nanotube titanium were much larger than those on titania nanotubes loaded with gentamicin. The osteocompatibility of the gentamicin loaded nanotubes was confirmed by culturing preosteoblast cells, which indicated no significant difference in cell adhesion and proliferation in comparison to titania nanotube surfaces.

Another study demonstrated the efficacy of titania nanotube as a localized protein delivery vehicle [49]. A significant interest has gone to develop protein releasing implants and scaffolds for improving osseointegration since several bioactive macromolecules such as growth factors are implicated in accelerating bone regeneration and tissue in-growth. Titania nanotubes of 80 nm diameter and 400 nanometer length were used in the study. The study evaluated the loading efficiency and release kinetics of two model proteins from titania nanotube surfaces: bovine serum albumin, a high molecular weight protein with a net negative charge at physiological pH and lysozyme, and a small molecular weight protein with a net positive charge at physiological pH. As in the case of antibiotics, the protein loading showed efficiency in the range of 60–80%. Also, a slower and sustained release of protein was obtained from nanotubes with higher initial protein loading. Among the two proteins studied, the positively charged lysozyme showed the slowest release, and it has been attributed to the negatively charged terminal oxide groups on the surface of titania nanotubes. The study clearly demonstrated the potential of using titania nanotube as a localized macromolecular delivery vehicle.

2.2.4 Surface Modification of Titania Nanotubes. Balasundaram et al. [45] demonstrated the feasibility of developing osteogenic titania nanotube structures by immobilizing a 20 amino acid peptide sequence (CKIP-KASSVPTELSAISTLYL) derived from a highly osteogenic molecule "bone morphogenetic protein-2." Titania nanotubes of $\sim$70 nm diameter and 200 nm long were used in the study. The immobilization process involved functionalizing the titania nanotube surface with aminosilane. Scanning electron micrograph (SEM) and atomic force micrograph (AFM) demonstrated slight changes in surface structure after chemical modification. However, the AFM results showed that the root mean square surface roughness values of all forms of functionalized and nonfunctionalized anodized titanium was much higher than that of unanodized titanium. The evaluation of cell response to modified titania nanotubes showed interesting results. The amine functionalized titania nanotubes itself showed significant improvement in osteoblast adhesion. The presence of BMP-2 peptide sequence on titania nanotubes improved osteoblast cell adhesion. The study demonstrated that chemical and biological modifications can be used to improve bone cell adhesion onto titania nanotube surfaces.

In addition to the chemical and biological properties, the physical properties of the titania nanotube surface such as wettability can be significantly modified by appropriate surface modifications. Bauer et al. [50] demonstrated that titania nanotube surfaces having diameters in the range 15–100 nm formed by anodic oxidation is superhydrophilic. The feasibility of varying diameter-dependent wetting behavior has been demonstrated using a self-assembled monolayer process. The wetting behavior ranged from super hydrophilic to hydrophobic (contact angle $\sim 108° \pm 2°$) and to superhydrophobic ($167° \pm 2°$) [47].

2.2.5 In Vivo Studies Using Titania Nanotubes. Studies were performed to evaluate if the increased in vitro bone responses toward titania nanotubes can be translated to increase in vivo bone bonding. However, it is to be noted that the titania nanotube surfaces used for the reported in vitro studies and in vivo studies does not completely match in terms of all their properties, such as diameter, spacing, length, and crystallinity. Therefore, a direct cor-

relation between the in vitro and in vivo results is hard to derive at this point since all these properties of the titania nanotubes (diameter, spacing, length, and crystallinity) collectively contribute to their biological responses.

Wilmowsky et al. [51] determined the efficacy of anodic titania nanotubes in promoting peri-implant bone formation in the frontal skull of pigs and compared the response to the untreated titanium oxide surface. The diameter of the titania nanotubes used in the study was ~30 nm. The in vivo study confirmed that anodic titania nanotubes are able to trigger bone formation around the implant surface by significantly enhancing collagen type-I expression at an early stage of bone formation and bone remodeling. Since collagen I modulate the differentiation and morphogenesis, the authors concluded that the anodic titania nanotubes have an accelerating effect on the differentiation of the surrounding osteoblasts and thereby might trigger fast initialization of bone formation around the modified implants. However, no statistically significant differences in the expression of osteocalcin, an extracellular matrix protein, which is synthesized and secreted during the process of osteoblast differentiation and mineralization, was found between the modified and unmodified implants. This indicates that the nanosurface properties might not be influencing the mineralization process during bone formation and remodeling. Based on the results, the authors concluded that the titania nanotube surface of ~30 nm in diameter could enhance osteoblast function but not the cell proliferation rate. This emphasizes the need to investigate titania nanotubes of different diameters in vivo to find out the optimal size range capable of modulating both cell proliferation and functions. Furthermore, the SEM of the implant surface in the present study revealed that the titania nanotube coatings were not damaged during insertion and hence could resist shearing forces that evoked by implant insertion demonstrating the efficacy of the surface as a drug delivery vehicle.

Bjursten et al. [52] compared the in vivo osseointegration of titania nanotube coated surface to titania gritblasted surface using a rabbit tibial model. The grit blasted surface had a surface roughness of ~6 μm diameter and ~2 μm depth. The surface was covered with an amorphous titanium oxide layer of ~5 nm thick. The titania nanotube surfaces were developed via anodization and the nanotubes were found to have ~100 nm outer diameter, ~80 nm inner diameter, and a height of ~250 nm. The study demonstrated the significantly increased osseointegration of titania nanotube coated implants in comparison to the grit blasted implants. The fracture force required to remove the nanotube implant from the rabbit tibia was significantly greater than for the grit blasted controls (10.8 ± 3.1 N and 1.2 ± 2.7 N, respectively). Furthermore, the titania nanotube implants showed significantly higher bone-implant contact area of $78.3 \pm 33.3\%$ in comparison to $21.7 \pm 24.7\%$ in the case of grit blasted implants. The histological evaluation corroborated this indicating significantly increased bone formation and bone-implant contact in comparison to grit blasted controls. The SEM. Energy dispersive x-ray (EDX) mapping of the interface after tensile testing indicated the presence of high concentrations of calcium and phosphorus on titania nanotube samples, but not on the gritblasted implants surface. The data show that the interface bonding between newly formed bone and titania nanotube surfaces were so strong that the fracture occurred within the growing bone rather than at the implant-bone interface. Thus, the calcium and phosphorous concentrations, which are indicative of strong implant osseointegration, was ~41.7% on titania nanotube surface in comparison to ~8.3% for the grit blasted surface. To confirm the increased osseointegration, a pull out test was performed, which showed as much as ninefold increase in in vivo bone bonding strength of titania nanotube coated implants in comparison to grit blasted implants.

Thus, even though direct correlations between reported in vitro cell behavior and in vivo results cannot be made at this point, these studies show the positive effects of titania nanotubes with diameters in the range 10–100 nm in improving in vivo osseointegration.

3 Conclusions

Surface morphology and roughness have been extensively investigated to modulate and influence cell and tissue responses. When compared with earlier implants with smooth surfaces, porous coatings have found to give mechanical interlocking, bone in growth, and better implant stability. Developments in nanotechnology have raised significant interest in the biomedical field as the unique interactions between nanostructures and cells have been unrevealed. Several nanofabrication methods and nanostructures are currently being investigated for tissue regeneration via the biomimetic approach. The excellent biocompatibility combined with the nanostructure makes titania nanotube a unique substrate for biomedical applications. The in vitro and in vivo studies performed so far clearly demonstrate the efficacy of titania nanotube structures in enhancing osseointegration.

Much of the recent innovation in the titania nanotube field is focused on modifying the nanotube wall and inside for enhanced electronic, optical, and biomedical functionalities. This includes methods of spin-coating, electrodeposition, and electrophoretic trapping to introduce materials of specific functionalities inside the nanotubes. Much of the future work is hence expected to be focused on the control of trapping and release of these species and their effects on biofunctionality.

The versatility of the fabrication processes in terms of creating titania nanotubes of varying diameters, spacing between the nanotubes, crystallinity, and length of the tubes allows for the development of a wide range of surfaces having unique physical, chemical, and biological properties. Since all these parameters can individually and collectively modulate cellular responses, these nanostructures present unique substrates to understand cell-nanostructure interactions and also to design novel regenerative biomaterials that could favorably modulate cellular responses to promote tissue regeneration. Much of the future work in this respect is therefore expected to focus on improving implant functions by modulating the physical and chemical properties of the nanotubes and by locally delivering bioactive molecules in a sustained manner. It is anticipated that these unique nanostructures have the potential to be considered for the development of next generation orthopedic and dental implants.

Acknowledgment

We acknowledge support from NSF EFRI 0736002. N.S. acknowledges assistance from Dr. Lingling Wu on synthesis of titania nanotubes and discussion with Professor Giovanni Zangari, Materials Science at the University of Virginia.

References

[1] Palsson, B., Hubbell, J. A., Plonsey, R., and Bronzino, J. D., eds., 2003, "Tissue Engineering," *Principles and Applications* (Engineering Series), CRC, Boca Raton, FL.

[2] Nair, L. S., Bhattacharya, S., and Laurencin, C. T., 2006, "Nanotechnology and Tissue Engineering: The Scaffold Based Approach," *Nanotechnologies for Life Sciences, Vol. 8: Nanotechnologies for Tissue, Cell and Organ Engineering*, C. Kumar, ed., Wiley, New York, pp. 1–56.

[3] Puckett, S., Pareta, R., and Webster, T. J., 2008, "Nano Rough Micron Patterned Titanium for Directing Osteoblast Morphology and Adhesion," Int. J. Nanomedicine, **3**, pp. 229–241.

[4] Laurencin, C. T., and Nair, L. S., 2008, *Nanotechnology and Tissue Engineering: The Scaffold*, Taylor & Francis, London.

[5] Closkey, R. F., and Buly, R. L., 2001, "Surgical Exposures in Revision Total Hip Arthroplasty," Tech. Orthop., **16**, pp. 222–226.

[6] Burger, N. D. L., de Vaal, P. L., and Meyer, J. P., 2007, "Failure Analysis on Retrieved Ultra High Molecular Weight Polyethylene (UHMWPE) Acetabular Cups," Eng. Failure Anal., **14**, pp. 1329–1345.

[7] Cooper, L. F., 2000, "A Role of Surface Topography in Creating and Maintaining Bone at Titanium Endosseous Implants," J. Prosthet. Dent., **84**, pp. 522–534.

[8] Le Guehennec, L. L., Soueiden, A., Layrolle, P., and Amouriq, Y., 2007, "Surface Treatments of Titanium Dental Implants for Rapid Osseointegration,"

Dent. Mater., **23**, pp. 844–854.
[9] Jonge, L. T., Leeuwenburgh, S. C. G., Wolke, J. G. C., and Janser, J. A., 2008, "Organic-Inorganic Surface Modifications for Titanium Implant Surfaces," Pharm. Res., **25**, pp. 2357–2369.
[10] Schmidmaier, G., Lucke, M., Schwabe, P., Raschke, M., Haas, N. P., and Wildemann, B., 2006, "Collective Review: Bioactive Implants Beta1 or BMP-2 for Stimulation of Fracture Healing," Journal of Long Term Effects of Medical Implants, **16**, pp. 61–69.
[11] Webster, T. J., Ergan, C., Doremus, R. H., Siegel, R. W., and Bizios, R., 2000, "Enhanced Functions of Osteoblasts on Nanophase Ceramics," Biomaterials, **21**, pp. 1803–1810.
[12] Oh, S., Brammer, K. S., Li, Y. S. L., Teng, D., Engler, A. J., Chien, S., and Jin, S., 2009, "Stem Cell Fate Dictated Solely by Altered Nanotube Dimension," Proc. Natl. Acad. Sci. U.S.A., **106**, pp. 2130–2135.
[13] Jung, J. H., Kobayashi, H., van Bommel, K. J. C., Shinkai, S., and Shimizu, T., 2002, "Creation of Novel Helical Ribbon and Double-Layered Nanotube TiO_2 Structures Using an Organogel Template," Chem. Mater., **14**, pp. 1445–1447.
[14] Kasuga, T., Hiramatsu, M., Hoson, A., Sekino, T., and Niihara, K., 1998, "Formation of Titanium Oxide Nanotube," Langmuir, **14**, pp. 3160–3163.
[15] Gong, D., Grimes, C. A., Varghese, O. K., Hu, W., Singh, R. S., Chen, Z., and Dickey, E. C., 2001, "Titanium Oxide Nanotube Arrays Prepared by Anodic Oxidation," J. Mater. Res., **16**, pp. 3331–3334.
[16] Varghese, O. K., Gong, D., Paulose, M., Grimes, C. A., and Dickey, E. C., 2003, "Crystallization and High-Temperature Structural Stability of Titanium Oxide Nanotube Arrays," J. Mater. Res., **18**, pp. 156–165.
[17] Varghese, O. K., Paulose, M., Shankar, K., Mor, G. K., and Grimes, C. A., 2005, "Water-Photolysis Properties of Micro-Length Highly-Ordered Titanate Nanotubes-Arrays," J. Nanosci. Nanotechnol., **5**, pp. 1158–1165.
[18] Chen, Q., Zhou, W. Z., Du, G. H., and Peng, L. M., 2002, "Tritanate Nanotubes Made via a Single Alkali Treatment," Adv. Mater., **14**, pp. 1208–1211.
[19] Chen, Q., Du, G. H., Zhang, S., and Peng, L. M., 2002, "The Structure of Tritinate Nanotubes," Acta Crystallogr. B, **58**, pp. 587–593.
[20] Zhang, S., Peng, L. M., Chen, Q., Du, G. H., Dawson, G., and Zhou W. Z., 2003, "Formation Mechanism of $H_2Ti_3O_7$ Nanotubes," Phys. Rev. Lett., **91**, p. 256103.
[21] Yang, J., Jin, Z., Wang, X., Li, W., Zhang, J., Zhang, S., Guo, X., and Zhang, Z., 2003, "Study on Composition, Structure and Formation Process of Nanotube $Na_2Ti_2O_4(OH)_2$," Dalton Trans., **2003**, pp. 3898–3901.
[22] Chen, X., and Mao, S. S., 2006, "Synthesis of Titanium Dioxide Nanomaterials," J. Nanosci. Nanotechnol., **6**, pp. 906–925.
[23] Yao, C., and Webster, T., 2006, "Anodization: A Promising Nano-Modification Technique of Titanium Implants for Orthopaedic Applications," J. Nanosci. Nanotechnol., **6**, pp. 2682–2692.
[24] Mor, G. K., Varghese, O. K., Paulose, M., Shankar, K., and Grimes, C. A., 2006, "A Review on Highly Ordered, Vertically Oriented TiO_2 Nanotube Arrays: Fabrication, Material Properties and Solar Energy Applications," Sol. Energy Mater. Sol. Cells, **90**, pp. 2011–2075.
[25] Beranek, R., Hildebrand, H., and Schmuki, P., 2003, "Self-Organized Porous Titanium Oxide Prepared in H_2SO_4/HF Electrolytes," Electrochem. Solid-State Lett., **6**, pp. B12–B14.
[26] Macak, J. M., Sirotna, K., and Schmuki, P., 2005, "Self-Organized Porous Titanium Oxide Prepared in Na_2SO_4/NaF Electrolytes," Electrochim. Acta, **50**, pp. 3679–3684.
[27] Macak, J. M., Tsuchiya, H., Taveira, L., and Schmuki, P., 2005, "Smooth Anodic TiO_2 Nanotubes," Angew. Chem., Int. Ed., **44**, pp. 7463–7465.
[28] Paulose, M., Shankar, K., Varghese, O. K., Mor, G. K., and Grimes, C. A., 2006, "Application of Highly-Ordered TiO_2 Nanotube-Arrays in Heterojunction Dye-Sensitized Solar Cells," J. Phys. D: Appl. Phys., **39**, pp. 2498–2503.
[29] Mor, G. K., Varghese, O. K., Paulose, M., and Grimes, C. A., 2005, "Transparent Highly Ordered TiO_2 Nanotube Arrays via Anodization of Titanium Thin Films," Adv. Funct. Mater., **15**, pp. 1291–1296.
[30] Mor, G. K., Shankar, K., Paulose, M., Varghese, O. K., and Grimes, C. A., 2005, "Enhanced Photocleavage of Water Using Titania Nanotube Arrays," Nano Lett., **5**, pp. 191–195.
[31] Allam, N. K., Shankar, K., and Grimes, C. A., 2008, "A General Method for the Anodic Formation of Crystalline Metal Oxide Nanotube Arrays Without the Use of Thermal Annealing," Adv. Mater., **20**, pp. 3942–3946.
[32] Ou, H.-H., and Lo, S.-L., 2007, "Review of Titania Nanotubes Synthesized via the Hydrothermal Treatment: Fabrication, Modification, and Application," Separ. Purif. Technol., **58**, pp. 179–191.
[33] Seo, S., Kim, J. K., and Kim, H., 2001, "Preparation of Nanotube-Shaped TiO_2 Powder," J. Cryst. Growth, **229**, pp. 428–432.
[34] Poudel, B., Wang, W. Z., Dames, C., Huang, J. Y., Kunwar, S., Wang, D. Z., Banerjee, D., Chen, G., and Ren, Z. F., 2005, "Formation of Crystallized Titania Nanotubes and Their Transformation Into Nanowires," Nanotechnology, **16**, pp. 1935–1940.
[35] Yoshida, R., Suzuki, Y., and Yoshikawa, S., 2005, "Effects of Synthetic Conditions and Heat-Treatment on the Structure of Partially Ion-Exchanged Titanate Nanotubes," Mater. Chem. Phys., **91**, pp. 409–416.
[36] Tsai, C. C., and Teng, H., 2004, "Regulation of the Physical Characteristics of Titania Nanotube Aggregates Synthesized From Hydrothermal Treatment," Chem. Mater., **16**, pp. 4352–4358.
[37] Yu, J., Yu, H., Cheng, B., Zhao, X., and Zhang, Q., 2006, "Preparation and Photocatalytic Activity of Mesoporous Anatase TiO_2 Nanofibers by a Hydrothermal Method," J. Photochem. Photobiol., A, **182**, pp. 121–127.
[38] Yuan, Z. Y., Colomer, J. F., and Su, B. L., 2002, "Titanium Oxide Nanoribbons," Chem. Phys. Lett., **363**, pp. 362–366.
[39] Zhu, H. Y., Lan, Y., Gao, X. P., Ringer, S. P., Zheng, R. F., Song, D. Y., and Zhao, J. C., 2005, "Phase Transition Between Nanostructures of Titanate and Titanium Dioxides via Simple Wet-Chemical Reactions," J. Am. Chem. Soc., **127**, pp. 6730–6736.
[40] Oh, S., Daraio, C., Chen, L. H., Pisanic, T. R., Finones, R. R., and Jin, S., 2006, "Significantly Accelerated Osteoblast Cell Growth on Aligned TiO_2 Nanotubes," J. Biomed. Mater. Res. Part A, **78A**, pp. 97–103.
[41] Yao, C., Perla, V., McKenzie, J., Slamovich, E. B., and Webster, T. J., 2005, "Anodized Ti and Ti6Al4V Possessing Nanometer Surface Features Enhances Osteoblast Adhesion," J Biomed Nanotechnol, **1**, pp. 68–73.
[42] Burns, K., Yao, C., and Webster, T. J., 2009, "Increased Chondrocyte Adhesion on Nanotubular Anodized Titanium," J. Biomed. Mater. Res. Part A, **88A**, pp. 561–568.
[43] Brammer, K. S., Oh, S., Gallangher, J. O., and Jin, S., 2008, "Enhanced Cellular Mobility Guided by TiO_2 Nanotube Surfaces," Nano Lett., **8**, pp. 786–793.
[44] Popat, K. C., Eltgroth, M., LaTempa, T. J., Grimes, C. A., and Desai, T. A., 2007, "Decreased Staphylococcus Epidermis Adhesion and Increased Osteoblast Functionality on Antibiotic-Loaded Titania Nanotubes," Biomaterials, **28**, pp. 4880–4888.
[45] Balasundaram, G., Yao, C., and Webster, T. J., 2008, "TiO_2 Nanotubes Functionalized With Regions of Bone Morphogenetic Protein-2 Increases Osteoblast Adhesion," J. Biomed. Mater. Res. Part A, **84A**, pp. 447–453.
[46] Park, J., Bauer, S., Mark, K. V., and Schmuki, P., 2007, "Nanosize and Vitality: TiO_2 Diameter Directs Cell Fate," Nano Lett., **7**, pp. 1686–1691.
[47] Park, J., Bauer, S., Schlegel, K. A., Neukam, F. W., Mark, K. V., and Schmuki, P., 2009, "TiO_2 Nanotube Surfaces: 15 nm—An Optimal Length Scale of Surface Topography for Cell Adhesion and Differentiation," Small, **5**, pp. 666–671.
[48] Hendriks, J. G., van Horn, J. R., van der Mei, H. C., and Busscher, H., 2004, "Backgrounds of Antibiotic Loaded Bone Cement and Prosthesis Related Infection," Biomaterials, **25**, pp. 545–556.
[49] Popat, K. C., Eltgroth, M., LaTempa, T. J., Grimes, C. A., and Desai, T. A., 2007, "Titania Nanotubes: A Novel Platform for Drug Eluting Coatings for Medical Implants," Small, **3**, pp. 1878–1881.
[50] Bauer, S., Park, J., von der Mark, K., and Schmuki, P., 2008, "Improved Attachment of Mesenchymal Stem Cells on Super-Hydrophobic TiO_2 Nanotubes," Acta Biomater., **4**, pp. 1576–1582.
[51] Von Wilmowsky, C., Bauer, S., Lutz, R., Meisel, M., Neukam, F. W., Toyoshima, T., Schmuki, P., Nkenke, E., and Schlegel, K. A., 2009, "*In Vivo* Evaluation of Anodic TiO_2 Nanotubes: An Experimental Study in the Pig," J. Biomed. Mater. Res., Part B: Appl. Biomater., **89B**, pp. 165–171.
[52] Bjursten, L. M., Rasmusson, L., Oh, S., Smith, G. C., Brammer, K. S., and Jin, S., 2010, "Titanium Dioxide Nanotubes Enhance Bone Bonding *In Vivo*," J. Biomed. Mater. Res. Part A, **92**(3), pp. 1218-1224.